UNIVERSTY OF CALIFORNIA

Los Angeles

Fundamental Studies of Two-Dimensional Semiconductor Nanoplatelets: Exploring Photophysics and Synthesis via Kinetic Monte Carlo Method

A dissertation submitted in partial satisfaction

of the requirements for the degree Doctor of Philosophy

in Chemistry

by

Xuanheng Tan

2024

ABSTRACT OF THE DISSERTATION

Fundamental Studies of Two-Dimensional Semiconductor Nanoplatelets:

Exploring Photophysics and Synthesis via Kinetic Monte Carlo Method

by

Xuanheng Tan

Doctor of Philosophy in Chemistry

University of California, Los Angeles, 2024

Professor Justin Ryan Caram, Chair

Semiconductor nanoplatelets (NPLs) are a type of two-dimensional (2D) nanomaterials with quantum confinement in the dimension of thickness. Similar to quantum confined quantum dots (QDs), photophysical properties of NPLs depends strongly on their thickness, but their large size in the unconfined lateral dimensions give rise to their other unique properties. The special 2D geometry also requires anisotropic synthesis in the colloidal solution. In this thesis, I study the photophysical properties and anisotropic growth by combing experiments with a powerful tool of kinetic Monte Carlo methods.

Chapter 1 provides a review of the development of quantum confined nanocrystals on including discussions on their photophysical properties and anisotropic growth, gives a brief introduction to the kinetic Monte Carlo methods, and proposed some challenges in the field this thesis aims to address.

In chapter 2, we propose a quantitative model of fluorescence quenching based on energy transfer mechanism of Förster Resonance Energy Transfer (FRET) for binary mixtures of nanocrystals in colloidal solutions in the short-wavelength infrared (SWIR) region. This model is used to explain the fluorescence quenching of long-lifetime lead sulfide (PbS) quantum dots (QDs) mixed with plasmonic covellite copper sulfide (CuS) nanodisks (NDs), which serve as perfect fluorescent quenchers. By applying kinetic Monte Carlo methods which consider particle distributions and diffusion we are able to quantitatively reproduce experimental data which shows significant quenching at very small concentrations of NDs. The high concentration case is examined by conducting similar mixing experiments of mercury telluride (HgTe) NPLs and QDs, where we specifically discuss the impact of geometry on the distance dependence of energy transfer efficiency.

Chapter 3 deals with a classic yet still puzzling phenomena in single-nanocrystal: photoluminescence intermittency (blinking). We apply Marcus theory of electron transfer to the blinking model of carrier trapping and detrapping, with meticulous mathematical analysis and kinetic Monte Carlo modeling. With canonical distribution of trap state energy, we quantitatively explain the difference between on and off time statistic in blinking cadmium telluride (CdTe) NPLs, as well as the temperature dependence of their quantum yield.

In chapter 4, we focus on the anisotropic growth of NPLs, more specifically the different behaviors between cadmium selenide (CdSe) and cadmium telluride (CdTe) NPLs in terms of thickness selectivity and lateral size. We propose a simple kinetic model with 3 most important energetic parameters, on which kinetic Monte Carlo simulations of lattice are based. Using population percentage and evolution of size distribution from correlation function analysis, we offer a reasonable answer to questions regarding the difference of CdSe and CdTe NPLs.

Finally, in chapter 5 we describe some of our ongoing effort towards further understanding of NPLs and QDs of interest, including using machine learning (ML) method to assist the optimization of synthetic conditions of NPLs and an in-depth study of correlation growth/ripening mechanisms with size distribution of QDs.

The dissertation of Xuanheng Tan is approved.

Chong Liu

Daniel Neuhauser

Benjamin Joel Schwartz

Justin Ryan Caram, Committee Chair

University of California, Los Angeles

2024

To my mom and dad, for their love and support

TABLE OF CONTENTS

Chapter 1 Introduction to Two-Dimensional Semiconductor Nanoplatelets and Kinetic Monte Carlo Method 1

1.1 History of Quantum Confined Semiconductor Nanocrystals (NCs) 1

1.2 Photophysical Properties of Two-dimensional (2D) Semiconductor Nanoplatelets (NPLs).4

1.3 Growth Mechanisms of Two-dimensional (2D) Semiconductor Nanoplatelets (NPLs) 7

1.4 Kinetic Monte Carlo (KMC) Methods and Applications in Chemistry.....9

1.5 Conclusions.....11

References.....13

Chapter 2 On the Inadequacy of Stern-Volmer and FRET in Describing Quenching in Binary Donor-Acceptor Solutions 36

2.1 Importance of Förster Resonance Energy Transfer (FRET) for SWIR-Emitting Nanocrystals (NCs).....37

2.2 Synthesis of PbS Quantum Dots (QDs) and Covellite CuS Nanodisks (NDs).....39

2.3 Comparison of Experiments to Analytical and Simulated Quenching Behaviors.....43

2.4 Results of Simulations and Role of FRET Radius and Diffusion in Quenching.....47

2.5 Near-field FRET: Ex-situ Mixing of HgTe QDs and NPLs and 2D-0D Energy Transfer 51

2.6 Conclusion 54

2.7 Experimental Details.....55

2.8 Supporting Information.....58

References.....77

Chapter 3 Applying Marcus Theory to Describe Photoluminescent Intermittency and Temperature Dependent Emission in CdTe Nanoplatelets.....86

3.1 Photoluminescence Intermittency (Blinking): Impact and Current Mechanisms.....87

3.2 Synthesis and Blinking Measurements of CdTe Nanoplatelets (NPLs).....89

3.3 Quantitative Analysis on the Power-law Distribution of On- and Off- Times.....92

3.4 Temperature Dependence of PLQY.....99

3.5 Conclusion.....104

3.6 Experimental Details.....106

3.7 Supporting Information.....108

References.....119

Chapter 4 Kinetic Monte Carlo Simulation Assisted Study of Anisotropic Growth of Semiconductor Nanoplatelets.....129

4.1 Observed Difference in Anisotropic Growth of CdSe and CdTe Nanoplatelets (NPLs).....130

4.2 Synthesis of 3 Monolayer (ML) CdTe Nanoplatelets (NPLs) with Heterostructures.....132

4.3 Correlation of 4 ML and Mid-gap Emission with 3 ML NPLs: Confirmation of Heterostructure.....135

4.4 Kinetic Monte Carlo (KMC) Simulations of Nanoplatelets (NPLs) Growth.....139

4.5 Conclusion.....143

4.6 Experimental Details.....144

4.7 Supporting Information.....148

References.....163

Chapter 5 Future Work and Perspectives 171

5.1 Machine Learning Assisted Study of Anisotropic Growth of Nanoplatelets (NPLs) 171

5.2 Growth Mechanisms of HgTe Quantum Dots (QDs) and Evolution of Size Distribution 174

References 177

LIST OF FIGURES

Figure 1.1 Quantum confinement effect in semiconductor nanocrystals (NCs).....2

Figure 1.2 Photophysical properties of semiconductor nanoplatelets (NPLs).....6

Figure 1.3 Mechanisms of anisotropic growth of 2D nanoplatelets (NPLs) 8

Figure 1.4 Kinetic Monte Carlo (KMC) method and applications in materials and chemistry...10

Figure 2.1 Synthesized PbS QDs and covellite CuS nanodisks (NDs) and titration experiments 41

Figure 2.2 Titration experiments and possible models of fluorescence quenching.....42

Figure 2.3 Comparison of quenching ratio-CuS NDs concentration curves between experiments and different models/simulations.....46

Figure 2.4 A color-coded map of enhancement of quenching ratio by diffusion with changing diffusion length and FRET radius at different quencher concentrations 49

Figure 2.5 Model for studying the distance dependence of NPL-QD FRET system 52

Figure 2.6 Size distribution of PbS QDs (top) and CuS NDs.....59

Figure 2.7 TEM image of the mixture of PbS QDs and CuS NDs 59

Figure 2.8 Absorption spectra of a series of CuS NDs solutions and linear fitting of absorbance-concentration for extracting extinction coefficient 60

Figure 2.9 Experimental setup for steady-state PL measurements 61

Figure 2.10 Correction for IFE and comparison between experiment quenching ratio after IFE correction and simulations 62

Figure 2.11 A plot of quenching ratio-quencher concentration for titration experiments showing non-linear dependence 63

Figure 2.12 Time-resolved PL trace and fitting result of PbS QDs.....64

Figure 2.13 An example of mono-exponential fitting of time-resolved PL trace of PbS-CuS mixture 65
Figure 2.14 An example of bi-exponential fitting of time-resolved PL trace of PbS-CuS mixture 66
Figure 2.15 Experimental time-resolved PL traces of pure PbS and quenched PbS samples 67
Figure 2.16 Number of quenching events monitored over time in the simulations.....67
Figure 2.17 Visualization of the box used in kMC simulations 68
Figure 2.18 A control simulation of pure PbS QDs.....70
Figure 2.19 2D diagram of distance sphere and diffusion sphere.....71
Figure 2.20 Functional dependence of the scaling factor on $(\frac{d}{r})^2$ 73
Figure 2.21 Non-linearity dependence predicted by crystalline defect model at higher quencher concentrations 74
Figure 2.22 Quenching enhancement by diffusion for a pair of cyanine dyes 75
Figure 3.1 Synthesized 3 ML CdTe nanoplatelets (NPLs) and analysis of blinking.....90
Figure 3.2 Possible models for explaining "distributed kinetics" and their predictions on time distributions.....92
Figure 3.3 Comparison of analytical and simulated results between normal region and inverted region of Marcus theory.....98
Figure 3.4 Experimental and theoretical study on temperature dependence of PLQY of blinking 3 ML CdTe NPLs.....100
Figure 3.5 Reconstruction and confirmation of energetic structure with extracted parameters ..104
Figure 3.6 Incomplete gamma functions describing the theoretical results for distributions of time with 3 different attempt frequencies 109

Figure 3.7 Energy diagram of Marcus theory 110
Figure 3.8 QY calculation at low temperature and at high temperature 115
Figure 3.9 Simulation of blinking based on Gaussian distribution of trap state energies 118
Figure 4.1 Synthesis and spectroscopic characterization of 3 ML CdTe NPLs 133
Figure 4.2 Correlation between emission spectra and images from PL microscopy measurements 137
Figure 4.3 Correlation of emission spectra and AFM measurements 138
Figure 4.4 Kinetic Monte Carlo (KMC) simulations on thickness ripening of 2D nanoplatelets (NPLs) 141
Figure 4.5 Extracting size distribution from pair correlation function (PCF) based on the simulation 144
Figure 4.6 2D fitting of PL images 151
Figure 4.7 PL images and 2D fitting results for 3ML and 4 ML hetero-structure 155
Figure 4.8 PL images and 2D fitting results for mixture of 2 ML and 3 ML 155
Figure 4.9 Spectra of aliquots during growth period 156
Figure 4.10 PL lifetime of CdTe NPLs 157
Figure 4.11 Emission spectra of CdTe NPLs 158
Figure 4.12 AFM image of CdTe NPLs 159
Figure 4.13 PL blinking trace of CdTe NPLs 160
Figure 4.14 Transient absorption spectra 161
Figure 4.15 Tuning E_a and Temperature in simulations 162
Figure 5.1 A workflow of applying machine learning method to the study of NPLs growth 174
Figure 5.2 Connecting mechanisms of growth with time evolution of emission spectra 175

LIST OF TABLES

Table 1.1 Type and Chemical Compositions of Semiconductor Nanocrystals (NCs).....3

Table 2.1 Parameters used in modeling and simulations.....40

Table 2.2 Mono-exponential fitting parameters of experimental time-resolved PL traces 64

Table 2.3 Bi-exponential fitting parameters of experimental time-resolved PL traces 65

Table 2.4 Parameters for cyanine dyes 75

Table 3.1 Examples of power-law exponents values for blinking materials 106

Table 4.1 PL decay parameters of NPLs probed at different emission wavelength.....157

ACKNOWLEDGMENTS

It has been more than 20 years since I started this journey of studying and exploring, from the elementary school in my hometown in China, all the way to the PhD program in UCLA. Looking back at my life at this point, I feel glad as well as fortunate that I was able to reach one milestone after another through this journey, and this achievement would never be possible without all the help I received from people I met along the road. I would like to express my sincere gratitude to the following people.

First, I would like to thank my supervisor Justin Caram. I joined Justin's group with interest in projects related to physical chemistry of nanomaterials, and it turned out to be an excellent fit for me, in terms of both science and style. Justin is a great resource of knowledge on physics and chemistry, with a broad vision of science overall. It is a great pleasure to work with Justin as he provides me just the push I need to explore more possibilities of science, as well as support and encouragement. Justin, thank you for being an intelligent and supportive advisor.

I would also like to thank my committee, Chong Liu, Daniel Neuhauser and Benjamin Schwartz. Chong is an amazing teacher and I learned a lot about electrochemistry in his course. Danny's courses are important windows for me to gain more knowledge about theorists' work. Ben gave me insightful feedbacks in my candidacy exam. All committee members provided useful suggestions about program progress and career development that help me shape the future ahead.

I am extremely grateful to be able to work with all the amazing members of Caram lab. Tim Atallah, you encouraged me to trust myself to be a scientist and gave me many good advice on my presentations for candidacy exam. Stephanie Tenney, I feel extremely lucky to be able to learn from you when I first joined the group, and I am deeply motivated by your passion about research. Barry Li, you are a knowledgeable theorist and thank you for so many good discussions

on all kinds of scientific questions. Ashley Shin, thank you for your heartwarming concern when I am away from my family during challenging times. Anthony Sica and Ash Hua, you are the experts on spectroscopy and thank you for your help with taking all the spectra for my projects. Anu Deshmukh and Hannah Friedman, thank you for all of your help for my candidacy exam and useful discussions about science. Tasnim Ahmed, Eugenia Vasileiadou, Belle Coffey, Elijah Cook and Caleb Pike, you are all doing amazing work in our subgroup of nanocrystals, and it sparkled many inspirations for my projects. Jill Williams, Richard Liu, Yongjia He, Arthur Odenheimer and Lexi Wright, it is always joyful to have you around in the office. Jesus Hernandez, Sohan Jadhav and Jae Lee, we didn't get to spend much time together in the group but I am sure you will do impactful research in the near future. I am also fortunate enough to get to know some of the best undergraduate students: Laurie Tan, Ricky Ronquillo and Linus Murphy, you did great research and it is a pleasure to share my points of view on science with you. I wish everyone in Caram lab a bright future and happy life.

Last but not least, I would like to thank my friends and my family. Yifei Chen, you were the best deskmate I had in high school and I still missed the time we got to hang out together in the first 3 years in UCLA. Zhouyi He, we talked about our life in graduate school a lot via facetime and it is very pressure-lifting. Finally, mom and dad, you always encourage and respect me to make my own decisions, and you always support me to explore all the different opportunities in life. I could never be who I am today without you. I love you all so much.

This work was supported by NSF Career Award No. 1945572. I would like to thank the Graduate Division at UCLA for fellowships I received. I would also like to acknowledge the California NanoSystems Institute (CNSI) and Materials Instrumentation Center (MIC) at UCLA for allowing me to use instrumentation for conducting my research.

Chapter 2 contains work from the published paper "Tan, X.; Caram, J. R. On the Inadequacy of Stern-Volmer and FRET in Describing Quenching in Binary Donor-Acceptor Solutions. *J. Chem. Phys.* **2023**, *158* (20). https://doi.org/10.1063/5.0148170." and results I contributed to the paper "Tenney, S. M.; Tan, L. A.; Tan, X.; Sonnleitner, M. L.; Coffey, B.; Williams, J. A.; Ronquillo, R.; Atallah, T. L.; Ahmed, T.; Caram, J. R. Efficient 2D to 0D Energy Transfer in HgTe Nanoplatelet-Quantum Dot Heterostructures through High-Speed Exciton Diffusion. *J. Phys. Chem. Lett.* **2023**, *14* (42), 9456–9463. https://doi.org/10.1021/acs.jpclett.3c02168.".

Chapter 3 contains unpublished work from "Tan, X.; Ahmed, T.; Murphy, L.; Coffey, B.; Caram, J.R. Applying Marcus Theory to Describe Photoluminescent Intermittency and Temperature Dependent Emission in CdTe Nanoplatelets. *ChemRxiv*. 2024. https://10.26434/chemrxiv-2024-zcggj." This work is under peer review at the time of finishing this thesis.

Chapter 4 contains unpublished work from "Ahmed, T.; Tan, X.; Li, B.; Williams, J.; Cook, E.; Tiano, S.; Tenney, S. M.; Hayes, D.; Caram, J. R. Hetero-confinement in Single CdTe Nanoplatelets. *ChemRxiv*. 2024. https://doi:10.26434/chemrxiv-2024-85hg8." This work is under peer review at the time of finishing this thesis.

Chapter 5 contains unpublished work and considerations by Xuanheng Tan, Belle Coffey, Caleb Pike, Linus Murphy, Lucas Tecot and Justin Caram.

BIOGRAPHICAL SKETCH

Education

2021 M.S. in Chemistry

University of California, Los Angeles (UCLA)

2019 B.S. in Chemistry

University of Science and Technology of China (USTC)

Selected Publications

6. **Tan, X.**; Ahmed, T.; Murphy, L.; Coffey, B.; Caram, J.R. Applying Marcus Theory to Describe Photoluminescent Intermittency and Temperature Dependent Emission in CdTe Nanoplatelets. *ChemRxiv*. **2024**. https://10.26434/chemrxiv-2024-zcggj.

5. Ahmed, T.; **Tan, X.**; Li, B.; Williams, J.; Cook, E.; Tiano, S.; Tenney, S. M.; Hayes, D.; Caram, J. R. Hetero-confinement in Single CdTe Nanoplatelets. *ChemRxiv*. **2024**. https://doi:10.26434/chemrxiv-2024-85hg8.

4. Tenney, S. M.; Tan, L. A.; **Tan, X.**; Sonnleitner, M. L.; Coffey, B.; Williams, J. A.; Ronquillo, R.; Atallah, T. L.; Ahmed, T.; Caram, J. R. Efficient 2D to 0D Energy Transfer in HgTe Nanoplatelet-Quantum Dot Heterostructures through High-Speed Exciton Diffusion. *J. Phys. Chem. Lett.* **2023**, *14* (42), 9456–9463. https://doi.org/10.1021/acs.jpclett.3c02168.

3. **Tan, X.**; Caram, J. R. On the Inadequacy of Stern-Volmer and FRET in Describing Quenching in Binary Donor-Acceptor Solutions. *J. Chem. Phys.* **2023**, *158* (20). https://doi.org/10.1063/5.0148170.

2. Shin, A. J.; Hossain, A. A.; Tenney, S. M.; **Tan, X.**; Tan, L. A.; Foley, J. J.; Atallah, T. L.; Caram, J. R. Dielectric Screening Modulates Semiconductor Nanoplatelet Excitons. *J. Phys. Chem. Lett.* **2021**, *12* (20), 4958–4964. https://doi.org/10.1021/acs.jpclett.1c00624.

1. Yu, Y.; **Tan, X.**; Ning, S.; Wu, Y. Machine Learning for Understanding Compatibility of Organic-Inorganic Hybrid Perovskites with Post-Treatment Amines. *ACS Energy Lett.* **2019**, *4* (2), 397–404. https://doi.org/10.1021/acsenergylett.8b02451.

Awards and Honors

2019 Graduate with Honors

2018 National Scholarship

2017 Outstanding Student Scholarship, 1st prize

2016 8412 Scholarship

2015 Outstanding Freshman Scholarship. 2nd Prize

Chapter 1

Introduction to Two-Dimensional Semiconductor Nanoplatelets and Kinetic Monte Carlo Method

1.1 History of Quantum Confined Semiconductor Nanocrystals (NCs)

It has been over 40 years since the first synthesis of small semiconductor crystallite, more commonly known as "quantum dots (QDs)", a category of materials with sizes on the scale of several nanometers, and discovers of which were awarded The Nobel Prize in Chemistry in 2023. In 1981, Aleksey Ekimov and Alexei Onushchenko first studied small crystalline phase of copper chloride (CuCl) dispersed in insulated transparent glass matrix.[1] Independently in 1983, Louis Brus reported the synthesis of small crystalline cadmium sulfide (CdS) in colloidal solution.[2] Along with the progress in experiments, theoretical efforts have also been made since 1982 to understand the optical features of QDs, which is believed to inherit the properties of bulk materials possessing the same chemical compositions, with additional influence from the small size effect. To describe the formed bound state of an exciton when an electron is promoted across the band gap to conduction band in a semiconductor, creating a positively charged hole in valence band, we use the hydrogenic Hamiltonian:

$$\widehat{H} = -\frac{\hbar^2}{2m_h}\nabla_h^2 - \frac{\hbar^2}{2m_e}\nabla_e^2 - \frac{e^2}{\varepsilon|r_e - r_h|} \tag{1.1}$$

where m_h and m_e are the effective mass of hole and electron, respectively, and the third term describes the Coulomb interaction between electron and hole.[3] The size effect of a semiconductor depends on 2 characterizing distances, namely the electron Bohr radius $a_e = \frac{\hbar^2\mathcal{E}}{m_e e^2}$ and the hole Bohr radius $a_h = \frac{\hbar^2\mathcal{E}}{m_h e^2}$.[4] When the size of crystallite is reduced to be less than the electron and hole Bohr radius, the quantum confinement effect due to the small size starts to play a role in the

quantization of the states (Figure 1.1a).[5] This can be captured by simply considering the model of particle in a spherical box, where the energy of bound states depends on the size of the box (namely QDs):

$$E_n = \frac{\hbar^2 \pi^2 n^2}{8\mu R^2}, n = 1,2,3, \ldots \quad (1.2)$$

where $\mu = \frac{m_e m_h}{m_e + m_h}$ is the reduced exciton mass and R is the radius of the spherical QDs. Under above circumstances, more specifically in the regime of strong confinement, the Coulomb interaction term in equation (1.1) is small and can be treated as a perturbation.[6,7] The expression for energy of the lowest excited states of QDs is then given by:

$$E = E_g + \frac{\hbar^2 \pi^2}{8\mu R^2} - \frac{1.8e^2}{\varepsilon R} \quad (1.3)$$

where E_g is the bulk band gap. The second and third term represents the quantum confinement energy and Coulomb interaction, respectively. This reflects the increase in the spectral energy when decreasing the size of QDs (Figure 1.1b).

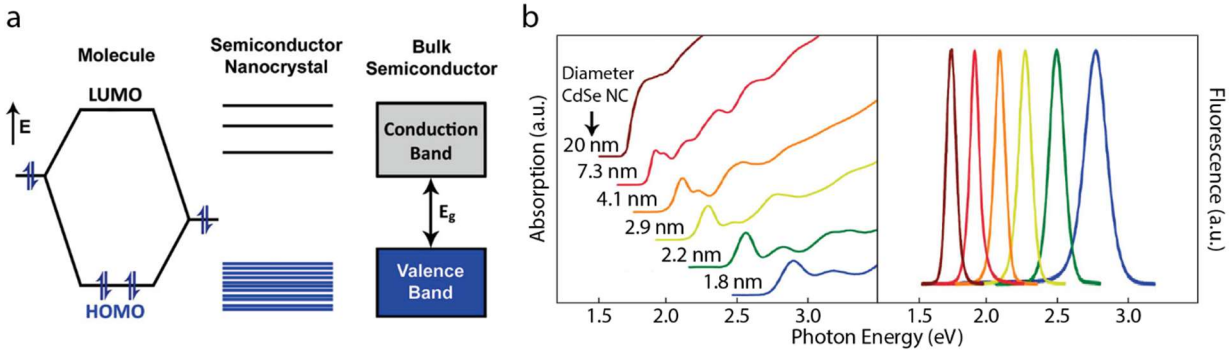

Figure 1.1 Quantum confinement effect in semiconductor nanocrystals (NCs). (a) Comparison among electronic states of molecule, semiconductor nanocrystal and bulk semiconductor. (b) Size dependence of absorption (left) and fluorescence (right) spectra of cadmium selenide (CdSe) NCs. The photon energy increases with decreasing sizes. Adapted from Ref 8, copyright 2010 American Chemical Society.[8]

In 1993, Moungi Bawendi and coworkers successfully synthesized monodisperse cadmium chalcogenide (CdX, X = S, Se, Te) QDs through a simple route based on pyrolysis of organometallic precursors by fast hot injection into a coordinating solvent, resulting in sharp

absorption and strong emission features due to organic capping ligands.[9] Simultaneously in early 1990s, another approach to mitigating the emergence of mid-gap states in QDs was applied in the synthesis by adding extra layers of inorganic composite, namely the core/shell structure.[10–13] In 1996, the two strategies above were combined to produce high-quality core/shell QDs with monodisperse core materials, including CdSe/ZnS QDs and CdSe/ZnSe QDs, which showed strong fluorescence insensitive to environmental exposure.[14,15] The invention of core/shell structure also opened up more opportunities of band-gap engineering of QDs through the band alignment between core and shell materials.[8]

Since the discovery of QDs in 1980s, the scope of these materials has been significantly expanded in terms of chemistry and morphology. QDs with various chemical compositions including some alloyed systems have been successfully synthesized, bringing an extensive amount of color in electromagnetic spectrum into the world of nanomaterials (Table 1.1). Other breakthroughs took place in the morphology of NCs through transitions from QDs, known as

Table 1.1 Type and Chemical Compositions of Semiconductor Nanocrystals (NCs)

Type	Chemical Compositions	Reference
I-VI	$Cu_{2-x}S$, $Cu_{2-x}Se$, $Cu_{2-x}Se_{1-y}S_y$	Ref 16-20[16–20]
	Ag_2S, Ag_2Se, Ag_2Te	Ref 21-28[21–28]
I-VII	CuCl, AgBr	Ref 1, 29-32[1,29–32]
I-II-IV-VI	Cu_2ZnSnS_4, $Cu_2ZnSnSe_4$, $Cu_2ZnSn(S_{1-y}Se_y)_4$, $Cu_2Zn(Sn_{1-x}Ge_x)(S_{1-y}Se_y)_4$	Ref 33-39[33–39]
	Ag_2ZnSnS_4, $Ag_2ZnSnSe_4$	Ref 40-42[40–42]
I-III-VI	$CuAlS_2$, $CuGaS_2$, $CuGaSe_2$, $CuInS_2$, $CuInSe_2$, $CuInTe_2$, $Cu(In_{1-x}Ga_x)Se_2$, $CuFeS_2$, $CuFeSe_2$	Ref 43-50[43–50]
	$AgGaS_2$, $AgGaSe_2$, $AgInS_2$, $AgInSe_2$, $AgInTe_2$, $AgFeS_2$	Ref 51-56[51–56]
II-VI	MX (M = Zn, Cd, Hg; X = S, Se, Te), ZnO	Ref 57-63[57–63]
	$Cd_{1-x}Zn_xSe$, $CdSe_{1-y}Te_y$	Ref 64, 65[64,65]
III-V	GaAs, InP, InAs	Ref 66-69[66–69]
IV	Si, Ge	Ref 70, 71[70,71]
IV-VI	PbS, PbSe, PbTe, $PbS_{1-y}Se_y$	Ref 72-75[72–75]
Perovskite	$CsPbX_3$, $CsSnX_3$, $MAPbX_3$, $FAPbX_3$ (X = Cl, Br, I)[a]	Ref 76-79[76–79]

[a] MA = methylammonium, $CH_3NH_3^+$; FA = formamidinium, $H_2NCH{=}NH_2^+$.

zero-dimensional (0D) materials due to confinement in all 3 dimensions, to other low-dimensional NCs including one-dimensional (1D) materials like nanowires and nanorods as well as two-dimensional (2D) materials such as nanosheets and nanoplatelets (NPLs). Anisotropic growth of these non-QDs materials usually involves careful control of monomer concentration and selective binding of capping ligands in solution-based synthesis, vapor-liquid-solid (VLS) and vapor-solid-solid (VSS) mechanisms in chemical vapor deposition (CVD), vapor-solid mechanism without using catalysts in physical vapor deposition (PVD), or templated growth through CVD, electrodeposition and atomic layer deposition (ALD).[80–96] In particular, our interest in the field is focused mostly on II-VI and IV-VI nanocrystals, including CdSe NPLs, CdTe NPLs, HgTe NPLs, HgTe QDs and PbS QDs.

Until nowadays, semiconductor NCs have been not only studied in the laboratories, but also utilized in a variety of scientific and technical applications, including photodetector, quantum information, light-emitting diodes (LEDs) and display, photocatalysis, photovoltaic energy conversion, bioimaging and biosensing, medical diagnosis and therapy, etc.[97–116] With further understanding and development of these materials, they will make more significant impact on every aspects of our life.

1.2 Photophysical Properties of Two-dimensional (2D) Semiconductor Nanoplatelets (NPLs)

2D semiconductor NPLs are also influenced by the quantum confinement effect similar to QDs, but the confinement only takes effect in the dimension of thickness, leaving NPLs two degrees of freedom in other two unconfined dimensions. In fact, the dimensionality of NCs plays an important role when considering their density of states (DoS), resulting in different spectral features. DoS of bulk (3D) semiconductor materials follows the functional form of $\sqrt{E}$, while DoS

of nanoplatelets (also known as quantum well; 2D), nanowires (1D) and QDs (0D) take the form of $\theta(E)$ (step functions), $\frac{1}{\sqrt{E}}$ and $\delta(E)$ (delta functions), respectively (Figure 1.2a).[117] As a result, spectra of semiconductor NPLs demonstrate thickness dependence similar to QDs (Figure 1.2b). Consisting of excitonic and continuum features, the absorption spectra of NPLs are further complicated by their band structures, where the valence band is split into three sub-bands: heavy-hole (HH), light-hole (LH) and spin-orbit (SO) bands, (Figure 1.2c).[118,119] The extinction coefficients $\varepsilon(E)$, a measure of light absorption on the basis of per particle or concentration, are generally much higher for NPLs than QDs with same chemical composition due to the large lateral area of NPLs.[120] Peak positions in absorption spectra are also dependent on the dielectric environment of the NPLs, as a result of changing exciton binding energy.[121]

The photoluminescence (PL) spectrum is another intriguing realm of the photophysical properties of NPLs. Similar to absorption spectra, PL traces show thickness-dependent emission energy (Figure 1.2b). Broad features with photon energy lower than band gap can be commonly observed in PL spectra, as a result of mid-gap emission arising from surface defects or doping.[122–124] Mid-gap emission can be mitigated by introducing strong passivating ligands or core/shell and core/crown structures in synthesis, improving quantum yield (QY) of NPLs as well.[125–128] Unlike QDs which suffer from PL broadening due to size polydispersity, the line width of ensemble of NPLs has much smaller discrepancy with that of single-NPL, due to precise synthetic control of thickness of NPLs (Figure 1.2d).[118] Another characteristic feature in emission spectrum of single-NPL is PL intermittency (blinking), a phenomena of temporal fluctuations of PL intensity even under continuous radiation that is also existing in single-QD (Figure 1.2e).[126,129] Blinking is often attributed to trapping and detrapping of charge carriers that switches the system between on-state cycling of absorption and fluorescence and off-state cycling of absorption and non-radiative Auger

recombination.[130,131]. Further explorations on the mechanisms of blinking will be given in chapter 3. Dynamics of NPLs show a temperature dependence where fluorescence lifetime decreases at lower temperature, which is considered to be a unique feature of giant oscillator strength because exciton scattering by phonon is suppressed at lower temperature, enlarging the coherent area of exciton motion to the entire lateral extent of NPLs (Figure 1.2f).[118,132]

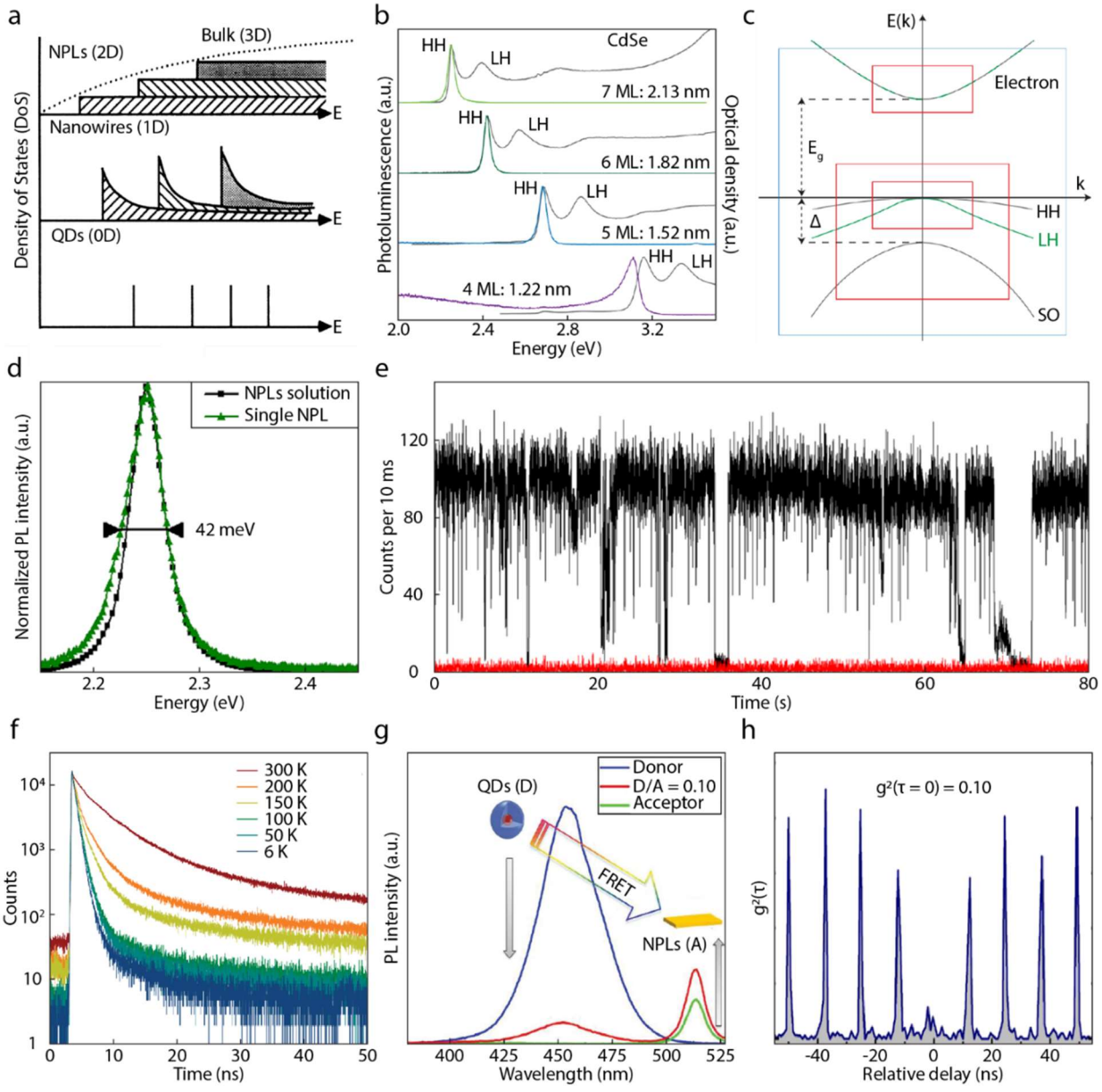

Figure 1.2 Photophysical properties of semiconductor nanoplatelets (NPLs). (a) Density of states for semiconductors with different morphology (degree of freedom). (b) Absorption and PL spectra of CdSe NPLs with different number of monolayer (ML) and thickness. (c) Band diagram of semiconductor NPLs

showing split valence band. (d) PL spectra of CdSe NPLs solution and single-NPL showing nearly identical linewidth. (e) Time traces for PL intensity of single CdSe/CdS core/shell NPLs showing PL intermittency (blinking). (f) Temperature dependence of fluorescence lifetime of CdSe NPLs. (g) PL spectra of QDs-NPLs donor-acceptor system demonstrating FRET process. (h) Second-order PL intensity correlation measured for a single $CsPbBr_3$ NPL with features of antibunching. Figure a adapted from Ref 117, copyright 2002 World Scientific Publishing Company.[117] Figure b, c and f adapted from Ref 118, copyright 2011 Springer Nature Limited.[118] Figure d adapted from Ref 133, copyright 2012 American Chemical Society.[133] Figure e adapted from Ref 126, copyright 2013 American Chemical Society.[126] Figure g adapted from Ref 134, copyright 2016 WILEY-VCH Verlag GmbH & Co. KGaA, Weinheim.[134] Figure h adapted from Ref 135, copyright 2020 American Chemical Society.[135]

Some photophysical properties of NPLs are advantageous when considering practical utilizations of the materials. For example, due to the large extinction coefficient, NPLs typically have high rates of Förster resonance energy transfer (FRET), making them promising materials for optoelectronic applications (Figure 1.2g).[134,136] Efforts towards the quantitative elucidation of FRET processes in binary solutions of nanocrystals will be presented in chapter 2. An alternative approach is the Dexter energy transfer (DET) processes in organic-NPL hybrid composite where energy harvesting is made possible through upconversion.[137] Last but not least, NPLs also have the potential to be used as single-photon emitters in quantum information for their narrow spectral features and convenient scalability (Figure 1.2h).[135,138,139]

1.3 Growth Mechanisms of Two-dimensional (2D) Semiconductor Nanoplatelets (NPLs)

The first synthesis of quantum well structure was achieved by Joo et al. in 2006 where CdSe nanoribbons with quantum well structure were produced through solution-phase synthesis.[140] In 2008, the 2D CdSe NPLs with relatively large 2D area were first successfully synthesized by Ithurria et al. in colloidal solution.[122] Similar to QDs, core/shell structure were synthesized in solution using CdSe NPLs as core materials and shell materials growing on both top and bottom facets.[141,142] Another type of heterostructures related to NPLs, namely core/crown structures have also been synthesized where the growth of shell only extends the lateral area of NPLs cores without changing thickness.[143–145] Other than traditional solution-based synthesis of core/shell heterostructures, a method called colloidal-ALD (c-ALD) has also been used, where

self-limiting half reactions of depositing cations and anions are sequentially carried out through phase-transfer or proper ligand passivation.[146] For NPLs with some chemical compositions that are challenging for direct synthesis, an alternative approach of cation exchange has been used to achieve 2D morphology.[147,148] Effort has also been dedicated to expanding the lateral area of NPL through a technique of seeded growth.[149]

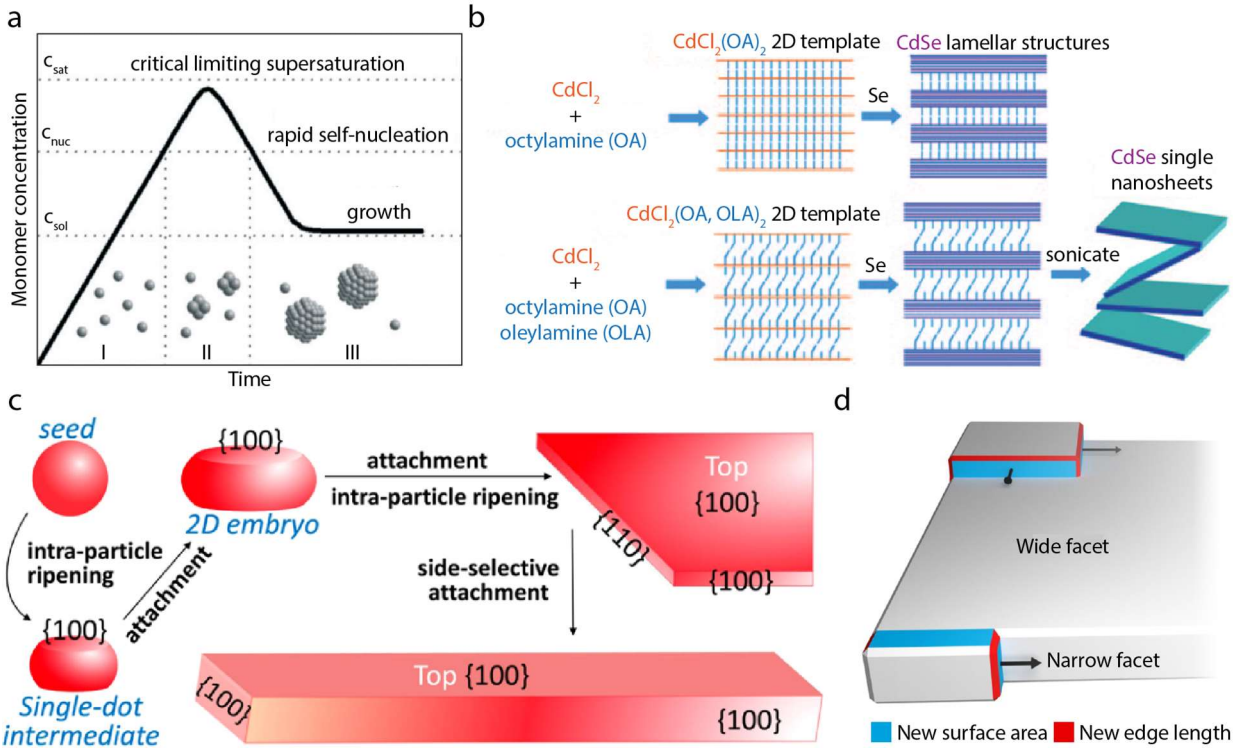

Figure 1.3 Mechanisms of anisotropic growth of 2D nanoplatelets (NPLs). (a) LaMer model of nucleation and growth. (b) Templated growth of 2D CdSe nanosheets with lamellar structures. (c) Self-assembly and oriented attachment mechanism of the growth of CdSe NPLs. (d) Quantitative model of anisotropic growth based on energy change for different dimensions. Figure a adapted from Ref 150, copyright 2015 The Royal Society of Chemistry.[150] Figure b adapted from Ref 151, copyright 2009 WILEY-VCH Verlag GmbH & Co. KGaA, Weinheim.[151] Figure c adapted from Ref 152,copyright 2017 American Chemical Society.[152] Figure d adapted from Ref 153, copyright 2017 Macmillan Publishers Limited, part of Springer Nature.[153]

Beyond synthetic procedures, the underlying mechanisms of anisotropic growth is of great interest. The general theory that is used to describe the growth of NCs is the LaMer model, where the synthetic reactions of NCs are considered to be a 3-phase process: in the first phase, the precursors decompose and react to form monomers, resulting in rising of monomer concentration; in the second phase, when the monomer concentration accumulates to exceed the minimal

concentration of "burst nucleation", the activation barrier for nucleation is overcome and the monomers start to coalesce into nuclei clusters, causing the monomer concentration to decrease; in the last phase, the nucleation stops and the monomers only attach to existing nuclei to grow NCs (Figure 1.3a).[150] The relatively simple LaMer model was used to describe the synthesis of crystals and QDs with isotropic spherical shape.[154] For anisotropic growth of 2D NPLs, it is important to clarify the possible mechanisms of shape control. One of the proposed models is inspired by the fact that the choice of ligands is highly influential in determining the shape of NCs.[155–157] The templated growth model is based on the formation of lamellar templates by dissolving precursor in organic ligands (Figure 1.3b).[151,158] Another mechanism proposed that the formation of 2D structures was achieved by self-assembly of nuclei in the growth step, namely oriented attachment, where adjacent clusters rearrange to certain orientations to form NPLs by decreasing the surface energy at the interface (Figure 1.3c).[152,159] Riedinger et al. proposed a model of quantitative analysis on energy change for different dimensions (Figure 1.3d).[153] This provides a foundation for further detailed investigation on anisotropic growth of 2D semiconductor NPLs, which becomes more and more necessary with the emergence of an increasing amount of experimental observations in synthetic reactions. In chapter 4, more detailed studies on anisotropic growth of NPLs inspired by the Riedinger model will be described.

1.4 Kinetic Monte Carlo (KMC) Methods and Applications in Chemistry

The origin of Monte Carlo method date back to early 20th century when it was proposed by a group of researchers at Los Alamos including Nicholas Metropolis, John von Neumann and Stanilaw Ulam in late 1940s. This method was considered as a "mid-ground" solution for physical problems, as other two popular methods at the time were classical mechanics and statistical mechanics, which worked well for small-scale problems involving only a few particles and large-

scale problems focusing on a large ensemble of particles, respectively. By considering a moderate number of particles bound a series of constraints, one can get distributions of properties that reflects physical processes of a real system satisfying the same constraining conditions, without the necessity of solving differential equations or probability matrices. It is worth mentioning that this method was only made possible due to the development of modern computers which can produce random numbers with realistic distributions of parameters and calculate values of parameters through algebraic calculations. In fact, the computational method got its name after a district famous for casinos in Monaco, hinting its connection with gambling in terms of randomness. It provides us with a new way of approaching the answers towards physical problems by combining stochastic sampling and deterministic calculations.[160] Later in 1975, Bortz, Kalos and Lebowitz developed a new algorithm for Monte Carlo situations known as BKL algorithm with significantly higher computational efficiency.[161]

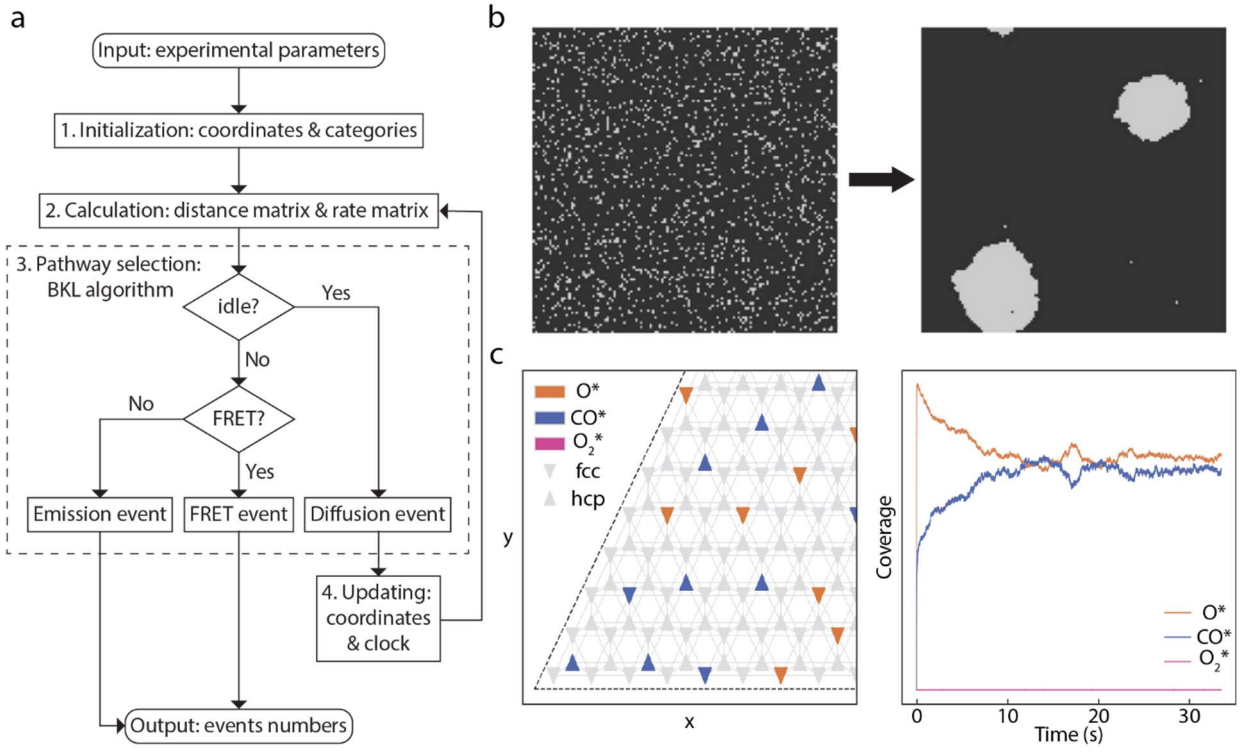

Figure 1.4 Kinetic Monte Carlo (KMC) method and applications in materials and chemistry. (a) Flowchart of general KMC algorithm. (b) KMC simulated process of vacancy diffusion. (c) Heterogeneous catalysis of

CO oxidation on Pd (111) facet modeled using KMC methods. Left: a snapshot of desorption sites; right: temporal evolution of species coverage on the surface of catalysts. Figure b adapted from Ref 162, copyright 2008 Elsevier B.V.[162] Figure c adapted from Ref 163, copyright 2022 AIP Publishing.[163]

The kinetic Monte Carlo (KMC) method takes the knowledge of kinetic processes in the system, and as a result produces temporal evolution of the system. Generally, the KMC simulation is carried out in this way: first, the initial values of parameters are required as input of the program; 1. the rate matrix is calculated depending on the specific kinetic problems of interest; 2. with the rate matrix and random number generator (RNG), the system further goes through the pathway selection to determine the outcome; 3. the global clock is advanced, and the changes to the system are recorded to be used in a new round of rate calculation; finally, the frequency of events and generated times are given as the results to describe the temporal evolution (Figure 1.4a). KMC method has been applied in studies in a series of realms such as materials science and chemistry, including vacancy diffusion in materials and heterogeneous catalysis (Figure 1.4b and c).[162,164,165] The following chapters will demonstrate my effort of applying

1.5 Conclusions

Among all the interesting properties of NPLs, several topics remain open to discussion and exploration. For example, the energy transfer processes including FRET was understudied in mixture of nanocrystals solutions, due to the lack of analytical description about spatial distribution of binary solution. On the other hand, some long-standing observations on blinking phenomena have not been explained very well. Last but not least, new challenges arise for mechanism of anisotropic growth of NPLs since more and more new experimental evidences emerges as new frontiers of synthetic reactions. Having noticed that there is a large gap of theoretical and fundamental understanding on these questions regarding NPLs, my thesis focused on applying the tried and true kinetic Monte Carlo method to the investigations of photophysical properties and growth mechanisms of 2D semiconductor NPLs.

In chapter 2, I combine my paper as first author "Tan, X.; Caram, J. R. On the Inadequacy of Stern-Volmer and FRET in Describing Quenching in Binary Donor-Acceptor Solutions. *J. Chem. Phys.* **2023**, *158* (20). https://doi.org/10.1063/5.0148170." with the results I contributed to the paper "Tenney, S. M.; Tan, L. A.; Tan, X.; Sonnleitner, M. L.; Coffey, B.; Williams, J. A.; Ronquillo, R.; Atallah, T. L.; Ahmed, T.; Caram, J. R. Efficient 2D to 0D Energy Transfer in HgTe Nanoplatelet-Quantum Dot Heterostructures through High-Speed Exciton Diffusion. *J. Phys. Chem. Lett.* **2023**, *14* (42), 9456–9463. https://doi.org/10.1021/acs.jpclett.3c02168.", which both deal with the dynamics of energy transfer process in the mixture of nanocrystals.

Chapter 3 contains unpublished work from "Tan, X.; Ahmed, T.; Murphy, L.; Coffey, B.; Caram, J.R. Applying Marcus Theory to Describe Photoluminescent Intermittency and Temperature Dependent Emission in CdTe Nanoplatelets. *ChemRxiv*. 2024. https://10.26434/chemrxiv-2024-zcggj." This work is under peer review at the time of finishing this thesis. In this chapter I discuss the application of Marcus theory as an intuitive and reasonable foundation for explaining various blinking phenomena with quantitative accuracy.

Chapter 4 contains unpublished work from "Ahmed, T.; Tan, X.; Li, B.; Williams, J.; Cook, E.; Tiano, S.; Tenney, S. M.; Hayes, D.; Caram, J. R. Hetero-confinement in Single CdTe Nanoplatelets. *ChemRxiv*. 2024. https://doi:10.26434/chemrxiv-2024-85hg8." This work is under peer review at the time of finishing this thesis. In chapter 4, a simple model of anisotropic growth of NPLs with minimal physics and kinetic Monte Carlo simulations based on it are described, and they are capable of answering some novel questions about ripening and lateral growth.

REFERENCES

(1) Ekimov, A. I.; Onushchenko, A. A. Quantum Size Effect in Three-Dimensional Microscopic Semiconductor Crystals. *JETP Lett.* **1981**, *34* (6), 345–349.

(2) Rossetti, R.; Nakahara, S.; Brus, L. E. Quantum Size Effects in the Redox Potentials, Resonance Raman Spectra, and Electronic Spectra of CdS Crystallites in Aqueous Solution. *J. Chem. Phys.* **1983**, *79* (2), 1086–1088. https://doi.org/10.1063/1.445834.

(3) Brus, L. E. Electron–Electron and Electron-Hole Interactions in Small Semiconductor Crystallites: The Size Dependence of the Lowest Excited Electronic State. *J. Chem. Phys.* **1984**, *80* (9), 4403–4409. https://doi.org/10.1063/1.447218.

(4) Efros, A. L.; Efros, A. L. Interband Light Absorption in Semiconductor Spheres. *Sov. Phys. Semicond.* **1982**, *16* (7), 772–775.

(5) Alivisatos, A. P. Perspectives on the Physical Chemistry of Semiconductor Nanocrystals. *J. Phys. Chem.* **1996**, *100* (31), 13226–13239. https://doi.org/10.1021/jp9535506.

(6) Bawendi, M. G.; Steigerwald, M. L.; Brus, L. E. The Quantum Mechanics of Larger Semiconductor Clusters ("Quantum Dots"). *Annu. Rev. Phys. Chem.* **1990**, *41* (1), 477–496. https://doi.org/10.1146/annurev.pc.41.100190.002401.

(7) Yoffe, A. D. Low-Dimensional Systems: Quantum Size Effects and Electronic Properties of Semiconductor Microcrystallites (Zero-Dimensional Systems) and Some Quasi-Two-Dimensional Systems. *Adv. Phys.* **1993**, *42* (2), 173–262. https://doi.org/10.1080/00018739300101484.

(8) Smith, A. M.; Nie, S. Semiconductor Nanocrystals: Structure, Properties, and Band Gap Engineering. *Acc. Chem. Res.* **2010**, *43* (2), 190–200. https://doi.org/10.1021/ar9001069.

(9) Murray, C. B.; Norris, D. J.; Bawendi, M. G. Synthesis and Characterization of Nearly

Monodisperse CdE (E = Sulfur, Selenium, Tellurium) Semiconductor Nanocrystallites. *J. Am. Chem. Soc.* **1993**, *115* (19), 8706–8715. https://doi.org/10.1021/ja00072a025.

(10) Kortan, A. R.; Hull, R.; Opila, R. L.; Bawendi, M. G.; Steigerwald, M. L.; Carroll, P. J.; Brus, L. E. Nucleation and Growth of CdSe on ZnS Quantum Crystallite Seeds, and Vice Versa, in Inverse Micelle Media. *J. Am. Chem. Soc.* **1990**, *112* (4), 1327–1332. https://doi.org/10.1021/ja00160a005.

(11) Hoener, C. F.; Allan, K. A.; Bard, A. J.; Campion, A.; Fox, M. A.; Mallouk, T. E.; Webber, S. E.; White, J. M. Demonstration of a Shell-Core Structure in Layered CdSe-ZnSe Small Particles by x-Ray Photoelectron and Auger Spectroscopies. *J. Phys. Chem.* **1992**, *96* (9), 3812–3817. https://doi.org/10.1021/j100188a045.

(12) Eychmüller, A.; Mews, A.; Weller, H. A Quantum Dot Quantum Well: CdS/HgS/CdS. *Chem. Phys. Lett.* **1993**, *208* (1–2), 59–62. https://doi.org/10.1016/0009-2614(93)80076-2.

(13) Mews, A.; Eychmueller, A.; Giersig, M.; Schooss, D.; Weller, H. Preparation, Characterization, and Photophysics of the Quantum Dot Quantum Well System Cadmium Sulfide/Mercury Sulfide/Cadmium Sulfide. *J. Phys. Chem.* **1994**, *98* (3), 934–941. https://doi.org/10.1021/j100054a032.

(14) Hines, M. A.; Guyot-Sionnest, P. Synthesis and Characterization of Strongly Luminescing ZnS-Capped CdSe Nanocrystals. *J. Phys. Chem.* **1996**, *100* (2), 468–471. https://doi.org/10.1021/jp9530562.

(15) Danek, M.; Jensen, K. F.; Murray, C. B.; Bawendi, M. G. Synthesis of Luminescent Thin-Film CdSe/ZnSe Quantum Dot Composites Using CdSe Quantum Dots Passivated with an Overlayer of ZnSe. *Chem. Mater.* **1996**, *8* (1), 173–180. https://doi.org/10.1021/cm9503137.

(16) Klimov, V.; Haring Bolivar, P.; Kurz, H.; Karavanskii, V.; Krasovskii, V.; Korkishko, Y.

Linear and Nonlinear Transmission of Cux S Quantum Dots. *Appl. Phys. Lett.* **1995**, *67*, 653. https://doi.org/10.1063/1.115192.

(17) Yumashev, K. V.; Prokoshin, P. V.; Malyarevich, A. M.; Mikhailov, V. P.; Artemyev, M. V.; Gurin, V. S. Optical Transient Bleaching and Induced Absorption of Surface-Modified Copper Sulfide Nanocrystals. *Appl. Phys. B Lasers Opt.* **1996**, *64* (1), 73–78. https://doi.org/10.1007/s003400050147.

(18) Yumashev, K. V.; Gurin, V. S.; Prokoshin, P. V.; Prokopenko, V. B.; Alexeenko, A. A. Nonlinear Optical Properties and Laser Applications of Copper Chalcogenide Quantum Dots in Glass. *Phys. status solidi* **2001**, *224* (3), 815–818. https://doi.org/10.1002/(SICI)1521-3951(200104)224:3<815::AID-PSSB815>3.0.CO;2-H.

(19) Kumar, P.; Singh, K. Synthesis, Characterizations, and Optical Properties of Copper Selenide Quantum Dots. *Struct. Chem.* **2011**, *22* (1), 103–110. https://doi.org/10.1007/s11224-010-9698-3.

(20) Tong, X.; Li, X.; Channa, A. I.; Liu, R.; Xu, J.-Y.; Yu, P.; Chang, L.; Ji, H.; Wang, Q.; Wang, Z. M. Engineering the Optoelectronic Properties of Colloidal Alloyed Copper Chalcogenide Quantum Dots for High-Efficiency Solar Energy Conversion. *Sol. RRL* **2019**, *3* (10), 1–8. https://doi.org/10.1002/solr.201900186.

(21) Motte, L.; Lacaze, E.; Maillard, M.; Pileni, M. P. Influence of the Substrate on the Self-Assemblies of Silver Sulfide Nanocrystals. *Appl. Surf. Sci.* **2000**, *162–163* (16), 604–612. https://doi.org/10.1016/S0169-4332(00)00258-0.

(22) Du, Y.; Xu, B.; Fu, T.; Cai, M.; Li, F.; Zhang, Y.; Wang, Q. Near-Infrared Photoluminescent Ag 2 S Quantum Dots from a Single Source Precursor. *J. Am. Chem. Soc.* **2010**, *132* (5), 1470–1471. https://doi.org/10.1021/ja909490r.

(23) Yarema, M.; Pichler, S.; Sytnyk, M.; Seyrkammer, R.; Lechner, R. T.; Fritz-Popovski, G.; Jarzab, D.; Szendrei, K.; Resel, R.; Korovyanko, O.; Loi, M. A.; Paris, O.; Hesser, G.; Heiss, W. Infrared Emitting and Photoconducting Colloidal Silver Chalcogenide Nanocrystal Quantum Dots from a Silylamide-Promoted Synthesis. *ACS Nano* **2011**, *5* (5), 3758–3765. https://doi.org/10.1021/nn2001118.

(24) Gu, Y.-P.; Cui, R.; Zhang, Z.-L.; Xie, Z.-X.; Pang, D.-W. Ultrasmall Near-Infrared Ag 2 Se Quantum Dots with Tunable Fluorescence for in Vivo Imaging. *J. Am. Chem. Soc.* **2012**, *134* (1), 79–82. https://doi.org/10.1021/ja2089553.

(25) Zhang, Y.; Hong, G.; Zhang, Y.; Chen, G.; Li, F.; Dai, H.; Wang, Q. Ag 2 S Quantum Dot: A Bright and Biocompatible Fluorescent Nanoprobe in the Second Near-Infrared Window. *ACS Nano* **2012**, *6* (5), 3695–3702. https://doi.org/10.1021/nn301218z.

(26) Dong, B.; Li, C.; Chen, G.; Zhang, Y.; Zhang, Y.; Deng, M.; Wang, Q. Facile Synthesis of Highly Photoluminescent Ag 2 Se Quantum Dots as a New Fluorescent Probe in the Second Near-Infrared Window for in Vivo Imaging. *Chem. Mater.* **2013**, *25* (12), 2503–2509. https://doi.org/10.1021/cm400812v.

(27) Liu, Z.-Y.; Liu, A.-A.; Fu, H.; Cheng, Q.-Y.; Zhang, M.-Y.; Pan, M.-M.; Liu, L.-P.; Luo, M.-Y.; Tang, B.; Zhao, W.; Kong, J.; Shao, X.; Pang, D.-W. Breaking through the Size Control Dilemma of Silver Chalcogenide Quantum Dots via Trialkylphosphine-Induced Ripening: Leading to Ag 2 Te Emitting from 950 to 2100 Nm. *J. Am. Chem. Soc.* **2021**, *143* (32), 12867–12877. https://doi.org/10.1021/jacs.1c06661.

(28) Hafiz, S. B.; Scimeca, M. R.; Zhao, P.; Paredes, I. J.; Sahu, A.; Ko, D.-K. Silver Selenide Colloidal Quantum Dots for Mid-Wavelength Infrared Photodetection. *ACS Appl. Nano Mater.* **2019**, *2* (3), 1631–1636. https://doi.org/10.1021/acsanm.9b00069.

(29) Johansson, K. P.; Marchetti, A. P.; McLendon, G. L. Effect of Size Restriction on the Static and Dynamic Emission Behavior of Silver Bromide. *J. Phys. Chem.* **1992**, *96* (7), 2873–2879. https://doi.org/10.1021/j100186a018.

(30) Masumoto, Y.; Kawamura, T.; Ohzeki, T.; Urabe, S. Lifetime of Indirect Excitons in AgBr Quantum Dots. *Phys. Rev. B* **1992**, *46* (3), 1827–1830. https://doi.org/10.1103/PhysRevB.46.1827.

(31) Chen, W.; McLendon, G.; Marchetti, A.; Rehm, J. M.; Freedhoff, M. I.; Myers, C. Size Dependence of Radiative Rates in the Indirect Band Gap Material AgBr. *J. Am. Chem. Soc.* **1994**, *116* (4), 1585–1586. https://doi.org/10.1021/ja00083a060.

(32) Correa, N. M.; Zhang, H.; Schelly, Z. A. Preparation of AgBr Quantum Dots via Electroporation of Vesicles. *J. Am. Chem. Soc.* **2000**, *122* (27), 6432–6434. https://doi.org/10.1021/ja000073i.

(33) Liu, W. C.; Guo, B. L.; Wu, X. S.; Zhang, F. M.; Mak, C. L.; Wong, K. H. Facile Hydrothermal Synthesis of Hydrotropic Cu2ZnSnS4 Nanocrystal Quantum Dots: Band-Gap Engineering and Phonon Confinement Effect. *J. Mater. Chem. A* **2013**, *1* (9), 3182. https://doi.org/10.1039/c3ta00357d.

(34) Rajesh, G.; Muthukumarasamy, N.; Subramanian, E. P.; Venkatraman, M. R.; Agilan, S.; Ragavendran, V.; Thambidurai, M.; Velumani, S.; Yi, J.; Velauthapillai, D. Solution-Based Synthesis of High Yield CZTS (Cu 2 ZnSnS 4) Spherical Quantum Dots. *Superlattices Microstruct.* **2015**, *77*, 305–312. https://doi.org/10.1016/j.spmi.2014.11.016.

(35) Zeng, X.; Xiong, D.; Zhang, W.; Ming, L.; Xu, Z.; Huang, Z.; Wang, M.; Chen, W.; Cheng, Y.-B. Spray Deposition of Water-Soluble Multiwall Carbon Nanotube and Cu2ZnSnSe4 Nanoparticle Composites as Highly Efficient Counter Electrodes in a Quantum Dot-Sensitized Solar Cell System. *Nanoscale* **2013**, *5* (15), 6992. https://doi.org/10.1039/c3nr01564e.

(36) Colombara, D.; Robert, E. V. C.; Crossay, A.; Taylor, A.; Guennou, M.; Arasimowicz, M.; Malaquias, J. C. B.; Djemour, R.; Dale, P. J. Quantification of Surface ZnSe in Cu2ZnSnSe4-Based Solar Cells by Analysis of the Spectral Response. *Sol. Energy Mater. Sol. Cells* **2014**, *123*, 220–227. https://doi.org/10.1016/j.solmat.2014.01.015.

(37) Guo, Q.; Ford, G. M.; Yang, W.-C.; Walker, B. C.; Stach, E. A.; Hillhouse, H. W.; Agrawal, R. Fabrication of 7.2% Efficient CZTSSe Solar Cells Using CZTS Nanocrystals. *J. Am. Chem. Soc.* **2010**, *132* (49), 17384–17386. https://doi.org/10.1021/ja108427b.

(38) Singh, A.; Singh, S.; Levcenko, S.; Unold, T.; Laffir, F.; Ryan, K. M. Compositionally Tunable Photoluminescence Emission in Cu 2 ZnSn(S 1− x Se x) 4 Nanocrystals. *Angew. Chemie Int. Ed.* **2013**, *52* (35), 9120–9124. https://doi.org/10.1002/anie.201302867.

(39) Guo, Q.; Ford, G. M.; Yang, W.-C.; Hages, C. J.; Hillhouse, H. W.; Agrawal, R. Enhancing the Performance of CZTSSe Solar Cells with Ge Alloying. *Sol. Energy Mater. Sol. Cells* **2012**, *105*, 132–136. https://doi.org/10.1016/j.solmat.2012.05.039.

(40) Saha, A.; Figueroba, A.; Konstantatos, G. Ag 2 ZnSnS 4 Nanocrystals Expand the Availability of RoHS Compliant Colloidal Quantum Dots. *Chem. Mater.* **2020**, *32* (5), 2148–2155. https://doi.org/10.1021/acs.chemmater.9b05370.

(41) Saha, A.; Konstantatos, G. Ag 2 ZnSnS 4 –ZnS Core–Shell Colloidal Quantum Dots: A near-Infrared Luminescent Material Based on Environmentally Friendly Elements. *J. Mater. Chem. C* **2021**, *9* (17), 5682–5688. https://doi.org/10.1039/D1TC00421B.

(42) Gershon, T.; Sardashti, K.; Gunawan, O.; Mankad, R.; Singh, S.; Lee, Y. S.; Ott, J. A.; Kummel, A.; Haight, R. Photovoltaic Device with over 5% Efficiency Based on an N-Type Ag 2 ZnSnSe 4 Absorber. *Adv. Energy Mater.* **2016**, *6* (22). https://doi.org/10.1002/aenm.201601182.

(43) Bhattacharyya, B.; Pandit, T.; Rajasekar, G. P.; Pandey, A. Optical Transparency Enabled

by Anomalous Stokes Shift in Visible Light-Emitting CuAlS 2 -Based Quantum Dots. *J. Phys. Chem. Lett.* **2018**, *9* (15), 4451–4456. https://doi.org/10.1021/acs.jpclett.8b01787.

(44) Ma, W.; Zhang, Z.; Ma, M.; Liu, Y.; Pan, G.; Gao, H.; Mao, Y. CuGaS2 Quantum Dots with Controlled Surface Defects as an Hole-Transport Material for High-Efficient and Stable Perovskite Solar Cells. *Sol. Energy* **2020**, *211* (September), 55–61. https://doi.org/10.1016/j.solener.2020.09.058.

(45) Malik, S. N.; Mahboob, S.; Haider, N.; Malik, M. A.; O'Brien, P. A Colloidal Synthesis of CuInSe2, CuGaSe2 and CuIn1−xGaxSe2 Nanoparticles from Diisopropyldiselenophosphinatometal Precursors. *Nanoscale* **2011**, *3* (12), 5132. https://doi.org/10.1039/c1nr10888c.

(46) Li, T.-L.; Lee, Y.-L.; Teng, H. High-Performance Quantum Dot-Sensitized Solar Cells Based on Sensitization with CuInS2quantum Dots/CdS Heterostructure. *Energy Environ. Sci.* **2012**, *5* (1), 5315–5324. https://doi.org/10.1039/C1EE02253A.

(47) Allen, P. M.; Bawendi, M. G. Ternary I-III-VI Quantum Dots Luminescent in the Red to near-Infrared. *J. Am. Chem. Soc.* **2008**, *130* (29), 9240–9241. https://doi.org/10.1021/ja8036349.

(48) Kim, S.; Kang, M.; Kim, S.; Heo, J.-H.; Noh, J. H.; Im, S. H.; Seok, S. Il; Kim, S.-W. Fabrication of CuInTe 2 and CuInTe 2– x Se x Ternary Gradient Quantum Dots and Their Application to Solar Cells. *ACS Nano* **2013**, *7* (6), 4756–4763. https://doi.org/10.1021/nn401274e.

(49) Bhattacharyya, B.; Pandey, A. CuFeS 2 Quantum Dots and Highly Luminescent CuFeS 2 Based Core/Shell Structures: Synthesis, Tunability, and Photophysics. *J. Am. Chem. Soc.* **2016**, *138* (32), 10207–10213. https://doi.org/10.1021/jacs.6b04981.

(50) Jiang, X.; Zhang, S.; Ren, F.; Chen, L.; Zeng, J.; Zhu, M.; Cheng, Z.; Gao, M.; Li, Z. Ultrasmall Magnetic CuFeSe 2 Ternary Nanocrystals for Multimodal Imaging Guided

Photothermal Therapy of Cancer. *ACS Nano* **2017**, *11* (6), 5633–5645. https://doi.org/10.1021/acsnano.7b01032.

(51) Li, X.; Tong, X.; Yue, S.; Liu, C.; Channa, A. I.; You, Y.; Wang, R.; Long, Z.; Zhang, Z.; Zhao, Z.; Liu, X.-F.; Wang, Z. M. Rational Design of Colloidal AgGaS2/CdSeS Core/Shell Quantum Dots for Solar Energy Conversion and Light Detection. *Nano Energy* **2021**, *89* (PA), 106392. https://doi.org/10.1016/j.nanoen.2021.106392.

(52) Li, T.; Liu, C.; Li, R.; Huang, X.; Qi, X.; Mi, X.; Bai, T.; Xing, S. Luminescent AgGaSe 2 /ZnSe Nanocrystals: Rapid Synthesis, Color Tunability, Aqueous Phase Transfer, and Bio-Labeling Application. *Dalt. Trans.* **2023**, *52* (14), 4554–4561. https://doi.org/10.1039/D2DT03979F.

(53) Hamanaka, Y.; Ogawa, T.; Tsuzuki, M.; Kuzuya, T. Photoluminescence Properties and Its Origin of AgInS2 Quantum Dots with Chalcopyrite Structure. *J. Phys. Chem. C* **2011**, *115* (5), 1786–1792. https://doi.org/10.1021/jp110409q.

(54) Deng, D.; Qu, L.; Gu, Y. Near-Infrared Broadly Emissive AgInSe2/ZnS Quantum Dots for Biomedical Optical Imaging. *J. Mater. Chem. C* **2014**, *2* (34), 7077–7085. https://doi.org/10.1039/c4tc01147c.

(55) Langevin, M.-A.; Pons, T.; Ritcey, A. M.; Nì. Allen, C. Near-Infrared Emitting AgInTe2 and Zn-Ag-In-Te Colloidal Nanocrystals. *Nanoscale Res. Lett.* **2015**, *10* (1), 255. https://doi.org/10.1186/s11671-015-0951-y.

(56) Peng, X.; Liu, J.; Ming, C.; Li, B.; Zhao, Z.; Ye, K.; Zeng, M.; Zou, R.; Lu, X.; Hu, J. AgFeS 2 Nanoparticles as a Novel Photothermal Platform for Effective Artery Stenosis Therapy. *Nanoscale* **2020**, *12* (20), 11288–11296. https://doi.org/10.1039/D0NR01587C.

(57) Brus, L. Electronic Wave Functions in Semiconductor Clusters: Experiment and Theory.

J. Phys. Chem. **1986**, *90* (12), 2555–2560. https://doi.org/10.1021/j100403a003.

(58) Zhang, L.; Yin, L.; Wang, C.; Lun, N.; Qi, Y.; Xiang, D. Origin of Visible Photoluminescence of ZnO Quantum Dots: Defect-Dependent and Size-Dependent. *J. Phys. Chem. C* **2010**, *114* (21), 9651–9658. https://doi.org/10.1021/jp101324a.

(59) Rajh, T.; Micic, O. I.; Nozik, A. J. Synthesis and Characterization of Surface-Modified Colloidal Cadmium Telluride Quantum Dots. *J. Phys. Chem.* **1993**, *97* (46), 11999–12003. https://doi.org/10.1021/j100148a026.

(60) Lincheneau, C.; Amelia, M.; Oszajca, M.; Boccia, A.; D'Orazi, F.; Madrigale, M.; Zanoni, R.; Mazzaro, R.; Ortolani, L.; Morandi, V.; Silvi, S.; Szaciłowski, K.; Credi, A. Synthesis and Properties of ZnTe and ZnTe/ZnS Core/Shell Semiconductor Nanocrystals. *J. Mater. Chem. C* **2014**, *2* (16), 2877–2886. https://doi.org/10.1039/C3TC32385D.

(61) Higginson, K. A.; Kuno, M.; Bonevich, J.; Qadri, S. B.; Yousuf, M.; Mattoussi, H. Synthesis and Characterization of Colloidal β-HgS Quantum Dots. *J. Phys. Chem. B* **2002**, *106* (39), 9982–9985. https://doi.org/10.1021/jp026232x.

(62) Howes, P.; Green, M.; Johnston, C.; Crossley, A. Synthesis and Shape Control of Mercury Selenide (HgSe) Quantum Dots. *J. Mater. Chem.* **2008**, *18* (29), 3474. https://doi.org/10.1039/b804158j.

(63) Keuleyan, S.; Lhuillier, E.; Guyot-Sionnest, P. Synthesis of Colloidal HgTe Quantum Dots for Narrow Mid-IR Emission and Detection. *J. Am. Chem. Soc.* **2011**, *133* (41), 16422–16424. https://doi.org/10.1021/ja2079509.

(64) Fitzmorris, B. C.; Pu, Y.-C.; Cooper, J. K.; Lin, Y.-F.; Hsu, Y.-J.; Li, Y.; Zhang, J. Z. Optical Properties and Exciton Dynamics of Alloyed Core/Shell/Shell Cd 1– x Zn x Se/ZnSe/ZnS Quantum Dots. *ACS Appl. Mater. Interfaces* **2013**, *5* (8), 2893–2900.

https://doi.org/10.1021/am303149r.

(65) Elibol, E. Synthesis of near Unity Photoluminescence CdSeTe Alloyed Quantum Dots. *J. Alloys Compd.* **2020**, *817*, 152726. https://doi.org/10.1016/j.jallcom.2019.152726.

(66) Zhai, L.; Löbl, M. C.; Nguyen, G. N.; Ritzmann, J.; Javadi, A.; Spinnler, C.; Wieck, A. D.; Ludwig, A.; Warburton, R. J. Low-Noise GaAs Quantum Dots for Quantum Photonics. *Nat. Commun.* **2020**, *11* (1), 4745. https://doi.org/10.1038/s41467-020-18625-z.

(67) Chen, B.; Li, D.; Wang, F. InP Quantum Dots: Synthesis and Lighting Applications. *Small* **2020**, *16* (32), 1–20. https://doi.org/10.1002/smll.202002454.

(68) Guzelian, A. A.; Banin, U.; Kadavanich, A. V.; Peng, X.; Alivisatos, A. P. Colloidal Chemical Synthesis and Characterization of InAs Nanocrystal Quantum Dots. *Appl. Phys. Lett.* **1996**, *69* (10), 1432–1434. https://doi.org/10.1063/1.117605.

(69) Olshavsky, M. A.; Goldstein, A. N.; Alivisatos, A. P. Organometallic Synthesis of Gallium-Arsenide Crystallites, Exhibiting Quantum Confinement. *J. Am. Chem. Soc.* **1990**, *112* (25), 9438–9439. https://doi.org/10.1021/ja00181a080.

(70) Cheng, X.; Lowe, S. B.; Reece, P. J.; Gooding, J. J. Colloidal Silicon Quantum Dots: From Preparation to the Modification of Self-Assembled Monolayers (SAMs) for Bio-Applications. *Chem. Soc. Rev.* **2014**, *43* (8), 2680–2700. https://doi.org/10.1039/C3CS60353A.

(71) Heath, J. R.; Shiang, J. J.; Alivisatos, A. P. Germanium Quantum Dots: Optical Properties and Synthesis. *J. Chem. Phys.* **1994**, *101* (2), 1607–1615. https://doi.org/10.1063/1.467781.

(72) Moreels, I.; Lambert, K.; Smeets, D.; De Muynck, D.; Nollet, T.; Martins, J. C.; Vanhaecke, F.; Vantomme, A.; Delerue, C.; Allan, G.; Hens, Z. Size-Dependent Optical Properties of Colloidal PbS Quantum Dots. *ACS Nano* **2009**, *3* (10), 3023–3030. https://doi.org/10.1021/nn900863a.

(73) Moreels, I.; Lambert, K.; De Muynck, D.; Vanhaecke, F.; Poelman, D.; Martins, J. C.; Allan, G.; Hens, Z. Composition and Size-Dependent Extinction Coefficient of Colloidal PbSe Quantum Dots. *Chem. Mater.* **2007**, *19* (25), 6101–6106. https://doi.org/10.1021/cm071410q.

(74) Ma, W.; Luther, J. M.; Zheng, H.; Wu, Y.; Alivisatos, A. P. Photovoltaic Devices Employing Ternary PbS x Se 1 -x Nanocrystals. *Nano Lett.* **2009**, *9* (4), 1699–1703. https://doi.org/10.1021/nl900388a.

(75) Pan, Y.; Bai, H.; Pan, L.; Li, Y.; Tamargo, M. C.; Sohel, M.; Lombardi, J. R. Size Controlled Synthesis of Monodisperse PbTe Quantum Dots: Using Oleylamine as the Capping Ligand. *J. Mater. Chem.* **2012**, *22* (44), 23593. https://doi.org/10.1039/c2jm15540k.

(76) Li, X.; Wu, Y.; Zhang, S.; Cai, B.; Gu, Y.; Song, J.; Zeng, H. CsPbX 3 Quantum Dots for Lighting and Displays: Room-Temperature Synthesis, Photoluminescence Superiorities, Underlying Origins and White Light-Emitting Diodes. *Adv. Funct. Mater.* **2016**, *26* (15), 2435–2445. https://doi.org/10.1002/adfm.201600109.

(77) Liu, F.; Jiang, J.; Toyoda, T.; Kamarudin, M. A.; Hayase, S.; Wang, R.; Tao, S.; Shen, Q. Ultra-Halide-Rich Synthesis of Stable Pure Tin-Based Halide Perovskite Quantum Dots: Implications for Photovoltaics. *ACS Appl. Nano Mater.* **2021**, *4* (4), 3958–3968. https://doi.org/10.1021/acsanm.1c00324.

(78) Zhenfu, Z.; Liang, J.; Zhihai, W.; Jiong, C.; Miaomiao, Z.; Yafei, H. Perovskite Quantum Dots as Fluorescent Materials for Multi-Colored Lighting. *J. Mater. Sci.* **2018**, *53* (22), 15430–15441. https://doi.org/10.1007/s10853-018-2774-6.

(79) Zhang, T.; Li, H.; Yang, P.; Wei, J.; Wang, F.; Shen, H.; Li, D.; Li, F. Room-Temperature Synthesized Formamidinium Lead Halide Perovskite Quantum Dots with Bright Luminescence and Color-Tunability for Efficient Light Emitting. *Org. Electron.* **2019**, *68* (February), 76–84.

https://doi.org/10.1016/j.orgel.2019.02.007.

(80) Thersleff, T.; Budnyk, S.; Drangai, L.; Slabon, A. Dissecting Complex Nanoparticle Heterostructures via Multimodal Data Fusion with Aberration-Corrected STEM Spectroscopy. *Ultramicroscopy* **2020**, *219* (July), 113116. https://doi.org/10.1016/j.ultramic.2020.113116.

(81) Tachiya, M.; Mozumder, A. Kinetics of Geminate-Ion Recombination by Electron Tunnelling. *Chem. Phys. Lett.* **1975**, *34* (1), 77–79. https://doi.org/10.1016/0009-2614(75)80204-1.

(82) Ma, X.-H.; Cho, K.-H.; Sung, Y.-M. Growth Mechanism of Vertically Aligned SnSe Nanosheets via Physical Vapour Deposition. *CrystEngComm* **2014**, *16* (23), 5080–5086. https://doi.org/10.1039/C4CE00213J.

(83) Son, J. S.; Yu, J. H.; Kwon, S. G.; Lee, J.; Joo, J.; Hyeon, T. Colloidal Synthesis of Ultrathin Two-Dimensional Semiconductor Nanocrystals. *Adv. Mater.* **2011**, *23* (28), 3214–3219. https://doi.org/10.1002/adma.201101334.

(84) Lv, L.; Xu, Y.; Fang, H.; Luo, W.; Xu, F.; Liu, L.; Wang, B.; Zhang, X.; Yang, D.; Hu, W.; Dong, A. Generalized Colloidal Synthesis of High-Quality, Two-Dimensional Cesium Lead Halide Perovskite Nanosheets and Their Applications in Photodetectors. *Nanoscale* **2016**, *8* (28), 13589–13596. https://doi.org/10.1039/C6NR03428D.

(85) Kanungo, P. Das; Schmid, H.; Björk, M. T.; Gignac, L. M.; Breslin, C.; Bruley, J.; Bessire, C. D.; Riel, H. Selective Area Growth of III–V Nanowires and Their Heterostructures on Silicon in a Nanotube Template: Towards Monolithic Integration of Nano-Devices. *Nanotechnology* **2013**, *24* (22), 225304. https://doi.org/10.1088/0957-4484/24/22/225304.

(86) Peña, D. J.; Mbindyo, J. K. N.; Carado, A. J.; Mallouk, T. E.; Keating, C. D.; Razavi, B.; Mayer, T. S. Template Growth of Photoconductive Metal−CdSe−Metal Nanowires. *J. Phys. Chem.*

B **2002**, *106* (30), 7458–7462. https://doi.org/10.1021/jp0256591.

(87) Tigli, O.; Juhala, J. ZnO Nanowire Growth by Physical Vapor Deposition. In *2011 11th IEEE International Conference on Nanotechnology*; IEEE, 2011; pp 608–611. https://doi.org/10.1109/NANO.2011.6144585.

(88) Wagner, R. S.; Ellis, W. C. VAPOR-LIQUID-SOLID MECHANISM OF SINGLE CRYSTAL GROWTH. *Appl. Phys. Lett.* **1964**, *4* (5), 89–90. https://doi.org/10.1063/1.1753975.

(89) Li, D.; Li, W.; Zhang, J. Catalytic CO Oxidation by Fe Doped Penta-Graphene: A Density Functional Study. *Mol. Catal.* **2019**, *470* (March), 48–55. https://doi.org/10.1016/j.mcat.2019.03.023.

(90) Dong, A.; Tang, R.; Buhro, W. E. Solution-Based Growth and Structural Characterization of Homo- and Heterobranched Semiconductor Nanowires. *J. Am. Chem. Soc.* **2007**, *129* (40), 12254–12262. https://doi.org/10.1021/ja0737772.

(91) Woodruff, J. H.; Ratchford, J. B.; Goldthorpe, I. A.; McIntyre, P. C.; Chidsey. Vertically Oriented Germanium Nanowires Grown from Gold Colloids on Silicon Substrates and Subsequent Gold Removal. *Nano Lett.* **2007**, *7* (6), 1637–1642. https://doi.org/10.1021/nl070595x.

(92) Wang, F.; Dong, A.; Sun, J.; Tang, R.; Yu, H.; Buhro, W. E. Solution−Liquid−Solid Growth of Semiconductor Nanowires. *Inorg. Chem.* **2006**, *45* (19), 7511–7521. https://doi.org/10.1021/ic060498r.

(93) Peng, X. Mechanisms for the Shape-Control and Shape-Evolution of Colloidal Semiconductor Nanocrystals. *Adv. Mater.* **2003**, *15* (5), 459–463. https://doi.org/10.1002/adma.200390107.

(94) Tang, Z.; Kotov, N. A.; Giersig, M. Spontaneous Organization of Single CdTe Nanoparticles into Luminescent Nanowires. *Science (80-.).* **2002**, *297* (5579), 237–240.

https://doi.org/10.1126/science.1072086.

(95) Tu, X.; Li, M.; Su, Y.; Yin, G.; Lu, J.; He, D. Self-Templated Growth of CuInS2 Nanosheet Arrays for Photoelectrochemical Water Splitting. *J. Alloys Compd.* **2019**, *809*, 151794. https://doi.org/10.1016/j.jallcom.2019.151794.

(96) Liu, B.; Yang, W.; Li, J.; Zhang, X.; Niu, P.; Jiang, X. Template Approach to Crystalline GaN Nanosheets. *Nano Lett.* **2017**, *17* (5), 3195–3201. https://doi.org/10.1021/acs.nanolett.7b00754.

(97) Saran, R.; Curry, R. J. Lead Sulphide Nanocrystal Photodetector Technologies. *Nat. Photonics* **2016**, *10* (2), 81–92. https://doi.org/10.1038/nphoton.2015.280.

(98) Krishna, S. Quantum Dots-in-a-Well Infrared Photodetectors. *J. Phys. D. Appl. Phys.* **2005**, *38* (13), 2142–2150. https://doi.org/10.1088/0022-3727/38/13/010.

(99) Huang, M. H.; Madasu, M. Facet-Dependent and Interfacial Plane-Related Photocatalytic Behaviors of Semiconductor Nanocrystals and Heterostructures. *Nano Today* **2019**, *28*, 100768. https://doi.org/10.1016/j.nantod.2019.100768.

(100) Khon, E.; Lambright, K.; Khnayzer, R. S.; Moroz, P.; Perera, D.; Butaeva, E.; Lambright, S.; Castellano, F. N.; Zamkov, M. Improving the Catalytic Activity of Semiconductor Nanocrystals through Selective Domain Etching. *Nano Lett.* **2013**, *13* (5), 2016–2023. https://doi.org/10.1021/nl400715n.

(101) Kamat, P. V. Quantum Dot Solar Cells. Semiconductor Nanocrystals as Light Harvesters. *J. Phys. Chem. C* **2008**, *112* (48), 18737–18753. https://doi.org/10.1021/jp806791s.

(102) Antunez, P. D.; Buckley, J. J.; Brutchey, R. L. Tin and Germanium Monochalcogenide IV–VI Semiconductor Nanocrystals for Use in Solar Cells. *Nanoscale* **2011**, *3* (6), 2399. https://doi.org/10.1039/c1nr10084j.

(103) McVey, B. F. P.; Tilley, R. D. Solution Synthesis, Optical Properties, and Bioimaging Applications of Silicon Nanocrystals. *Acc. Chem. Res.* **2014**, *47* (10), 3045–3051. https://doi.org/10.1021/ar500215v.

(104) Martynenko, I. V.; Litvin, A. P.; Purcell-Milton, F.; Baranov, A. V.; Fedorov, A. V.; Gun'ko, Y. K. Application of Semiconductor Quantum Dots in Bioimaging and Biosensing. *J. Mater. Chem. B* **2017**, *5* (33), 6701–6727. https://doi.org/10.1039/C7TB01425B.

(105) Kairdolf, B. A.; Smith, A. M.; Stokes, T. H.; Wang, M. D.; Young, A. N.; Nie, S. Semiconductor Quantum Dots for Bioimaging and Biodiagnostic Applications. *Annu. Rev. Anal. Chem.* **2013**, *6* (1), 143–162. https://doi.org/10.1146/annurev-anchem-060908-155136.

(106) Sapsford, K. E.; Pons, T.; Medintz, I. L.; Mattoussi, H. Biosensing with Luminescent Semiconductor Quantum Dots. *Sensors* **2006**, *6* (8), 925–953. https://doi.org/10.3390/s6080925.

(107) Sukhanova, A.; Nabiev, I. Fluorescent Nanocrystal-Encoded Microbeads for Multiplexed Cancer Imaging and Diagnosis. *Crit. Rev. Oncol. Hematol.* **2008**, *68* (1), 39–59. https://doi.org/10.1016/j.critrevonc.2008.05.006.

(108) Michalet, X.; Pinaud, F.; Lacoste, T. D.; Dahan, M.; Bruchez, M. P.; Alivisatos, A. P.; Weiss, S. Properties of Fluorescent Semiconductor Nanocrystals and Their Application to Biological Labeling. *Single Mol.* **2001**, *2* (4), 261–276. https://doi.org/10.1002/1438-5171(200112)2:4<261::AID-SIMO261>3.0.CO;2-P.

(109) Almutlaq, J.; Liu, Y.; Mir, W. J.; Sabatini, R. P.; Englund, D.; Bakr, O. M.; Sargent, E. H. Engineering Colloidal Semiconductor Nanocrystals for Quantum Information Processing. *Nat. Nanotechnol.* **2024**. https://doi.org/10.1038/s41565-024-01606-4.

(110) Kagan, C. R.; Bassett, L. C.; Murray, C. B.; Thompson, S. M. Colloidal Quantum Dots as Platforms for Quantum Information Science. *Chem. Rev.* **2021**, *121* (5), 3186–3233.

https://doi.org/10.1021/acs.chemrev.0c00831.

(111) Rogach, A. L.; Gaponik, N.; Lupton, J. M.; Bertoni, C.; Gallardo, D. E.; Dunn, S.; Li Pira, N.; Paderi, M.; Repetto, P.; Romanov, S. G.; O'Dwyer, C.; Sotomayor Torres, C. M.; Eychmüller, A. Light-Emitting Diodes with Semiconductor Nanocrystals. *Angew. Chemie Int. Ed.* **2008**, *47* (35), 6538–6549. https://doi.org/10.1002/anie.200705109.

(112) Mueller, A. H.; Petruska, M. A.; Achermann, M.; Werder, D. J.; Akhadov, E. A.; Koleske, D. D.; Hoffbauer, M. A.; Klimov, V. I. Multicolor Light-Emitting Diodes Based on Semiconductor Nanocrystals Encapsulated in GaN Charge Injection Layers. *Nano Lett.* **2005**, *5* (6), 1039–1044. https://doi.org/10.1021/nl050384x.

(113) Dai, Q.; Duty, C. E.; Hu, M. Z. Semiconductor-Nanocrystals-Based White Light-Emitting Diodes. *Small* **2010**, *6* (15), 1577–1588. https://doi.org/10.1002/smll.201000144.

(114) Li, Y.; Rizzo, A.; Cingolani, R.; Gigli, G. White-Light-Emitting Diodes Using Semiconductor Nanocrystals. *Microchim. Acta* **2007**, *159* (3–4), 207–215. https://doi.org/10.1007/s00604-007-0740-0.

(115) Todescato, F.; Fortunati, I.; Minotto, A.; Signorini, R.; Jasieniak, J.; Bozio, R. Engineering of Semiconductor Nanocrystals for Light Emitting Applications. *Materials (Basel).* **2016**, *9* (8), 672. https://doi.org/10.3390/ma9080672.

(116) Vaneski, A.; Schneider, J.; Susha, A. S.; Rogach, A. L. Colloidal Hybrid Heterostructures Based on II–VI Semiconductor Nanocrystals for Photocatalytic Hydrogen Generation. *J. Photochem. Photobiol. C Photochem. Rev.* **2014**, *19* (1), 52–61. https://doi.org/10.1016/j.jphotochemrev.2013.12.001.

(117) ALFEROV, Z. I. THE DOUBLE HETEROSTRUCTURE: CONCEPT AND ITS APPLICATIONS IN PHYSICS, ELECTRONICS AND TECHNOLOGY. *Int. J. Mod. Phys. B*

2002, *16* (05), 647–675. https://doi.org/10.1142/S0217979202010233.

(118) Ithurria, S.; Tessier, M. D.; Mahler, B.; Lobo, R. P. S. M.; Dubertret, B.; Efros, A. L. Colloidal Nanoplatelets with Two-Dimensional Electronic Structure. *Nat. Mater.* **2011**, *10* (12), 936–941. https://doi.org/10.1038/nmat3145.

(119) Diroll, B. T.; Guzelturk, B.; Po, H.; Dabard, C.; Fu, N.; Makke, L.; Lhuillier, E.; Ithurria, S. 2D II–VI Semiconductor Nanoplatelets: From Material Synthesis to Optoelectronic Integration. *Chem. Rev.* **2023**, *123* (7), 3543–3624. https://doi.org/10.1021/acs.chemrev.2c00436.

(120) Jasieniak, J.; Smith, L.; van Embden, J.; Mulvaney, P.; Califano, M. Re-Examination of the Size-Dependent Absorption Properties of CdSe Quantum Dots. *J. Phys. Chem. C* **2009**, *113* (45), 19468–19474. https://doi.org/10.1021/jp906827m.

(121) Shin, A. J.; Hossain, A. A.; Tenney, S. M.; Tan, X.; Tan, L. A.; Foley, J. J.; Atallah, T. L.; Caram, J. R. Dielectric Screening Modulates Semiconductor Nanoplatelet Excitons. *J. Phys. Chem. Lett.* **2021**, *12* (20), 4958–4964. https://doi.org/10.1021/acs.jpclett.1c00624.

(122) Ithurria, S.; Dubertret, B. Quasi 2D Colloidal CdSe Platelets with Thicknesses Controlled at the Atomic Level. *J. Am. Chem. Soc.* **2008**, *130* (49), 16504–16505. https://doi.org/10.1021/ja807724e.

(123) Sharma, M.; Gungor, K.; Yeltik, A.; Olutas, M.; Guzelturk, B.; Kelestemur, Y.; Erdem, T.; Delikanli, S.; McBride, J. R.; Demir, H. V. Near-Unity Emitting Copper-Doped Colloidal Semiconductor Quantum Wells for Luminescent Solar Concentrators. *Adv. Mater.* **2017**, *29* (30), 1–10. https://doi.org/10.1002/adma.201700821.

(124) Delikanli, S.; Yu, G.; Yeltik, A.; Bose, S.; Erdem, T.; Yu, J.; Erdem, O.; Sharma, M.; Sharma, V. K.; Quliyeva, U.; Shendre, S.; Dang, C.; Zhang, D. H.; Sum, T. C.; Fan, W.; Demir, H. V. Ultrathin Highly Luminescent Two-Monolayer Colloidal CdSe Nanoplatelets. *Adv. Funct.*

Mater. **2019**, *29* (35), 1–9. https://doi.org/10.1002/adfm.201901028.

(125) Altintas, Y.; Quliyeva, U.; Gungor, K.; Erdem, O.; Kelestemur, Y.; Mutlugun, E.; Kovalenko, M. V.; Demir, H. V. Highly Stable, Near-Unity Efficiency Atomically Flat Semiconductor Nanocrystals of CdSe/ZnS Hetero-Nanoplatelets Enabled by ZnS-Shell Hot-Injection Growth. *Small* **2019**, *15* (8), 1–11. https://doi.org/10.1002/smll.201804854.

(126) Tessier, M. D.; Mahler, B.; Nadal, B.; Heuclin, H.; Pedetti, S.; Dubertret, B. Spectroscopy of Colloidal Semiconductor Core/Shell Nanoplatelets with High Quantum Yield. *Nano Lett.* **2013**, *13* (7), 3321–3328. https://doi.org/10.1021/nl401538n.

(127) Leemans, J.; Singh, S.; Li, C.; Ten Brinck, S.; Bals, S.; Infante, I.; Moreels, I.; Hens, Z. Near-Edge Ligand Stripping and Robust Radiative Exciton Recombination in CdSe/CdS Core/Crown Nanoplatelets. *J. Phys. Chem. Lett.* **2020**, *11* (9), 3339–3344. https://doi.org/10.1021/acs.jpclett.0c00870.

(128) Singh, S.; Tomar, R.; ten Brinck, S.; De Roo, J.; Geiregat, P.; Martins, J. C.; Infante, I.; Hens, Z. Colloidal CdSe Nanoplatelets, A Model for Surface Chemistry/Optoelectronic Property Relations in Semiconductor Nanocrystals. *J. Am. Chem. Soc.* **2018**, *140* (41), 13292–13300. https://doi.org/10.1021/jacs.8b07566.

(129) Nirmal, M.; Dabbousi, B. O.; Bawendi, M. G.; Macklin, J. J.; Trautman, J. K.; Harris, T. D.; Brus, L. E. Fluorescence Intermittency in Single Cadmium Selenide Nanocrystals. *Nature* **1996**, *383* (6603), 802–804. https://doi.org/10.1038/383802a0.

(130) Cordones, A. A.; Leone, S. R. Mechanisms for Charge Trapping in Single Semiconductor Nanocrystals Probed by Fluorescence Blinking. *Chem. Soc. Rev.* **2013**, *42* (8), 3209. https://doi.org/10.1039/c2cs35452g.

(131) Efros, A. L.; Nesbitt, D. J. Origin and Control of Blinking in Quantum Dots. *Nat.*

Nanotechnol. **2016**, *11* (8), 661–671. https://doi.org/10.1038/nnano.2016.140.

(132) Feldmann, J.; Peter, G.; Göbel, E. O.; Dawson, P.; Moore, K.; Foxon, C.; Elliott, R. J. Linewidth Dependence of Radiative Exciton Lifetimes in Quantum Wells. *Phys. Rev. Lett.* **1987**, *59* (20), 2337–2340. https://doi.org/10.1103/PhysRevLett.59.2337.

(133) Tessier, M. D.; Javaux, C.; Maksimovic, I.; Loriette, V.; Dubertret, B. Spectroscopy of Single CdSe Nanoplatelets. *ACS Nano* **2012**, *6* (8), 6751–6758. https://doi.org/10.1021/nn3014855.

(134) Olutas, M.; Guzelturk, B.; Kelestemur, Y.; Gungor, K.; Demir, H. V. Highly Efficient Nonradiative Energy Transfer from Colloidal Semiconductor Quantum Dots to Wells for Sensitive Noncontact Temperature Probing. *Adv. Funct. Mater.* **2016**, *26* (17), 2891–2899. https://doi.org/10.1002/adfm.201505108.

(135) Huo, C.; Fong, C. F.; Amara, M.-R.; Huang, Y.; Chen, B.; Zhang, H.; Guo, L.; Li, H.; Huang, W.; Diederichs, C.; Xiong, Q. Optical Spectroscopy of Single Colloidal CsPbBr 3 Perovskite Nanoplatelets. *Nano Lett.* **2020**, *20* (5), 3673–3680. https://doi.org/10.1021/acs.nanolett.0c00611.

(136) Liu, J.; Guillemeney, L.; Abécassis, B.; Coolen, L. Long Range Energy Transfer in Self-Assembled Stacks of Semiconducting Nanoplatelets. *Nano Lett.* **2020**, *20* (5), 3465–3470. https://doi.org/10.1021/acs.nanolett.0c00376.

(137) VanOrman, Z. A.; Bieber, A. S.; Wieghold, S.; Nienhaus, L. Green-to-Blue Triplet Fusion Upconversion Sensitized by Anisotropic CdSe Nanoplatelets. *Chem. Mater.* **2020**, *32* (11), 4734–4742. https://doi.org/10.1021/acs.chemmater.0c01354.

(138) Hinterding, S. O. M.; Salzmann, B. B. V.; Vonk, S. J. W.; Vanmaekelbergh, D.; Weckhuysen, B. M.; Hutter, E. M.; Rabouw, F. T. Single Trap States in Single CdSe Nanoplatelets.

ACS Nano **2021**, *15* (4), 7216–7225. https://doi.org/10.1021/acsnano.1c00481.

(139) Vong, A. F.; Irgen-Gioro, S.; Wu, Y.; Weiss, E. A. Origin of Low Temperature Trion Emission in CdSe Nanoplatelets. *Nano Lett.* **2021**, *21* (23), 10040–10046. https://doi.org/10.1021/acs.nanolett.1c03726.

(140) Joo, J.; Son, J. S.; Kwon, S. G.; Yu, J. H.; Hyeon, T. Low-Temperature Solution-Phase Synthesis of Quantum Well Structured CdSe Nanoribbons. *J. Am. Chem. Soc.* **2006**, *128* (17), 5632–5633. https://doi.org/10.1021/ja0601686.

(141) Mahler, B.; Nadal, B.; Bouet, C.; Patriarche, G.; Dubertret, B. Core/Shell Colloidal Semiconductor Nanoplatelets. *J. Am. Chem. Soc.* **2012**, *134* (45), 18591–18598. https://doi.org/10.1021/ja307944d.

(142) Polovitsyn, A.; Dang, Z.; Movilla, J. L.; Martín-García, B.; Khan, A. H.; Bertrand, G. H. V.; Brescia, R.; Moreels, I. Synthesis of Air-Stable CdSe/ZnS Core–Shell Nanoplatelets with Tunable Emission Wavelength. *Chem. Mater.* **2017**, *29* (13), 5671–5680. https://doi.org/10.1021/acs.chemmater.7b01513.

(143) Prudnikau, A.; Chuvilin, A.; Artemyev, M. CdSe–CdS Nanoheteroplatelets with Efficient Photoexcitation of Central CdSe Region through Epitaxially Grown CdS Wings. *J. Am. Chem. Soc.* **2013**, *135* (39), 14476–14479. https://doi.org/10.1021/ja401737z.

(144) Tessier, M. D.; Spinicelli, P.; Dupont, D.; Patriarche, G.; Ithurria, S.; Dubertret, B. Efficient Exciton Concentrators Built from Colloidal Core/Crown CdSe/CdS Semiconductor Nanoplatelets. *Nano Lett.* **2014**, *14* (1), 207–213. https://doi.org/10.1021/nl403746p.

(145) Pedetti, S.; Ithurria, S.; Heuclin, H.; Patriarche, G.; Dubertret, B. Type-II CdSe/CdTe Core/Crown Semiconductor Nanoplatelets. *J. Am. Chem. Soc.* **2014**, *136* (46), 16430–16438. https://doi.org/10.1021/ja509307m.

(146) Ithurria, S.; Talapin, D. V. Colloidal Atomic Layer Deposition (c-ALD) Using Self-Limiting Reactions at Nanocrystal Surface Coupled to Phase Transfer between Polar and Nonpolar Media. *J. Am. Chem. Soc.* **2012**, *134* (45), 18585–18590. https://doi.org/10.1021/ja308088d.

(147) Bouet, C.; Laufer, D.; Mahler, B.; Nadal, B.; Heuclin, H.; Pedetti, S.; Patriarche, G.; Dubertret, B. Synthesis of Zinc and Lead Chalcogenide Core and Core/Shell Nanoplatelets Using Sequential Cation Exchange Reactions. *Chem. Mater.* **2014**, *26* (9), 3002–3008. https://doi.org/10.1021/cm5008608.

(148) Izquierdo, E.; Robin, A.; Keuleyan, S.; Lequeux, N.; Lhuillier, E.; Ithurria, S. Strongly Confined HgTe 2D Nanoplatelets as Narrow Near-Infrared Emitters. *J. Am. Chem. Soc.* **2016**, *138* (33), 10496–10501. https://doi.org/10.1021/jacs.6b04429.

(149) Tenney, S. M.; Tan, L. A.; Sonnleitner, M. L.; Sica, A. V.; Shin, A. J.; Ronquillo, R.; Ahmed, T.; Atallah, T. L.; Caram, J. R. Mesoscale Quantum-Confined Semiconductor Nanoplatelets through Seeded Growth. *Chem. Mater.* **2022**, *34* (13), 6048–6056. https://doi.org/10.1021/acs.chemmater.2c01144.

(150) Polte, J. Fundamental Growth Principles of Colloidal Metal Nanoparticles – a New Perspective. *CrystEngComm* **2015**, *17* (36), 6809–6830. https://doi.org/10.1039/C5CE01014D.

(151) Son, J. S.; Wen, X.; Joo, J.; Chae, J.; Baek, S.; Park, K.; Kim, J. H.; An, K.; Yu, J. H.; Kwon, S. G.; Choi, S.; Wang, Z.; Kim, Y.; Kuk, Y.; Hoffmann, R.; Hyeon, T. Large-Scale Soft Colloidal Template Synthesis of 1.4 Nm Thick CdSe Nanosheets. *Angew. Chemie Int. Ed.* **2009**, *48* (37), 6861–6864. https://doi.org/10.1002/anie.200902791.

(152) Chen, Y.; Chen, D.; Li, Z.; Peng, X. Symmetry-Breaking for Formation of Rectangular CdSe Two-Dimensional Nanocrystals in Zinc-Blende Structure. *J. Am. Chem. Soc.* **2017**, *139* (29), 10009–10019. https://doi.org/10.1021/jacs.7b04855.

(153) Riedinger, A.; Ott, F. D.; Mule, A.; Mazzotti, S.; Knüsel, P. N.; Kress, S. J. P.; Prins, F.; Erwin, S. C.; Norris, D. J. An Intrinsic Growth Instability in Isotropic Materials Leads to Quasi-Two-Dimensional Nanoplatelets - SI. *Nat. Mater.* **2017**, *16* (7), 743–748. https://doi.org/10.1038/nmat4889.

(154) Mer, V. K. La. Nucleation in Phase Transitions. *Ind. Eng. Chem.* **1952**, *44* (6), 1270–1277. https://doi.org/10.1021/ie50510a027.

(155) Peng, Z. A.; Peng, X. Nearly Monodisperse and Shape-Controlled CdSe Nanocrystals via Alternative Routes: Nucleation and Growth. *J. Am. Chem. Soc.* **2002**, *124* (13), 3343–3353. https://doi.org/10.1021/ja0173167.

(156) Yin, Y.; Alivisatos, A. P. Colloidal Nanocrystal Synthesis and the Organic–Inorganic Interface. *Nature* **2005**, *437* (7059), 664–670. https://doi.org/10.1038/nature04165.

(157) Kumar, S.; Nann, T. Shape Control of II–VI Semiconductor Nanomaterials. *Small* **2006**, *2* (3), 316–329. https://doi.org/10.1002/smll.200500357.

(158) Wang, F.; Wang, Y.; Liu, Y.-H.; Morrison, P. J.; Loomis, R. A.; Buhro, W. E. Two-Dimensional Semiconductor Nanocrystals: Properties, Templated Formation, and Magic-Size Nanocluster Intermediates. *Acc. Chem. Res.* **2015**, *48* (1), 13–21. https://doi.org/10.1021/ar500286j.

(159) Zhang, J.; Huang, F.; Lin, Z. Progress of Nanocrystalline Growth Kinetics Based on Oriented Attachment. *Nanoscale* **2010**, *2* (1), 18–34. https://doi.org/10.1039/B9NR00047J.

(160) Metropolis, N.; Ulam, S. The Monte Carlo Method. *J. Am. Stat. Assoc.* **1949**, *44* (247), 335–341. https://doi.org/10.1080/01621459.1949.10483310.

(161) Bortz, A. B.; Kalos, M. H.; Lebowitz, J. L. A New Algorithm for Monte Carlo Simulation of Ising Spin Systems. *J. Comput. Phys.* **1975**, *17* (1), 10–18. https://doi.org/10.1016/0021-

9991(75)90060-1.

(162) Battaile, C. C. The Kinetic Monte Carlo Method: Foundation, Implementation, and Application. *Comput. Methods Appl. Mech. Eng.* **2008**, *197* (41–42), 3386–3398. https://doi.org/10.1016/j.cma.2008.03.010.

(163) Pineda, M.; Stamatakis, M. Kinetic Monte Carlo Simulations for Heterogeneous Catalysis: Fundamentals, Current Status, and Challenges. *J. Chem. Phys.* **2022**, *156* (12). https://doi.org/10.1063/5.0083251.

(164) Ravipati, S.; Savva, G. D.; Christidi, I.-A.; Guichard, R.; Nielsen, J.; Réocreux, R.; Stamatakis, M. Coupling the Time-Warp Algorithm with the Graph-Theoretical Kinetic Monte Carlo Framework for Distributed Simulations of Heterogeneous Catalysts. *Comput. Phys. Commun.* **2022**, *270*, 108148. https://doi.org/10.1016/j.cpc.2021.108148.

(165) Piccinin, S.; Stamatakis, M. Steady-State CO Oxidation on Pd(111): First-Principles Kinetic Monte Carlo Simulations and Microkinetic Analysis. *Top. Catal.* **2017**, *60* (1–2), 141–151. https://doi.org/10.1007/s11244-016-0725-5.

Chapter 2

On the Inadequacy of Stern-Volmer and FRET in Describing Quenching in Binary Donor-Acceptor Solutions

Quantitative fluorescence quenching is a common analytical approach to studying the mechanism of chemical reactions. The Stern-Volmer (S-V) equation is the most common expression used to analyzing quenching behavior, and can be used to extract kinetics in complex environments. However, the approximations underlying the S-V equation are incompatible with Förster Resonance Energy Transfer (FRET) acting as the primary quenching mechanism. The nonlinear distance dependence of FRET leads to significant departures from "standard" S-V quenching curves, both by modulating the interaction range of donor species, and increasing the effect of component diffusion. In this chapter, we discuss this inadequacy by probing the fluorescence quenching of long-lifetime lead sulfide quantum dots (QDs) mixed with plasmonic covellite copper sulfide (CuS) nanodisks (NDs), which serve as perfect fluorescent quenchers. By applying kinetic Monte Carlo methods which consider particle distributions and diffusion we are able to

quantitatively reproduce experimental data which shows significant quenching at very small concentrations of NDs. Distribution of interparticle distances and diffusion are concluded to play important roles in the fluorescence quenching, particularly in the shortwave infrared, where photoluminescent lifetimes are often long relative to diffusion time-scales. In the case of high concentration, geometry of nanocrystals plays a significant role in the distance dependence of the FRET rate.

2.1 Importance of Förster Resonance Energy Transfer (FRET) for SWIR-Emitting Nanocrystals (NCs)

Proposed in 1919 by Otto Stern and Max Volmer, the Stern-Volmer model quantitatively described the decrease in fluorescence intensity of emitters in the presence of quenchers, molecules that are capable of bringing the excited emitters back to ground states.[1] The linear relationship shown in a Stern-Volmer (S-V) plot between quenching ratio and quencher concentrations is often attributed to the collisions between emitters and quenchers. For this reason, Stern-Volmer model is usually referred to as collisional quenching and associated with measuring rate constants. Deviation from the linear Stern-Volmer law usually implies some factors other than collisional quenching, including attraction between particles, pre-formation of complexes, or incomplete quenching.[2–5]

While collisional quenching is treated in the Stern-Volmer formalism, Förster resonance energy transfer (FRET) is another process that can deplete the excited state of a donor molecule. In FRET, dipole-dipole interactions result in energy migration from donor to acceptor, provided the emission of the donor overlaps with the absorption of the acceptor.[6] FRET rates depend in a known non-linear fashion on the distance between donor and acceptor, and thus can be inverted to

experimentally determine the intramolecular distance (or distribution of distances) between each species. In a single molecule context, FRET is a powerful tool to deduce structural changes in polymers induced by folding or self-assembly among many other applications.[7–11] In ensemble contexts, Inokuti and Hirayama gave a generalized treatment of fluorescence quenching in crystals by comparing summed rates of energy transfer from donors to acceptors and decay rates of excited donors.[12] This treatment is useful for excitonic crystals, but has clear limitations in mixtures where the distribution is more complex and changing over time.

Surprisingly, despite considerable examples of fluorescent quenching due to FRET there exists no analytical expression that predicts quenching rate as a function of donor and acceptor concentration and FRET overlap in dilute mixtures of non-interacting particles. By simple inspection, while the collisional S-V rate of quenching depends linearly on the concentration of quencher, in FRET, the rate also depends on the interparticle distance ($\sim r^{-6}$). Given that that the interparticle distance is approximately given by $r \sim n^{-1/3}$ where n is the number density; one might expect that the quenching rate will vary with n^2, or quadratically with number density. Such a mechanism may lead to significant quenching of photoluminescence in the case of small impurities, or could be used as a method to probe analyte concentration in a biochemical assay, but only if the proper form is used. It is worth noting, however, that there is no analytic expression of the distinct interparticle distance distribution for even hard-sphere binary mixtures, complicating the development of a single equation which takes in concentration, transition dipole and lifetime, and predicts quenching efficiency.[13–17]

In this chapter, we study energy transfer between short-wavelength infrared (SWIR) emitters and plasmonic nanoparticles. We synthesize lead sulfide (PbS) quantum dots (QDs) and plasmonic covellite copper sulfide(CuS) nanodisks (NDs) before mixing them in colloidal

solution. These form an ideal FRET pair for exploring the effects of diffusion and energy transfer in dilute solutions, as the CuS nanodisks have complete overlap with the emission spectrum of the PbS, but do not interfere (shadow) our PbS absorption spectra. The relatively long lifetime of PbS also allows us to explore the role of diffusion in energy quenching. Given that many SWIR emitters have long lifetimes (e.g. quantum dots and lanthanide nanoparticles), the role of diffusion as highly pertinent to the dynamics of quenching in this spectral window.

Our experiments revealed a high degree of quenching at very low concentrations of CuS NDs, accompanied by a non-linear dependence between quenching ratio and concentrations of plasmonic CuS NDs, which cannot be explained by conventional Stern-Volmer modeling. We simulate several potential explanations to describe these results, exploring the role of interparticle distance distribution, nonlinear FRET rates and diffusion, and reach quantitative agreement with experiment using kinetic Monte Carlo (KMC) simulations that account for all effects. We discuss how Stern-Volmer descriptions of quenching are highly inadequate in describing FRET pairs in systems with large FRET radii and/or long lifetimes concomitant large diffusion lengths. As a final point, we study the impact of geometry of nanocrystals on the distance dependence of the FRET rate.

2.2 Synthesis of PbS Quantum Dots (QDs) and Covellite CuS Nanodisks (NDs)

We synthesized PbS QDs and CuS NDs as the model emitters and quenchers through traditional colloidal methods (See Section 2.7). Absorption spectroscopy of CuS NDs shows a plasmonic peak in SWIR region (Figure 2.1a) consistent with prior reports.[18,19] For PbS QDs, PL spectroscopy of PbS QDs shows a close resonance of the emission peak with the plasmonic absorption peak of CuS NDs (Figure 2.1a). Morphology of as-synthesized nanocrystals are confirmed by TEM images, where spherical PbS QDs and hexagonal CuS NDs are clearly

identified (Figure 2.1b). PbS QDs are measured to have an average radius of 3.6 nm, and CuS NDs are measured to have an average diagonal length of 19 nm as well as an average thickness of 5.0 nm (See Section 2.8, Figure 2.6). The absorption trace of CuS NDs and the PL trace of PbS QDs are used to calculate the spectral overlap, which is required to calculate the FRET radius.[20] From TEM images, size parameters of PbS QDs and CuS NDs are measured and used to calculated the diffusion coefficients of nanocrystals using Stokes-Einstein equation.[21] The concentrations of PbS QDs are determined using the sizing curve and extinction coefficients reported by Moreels, I. et al., and the concentrations of CuS NDs are estimated from synthetic procedure and corresponding extinction coefficient is extracted using Beer-Lambert law.[22] These parameters are then used to all modeling and simulation (Table 2.1). TEM of the mixture confirmed no interaction between PbS and CuS samples (See Section 2.8, Figure 2.7).

Table 2.1 Parameters used in modeling and simulations

Nanocrystals	Size[a] (nm)	Concentration[b] (μM)	Diffusion coefficient ($nm^2 \cdot ns^{-1}$)	Total decay rate (ns^{-1})	FRET radius (nm)
PbS QDs	3.6 ± 0.7	33.7 ± 3.1[*]	0.22 ± 0.04	0.00045[**]	17.40 ± 0.20
CuS NDs	5.0 ± 1.2 19.0 ± 9.0	0.36[†]	0.048 ± 0.005[‡]	/	

[a] Measured from statistics of TEM images (See Section 2.8, Figure 2.6). For PbS QDs, diameter is reported; For CuS NDs, thickness (top row) and diagonal length (bottom row) are reported.
[b] For stock solutions.
[*] Calculated using size-independent absorption coefficient.[22]
[**] Measured in time-resolved PL spectroscopy (See Section 2.8, Figure 2.12).
[†] Estimated from synthetic procedure of CuS NDs (See Section 2.7).
[‡] Calculated using corrected hydrodynamic radius due to non-spherical shape.[23]

To study the fluorescence quenching of emissive nanocrystals by plasmonic nanocrystals in SWIR region, a series of titration experiments of PbS QDs with CuS NDs were performed (See Section 2.7). Steady-state PL spectroscopy clearly shows a continuous decrease in fluorescence

intensities of PbS QDs upon serial addition of CuS NDs (See Figure 2.1c for one example trace). Note that due to relatively high absorptivity of CuS NDs, the secondary inner filter effect introduced by absorption of CuS NDs were accounted for and the corrected PL intensities were used to calculate the quenching ratio (See Section 2.8, Figure 2.8 – Figure 2.10). Another direct evidence of the quenching is demonstrated by time-resolved PL measurements, where an obvious decreasing in the donor lifetimes is observed (See Section 2.8: Table 2.2 and Table 2.3).

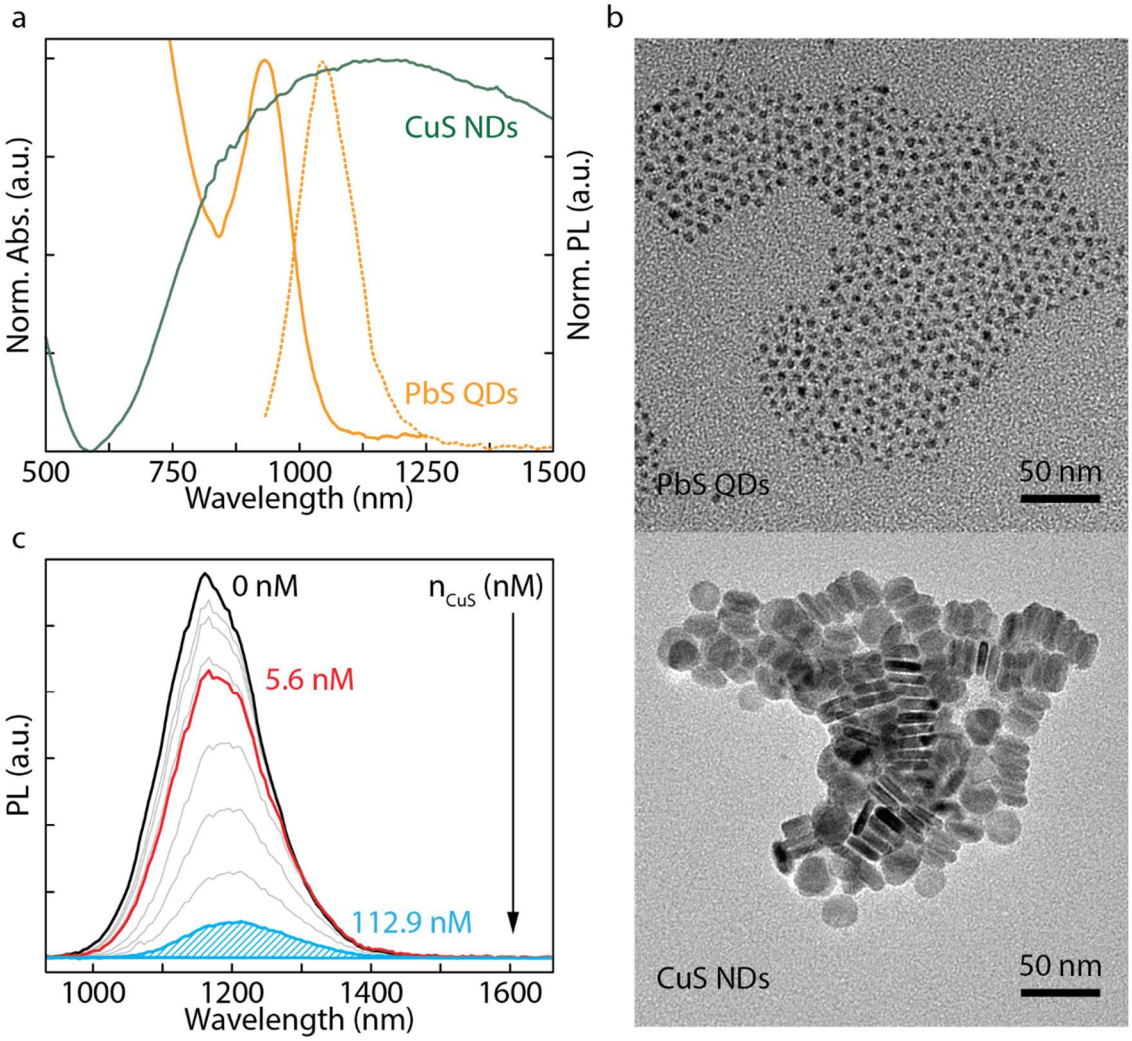

Figure 2.1 Synthesized PbS QDs and covellite CuS nanodisks (NDs) and titration experiments. (a) Normalized absorbance (solid lines) and PL (dashed line) spectra of synthesized PbS QDs (orange) and CuS NDs (green). (b) TEM images of synthesized PbS QDs (top) and CuS NDs (bottom). (c) PL traces of PbS QDs in one group of titration experiments with CuS NDs. The shaded area under the curve of a PL trace is considered as PL intensity and used to determine quenching ratios.

The results of fluorescence quenching in titration experiments show consistent patterns across the range of emitter concentrations tested (Figure 2.2a). We first observe that changing quencher concentration has the largest effect, consistent with it being the limiting quenching 'reagent'. Second, all the quencher concentrations experimented in the titrations were on nanomolar scale, which are significantly low given such a high degree of quenching (up to 95% extinction) compared to other reported emitter-quencher pairs including pairs of nanoparticles, pairs of fluorescent proteins, pairs of dye molecules, pairs of amino acids, dye molecule-DNA pairs and quantum dot-fluorescent protein pairs, which typically only display quenching at micromolar concentrations.[24–29] Second, besides the high quenching efficiency at low quencher concentrations, non-linear relationship between quenching ratios and quencher concentrations is also observed. These patterns suggest that additional complexity, not accounted in S-V quenching for PbS QDs – CuS NDs pair in SWIR region.

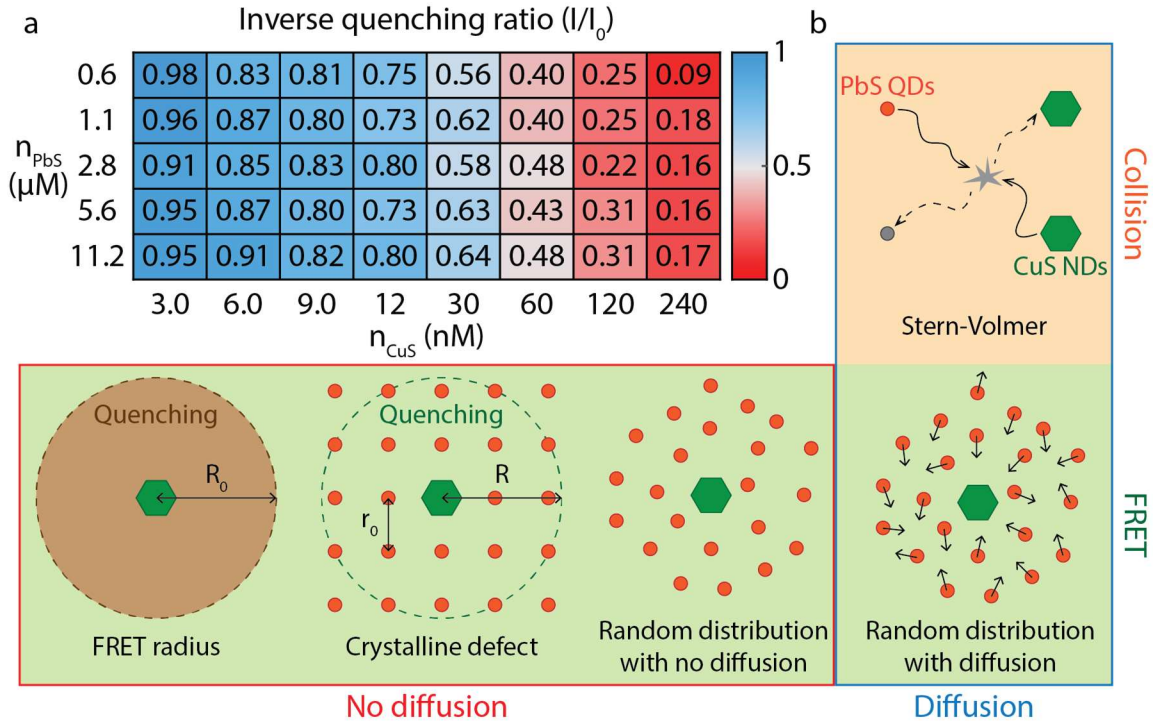

Figure 2.2 Titration experiments and possible models of fluorescence quenching. (a) A heatmap of inverse quenching ratios for all conditions of titration experiments (See also Figure 2.11). The inverse quenching

ratios have been corrected for inner filter effect. (b) A diagram of explored models in modeling & simulations. The models can be categorized into quenching by FRET (green background) and collisional quenching (orange background) based on the mechanism of energy transfer responsible for quenching, or into models considering diffusion (blue frame) and without considering diffusion (orange frame). PL of excited PbS QDs (orange circles) are by plasmonic CuS NDs (green hexagons), resulting in de-excited PbS QDs (gray circles).

2.3 Comparison of Experiments to Analytical and Simulated Quenching Behaviors

To explain the quenching patterns observed in experiments, we explored several models with and compared it to our experimental results (Figure 2.2b). They are enumerated and described in the next section.

2.3.1 Collisional quenching (Stern-Volmer)

In Stern-Volmer model, the cause of fluorescence quenching is attributed to collisions between emitters and quenchers. As a result, the relationship between quenching ratio and number density of quenchers (n_{CuS}) is given by:

$$\frac{I_0}{I} = 1 + \frac{k_q}{k_0} n_{CuS} \tag{2.1}$$

where k_q is the quenching rate, and k_0 is the total decay rate of emitters without quenchers.[1] Under this quenching scheme, a linear dependence is typically observed when k_q remains constant, which is indicative of a diffusion-limited collisional reaction between emitters and quenchers. The maximum possible quenching rate k_q is given by the maximum collision rate for diffusing particles:

$$k_q = 4\pi D R_C \tag{2.2}$$

where D is the sum of diffusion coefficients of emitter and quencher, and R_C is the sum of contact radius of emitter and quencher (For PbS QDs: radius; For CuS NDs: ½ of thickness), representing spontaneous reaction upon any collision.[30]

2.3.2 Quenching by FRET

Fluorescence quenching is fundamentally an energy transfer process between a donor and acceptor. If the quenching process is FRET mediated, it is based on dipole-dipole interactions each species. FRET rate depends non-linearly on the distance between emitters and quenchers (r):

$$k_{FRET} = k_0 \left(\frac{R_0}{r}\right)^6 \tag{2.3}$$

where R_0 is defined as the Förster distance. We will consider several ways that FRET can be introduced into a Stern-Volmer style equation.

2.3.2.1 FRET radius as effective quenching volume

FRET radius R_0 is calculated by the following equation

$$R_0^6 = 8.785 \times 10^{-5} \frac{\kappa^2 \phi_D J}{n^4} \tag{2.4}$$

where κ^2 is the dipole orientation factor, ϕ_D is the quantum yield of emitters, and n is the refractive index of solvent. The spectral overlap J is defined as:

$$J = \frac{\int F_D(\lambda)\varepsilon_A(\lambda)\lambda^4 d\lambda}{\int F_D(\lambda) d\lambda} \tag{2.5}$$

where $F_D(\lambda)$ is the emission spectrum of emitters, and $\varepsilon_A(\lambda)$ is the molar extinction coefficient of quenchers.[20] R_0 clearly depends only on spectral properties of emitter and quencher, requiring no knowledge of the concentrations. For large molecules such as polymers or proteins, intramolecular interchromophore distance (r) can be determined by measuring the FRET efficiency (E_{FRET}) through spectroscopy:

$$E_{FRET} = \frac{I}{I_0} = \frac{k_0}{k_0 + k_{FRET}} = \frac{1}{1 + (\frac{R_0}{r})^6} \tag{2.6}$$

where a 50% of FRET efficiency is achieved at an emitter-quencher distance equal to the FRET radius. We apply this idea of associating fluorescence quenching with only FRET radius to the mixture of PbS QDs and CuS NDs. Assuming the fluorescence of half of emitters within the range

of FRET radius are completely quenched, the quenching ratio would be given by a pseudo Stern-Volmer relation:

$$\frac{I_0}{I} = 1 + \frac{n_{PbS} \cdot \frac{1}{2} \cdot \frac{4\pi R_0^3}{3} \cdot n_{CuS} V}{n_{PbS} V} = 1 + \frac{2\pi R_0^3}{3} n_{CuS} \tag{2.7}$$

This is the equivalent of creating a quenched volume.

2.3.2.2 Crystalline Defect

One of the fundamental reasons that FRET efficiency measurements can be used to determine the interchromophore distance is that the variance of this intramolecular distance in the ensemble is relatively small.[31,32] For a mixture where emitters and quenchers are two different species in solution, the distance distribution is much larger and cannot be neglected.[16,33,34] To account for this, we add a layer of complexity on top of the "FRET radius only" calculation by introducing a crystalline distribution of interparticle distances, where CuS NDs are considered to be evenly distributed in a lattice of PbS QDs, and every PbS QDs are allowed to transferring energies only to the nearest CuS NDs. The quenching ratio is then calculated by comparing total FRET rate and total decay rate in the ensemble:

$$\frac{I_0}{I} = 1 + \frac{\int_{r_0}^{R} k_0 \left(\frac{R_0}{r}\right)^6 \cdot 4\pi r^2 n_{PbS} dr}{k_0 \frac{4\pi R^3}{3} n_{PbS}} \tag{2.8}$$

where the total FRET rate is calculated by integrating rates over all possible interparticle distances. Limits of the distance are determined given the number densities of PbS QDs and CuS NDs:

$$\frac{1}{n_{PbS}} = r_0^3; \frac{1}{n_{CuS}} = \frac{4\pi R^3}{3}$$

Finally, the quenching ratio is given by:

$$\frac{I_0}{I} = 1 + \frac{4\pi R_0^6}{3} n_{CuS}(n_{PbS} - \frac{4\pi}{3} n_{CuS}) \tag{2.9}$$

By inspection, this shows that a somewhat more realistic treatment of the variance due to FRET leads to a quadratic dependence on quencher concentration and a dependence on the concentration of the donor. However, this treatment does not consider the actual particle distribution, which requires a simulation described below.

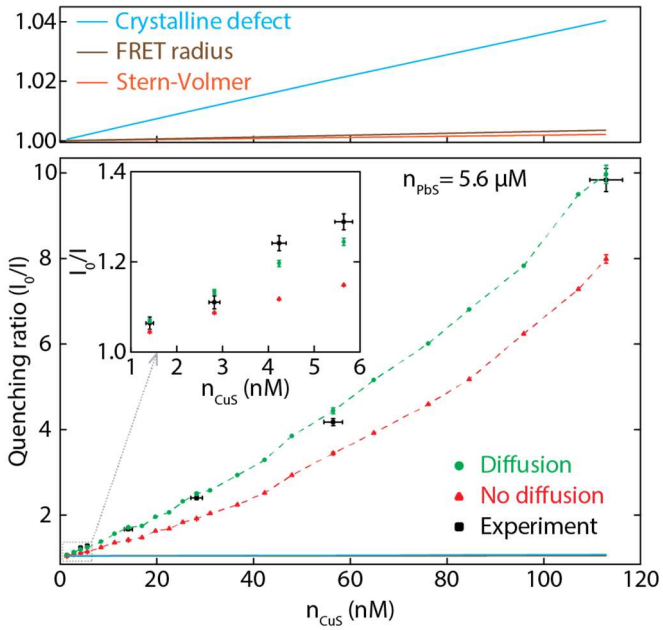

Figure 2.3 Comparison of quenching ratio-CuS NDs concentration curves between experiments and different models/simulations. Bottom: Full scale graph. Experimental result (black squares) and predictions based on random distribution with no diffusion (red triangles) and random distribution with diffusion (green circles) are plotted. Dashed lines are used to guide the eye and show the trend only. Top: Zoomed-in graph at low quenching ratio. Predictions based on Stern-Volmer (violet), FRET radius (cyan) and crystalline structure (orange) are plotted. Inset: Zoomed-in graph at low quencher concentrations.

2.3.2.3 Random distribution & diffusion

Several factors of quenching by FRET are not included in FRET radius-only model and crystalline structure model. First, the assumption that CuS NDs are evenly distributed among PbS QDs are invalid in an ideal/hard-sphere solution. Second, diffusion of species in solution is not taken into consideration, which could contribute to fluorescence quenching as the FRET rate is nonlinear with interparticle distance. Since an interparticle distance distribution function is not generally

analytic, we carried out a simulation of the quenching behavior using kinetic Monte-Carlo (KMC) modeling, considering both the distribution and fluctuation of interparticle distance and their influence on fluorescence quenching.[35] Briefly, PbS QDs and CuS NDs are randomly positioned in space with a defined number density. Complete matrices composed of FRET rates for every emitter-quencher pair in the ensemble are then calculated and used for pathway selection process to determine the fate of all emitters. Note that FRET rates between PbS QDs are much smaller than those between PbS QDs and CuS NDs (~10^4 times slower) thus are excluded from the rate matrices. Finally, the quenching ratio is extracted from the statistics of results (See Section 2.8, Figure 2.17). Diffusion is also implemented in the kMC simulation by three-dimensional random walk:

$$\boldsymbol{R}_{N+1} - \boldsymbol{R}_N = \sqrt{6D\Delta t} \cdot \boldsymbol{n}_{rand} \tag{2.10}$$

where $\boldsymbol{R}_i$ is the position vector of nanocrystals at the ith time step, D is the diffusion coefficient, Δt is the time step length limited by the lifetime of emitter, and $\boldsymbol{n}_{rand}$ is a random unit vector. It is worth mentioning here that the diffusion coefficients are calculated based on the size parameters obtained from TEM images where surface ligands are invisible, which is a potential source of error in modeling and simulations. This applies to both Stern-Volmer model and kinetic Monte Carlo simulations of FRET quenching where diffusion coefficients are used. The introduced deviations, however, are not as significant in the results since the surface ligands oleylamine on both PbS QDs and CuS NDs are inherently angled thus having limited contributions to the hydrodynamic radius. Predictions made based on different models are compared with experimental results (Figure 2.3).

2.4 Results of Simulations and Role of FRET Radius and Diffusion in Quenching

All models of quenching other than the KMC simulation grossly underestimate the observed quenching behavior at low acceptor densities and do not account for the apparent

nonlinear nature of quenching. We can conclude that quenching ratios are underestimated in Stern-Volmer model, FRET radius and crystalline structure models, while quenching by FRET with random nanocrystals distribution gives much higher predicted quenching ratios that that is comparable to the experimental data. This indicates that randomizing the distribution of nanocrystals in solution allows part of the PbS QDs to be in close vicinity of CuS NDs resulting in very high FRET rates and high probabilities of energy transfer. The second pattern of quenching observed in experimental data is the non-linear dependence of quenching ratios on quencher concentrations. This is natural when FRET is the mechanism of energy transfer responsible for quenching instead of collision, resulting from the r^{-6} dependence of FRET rate. It is worth mentioning that the only model that predicts a non-linear dependence is the crystalline defect model. The non-linearity is not obvious in the range of plotting, but is captured at much higher quencher concentrations (See Section 2.8: Figure 2.21). Both Stern-Volmer and FRET radius calculation give strictly linear relationships.

Furthermore, distance fluctuations introduced by diffusion contributes to higher quenching ratios and match experimental data more accurately. A brief explanation is given as follow. Although the interparticle distance can decrease or increase with diffusion, which will lead to raising or lowering of FRET rate respectively, this impact on FRET rate is clearly different for donor-quencher pairs separated at long distance and those separated at short distance due to the r^{-6} dependence. This difference in the rate of change is directly reflected in the differential of r^{-6} function. For donor-quencher pairs that are close in distance, the enhancement in FRET rate arising from decreasing distance is more significant than the decay in FRET rate induced by increasing distance, resulting in an overall higher FRET efficiency; such difference still exists for donor-quencher pairs that are distant away from each other, but at a much smaller scale. All taken into

consideration, in the scheme of quenching by FRET, diffusion has a positive contribution to fluorescence quenching (See Section 2.8, Figure 2.19 and Figure 2.20).

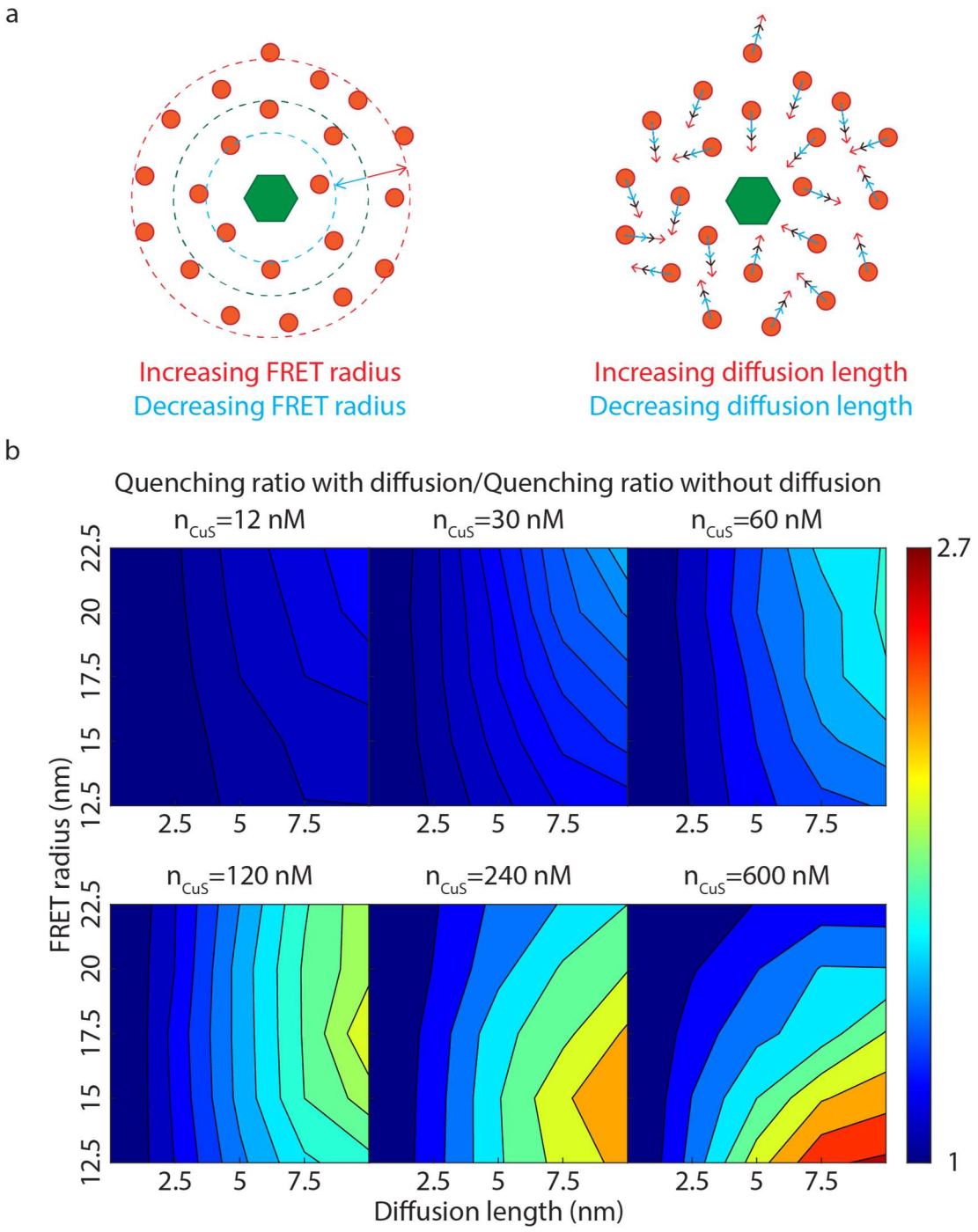

Figure 2.4 A color-coded map of enhancement of quenching ratio by diffusion with changing diffusion length and FRET radius at different quencher concentrations. The enhancement of quenching ratio is defined as the ratio between the quenching ratios with diffusion, $(\frac{I_0}{I})_d$, and the quenching ratios without diffusion, $(\frac{I_0}{I})_n$. Diffusion length is defined as $\sqrt{6D\Delta t}$.

Besides the clearly observed decrease in the donor lifetime, we also notice a shift in the time-resolved Pl traces from mono-exponential decay to multi-/bi-exponential decay when quenchers are introduced in the titration experiments. Such transition is not common for canonical quenching pairs, but could happen if the quenching rate is non-constant.[36,37] The non-constant quenching rate is true for our FRET system in the binary solution where spatial distribution of donors and quenchers makes a significant difference in FRET rate: donors in the close vicinity of quenchers will rapidly go through FRET deactivation pathway, while FRET rates for donor-quencher pairs that are more distantly separated will be lower and comparable with other decay rates. This type of quenching behaviors is indeed observed in time-resolved PL experiments: at early time, fast decay processes show up in samples with quenchers added, which are representative of the rapid FRET rates for donor-quencher pairs at close distances, but are not present in pure PbS samples; at later time, decay processes for quenched samples become slower and more comparable with the decay pattern for pure PbS (See Section 2.8, Figure 2.15). Furthermore, our simulations are also capable of capturing this behavior by monitoring the number of quenching events at every time steps (See Section 2.8, Figure 2.16). Again, a huge number of donors went through the FRET deactivation pathway at very early time; diffusion then plays a role at later times by increasing the FRET rate for more distantly separated donor-quencher pairs, resulting in more quenching at later times and eventually more quenching in total.

We explore how diffusion and FRET radius interact in Figure 2.4. Naturally, the enhancement by diffusion should increase as the diffusion length gets longer, which we observe at all quencher concentrations. However, the impact of FRET radius on enhancement by diffusion is different and shows a pattern of “saturation of quenching”. At low quencher concentrations, diffusion enhances quenching more at elevated FRET radii. At high quencher concentrations and

high FRET radii, diffusion does not enhance quenching. We note that FRET radius is a measurement of the quenching ability for each individual quencher, while quencher concentration reflects the total number of quenchers. When the quencher concentration is low, the number of emitters that all quenchers can access is not saturated, in this case the higher the FRET radius is, the more emitters reach the interaction region through diffusion, resulting in a higher enhancement. When the quencher concentration is high, most of the emitters are already accessible to quenchers without diffusion especially if the FRET radius is large -- hence the "saturation of quenching." For comparison, we carried out similar simulations for a canonical FRET pair (cyanine dyes) and it is clear that the contribution from diffusion is much less significant (See Section 2.8, Figure 2.22). In conclusion, the long FRET radius due to large absorption sections of CuS NDs and random distribution of particles in colloidal solutions gives rise to the high quenching ratio at low quencher concentrations, while also showing that diffusion can play significant role in nonlinear enhancement of quenching. Diffusion is not commonly considered in any model of FRET-based quenching, yet should be carefully monitored, especially in systems where the excited state lifetime is large.

2.5 Near-field FRET: Ex-situ Mixing of HgTe QDs and NPLs and 2D-0D Energy Transfer

Throughout the study of FRET quenching in the mixture of PbS QDs and CuS NDs, the conventional FRET rate equation with r^{-6} dependence has been used. This is due to the fact that in the range of titration experiments, the concentration of PbS QDs and CuS NDs are considerably low so that the chromophores can be considered as point-dipoles. The question then becomes the quenching efficiency in concentrated binary solution, where geometry of the chromophores makes a difference because of close distance. We perform another experiment by first separately

synthesizing oleylamine passivated HgTe QDs, and then mix a comparable concentration with 3 ML HgTe NPLs isolated immediately after cation exchange. We are able to observe energy transfer by mixing QDs and NPLs with low efficiencies of transfer. The mixed QDs are easily removed using gentle centrifugation which recovers NPL band edge PL. Separately synthesized QDs and NPLs are likely not adsorbing to the NPL surfaces, and thus constitute an "ideal" solution for which the model can be used to quantitatively analyze the efficiency of energy transfer.

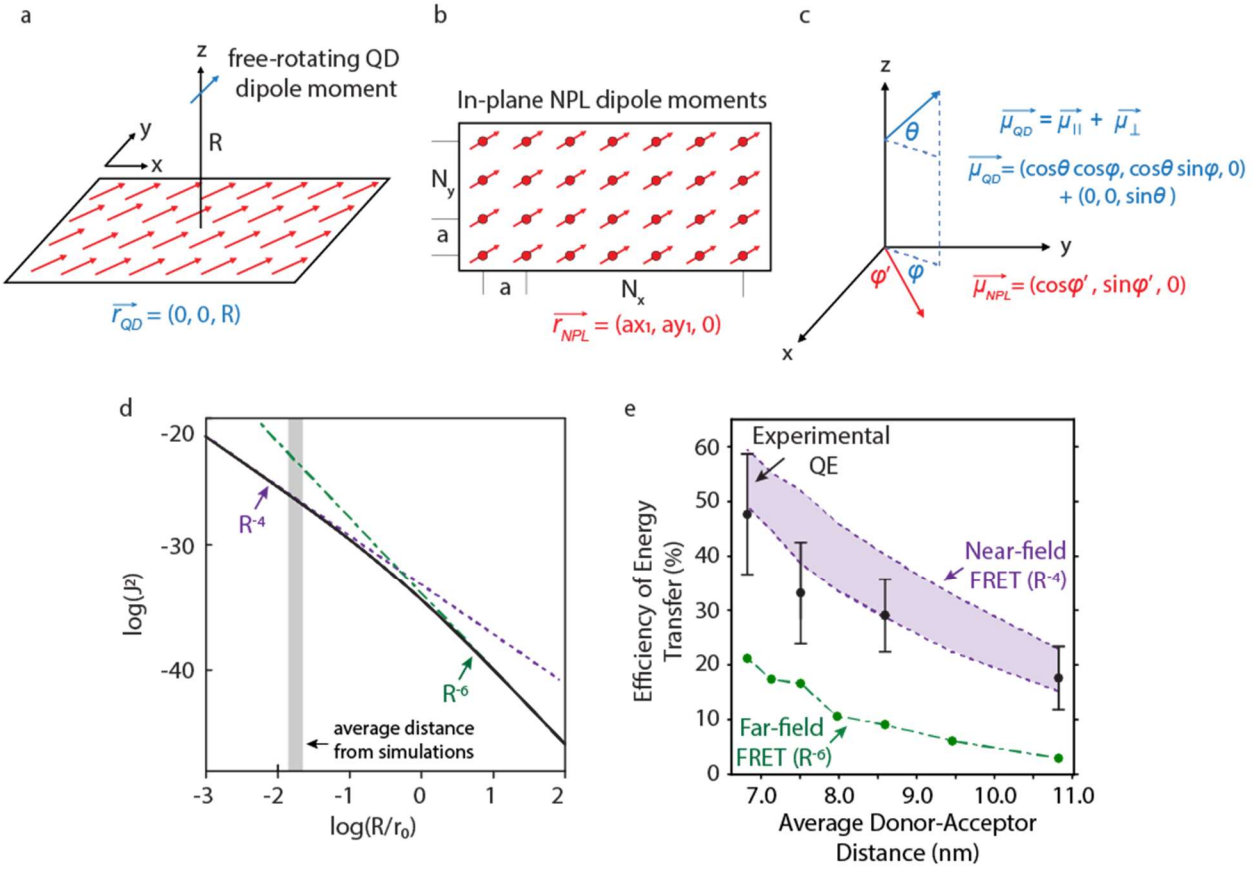

Figure 2.5 Model for studying the distance dependence of NPL-QD FRET system. (a) QD with a free-rotating dipole moment (blue vector) and NPL consisting of individual in-plane dipole moments (red vectors). The position vector of QD dipole is given in terms of Cartesian coordinates. (b) Top-down view of the in-plane dipole moments of the NPL. The position vector of NPL dipoles is given in Cartesian coordinates. (c)Diagram of altitude angle and azimuth angles for dipole moments. The "dipole vectors" are given in spherical coordinates. (d) The distance dependence of the FRET rate, plotted on a log-log scale to extract the index of R. The average donor-acceptor distances found in our simulations are indicated by the grey box. (e) The comparison of our experimental energy transfer efficiencies (black) to simulated results for both the near-field (purple) and far-field limit of FRET (green). The near-field results are represented as a range due to error (See Section 2.8), whereas the error on the far-field results is too low to be shown on the plot.

To explain the energy transfer, we again employed the Förster resonance energy transfer (FRET) model. This yielded an estimated efficiency of energy transfer (> 20%) that is significantly higher than the quantum yield of the donor alone (5-10%). The result is unusual as simplistically FRET is assumed to be bounded by QY of the donor (at low quantum yields), however this has proved to be an oversimplification both theoretically and experimentally.[38] In our case, this apparent mismatch prompted a more detailed study on the FRET mechanism for our specific NPL-QD system.

Following the work by Chuang et al., we first developed a more specific model for our 2D (NPLs) to 0D (QDs) energy transfer system, which takes the scale of donor-acceptor distances and the actual geometry of the dipole distribution into consideration.[39] Briefly, the relatively small HgTe QD is modeled as one single dipole, while the larger HgTe NPL consists of multiple dipoles (Figure 2.5a-c). The FRET rate equation is determined by calculating the summation of dipole-dipole coupling of donor-acceptor pairs over all possible dipole orientations (See Section 2.8). The summation can be calculated as a continuous integration to extract the distance dependence:

$$k_{FRET} \propto \begin{cases} \frac{3\pi^3}{8r_0^2}\left(1+\frac{1}{\pi}\right)\frac{1}{R^4} & R \ll r_0 \\ \frac{\pi^3}{4}\left(5-\frac{3}{\pi}\right)\frac{1}{R^6} & R \gg r_0 \end{cases} \tag{2.11}$$

where R is the distance between QD and NPL and r_0 is the size of the NPL. The traditional R^{-6} distance dependence is recovered at the far-field limit, but in the case of near-field FRET, the rate equation has a different distance dependence and pre-factor. This behavior is also shown through numerical calculation, where a transition of R^{-4} to R^{-6} dependence can be clearly seen with increasing donor-acceptor distances (Figure 2.5d). Considering the high QD-to-NPL ratio and the relatively large size of the NPL, it is likely that the traditional (R^{-6}) FRET rate equation fails to accurately describe the situation and it is necessary to use the near-field FRET rate equation. We

then used the obtained near-field FRET rate equation in kinetic Monte Carlo simulations to calculate the FRET efficiencies for different QD concentrations (See Section 2.8). Based on the simulations, we can confirm that the donor-acceptor distances are indeed in the near-field range where R^{-4} dependence should be used. The average distance depends on the QD-NPL ratio, but we found these R/r_0 distances to be between 0.0136 – 0.0216 (shown on a log scale in Figure 2.5d). By comparing the simulations with experimental results (Figure 2.5e), we can conclude that the near-field FRET is indeed the energy transfer mechanism in the mixed case.

2.6 Conclusion

Fluorescence quenching is a canonical method in the study of reacting systems, and is used broadly in biological and chemical assays. However, simple applications of Stern-Vollmer quenching are not appropriate in FRET pairs, given the nonlinearity of dipole-dipole coupling. Attempts to adapt other FRET models, or effective volume approaches also fail. While more complex behavior can be invoked to explain quenching behavior, the quantitative agreement between quenching studies and KMC simulations that take into account real interparticle separations and diffusion, suggest a simple general model captures the high magnitude and nonlinearity of quenching in a PbS-CuS system. Therefore, we conclude that non-interacting molecular systems can be effectively quenched with low-concentrations of impurities, provided energetic conditions are met. In the case of high-concentration mixture, the geometry of chromophores (nanocrystals) starts to play an important role in the distance dependence of FRET rate, exhibiting "near-field" FRET efficiency. Our results suggest that dipolar coupling and diffusion serve to 'superpower' quenching, concentrating a diffuse excitation on a few plasmonic defects. These effects will become more important in long-lived excitations in the near and

shortwave infrared (where diffusion can play a role), or in materials with high transition dipole moments (where FRET radius is elevated).

2.7 Experimental Details

2.7.1 Chemicals

Lead chloride ($PbCl_2$) (Alfa Aesar, 99%), *N,N'*-diphenylthiourea (DPTU) (Alfa Aesar, 98%), cuprous chloride (Cu(I)Cl) (Alfa Aesar, 97%), Cadmium oxide (CdO) (Alfa Aesar, 99.95%), sulfur (S) powder (Alfa Aesar, sublimed, 99.5%), tellurium (Te) powder (Acros, 99.8%), mercury (II) acetate ($Hg(OAc)_2$) (Chem-Impax International, 98.0%), oleylamine (OLAm) (Tokyo Chemical, >50.0%), oleic acid (Alfa Aesar, 99%), propionic acid (Fisher), tri-n-octylphosphine (TOP) (Alfa Aesar, 90%), 1-octadecene (ODE) (Alfa Aesar, 90%), toluene (Fisher, 99.9%), ethanol (Fisher, 95.27%), hexanes (Fisher, 98.5%), methanol (Fisher, 99.8%), acetone (Fisher, 99.5%).

2.7.2 Synthesis of Precursors

0.33 M N,N'-diphenylthiourea (DPTU). In a round bottom flask, 2.5 mmol of *N,N'*-diphenylthiourea (DPTU) was suspended in 7.5 mL of 1-octadecene (ODE). The suspensions was degassed under vacuum at 100 °C for 1 hour and then purged with Ar at 120 °C for 30 minutes.

1 M S-OLAm. In a round bottom flask, 5 mmol of elemental S powder was dissolved in 5 mL of OLAm under vaccum at room temperature.

Cadmium Propionate ($Cd(prop)_2$). In a round bottom flask, 1.036 g of CdO powder and 10 mL of propionic acid were mixed under argon flow for 1 hour. The flask was then open to atmosphere and heated to 140 C until the volume reduced by half. The while solution was precipitated with acetone and centrifuged. The supernatant was discarded, and the solution was dried and stored in a vacuum desiccator.

1M TOP-Te. Following Izquierdo et al.,[40] Te powder (0.254 g) and tri-n-octylphosphine (2 mL) were combined in a small flask and degassed under vacuum at room temperature. Under argon flow, the solution was stirred at 275 C until the dissolution was complete and solution turned yellow. The solution was cooled and diluted to 0.5M with additional tri-n-octylphosphine.

10 mM Mercury Acetate ($Hg(OAc)_2$). In a small vial, 9.2 mg of mercury (II) acetate and 3 mL of oleylamine were stirred at room temperature until dissolved.

2.7.3 Synthesis of Nanocrystals

Lead sulfide (PbS) quantum dots (QDs). We followed the procedure proposed by Chan et al.[18] In a round bottom flask, 3 mmol of lead chloride ($PbCl_2$) was suspended in 7.5 mL of oleylamine (OLAm). The precursor suspensions were degassed under vacuum at 100 °C for 1 hour and then purged with Ar at 120 °C for 30 minutes. The lead precursor suspension was then cooled to 80 °C and 2.25 mL of 0.33 M DPTU suspension was injected to initiate the reaction. The reaction was kept at 80 °C for 100 s to achieve the desired absorption wavelength. The reaction was quenched by the addition of a mixture of 10 mL of toluene and 25 mL of ethanol. The QDs were then washed for several times and finally re-suspended in toluene.

Covellite copper sulfide (CuS) nanodisks (NDs). We followed the procedure proposed by Xie et al.[19] In a round bottom flask, 0.5 mmol of cuprous chloride (CuCl) was dissolved in a mixture of 24 mmol of 1-octadecene (ODE) and 6 mmol oleylamine (OLAm) under vacuum at 130 °C. The copper precursor solution was then heated to 180 °C under Ar flow and 2 mL of 1 M S-OLAm solution was injected to initiate the reaction. The reaction was annealed at 180 °C for 10 minutes for complete crystal growth. The NDs were cooled to room temperature and precipitated with a mixture of methanol and acetone, before re-suspended in toluene. The washing cycles were repeated for several times before finally re-suspending the CuS NDs in toluene.

3ML CdTe NPLs. Adapted from Izquierdo et al.,[40,41] $Cd(prop)_2$ (260 mg), oleic acid (0.160 mL), and ODE (20 mL) were degassed under vacuum at 90 C for 1 hour in a three-neck flask. Under argon flow, the solution was heated to 210 C and a mixture of 1 M TOP-Te (0.200 mL) and ODE (3.75 mL) was injected with a syringe pump at a rate of 5 mL/hr. The reaction was quenched with oleic acid (0.500 mL) and cooled to room temperature. The NPLs were precipitated with ethanol and centrifuged at 14000 rpm for 5 min, then resuspended in hexanes (20 mL).

Cation Exchange from CdTe to HgTe NPLs. Following Tenney at al.,[41] In a round bottom flask, 6 mM CdTe NPL (0.240 mL) and hexanes (6 mL) were mixed. Then, 10 mM $Hg(OAc)_2$ in oleylamine (0.300 mL) was added and the solution was stirred at room temperature for 3-4 hours until appropriate location of the excitonic features on the absorption spectra. Once complete, the NPLs were centrifuged at 9000 rpm for 5 min then resuspended in hexanes (5 mL).

HgTe QDs. Adapted from Piepenbrock et al.[42] In a three-neck round bottom flask, mercury acetate (330 mg), oleylamine (1.380 mL), and ethanol (15 mL) were heated to 50 C under argon flow until the solution was clear. The flask was then placed in a water bath and 0.5 M TOP-Te (0.1 mL, diluted from the 1M stock solution) was injected once the solution reached the desired temperature. Lower temperatures (< 25C) were used for small QDs, while increasing temperatures (30, 40, 50 C) were used for larger QDs. The solution immediately turned brown and was allowed to stir for 30 s before quenching with an ice bath. The QDs were precipitated with an excess of ethanol and centrifuged at 14000 rpm for 5 min, then resuspended in hexanes (10 mL).

2.7.4 Mixing Experiments

PbS QDs and CuS NDs. To study the fluorescence quenching of PbS QDs by CuS NDs, we carried out a series of titration experiments. 50-1000 µL of PbS QDs suspension and 0-2000 µL of CuS NDs suspension were pipetted and mixed in a 4 mL vial, with extra toluene added to make

the total volume of the mixture 3 mL. The suspensions were then vortexed for 60 s to guarantee complete mixing of the nanocrystals. The titration samples were divided into several groups, and in each group the concentration of PbS QDs was kept constant and we only varied the concentrations of CuS NDs. Photoluminescence (PL) spectroscopy of all mixtures were measured and quenching ratios were calculated by dividing in each group the PL intensity without quenchers (I_0) by quenched PL intensities (I).

HgTe QDs and HgTe NPLs. The volume of NPLs added were determined using measured absorption spectra to ensure sufficient optical density (~ 0.5 OD at the NPL heavy hole). Using the QDs synthesized separately, varied amounts of QDs were added, from 8.5 x 10^{-5} mM to 3.4 x 10^{-4} mM total concentration in the mixture. Hexanes was added to ensure that all samples reached a total of 2 mL. The samples were then kept on ice following mixing to minimize growth of QDs during the reaction and absorption and PL spectra were recorded immediately.

2.7.5 Materials Characterization

Absorption spectra were obtained using an Agilent Cary 60 UV-Vis spectrophotometer (for UV-vis) and a Shimadzu UV/Vis/NIR Spectrophotometer (for SWIR). Photoluminescence (PL) spectra were obtained using a home-built setup with an Ocean Optics flame NIR detector. Lifetime were obtained using a home-built setup with superconducting nanowire single photon detectors (SNSPDs). Transmission electron microscopy (TEM) images are obtained using a T12 Quick Room Temperature TEM. TEM Samples are prepared by diluting nanocrystals solutions and drop-casting on Formvar 300 mesh copper grids (Ted Pella, Inc.).

2.8 Supporting Information

This section contains analysis and corrections on experimental results and detailed explanation of modeling and simulations.

TEM results and analysis of PbS QDs and CuS NDs

Sizes of nanocrystals are measured based on the TEM images and the size distribution curves are fitted with lognormal functions.[43]

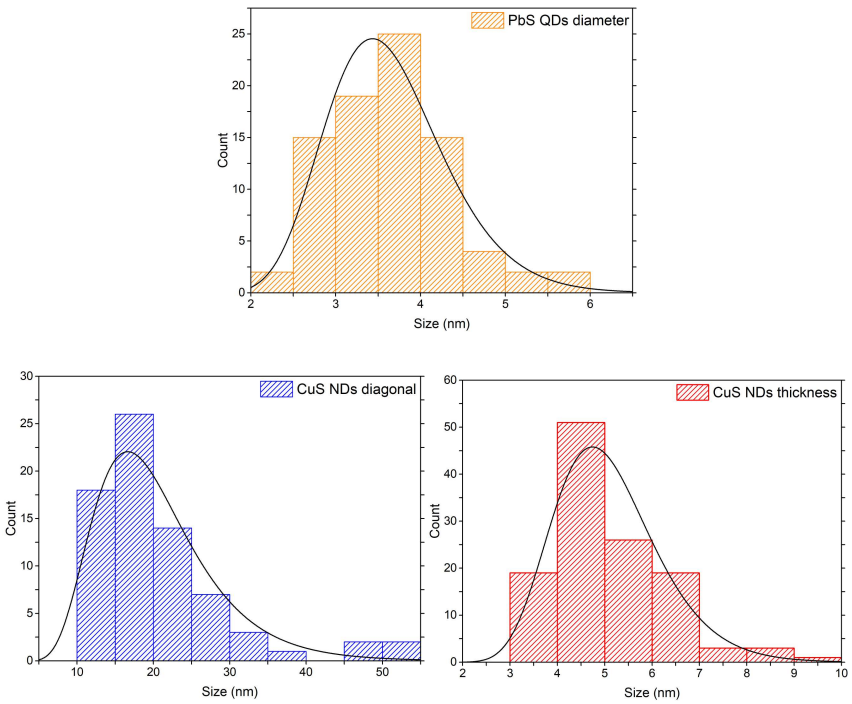

Figure 2.6 Size distribution of PbS QDs (top) and CuS NDs (bottom; left: diagonal size; right: thickness).

In the TEM images of mixture of PbS QDs and CuS NDs, no obvious change of shape or destruction of QDs and NDs was observed, suggesting no chemical reaction between quenchers and emitters.

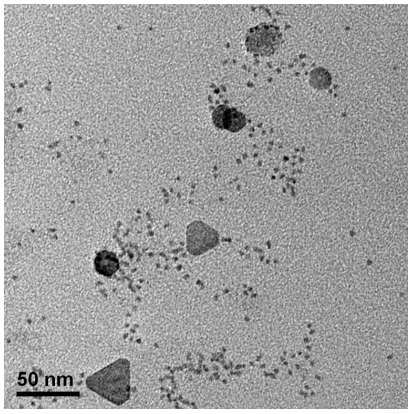

Figure 2.7 TEM image of the mixture of PbS QDs and CuS NDs.

Experimental setup & Correction for Inner filter effect (IFE)

To calibrate for the inner filter effect (IFE), we first calculate the extinction coefficient of CuS NDs. Absorbance are taken for a series of CuS NDs solutions:

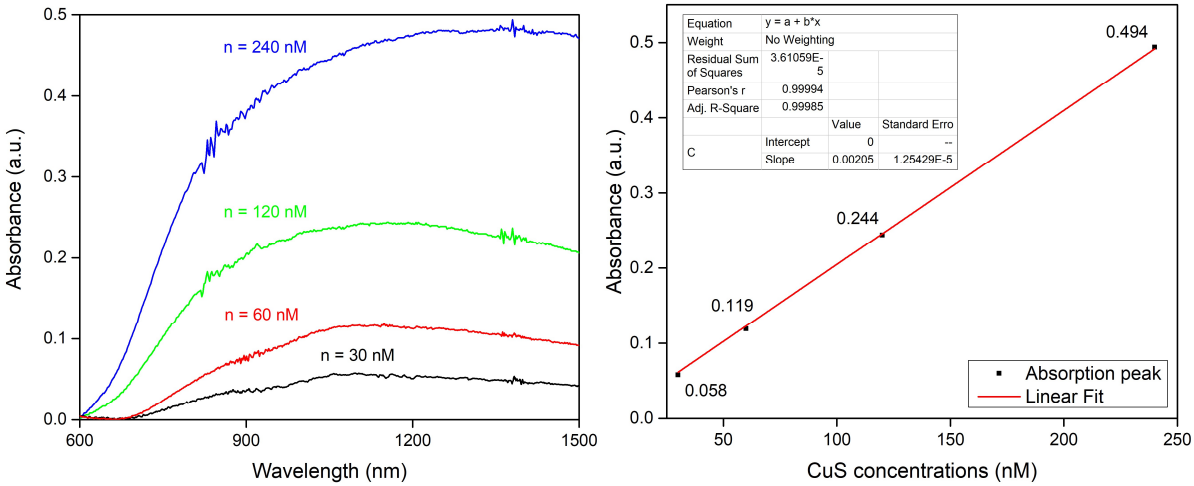

Figure 2.8 Absorption spectra of a series of CuS NDs solutions (left) and linear fitting of absorbance-concentration for extracting extinction coefficient (right).

The extracted extinction coefficient is 2.05×10^{6} $M^{-1}\cdot cm^{-1}$.

Steady-state PL measurements were carried out using the setup with a front-face cuvette configuration show below:

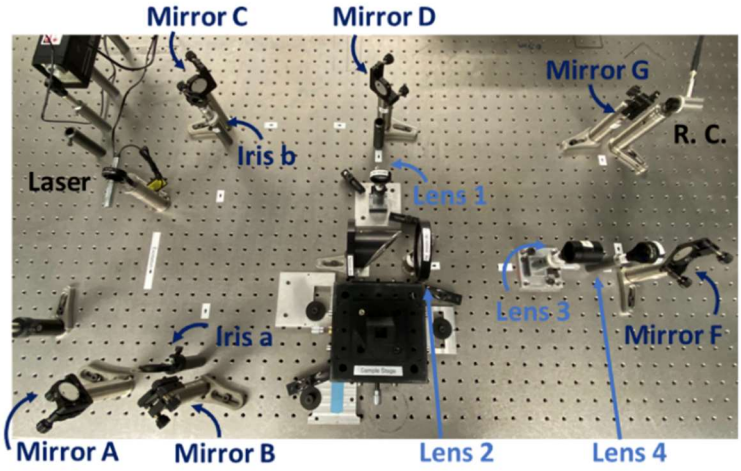

Figure 2.9 Experimental setup for steady-state PL measurements. The sample holder takes a front-face configuration.

For this geometry, the correction factor is given by Leese et al:

$$f = \frac{2.303(A_{ex} + A_{em})}{1 - 10^{-(A_{ex}+A_{em})}}$$

where A_{ex} is the absorbance of CuS NDs solution at the wavelength of excitation, and A_{em} is the absorbance of CuS NDs solution at the wavelength of emission of PbS QDs.[44] Note that the absorbance of CuS NDs at 532 nm (the wavelength of excitation) is negligibly small so essentially only A_{em} contributes to the correction factor.

The apparent quenching ratio, which is derived directly from experiments, is corrected for inner filter effect by dividing the apparent quenching ratio by the correction factor f. An example of such correction for IFE is given below:

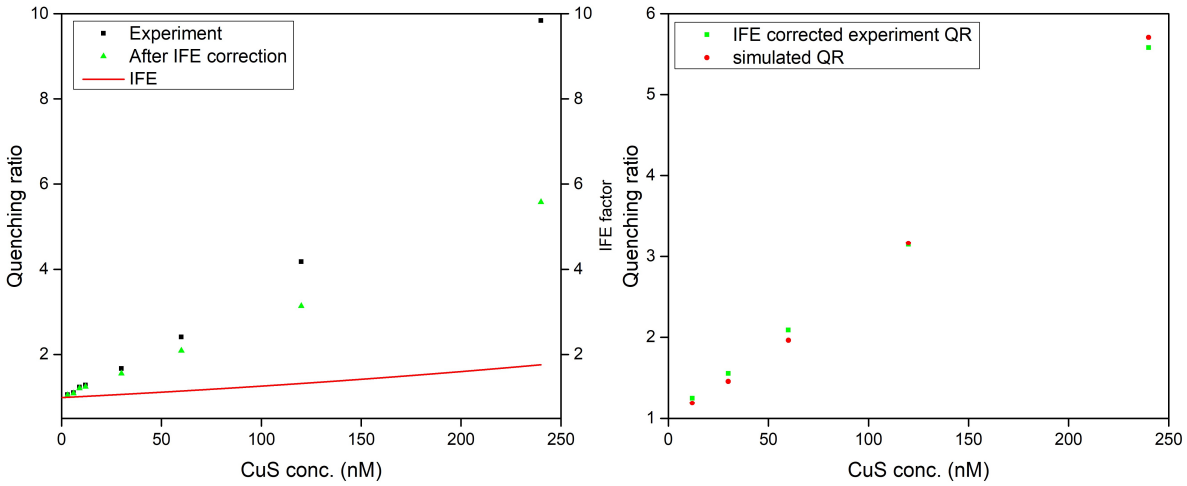

Figure 2.10 Correction for IFE (left) and comparison between experiment quenching ratio after IFE correction and simulations (right).

Non-linear plot of quenching ratios

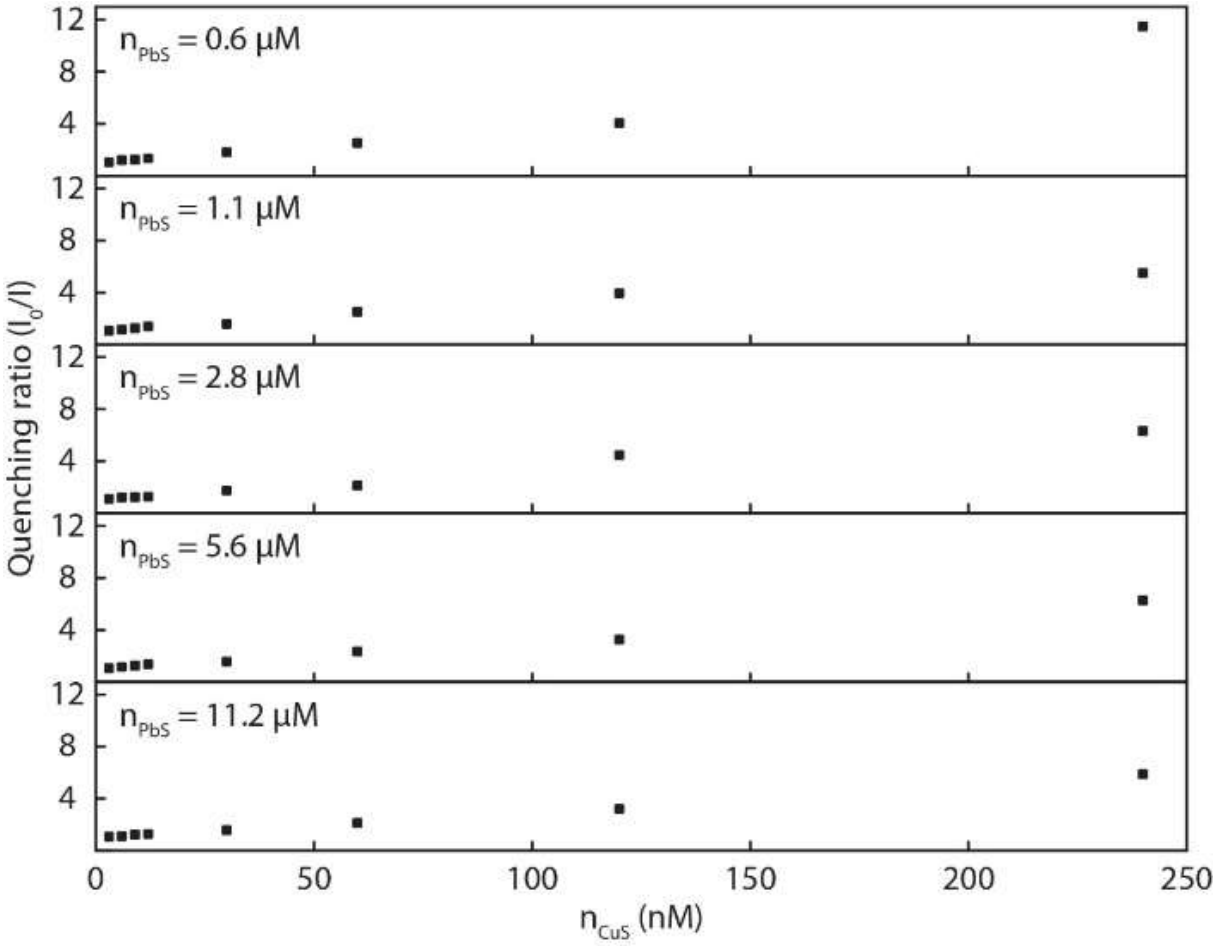

Figure 2.11 A plot of quenching ratio-quencher concentration for titration experiments showing non-linear dependence.

Time-resolved PL measurements & analysis

Pure PbS QDs without quenchers

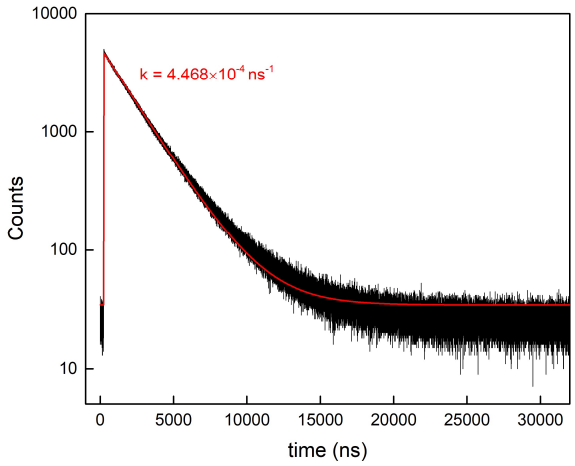

Figure 2.12 Time-resolved PL trace (black) and fitting result (red) of PbS QDs.

The time-resolved trace was fitted with a mono-exponential decay function. The extracted total decay rate (shown in the figure) was then used in modeling and simulations.

Mono-exponential fitting of experimental time-resolved PL traces with quenchers

Time-resolved PL traces of one subset of titration experiments are fitted to mono-exponential decay function given below as an example:

$$P_1 = Aexp(-kt) + C$$

and the fitting parameters are given below:

Table 2.2 Mono-exponential fitting parameters of experimental time-resolved PL traces

[CuS] (nM)	A ($\times 10^4$)	k ($\times 10^{-4}$ ns^{-1})	C
6.0	1.21 ± 0.09	4.18 ± 0.02	88 ± 1
12.0	1.09 ± 0.08	4.38 ± 0.02	92 ± 1
30.0	0.9 ± 0.1	5.11 ± 0.03	109 ± 1
60.0	0.61 ± 0.08	5.37 ± 0.04	90.6 ± 0.9
120.0	0.41 ± 0.05	5.83 ± 0.04	71.6 ± 0.9

A clear increase in the total decay rate of PbS QDs, which is indicative of a decrease in the lifetimes, is observed. However, mono-exponential function may not be the best fitting function to the PL traces:

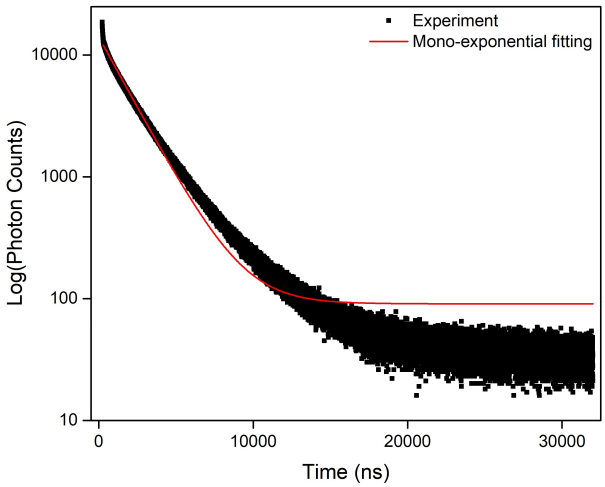

Figure 2.13 An example of mono-exponential fitting of time-resolved PL trace of PbS-CuS mixture. where an obvious deviation is observed.

Bi-exponential fitting of experimental time-resolved PL traces with quenchers

We then turned to bi-exponential functions for the fitting of time-resolved PL traces of the same subset of titration experiments. The bi-exponential fitting function is given below:

$$P_2 = A_1 exp(-k_1 t) + A_2 exp(-k_2 t) + C$$

and the fitting parameters are given below:

Table 2.3 Bi-exponential fitting parameters of experimental time-resolved PL traces

[CuS] (nM)	A_1 ($\times 10^4$)	k_1 ($\times 10^{-4}$ ns^{-1})	A_2 ($\times 10^3$)	k_2 ($\times 10^{-2}$ ns^{-1})	C	Average lifetime (ns)
6.0	1.16 ± 0.05	4.02 ± 0.01	4.0 ± 0.1	1.47 ± 0.06	65.7 ± 0.6	1867 ± 1
12.0	1.05 ± 0.04	4.20 ± 0.01	3.50 ± 0.08	1.36 ± 0.05	70.6 ± 0.4	1803 ± 1
30.0	0.88 ± 0.07	4.62 ± 0.02	3.88 ± 0.07	0.79 ± 0.03	73.5 ± 0.5	1538 ± 1
60.0	0.62 ± 0.02	4.73 ± 0.02	2.86 ± 0.04	0.63 ± 0.02	62.4 ± 0.4	1494 ± 1
120.0	0.37 ± 0.04	5.11 ± 0.05	1.6 ± 0.1	0.33 ± 0.02	48.0 ± 0.5	1465 ± 1

where the average lifetimes are calculated as below:

$$\bar{\tau} = \frac{\frac{A_1}{k_1} + \frac{A_2}{k_2}}{A_1 + A_2}$$

Again, a clear decrease in the average lifetime is observed.

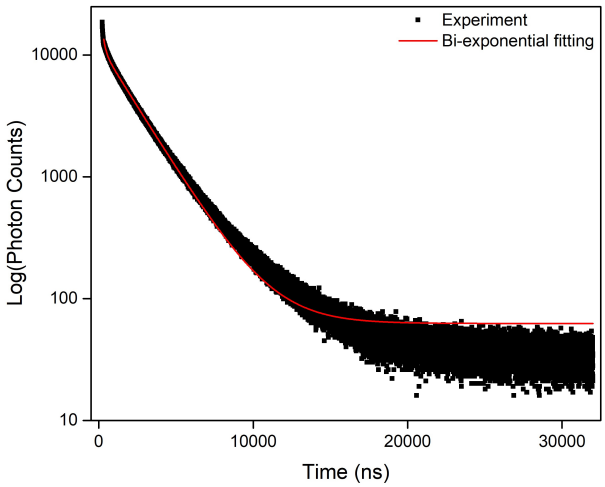

Figure 2.14 An example of bi-exponential fitting of time-resolved PL trace of PbS-CuS mixture.

Apparently bi-exponential decay functions are better choices for fitting. It is worth mentioning here that the fast and slow components extracted from fitting are not directly representative of the actual rates of fast and slow photophysical processes in the system but the exchange between different mechanisms of quenching.

Quenching behaviors at early time and later time: comparing experiments and simulations

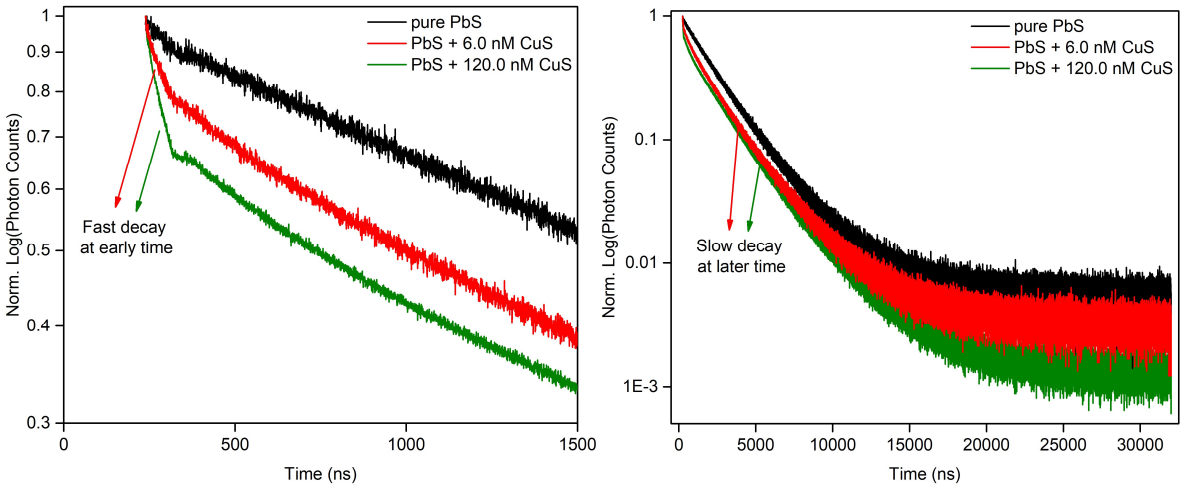

Figure 2.15 Experimental time-resolved PL traces of pure PbS and quenched PbS samples (Left: zoomed in at early time; right: full range).

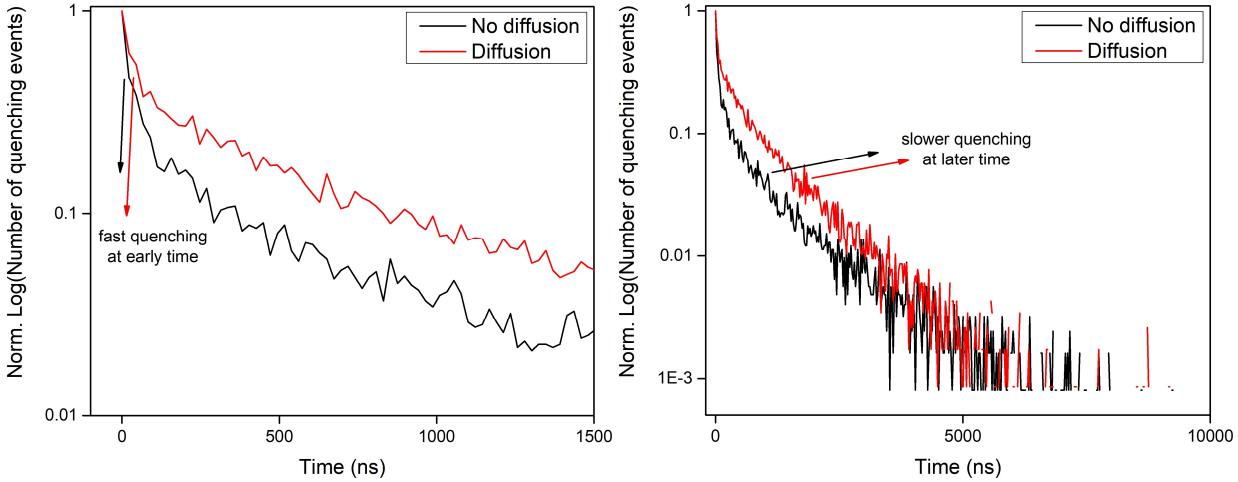

Figure 2.16 Number of quenching events monitored over time in the simulations (Left: zoomed in at early time; right: full range).

Kinetic Monte-Carlo (kMC) algorithm

The kinetic Monte-Carlo algorithm used in simulations is explained below.

Input. Parameters derived from characterization of nanocrystals are shown in main text (Table 2.1). The only other inputs are volumes of nanocrystals solutions used in titration experiments.

Initialization. The number of PbS QDs and CuS NDs are first determined using concentrations and volumes. A three-dimensional box consisting of identical discrete smaller boxes is then constructed as a representation of the positions of nanocrystals in colloidal solution. Size of the smaller boxes is also calculated by the total concentration of nanocrystals under corresponding experimental conditions and each nanocrystal, regardless of its chemical composition, is only capable of occupying one box. As the final step of initialization, sets of coordinates are randomly generated as the initial positions of nanocrystals (Figure 2.17).

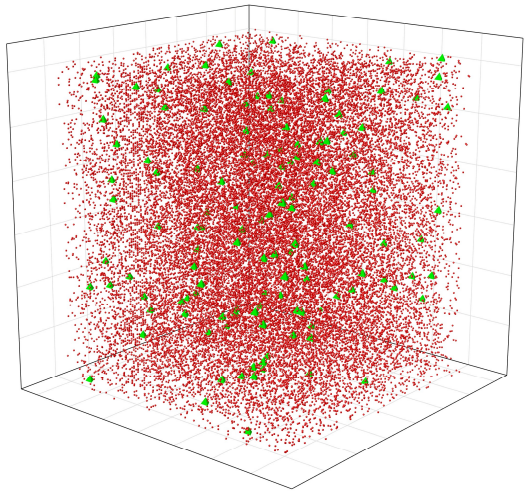

Figure 2.17 Visualization of the box used in kMC simulations. (Red: PbS QDs; Green: CuS NDs. The sizes do not reflect the real scale of nanocrystals.)

Calculation. After initialization, a distance matrix recording distances of all possible PbS-CuS pair is first obtained based on their coordinates. For the rate matrix that will be used for later pathway selection, three types of rates are considered: (1) Total decay/emission rate: The total

decay rate extracted from lifetime measuring experiments is used for each excited emitter.; (2) FRET rates: The quenching rates due to FRET from PbS QDs to CuS NDs. These are calculated for every possible PbS-CuS pair based on the distance matrix; (3) Idle rate: Idle rate is introduced to take diffusion of nanocrystals into consideration. In conventional kMC algorithm, only rates concerning the change of states (i.e., fluorescence decay or FRET) are considered, which makes it rather difficult to implement diffusion since it doesn't involve change of states but still has influence on rates due to change of distances. By introducing idling behavior, namely the situation where excited emitters do not go through any de-excitation pathway but stay excited during a certain period of time, we are not only able to monitor the regular change of states but also keep track of the impact of diffusion on the kinetics. The idle rate of excited emitters is calculated given a user-defined probability p:

$$\frac{k_0}{k_{idle} + k_0} = p \leftrightarrow k_{idle} = k_0 \cdot \frac{1-p}{p}$$

Pathway selection. The pathway selection procedure is achieved using the BKL algorithm, where partial sum of the rate matrix and RNG are used.[45] Particles that go through any de-excitation pathway are no longer considered in the next time step. For idle particles, the diffusions are described as three-dimensional random walk:

$$\boldsymbol{R}_{N+1} - \boldsymbol{R}_N = \sqrt{6D\Delta t} \cdot \boldsymbol{n}_{\text{rand}}$$

where $\boldsymbol{n}_{\text{rand}}$ is a randomly oriented unit vector indicating the direction of diffusion.

Updating. To advance the clock, the time step Δt is given by the following equation:

$$\Delta t = \frac{1}{k_{idle}} = \frac{1}{k_0} \cdot \frac{p}{1-p}$$

This constant time step makes it possible for an excited emitter to go through any of the de-excitation pathway during the corresponding period of time Δt. The coordinates of nanocrystals

and the rate matrix are then updated at each time step for a new round of pathway selection, and only after all emitters get de-excited the simulation ends. Note that a distance bound is also implemented to prevent donor and quencher from diffusing infinitely close to one another, so that the FRET rates do not go to infinity. As a control trial, the decay of a pure PbS QDs (without quenchers) sample was simulated and the time evolution of the number of excited donors was monitored. The correct lifetime was recovered (Figure 2.18).

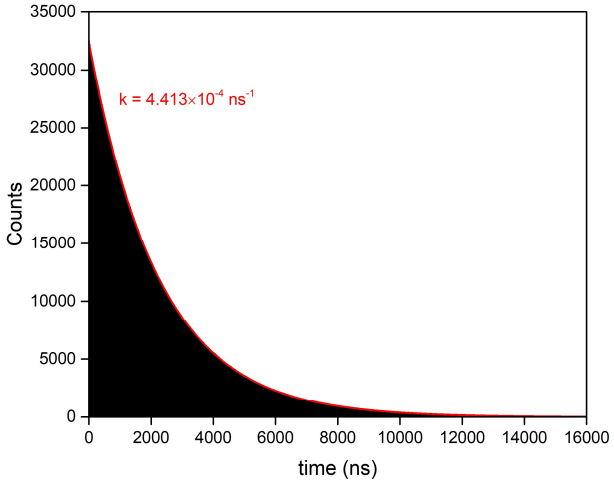

Figure 2.18 A control simulation of pure PbS QDs. (black: number of excited donors over time; red: fitting result.)

Output. The overall ratio of emitters that go through FRET or non-FRET pathway is recorded. Quenching ratio is then calculated and compared with experimental results.

A more detailed discussion about the influence of diffusion on FRET rate

For a pair of donor and acceptor, we introduce two spheres with specified radius to describe the impact of diffusion on interparticle distance and FRET rate (Figure 2.19):

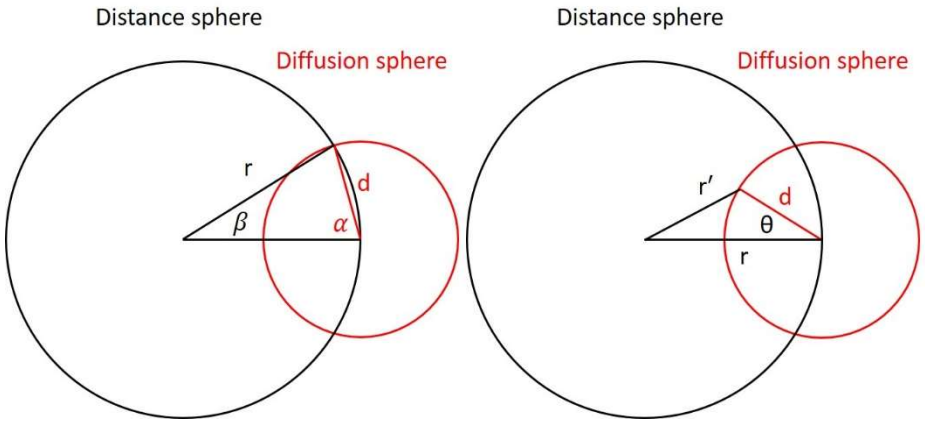

Figure 2.19 2D diagram of distance sphere and diffusion sphere (Left: for interparticle distance calculation; right: for FRET rate calculation). Quencher is located at the center of distance sphere and donor is located at the center of diffusion sphere. The center of diffusion sphere always sits on the surface of distance sphere.

We start with examining the change in interparticle distances caused by diffusion. Essentially, the interparticle distance could increase or decrease based on the direction of diffusion. The probability of FRET pairs getting closer can be calculated by determining solid angle of the spherical sector of the diffusion sphere that lies within the distance sphere:

$$p_c = \frac{\Omega_{in}}{\Omega_0}$$

where solid angle can be readily calculated by integration:

$$\Omega = \int d\Omega = \iint \sin\theta d\theta d\varphi$$

so the probability p_c can be calculated as follow:

$$p_c = \frac{\int_0^{2\pi} d\varphi \int_0^{\alpha} \sin\theta d\theta}{\int_0^{2\pi} d\varphi \int_0^{\pi} \sin\theta d\theta} = \frac{2\pi(1-\cos\alpha)}{4\pi}$$

where the planar angle α depends on the radius of distance sphere and diffusion sphere:

$$\cos\alpha = \frac{d}{2r}$$

and finally, the probability is given below:

$$p_c = \frac{1}{2}\left(1 - \frac{d}{2r}\right)$$

The probability of FRET pairs diffusing further away is then given by:

$$p_f = 1 - p_c = \frac{1}{2}\left(1 + \frac{d}{2r}\right)$$

By comparing p_c and p_f, it is immediately noticed that diffusion always favors pushing FRET pairs further away from each other.

We then take a look at the change of FRET rate. New interparticle distance after diffusion is given by:

$$r' = \sqrt{r^2 + d^2 - 2rd \cdot cos\,\theta}$$

The average FRET rate is calculated by integration with a different integrand:

$$\langle k_{FRET} \rangle = \iint \frac{sin\,\theta\, d\theta d\varphi}{4\pi} \cdot k_0 (\frac{R_0}{r'})^6$$

where the first part is the percentage of the differential solid angle that has the same new interparticle distance r'. This integration is actually straightforward and the result is given below:

$$\langle k_{FRET} \rangle = \frac{k_0 R_0^6}{r^6} \cdot \frac{1 + \left(\frac{d}{r}\right)^2}{\left(1 - \left(\frac{d}{r}\right)^2\right)^4} = \frac{k_0 R_0^6}{r^6} \cdot f$$

where the first term is the ordinary FRET rate without diffusion and the second term is a scaling factor f. To understand the dependence more intuitively, we plot the second term against $(\frac{d}{r})^2$:

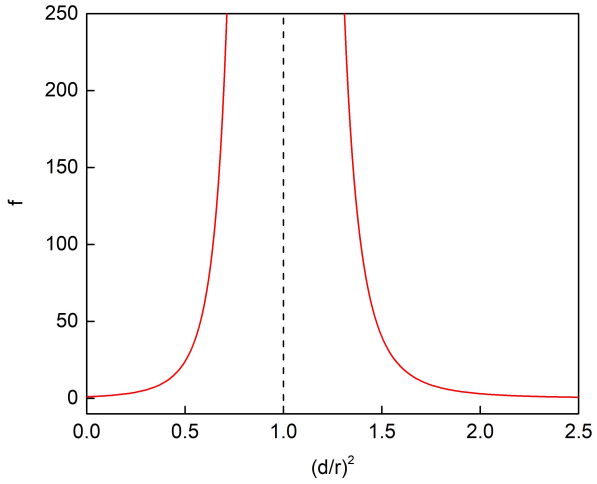

Figure 2.20 Functional dependence of the scaling factor on $(\frac{d}{r})^2$. The dashed line represents $x = 1$, which is an asymptote of this function. Equation $f = 1$ has two solutions: $x = 0$ or $x = 2.3532$.

In most cases of our simulations, $(\frac{d}{r})^2$ lies in the range from 0 to 1, thus resulting in a higher average FRET rate for most FRET pairs. Again, we implemented a lower bound of the interparticle distances in simulations so all the FRET rates don't become infinitely large. It is also possible to have cases where $(\frac{d}{r})^2 > 2.3532$ if the original interparticle distance r is very small, on which diffusion will have a negative impact on FRET rates, but in these cases the original FRET rate is already very high and the donor will very likely go through the FRET de-excitation pathway before diffusion can play a role. One last point related to this analysis is that the number of donors that have the same interparticle distance to a certain quencher is also distance-dependent, which follows a simple spherical differential (note that this is for only one quencher and as we mentioned in main text there is no known analytical form of this distribution in binary solutions):

$$dN(r) = n \cdot 4\pi r^2 dr$$

where n is the donor number density. This also means the FRET pairs that are close should have less impact from diffusion compared to those that are more distantly separated. Overall, diffusion will have a positive impact on FRET rates and thus on quenching as well.

Non-linearity relationships shown at higher concentration

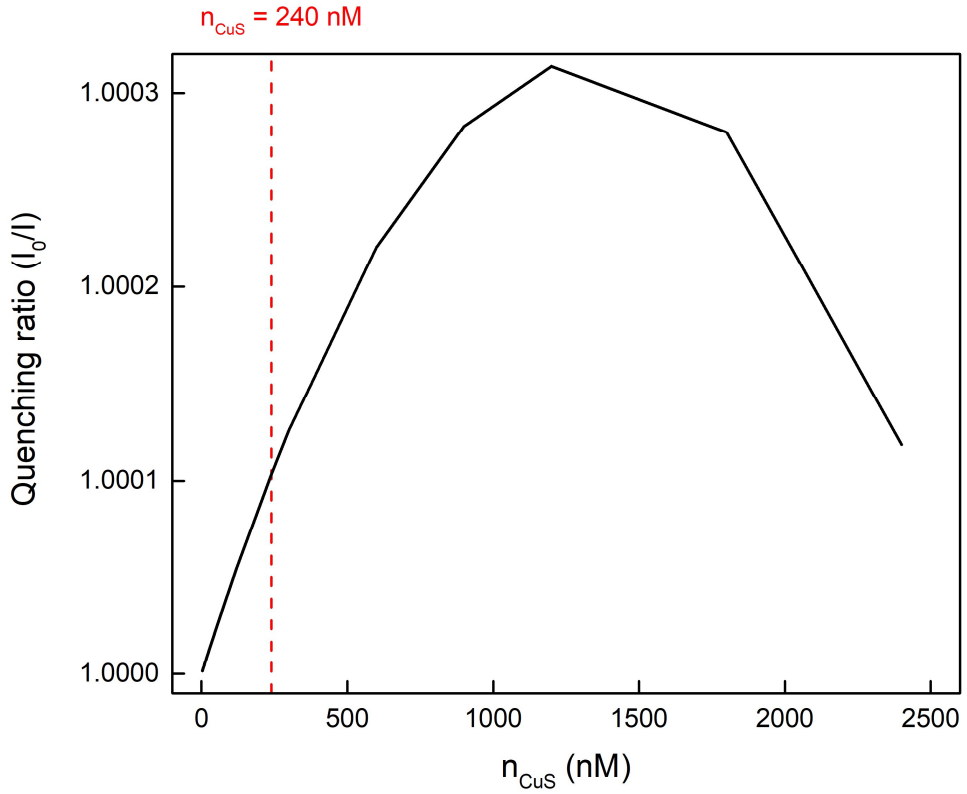

Figure 2.21 Non-linearity dependence predicted by crystalline defect model at higher quencher concentrations. Upper limit of concentrations tested in experiments is shown in the graphs with red dashed lines.

Quenching enhancement by diffusion in canonical FRET systems

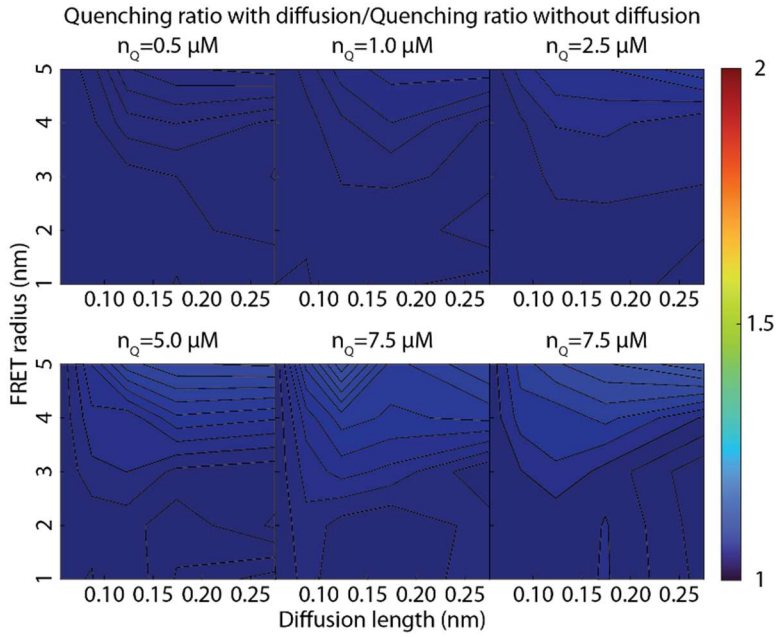

Figure 2.22 Quenching enhancement by diffusion for a pair of cyanine dyes.

To examine the impact of diffusion in other FRET systems, we ran the same simulations to calculate the quenching ratios of canonical FRET pairs: cyanine dyes. In general, cyanine dyes have higher diffusion coefficients, much shorter lifetimes and smaller FRET radius compared to PbS-CuS pairs we explored. The enhancement of quenching induced by diffusion for cyanine dyes pairs are obviously less significant than PbS-CuS system, mainly due to much lower diffusion length arising from their very short lifetimes (Figure 2.22). The range of parameters are determined based on literature about cyanine dyes (Table 2.4).[46–53]

Table 2.4 Parameters for cyanine dyes*

Nanocrystals	Concentration (μM)	Diffusion coefficient ($nm^2 \cdot ns^{-1}$)	Total decay rate (ns^{-1})	FRET radius (nm)
Cy3	0.1 (as donors)	0.28	5.56	1-5
Cy5	0.5-10 (as acceptors)	0.28	1.02	
Cy7		0.25	1.05	

* Parameters in the table are taken directly from related literatures. Acceptor concentrations, FRET radius and diffusion length are varied in a range to obtain a series of simulations.

Distance dependence of FRET rate for NPL-QD (2D-0D) energy transfer

The FRET rate for the 2D-0D system is calculated by the following equation:

$$k = \frac{2\pi}{\hbar}\frac{1}{N_x N_y}\sum_{i}^{N_x N_y} J_i^2 S_i$$

where S_i is the overlap integral between the lineshapes of donor and acceptor, and J_i is the dipole-dipole coupling term:

$$J_i = \frac{\overrightarrow{\mu_{QD}} \cdot \overrightarrow{\mu_{NPL,\,i}}}{r^3} - 3\frac{(\overrightarrow{\mu_{QD}} \cdot \vec{r})(\overrightarrow{\mu_{NPL,\,i}} \cdot \vec{r})}{r^5}$$

As S_i is considered to be a constant, we only need to calculate the summation of coupling terms over all small dipoles of the NPLs. Note that the energy scaling factor $k_e\mu^2$ is omitted for now at the convenience of extracting only the distance dependence. The analytical form is given by continuous integration:

$$k \propto \frac{1}{N_x N_y} \underbrace{\boxed{\int_0^{2\pi} d\varphi \int_{-\frac{\pi}{2}}^{\frac{\pi}{2}} d\theta}}_{\text{freely rotating QD}} \underbrace{\boxed{\int_0^{2\pi} d\varphi'}}_{\text{isotropic NPL dipole}} \underbrace{\boxed{\int_{-\frac{aN_x}{2}}^{\frac{aN_x}{2}} dx \int_{-\frac{aN_y}{2}}^{\frac{aN_y}{2}} dy}}_{\text{all NPL dipoles}}$$

$$\left[\frac{\cos\theta\,(\cos\varphi\cos\varphi' + \sin\varphi\sin\varphi')}{(R^2 + x^2 + y^2)^{\frac{3}{2}}}\right.$$

$$\left. - \frac{3(\cos\theta\cos\varphi\,x + \cos\theta\sin\varphi\,y - R\sin\theta)(\cos\varphi'\,x + \sin\varphi'\,y)}{(R^2 + x^2 + y^2)^{\frac{5}{2}}}\right]^2$$

$$= \frac{\pi^3}{r_0^2}\left\{\frac{5}{4}\left[\frac{1}{R^4} - \frac{1}{(R^2 + r_0^2)^2}\right] + \left(\frac{3}{2\pi} - 2\right)R^2\left[\frac{1}{R^6} - \frac{1}{(R^2 + r_0^2)^3}\right]\right.$$

$$\left. + \left(\frac{9}{8} - \frac{9}{8\pi}\right)R^4\left[\frac{1}{R^8} - \frac{1}{(R^2 + r_0^2)^4}\right]\right\}$$

$$= \begin{cases} \frac{3\pi^3}{8r_0^2}\left(1+\frac{1}{\pi}\right)\frac{1}{R^4} & R \ll r_0 \\ \frac{\pi^3}{4}\left(5-\frac{3}{\pi}\right)\frac{1}{R^6} & R \gg r_0 \end{cases}$$

Note that the area of integration over all NPL dipoles are converted to a circular area using polar coordinates for simplicity.

To find the pre-factor for the near-field FRET rate equation, we calculate the overlap of lineshapes based on experimental spectra. The dipole moment in the scaling factor $k_e\mu^2$ is estimated based on reported range of oscillator strength of HgTe QDs (2-10) using the following equation[54,55]:

$$\mu^2 = \frac{3e^2\hbar}{2m_e\omega} f_{osc}$$

REFERENCES

(1) Stern, O.; Volmer, M. Über Die Abklingzeit Der Fluoreszenz. *Zeitschrift für Phys.* **1919**, *20*, 183–188.

(2) Behera, P. K.; Mukherjee, T.; Mishra, A. K. Simultaneous Presence of Static and Dynamic Component in the Fluorescence Quenching for Substituted Naphthalene-CCl4 System. *J. Lumin.* **1995**, *65* (3), 131–136. https://doi.org/10.1016/0022-2313(95)00067-Z.

(3) Tong, J. Q.; Tian, F. F.; Li, Q.; Li, L. L.; Xiang, C.; Liu, Y.; Dai, J.; Jiang, F. L. Probing the Adverse Temperature Dependence in the Static Fluorescence Quenching of BSA Induced by a Novel Anticancer Hydrazone. *Photochem. Photobiol. Sci.* **2012**, *11* (12), 1868–1879. https://doi.org/10.1039/c2pp25162k.

(4) Htun, T. Excited-State Proton Transfer in Nonaqueous Solvent. *J. Fluoresc.* **2003**, *13* (4), 323–329. https://doi.org/10.1023/A:1025377711659.

(5) Geethanjali, H. S.; Nagaraja, D.; Melavanki, R. M.; Kusanur, R. A. Fluorescence Quenching of Boronic Acid Derivatives by Aniline in Alcohols - A Negative Deviation from Stern-Volmer Equation. *J. Lumin.* **2015**, *167*, 216–221. https://doi.org/10.1016/j.jlumin.2015.06.040.

(6) Forster, T. Energiewanderung Und Fluoreszenz. *Naturwissenschaften* **1946**, *33*, 166–175.

(7) Ermolenko, D. N.; Majumdar, Z. K.; Hickerson, R. P.; Spiegel, P. C.; Clegg, R. M.; Noller, H. F. Observation of Intersubunit Movement of the Ribosome in Solution Using FRET. *J. Mol. Biol.* **2007**, *370* (3), 530–540. https://doi.org/10.1016/j.jmb.2007.04.042.

(8) Borst, J. W.; Laptenok, S. P.; Westphal, A. H.; Kühnemuth, R.; Hornen, H.; Visser, N. V.; Kalinin, S.; Aker, J.; Van Hoek, A.; Seidel, C. A. M.; Visser, A. J. W. G. Structural Changes of Yellow Cameleon Domains Observed by Quantitative FRET Analysis and Polarized Fluorescence

Correlation Spectroscopy. *Biophys. J.* **2008**, *95* (11), 5399–5411. https://doi.org/10.1529/biophysj.107.114587.

(9) Taraska, J. W.; Puljung, M. C.; Olivier, N. B.; Flynn, G. E.; Zagotta, W. N. Mapping the Structure and Conformational Movements of Proteins with Transition Metal Ion FRET. *Nat. Methods* **2009**, *6* (7), 532–537. https://doi.org/10.1038/nmeth.1341.

(10) Dong, X.; Thomas, D. D. Time-Resolved FRET Reveals the Structural Mechanism of SERCA-PLB Regulation. *Biochem. Biophys. Res. Commun.* **2014**, *449* (2), 196–201. https://doi.org/10.1016/j.bbrc.2014.04.166.

(11) Mazal, H.; Haran, G. Single-Molecule FRET Methods to Study the Dynamics of Proteins at Work. *Curr. Opin. Biomed. Eng.* **2019**, *12*, 8–17. https://doi.org/10.1016/j.cobme.2019.08.007.

(12) Inokuti, M.; Hirayama, F. Influence of Energy Transfer by the Exchange Mechanism on Donor Luminescence. *J. Chem. Phys.* **1965**, *43* (6), 1978–1989. https://doi.org/10.1063/1.1697063.

(13) Edgal, U. F. Partial Nearest Neighbor PDF for Multi-Component Material Systems. *J. Math. Chem.* **2007**, *42* (4), 1101–1134. https://doi.org/10.1007/s10910-007-9291-1.

(14) Rohrmann, R. D.; Zorec, J. Thermostatistical Description of Gas Mixtures from Space Partitions. *Phys. Rev. E - Stat. Nonlinear, Soft Matter Phys.* **2006**, *74* (4), 1–14. https://doi.org/10.1103/PhysRevE.74.041120.

(15) Edgal, U. F. The Exact Statistical Thermodynamics of Classical Fluids. *J. Chem. Phys.* **1991**, *94* (12), 8179–8190. https://doi.org/10.1063/1.460101.

(16) Sur, P.; Bhattacharjee, B. Nth-Nearest Neighbour Distribution Functions of a Binary Fluid Mixture. *J. Chem. Sci.* **2009**, *121* (5), 929–934. https://doi.org/10.1007/s12039-009-0110-z.

(17) Torquato, S.; Lu, B.; Rubinstein, J. Nearest-Neighbor Distribution Functions in Many-

Body Systems. *Phys. Rev. A* **1990**, *41* (4).

(18) Chan, S.; Liu, M.; Latham, K.; Haruta, M.; Kurata, H.; Teranishi, T.; Tachibana, Y. Monodisperse and Size-Tunable PbS Colloidal Quantum Dots via Heterogeneous Precursors. *J. Mater. Chem. C* **2017**, *5* (8), 2182–2187. https://doi.org/10.1039/c6tc05329g.

(19) Xie, Y.; Carbone, L.; Nobile, C.; Grillo, V.; D'Agostino, S.; Della Sala, F.; Giannini, C.; Altamura, D.; Oelsner, C.; Kryschi, C.; Cozzoli, P. D. Metallic-like Stoichiometric Copper Sulfide Nanocrystals: Phase- and Shape-Selective Synthesis, Near-Infrared Surface Plasmon Resonance Properties, and Their Modeling. *ACS Nano* **2013**, *7* (8), 7352–7369. https://doi.org/10.1021/nn403035s.

(20) Wu, P. G.; Brand, L. Resonance Energy Transfer: Methods and Applications. *Analytical Biochemistry*. 1994, pp 1–13. https://doi.org/10.1006/abio.1994.1134.

(21) Einstein, A. Über Die von Der Molekularkinetischen Theorie Der Wärme Geforderte Bewegung von in Ruhenden Flüssigkeiten Suspendierten Teilchen. *Ann. Phys.* **1905**, *322* (8), 549–560.

(22) Moreels, I.; Lambert, K.; Smeets, D.; De Muynck, D.; Nollet, T.; Martins, J. C.; Vanhaecke, F.; Vantomme, A.; Delerue, C.; Allan, G.; Hens, Z. Size-Dependent Optical Properties of Colloidal PbS Quantum Dots. *ACS Nano* **2009**, *3* (10), 3023–3030. https://doi.org/10.1021/nn900863a.

(23) Jose, N. A.; Zeng, H. C.; Lapkin, A. A. Hydrodynamic Assembly of Two-Dimensional Layered Double Hydroxide Nanostructures. *Nat. Commun.* **2018**, *9* (1), 1–12. https://doi.org/10.1038/s41467-018-07395-4.

(24) Liu, Y.; Ouyang, Q.; Li, H.; Chen, M.; Zhang, Z.; Chen, Q. Turn-On Fluoresence Sensor for Hg2+ in Food Based on FRET between Aptamers-Functionalized Upconversion Nanoparticles

and Gold Nanoparticles. *J. Agric. Food Chem.* **2018**, *66* (24), 6188–6195. https://doi.org/10.1021/acs.jafc.8b00546.

(25) Liu, J.; Lu, Y. FRET Study of a Trifluorophore-Labeled DNAzyme. *J. Am. Chem. Soc.* **2002**, *124* (51), 15208–15216. https://doi.org/10.1021/ja027647z.

(26) Albertazzi, L.; Arosio, D.; Marchetti, L.; Ricci, F.; Beltram, F. Quantitative FRET Analysis with the E0GFP-MCherry Fluorescent Protein Pair. *Photochem. Photobiol.* **2009**, *85* (1), 287–297. https://doi.org/10.1111/j.1751-1097.2008.00435.x.

(27) Dennis, A. M.; Bao, G. Quantum Dot-Fluorescent Protein Pairs as Novel Fluorescence Resonance Energy Transfer Probes. *Nano Lett.* **2008**, *8* (5), 1439–1445. https://doi.org/10.1021/nl080358+.

(28) Ahmed, I. A.; Rodgers, J. M.; Eng, C.; Troxler, T.; Gai, F. PET and FRET Utility of an Amino Acid Pair: Tryptophan and 4-Cyanotryptophan. *Phys. Chem. Chem. Phys.* **2019**, *21* (24), 12843–12849. https://doi.org/10.1039/c9cp02126d.

(29) Massey, M.; Algar, W. R.; Krull, U. J. Fluorescence Resonance Energy Transfer (FRET) for DNA Biosensors: FRET Pairs and Förster Distances for Various Dye-DNA Conjugates. *Anal. Chim. Acta* **2006**, *568* (1–2), 181–189. https://doi.org/10.1016/j.aca.2005.12.050.

(30) Torney, D. C.; McConnell, H. M. Diffusion-Limited Reaction Rate Theory for Two-Dimensional Systems. *Proc. R. Soc. London, Ser. A Math. Phys. Sci.* **1983**, *387* (1792), 147–170. https://doi.org/10.1098/rspa.1983.0055.

(31) Wallace, B.; Atzberger, P. J. Förster Resonance Energy Transfer: Role of Diffusion of Fluorophore Orientation and Separation in Observed Shifts of FRET Efficiency. *PLoS One* **2017**, *12* (5), 2003.

(32) Haenni, D.; Zosel, F.; Reymond, L.; Nettels, D.; Schuler, B. Intramolecular Distances and

Dynamics from the Combined Photon Statistics of Single-Molecule FRET and Photoinduced Electron Transfer. *J. Phys. Chem. B* **2013**, *117* (42), 13015–13028. https://doi.org/10.1021/jp402352s.

(33) Chandrasekhar, S. Stochastic Problems in Physics and Astronomy. *Reviews of Modern Physics*. 1943, pp 1–89. https://doi.org/10.1103/RevModPhys.15.1.

(34) Zou, G.; Wu, H. Nearest-Neighbor Distribution of Interacting Biological Entities. *J. Theor. Biol.* **1995**, *172*, 347–353.

(35) Voter, A. F. Introduction to the Kinetic Monte Carlo Method. *Radiat. Eff.* **2005**, 1–23.

(36) Gopich, I. V.; Szabo, A. Theory of the Energy Transfer Efficiency and Fluorescence Lifetime Distribution in Single-Molecule FRET. *Proc. Natl. Acad. Sci. U. S. A.* **2012**, *109* (20), 7747–7752. https://doi.org/10.1073/pnas.1205120109.

(37) Barth, A.; Opanasyuk, O.; Peulen, T. O.; Felekyan, S.; Kalinin, S.; Sanabria, H.; Seidel, C. A. M. Unraveling Multi-State Molecular Dynamics in Single-Molecule FRET Experiments. I. Theory of FRET-Lines. *J. Chem. Phys.* **2022**, *156* (14). https://doi.org/10.1063/5.0089134.

(38) Lindsey, J. S.; Taniguchi, M.; Bocian, D. F.; Holten, D. The Fluorescence Quantum Yield Parameter in Förster Resonance Energy Transfer (FRET)—Meaning, Misperception, and Molecular Design. *Chem. Phys. Rev.* **2021**, *2* (1). https://doi.org/10.1063/5.0041132.

(39) Chuang, C.; Knoester, J.; Cao, J. Scaling Relations and Optimization of Excitonic Energy Transfer Rates between One-Dimensional Molecular Aggregates. *J. Phys. Chem. B* **2014**, *118* (28), 7827–7834. https://doi.org/10.1021/jp4124502.

(40) Izquierdo, E.; Robin, A.; Keuleyan, S.; Lequeux, N.; Lhuillier, E.; Ithurria, S. Strongly Confined HgTe 2D Nanoplatelets as Narrow Near-Infrared Emitters. *J. Am. Chem. Soc.* **2016**, *138* (33), 10496–10501. https://doi.org/10.1021/jacs.6b04429.

(41) Tenney, S. M.; Vilchez, V.; Sonnleitner, M. L.; Huang, C.; Friedman, H. C.; Shin, A. J.; Atallah, T. L.; Deshmukh, A. P.; Ithurria, S.; Caram, J. R. Mercury Chalcogenide Nanoplatelet-Quantum Dot Heterostructures as a New Class of Continuously Tunable Bright Shortwave Infrared Emitters. *J. Phys. Chem. Lett.* **2020**, *11* (9), 3473–3480. https://doi.org/10.1021/acs.jpclett.0c00958.

(42) Piepenbrock, M. O. M.; Stirner, T.; Kelly, S. M.; O'Neill, M. A Low-Temperature Synthesis for Organically Soluble HgTe Nanocrystals Exhibiting near-Infrared Photoluminescence and Quantum Confinement. *J. Am. Chem. Soc.* **2006**, *128* (21), 7087–7090. https://doi.org/10.1021/ja060721j.

(43) Smith, J. E.; Jordan, M. L. Mathematical and Graphical Interpretation of the Log-Normal Law for Particle Size Distribution Analysis. *J. Colloid Sci.* **1964**, *19* (6), 549–559. https://doi.org/10.1016/0095-8522(64)90069-8.

(44) Leese, R. A.; Wehry, E. L. Corrections for Inner-Filter Effects in Fluorescence Quenching Measurements via Right-Angle and Front-Surface Illumination. *Anal. Chem.* **1978**, *50* (8), 1193–1197. https://doi.org/10.1021/ac50030a047.

(45) Bortz, A. B.; Kalos, M. H.; Lebowitz, J. L. A New Algorithm for Monte Carlo Simulation of Ising Spin Systems. *J. Comput. Phys.* **1975**, *17* (1), 10–18. https://doi.org/10.1016/0021-9991(75)90060-1.

(46) Jazani, S.; Sgouralis, I.; Shafraz, O. M.; Levitus, M.; Sivasankar, S.; Pressé, S. An Alternative Framework for Fluorescence Correlation Spectroscopy. *Nat. Commun.* **2019**, *10* (1). https://doi.org/10.1038/s41467-019-11574-2.

(47) Niklas, B.; Zeno, F.-P.; Rudolf, R. The Incipient Stage in Thrombin-Induced Fibrin Polymerization Detected by FCS at the Single Molecule Level. *Biochem. Biophys. Res. Commun.*

1999, *260* (1), 35–41.

(48) Markovic, S.; Belz, J.; Kumar, R.; Cormack, R. A.; Sridhar, S.; Niedre, M. Near-Infrared Fluorescence Imaging Platform for Quantifying in Vivo Nanoparticle Diffusion from Drug Loaded Implants. *Int. J. Nanomedicine* **2016**, *11*, 1213–1223. https://doi.org/10.2147/IJN.S93324.

(49) Altman, R. B.; Zheng, Q.; Zhou, Z.; Terry, D. S.; Warren, J. D.; Blanchard, S. C. Enhanced Photostability of Cyanine Fluorophores across the Visible Spectrum. *Nat. Methods* **2012**, *9* (5), 428–429. https://doi.org/10.1038/nmeth.1988.

(50) Tinnefeld, P.; Herte, D. P.; Sauer, M. Photophysical Dynamics of Single Molecules Studied by Spectrally-Resolved Flourescence Lifetime Imaging Microscopy (SFLIM). *J. Phys. Chem. A* **2001**, *105* (34), 7989–8003. https://doi.org/10.1021/jp010365l.

(51) Kang, J.; Lhee, S. M.; Lee, J. K.; Zare, R. N.; Nam, H. G. Restricted Intramolecular Rotation of Fluorescent Molecular Rotors at the Periphery of Aqueous Microdroplets in Oil. *Sci. Rep.* **2020**, *10* (1), 1–11. https://doi.org/10.1038/s41598-020-73980-7.

(52) Son, H.; Mo, W.; Park, J.; Lee, J. W.; Lee, S. Single-Molecule FRET Detection of Sub-Nanometer Distance Changes in the Range below a 3-Nanometer Scale. *Biosensors* **2020**, *10* (11), 3–9. https://doi.org/10.3390/BIOS10110168.

(53) Feng, X. A.; Poyton, M. F.; Ha, T. Multicolor Single-Molecule FRET for DNA and RNA Processes. *Curr. Opin. Struct. Biol.* **2021**, *70*, 26–33. https://doi.org/10.1016/j.sbi.2021.03.005.

(54) Keuleyan, S.; Kohler, J.; Guyot-Sionnest, P. Photoluminescence of Mid-Infrared HgTe Colloidal Quantum Dots. *J. Phys. Chem. C* **2014**, *118* (5), 2749–2753. https://doi.org/10.1021/JP409061G/SUPPL_FILE/JP409061G_SI_001.PDF.

(55) Lhuillier, E.; Keuleyan, S.; Guyot-Sionnest, P. Optical Properties of HgTe Colloidal Quantum Dots. *Nanotechnology* **2012**, *23* (17), 175705. https://doi.org/10.1088/0957-

4484/23/17/175705.

Chapter 3

Applying Marcus Theory to Describe Photoluminescent Intermittency and Temperature Dependent Emission in CdTe Nanoplatelets

This chapter contains unpublished work "Tan, X.; Ahmed, T.; Murphy, L.; Coffey, B.; Caram, J.R. Applying Marcus Theory to Describe Photoluminescent Intermittency and Temperature Dependent Emission in CdTe Nanoplatelets. *ChemRxiv*. 2024. https://10.26434/chemrxiv-2024-zcggj." This work is under peer review. The results are preliminary and based on available data.

Photoluminescence (PL) intermittency (also known as blinking) is a critical aspect of the optical properties of molecules and nanomaterials. Considerable work has expounded on the mechanism of blinking in nanocrystals, with the canonical model arguing that intermittently trapped charges serve to quench emission via charge-exciton Auger recombination. The dynamics of the emission trace are analyzed by fitting a histogram of on- and off- times to power-law distributions. These histograms in turn, reveal non-exponential kinetics, arguing for a distribution of electron or hole traps. What is not revealed is the origin of these distributed states, whether they arise from various trap energetic depths, long-range electron or hole tunneling, or any other process which gives rise to distributions of rates. In this chapter, we explore a model which invokes both a distribution of trap energies, combined with the chemical intuition of charge transfer via Marcus theory. We find that a self-consistent Marcus theory model can explain different power-law slopes for on- and off-times, and the observed changes in intensity as a function of temperature in films of CdTe nanoplatelets (NPLs). We believe this provides a self-consistent model to describe blinking behavior that leads to unusually low PL quantum yield (QY) in CdTe, and argues that improved passivation will be critical to achieving higher QY.

3.1 Photoluminescence Intermittency (Blinking): Impact and Current Mechanisms

When studying single or small numbers of nanoparticles one observes temporally distributed on and off photoluminescence (PL) from the particle, typically on millisecond to second time scales.[1–3] This phenomenon known as PL intermittency, or blinking, is a critical aspect of the optical properties of molecules and nanomaterials. The quenching of PL quantum yield (QY) due to blinking negatively influences the potential applications of quantum dots (QDs) and nanoplatelets (NPLs) as fluorescent probes for biological imaging, phosphors for displays, LED applications and emergent technologies such as single photon emitters for quantum informatics.[4–7] On the other hand, blinking statistics can be leveraged to probe the surrounding environment of nanocrystals, or as super-resolution chromophores.[8,9]

There has been a large amount of effort unraveling the mechanism of blinking, with the most widely accepted model arguing that the on- and off- state arises from radiative fluorescent recombination and non-radiative charge-exciton Auger recombination, respectively. The switching between on-state and off-state is thus attributed to the trapping and detrapping of carriers.[10] Quantitatively analyzing the dynamics of the PL time traces, it is very common to histogram the duration of on- and off- times and fit the resultant distributions to power-law functions.[11] Exponentially distributed histogram arises from a constant rate for on-off kinetics while power-law distributions of on- and off- times can be attributed to distributed rates.

Unfortunately, distributed kinetics could arise from many underlying mechanisms, including distributed trap state energies, long-range electron/hole tunneling with fluctuating barrier or some other processes.[12,13] For example, Tang-Marcus theory, or more formally the diffusion-controlled electron transfer (DCET) theory, suggests that spectral diffusion between the potential energy surface (PES) of donor and acceptor to be responsible for trapping and detrapping processes.[14]

This model predicts power-law distributions of on- and off- times (both with a slope of $-\frac{3}{2}$) with deviations arising from more complex diffusion behavior.[15,16]

As mentioned before, the key factors in the kinetics of blinking systems that impact the blinking statistics are the trapping and detrapping processes. Intuitively, these processes could be considered as physical processes of charge transfer, which can be further described by Marcus theory of charge transfer. Proposed in a series of work on electron transfer reactions by R.A. Marcus starting from 1956, Marcus theory provides us with a general method of understanding process of charge transfer based on relatively simple but reasonable assumptions of parabolic form of PES for charge donor and acceptor.[17–30] In short, electron transfer proceeds between a donor and acceptor state separated along a general reaction coordinate. Parabolic potentials are well justified as a consequence of solvation either charged donor or charged acceptor rates. The barrier for electron/hole transfer arises from the reorganization energy associated with charge motion and the curvature of the potential.

In this work, we conducted detailed study on the blinking and related behaviors of CdTe NPLs. We synthesized 3 monolayers (MLs) CdTe NPLs (consisting of 3 layers of Te and 4 layers of Cd) to be used in the PL microscopic measurements. In general, CdTe NPLs show low PLQY relative to other II-VI nanocrystals. We observe that the blinking of CdTe NPLs show extremely short on-times and long off-times, manifesting as non-identical power-law exponents for distributions of on- and off- times. Combining the quantitative energetic relations between the activation barrier and trap state energy given by Marcus theory with the activated kinetics of trapping and detrapping, we explore the role of trap state energy distribution and reorganization energy in blinking systems both analytically with the help of kinetic Monte Carlo (KMC) simulations. The inclusion of a Marcus electron transfer picture also enables an analysis of the

temperature dependence of PLQY based on self-consistent model which shows quantitative agreement with experiments. To the best of our knowledge, no current models provide a solid explanation for both non-identical on- and off- statistics and temperature dependence of QY. We conclude by constructing an energy diagram of nanocrystals states that give rise to blinking statistics and temperature-dependent PLQY changes.

3.2 Synthesis and Blinking Measurements of CdTe Nanoplatelets (NPLs)

We synthesized 3 MLs CdTe NPLs following previously reported procedures with a few modifications (See Section 3.6). Absorption spectrum of as-synthesized NPLs shows characterizing features at 500 nm and 450 nm, corresponding to heavy hole-electron and light hole-electron transition, respectively (Figure 3.1a). PL spectrum exhibits a sharp peak at 500 nm with a full width at half maximum (FWHM) of ~7 nm and almost no Stokes shift (Figure 3.1a). TEM image shows NPLs with lateral sizes of 100-200 nm (Figure 3.1b). To study the PL intermittency of single 3 ML CdTe NPL, we performed a series of measurements on films of NPLs using a home-built wide-field PL microscope (See Section 3.6). The well-separated single NPL shows PL blinking with completely dark state (See attached video). There were a few areas in the film where we observed no blinking which we assigned to clusters of NPLs. We then collected PL time traces of 30 NPLs showing blinking, and three examples of representative particles are given below (Figure 3.1c). The time traces demonstrate that the PL intensity is fluctuating over different levels, which clearly represents the interconversion between emissive bright state (on-state) and non-emissive dark state (off-state). Immediately, we noticed very short-lived burst of on-state separated by extremely long off-state. This rapid blinking with very short-lived on-state has been observed before in nanoparticles of other morphology including CdSe NPLs, however, the durations of off-state were not as long as what we measured for CdTe NPLs.[31–33] In typical measurements of nearly

5 min recording time, CdTe NPL remains dark for more than 1 min and on-state lasts for not more than 10 sec. To characterize the PL intermittency more precisely, we investigated the statistical properties of the on-state durations (on-times, τ_{on}) and off-state durations (off-times, τ_{off}). As a common practice, we first separated the on- and off- state by setting a reasonable threshold and then histogram the on-times and off-times, which were used to calculate the weighted probability of on-times (P_{on}) and off-times (P_{off}) (Figure 3.1d).[13] The probability density functions of the distributions of on-times and off-times are best described by power-law functions ($P_{on} \propto \tau_{on}^{-m_{on}}$; $P_{off} \propto \tau_{off}^{-m_{off}}$) with power-law slopes $m_{on} = 1.53 \pm 0.18$ and $m_{off} = 1.24 \pm 0.09$, respectively. These statistical behaviors of power-law distribution of on- and off- times are similar to other blinking nanoparticles, but the obvious discrepancy between the power-law slopes of on-times and off-times is not trivial.[11,31,34]

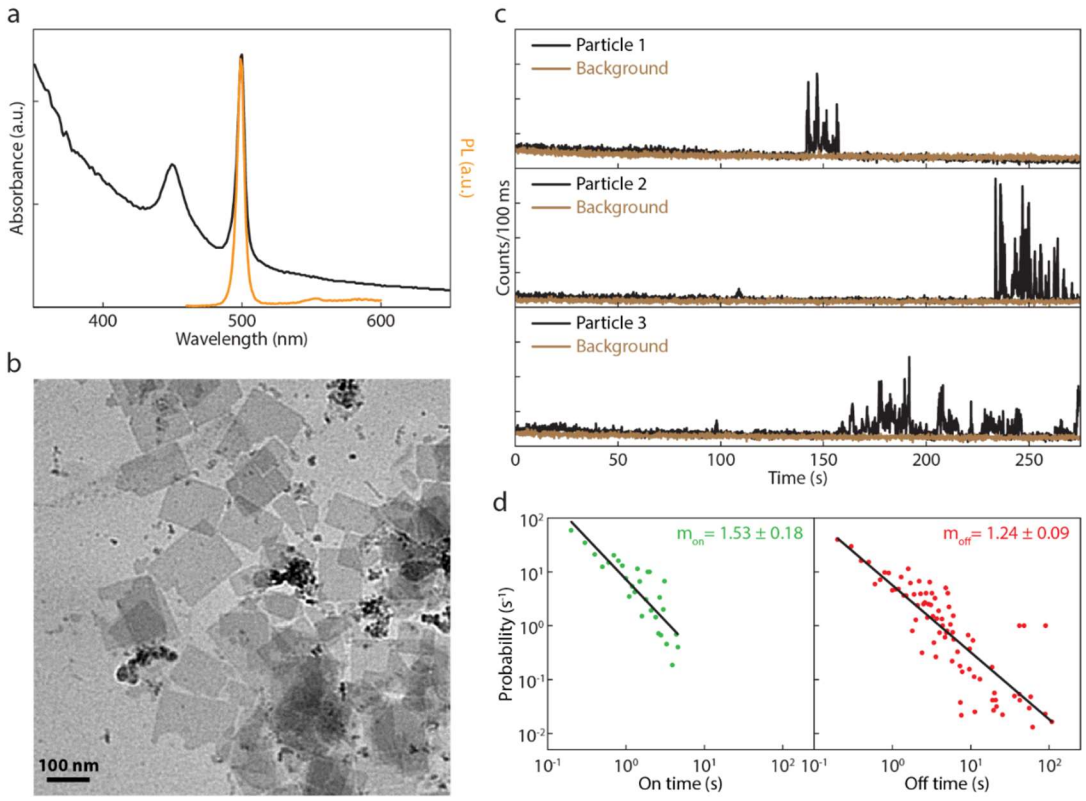

Figure 3.1 Synthesized 3 ML CdTe nanoplatelets (NPLs) and analysis of blinking. (a) Absorption (black) and PL (orange) spectra of as-synthesized 3 ML CdTe NPLs. (b) TEM images of 3 ML CdTe NPLs. (c)

Examples of PL time traces (black) and background (brown) for 3 different single-NPLs. (d) Histogram and power-law fitting of the weighted probability distribution for on-times (left) and off-times (right). Data are plotted in log-log scale.

Since the first report of PL blinking in single QDs by Nirmal et al., the fundamental mechanism of PL blinking has been intensively studied but is still not well understood.[1,35,36] Although the mechanism of PL blinking is still under debate, the widely accepted origin of off-state is the non-radiative Auger recombination due to charging, which involves the trapping and detrapping of carriers in the system.[10] Furthermore, the power-law distributions of time durations in blinking are often attributed to "distributed kinetics" in the system, since with constant trapping and detrapping rate resulting from single trap state exponential distributions for both on- and off-times are expected (Figure 3.2a). Various models have been proposed to account for the "distributed kinetics", including the model with a series of energetically distributed trap states. This type of model successfully predicts a power-law distribution for off-times, but the on-times still follow an exponential distribution (Figure 3.2b).[37] Other models based on diffusion of energies in the system, including the model of charge tunneling as the essence of trapping and detrapping processes where the energy of tunneling barrier is changing over time (Figure 3.2c), produces power-law distributions for both on- and off- times with identical power-law slopes.[14,34,38] Unfortunately none of the models provides a solid explanation for our experimental observations. Considering the important roles trapping and detrapping play in the blinking statistics, we intuitively think of the Marcus theory of charge transfer as a potential model we can implement in the study of blinking. Since Marcus theory only provides the relation between activation barrier energy with trap state energy, further analysis is required to unravel the new blinking behaviors (Figure 3.2d).

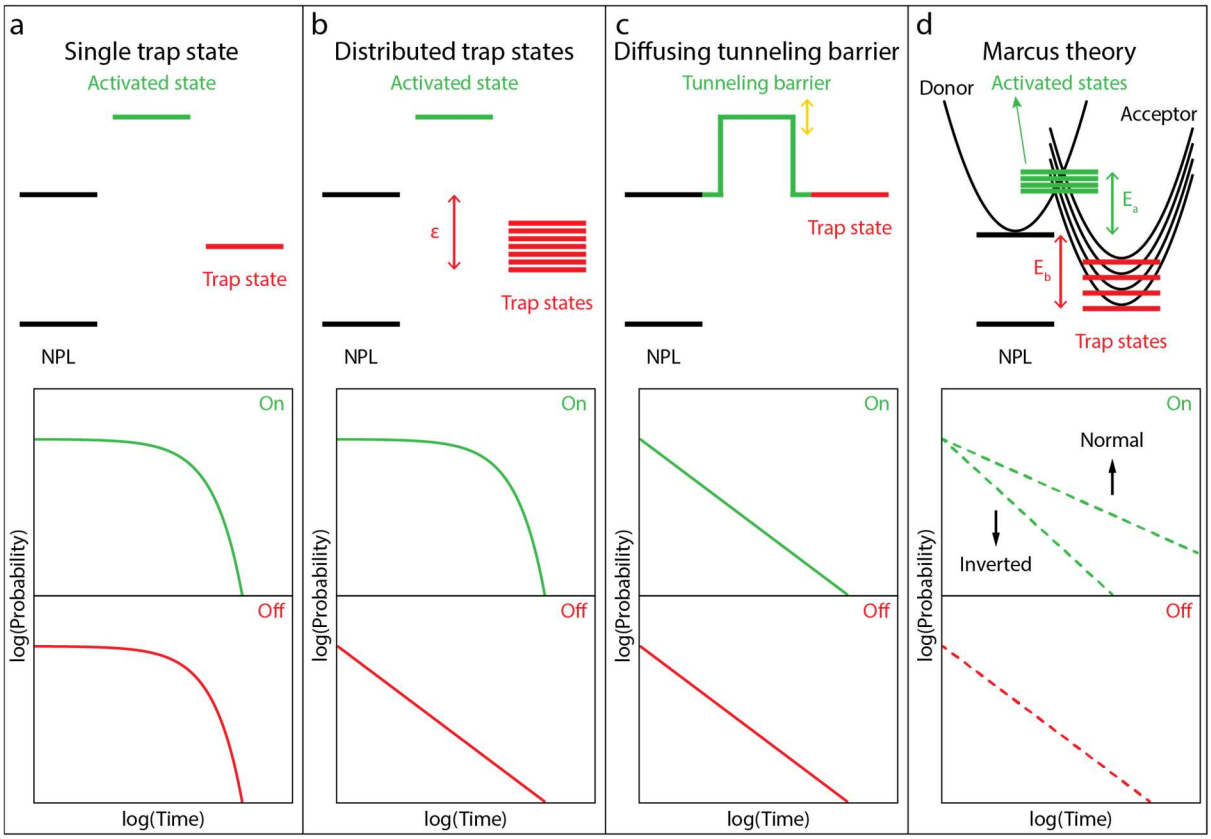

Figure 3.2 Possible models for explaining "distributed kinetics" and their predictions on time distributions. (a) Model of single trap state, predicting exponential distributions for both on-times and off-times. (b) Model of distributed trap states, predicting exponential distribution for on-times and power-law distribution for off-times. (c) Model of diffusing tunneling barrier, predicting power-law distributions for both on-times and off-times with identical power-law slopes. (d) Model of blinking based on Marcus theory of charge transfer. This intuitively correct model could potentially predict different power-law statistics for on-times and off-times.

3.3 Quantitative Analysis on the Power-law Distribution of On- and Off- Times

In this section we briefly summarize how distributed kinetics result in power-law distributions for on-times and off-times. We start with a canonical model with a fixed activation barrier and an exponential distribution of trap state energies (Figure 3.2b). First, we repeat the general mathematical treatment to derive power-law statistics.[39] The exponential distribution of energy ε can be described using the normalized probability distribution function $\rho(\varepsilon) = \alpha e^{-\alpha\varepsilon}$ $(\varepsilon > 0)$, where the exponent α is the characteristic parameter of the distribution. With the model of activated kinetics, the rate k naturally takes an exponential dependence on energy ε as well, following the conventional Arrhenius equation $k = k_0 e^{-\beta\varepsilon}$ $(0 < k < k_0)$, where the

exponent $\beta = \frac{1}{RT}$ depends on temperature and the pre-factor k_0 sets the upper bound of the rate (i.e., attempt frequency) which is achieved in the no-barrier case. Borrowing the notations from statistics, the probability distribution function of a rate random variable K is by definition calculated as:

$$f(k) = \frac{d}{dk}[\Pr(K < k)] \tag{3.1}$$

where $\Pr(K < k)$ is the probability of the value of random variable K being lower than a specified number k (i.e., the cumulative distribution function). This can be converted to the probability associated with energy random variable E using the Arrhenius equation: $K < k \Rightarrow E > \frac{1}{\beta}\ln\frac{k_0}{k}$. And the cumulative distribution function is given by:

$$\Pr(K < k) = \Pr\left(E > \frac{1}{\beta}\ln\frac{k_0}{k}\right) = 1 - \int_0^{\frac{1}{\beta}\ln\frac{k_0}{k}} \rho(\varepsilon)d\varepsilon \tag{3.2}$$

Combining (3.1) and (3.2), we get the probability distribution function of rate:

$$f(k) = -\frac{d}{dk}\int_0^{\frac{1}{\beta}\ln\frac{k_0}{k}} \rho(\varepsilon)d\varepsilon = \frac{\frac{\alpha}{\beta}k^{\frac{\alpha}{\beta}-1}}{k_0^{\frac{\alpha}{\beta}}}, k \in (0, k_0) \tag{3.3}$$

which already takes the form of a power-law function.

We then consider the distribution of times given the distribution of rate. For a process with a constant rate k, the times spent for this process t follow the Poisson distribution $P(t) = ke^{-kt}$ $(t > 0)$. To do the same calculation with distribute kinetics, we again use the cumulative distribution function of a time random variable T:

$$p(t) = \frac{d}{dt}[\Pr(T < t)] \tag{3.4}$$

where the probability $\Pr(T < t)$ should sample all possible rates:

$$\Pr(T < t) = \int_0^{k_0} f(k)dk \int_0^t P(T)dT = \int_0^{k_0} f(k)(1 - e^{-kt})dk \tag{3.5}$$

The probability distribution function of times is then given by:

$$p(t) = -\frac{d}{dt}\int_0^{k_0} f(k)e^{-kt}dk = -\int_0^{k_0} \frac{d}{dt}[f(k)e^{-kt}]dk = \int_0^{k_0} f(k)ke^{-kt}dk \tag{3.6}$$

Finally, plugging in previously obtained distribution of rate in equation (3.3), we have:

$$p(t) = \int_0^{k_0} \frac{\frac{\alpha}{\beta}k^{\frac{\alpha}{\beta}-1}}{k_0^{\frac{\alpha}{\beta}}} ke^{-tk}dk = \frac{\frac{\alpha}{\beta}\gamma(1+\frac{\alpha}{\beta}, k_0 t)}{k_0^{\frac{\alpha}{\beta}} t^{1+\frac{\alpha}{\beta}}} \tag{3.7}$$

where γ is the lower incomplete gamma function and can be reduced to the following form:

$$p(t) = \begin{cases} \dfrac{\frac{\alpha}{\beta}k_0}{1+\frac{\alpha}{\beta}} & k_0 t \ll 1 \quad \text{(I)} \\ \dfrac{\frac{\alpha}{\beta}\Gamma\left(1+\frac{\alpha}{\beta}\right)}{k_0^{\frac{\alpha}{\beta}}} t^{-(1+\frac{\alpha}{\beta})} & k_0 t \gg 1 \quad \text{(II)} \end{cases} \tag{3.8}$$

where Γ is the complete gamma function. Based on equation (3.8), when the measured time scale is faster than the attempt frequency k_0 the histogram averages out, resulting in a plateaued probability function; when the measured time scale is slower than the attempt frequency k_0 instead, the distribution follows the power-law distribution (See Section 3.7, Figure 3.6). Under experimental conditions the attempt frequency is typically very fast and the range of detection is limited, so we usually only observe the power-law distribution represented by equation (II). In log-log plot, the power-law distribution appears to be linear where the power-law slope $-(1+\frac{\alpha}{\beta})$ is determined by α and β, which are related to the width of energy distribution and temperature, respectively.

Now we introduce the more sophisticated model of electron transfer, Marcus theory, to the consideration of blinking process. Marcus theory quantitatively relates the activation energy E_a and the trap energy E_b with a newly defined reorganization energy λ (See Section 3.7, Figure 3.7):

$$E_a = \frac{1}{4\lambda}(\lambda - E_b)^2 \tag{3.9}$$

By combining the energetic relations in Marcus theory with the trapping and detrapping rates, we analyze blinking behaviors in the context of a variable electron trap energy. For simplicity, we keep the exponential distribution of trap state energy: $\rho(E_b) = \alpha_b e^{-\alpha_b(E_b - E_b^0)}$ $(E_b > E_b^0)$. Note that now the trap state energy has a non-zero lower bound. The trapping and detrapping rate naturally have the Arrhenius dependence on activation barrier energy E_a and reverse barrier energy E_r, respectively: $k_t = k_t^0 \exp(-\frac{E_a}{RT})$, $k_d = k_d^0 \exp(-\frac{E_r}{RT})$, where the reverse barrier E_r is simply defined as $E_r = E_a + E_b = \frac{1}{4\lambda}(\lambda + E_b)^2$. In order to find the distribution of rates, we first find the distribution of energies:

$$g_a(E) = \frac{d}{dE}\Pr(E_a < E) = \frac{d}{dE}\Pr\left[\left(\lambda - 2\sqrt{\lambda E}\right) < E_b < \left(\lambda + 2\sqrt{\lambda E}\right)\right] \tag{3.10}$$

$$g_r(E) = \frac{d}{dE}\Pr(E_r < E) = \frac{d}{dE}\Pr\left[E_b < \left(2\sqrt{\lambda E} - \lambda\right)\right] \tag{3.11}$$

There are two regimes of Marcus theory with very different behaviors depending on the relative distance of reaction coordinates: normal region and inverted region. We first discuss the case of inverted region where $\lambda < E_b$ always holds (i.e., $\lambda \leq E_b^0$). The cumulative distribution function in equation (3.10) is then reduced to:

$$\Pr(E_a < E) = \Pr\left[E_b < \left(\lambda + 2\sqrt{\lambda E}\right)\right] = \int_{E_b^0}^{\lambda + 2\sqrt{\lambda E}} \rho(E_b) dE_b \tag{3.12}$$

and similarly, for the distribution of reverse barrier energy described by equation (3.11):

$$\Pr(E_r < E) = \Pr\left[E_b < \left(2\sqrt{\lambda E} - \lambda\right)\right] = \int_{E_b^0}^{2\sqrt{\lambda E}-\lambda} \rho(E_b) dE_b \tag{3.13}$$

Plugging expressions (3.12) and (3.13) back in (3.10) and (3.11) respectively, we get:

$$g_a(E_a) = \sqrt{\frac{\lambda}{E_a}} \alpha_b e^{-\alpha_b(\lambda + 2\sqrt{\lambda E_a} - E_b^0)}, E_a \in \left(\frac{(\lambda - E_b^0)^2}{4\lambda}, \infty\right) \tag{3.14}$$

$$g_r(E_r) = \sqrt{\frac{\lambda}{E_r}} \alpha_b e^{-\alpha_b(2\sqrt{\lambda E_r} - \lambda - E_b^0)}, E_r \in \left(\frac{(\lambda + E_b^0)^2}{4\lambda}, \infty\right) \tag{3.15}$$

where $E_a^0 = \frac{(\lambda - E_b^0)^2}{4\lambda}$ and $E_r^0 = \frac{(\lambda + E_b^0)^2}{4\lambda}$ are the lower limits of E_a and E_r, respectively.

These distributions are not strictly exponential but we can still extract an exponential index that can be used to conveniently estimate the power-law distribution of on-times and off-times. Taking the logarithm of the probability distribution functions, we have: $\ln[g_a(E_a)] = C_a - \frac{1}{2}\ln E_a - 2\alpha_b\sqrt{\lambda E_a}$ and $\ln[g_r(E_r)] = C_r - \frac{1}{2}\ln E_r - 2\alpha_b\sqrt{\lambda E_r}$, where C_a and C_r are parameters independent of E_a and E_r. We then do Taylor expansion of both expressions to the first order at E_a^0 and E_r^0, respectively:

$$\ln[g_a(E_a)] \approx C_a' - \frac{1}{2}\frac{E_a}{E_a^0} - 2\alpha_b\sqrt{\lambda}\frac{E_a}{2\sqrt{E_a^0}} \propto -\left[\frac{2\lambda}{E_b^0 - \lambda}\alpha_b + \frac{2\lambda}{(E_b^0 - \lambda)^2}\right] E_a \tag{3.16}$$

$$\ln[g_r(E_r)] \approx C_r' - \frac{1}{2}\frac{E_r}{E_r^0} - 2\alpha_b\sqrt{\lambda}\frac{E_r}{2\sqrt{E_r^0}} \propto -\left[\frac{2\lambda}{E_b^0 + \lambda}\alpha_b + \frac{2\lambda}{(E_b^0 + \lambda)^2}\right] E_r \tag{3.17}$$

We can then further estimate the power-law slopes based on the results from Taylor expansions:

$$\text{slope}_{\text{on}} = -(1 + \alpha_{\text{on}} RT) \approx -\left\{1 + \left[\frac{2\lambda}{E_b^0 - \lambda}\alpha_b + \frac{2\lambda}{(E_b^0 - \lambda)^2}\right] RT\right\} \tag{3.18}$$

$$\text{slope}_{\text{off}} = -(1 + \alpha_{\text{off}} RT) \approx -\left\{1 + \left[\frac{2\lambda}{E_b^0 + \lambda}\alpha_b + \frac{2\lambda}{(E_b^0 + \lambda)^2}\right] RT\right\} \tag{3.19}$$

Since reorganization energy λ is positive, this naturally predicts a larger absolute value of power-law slope for on-times than that of off-times.

Finally, we discuss the case of normal region. Assuming $\lambda > E_b$ always holds, equation (3.10) is then equal to:

$$\Pr(E_a < E) = \Pr\left[E_b > \left(\lambda - 2\sqrt{\lambda E}\right)\right] = \int_{\lambda-2\sqrt{\lambda E}}^{\lambda} \rho(E_b) dE_b \tag{3.20}$$

Note that since $2\sqrt{\lambda E} - \lambda < \lambda$ always holds when $\lambda > E_b$ is true, the expression of distribution function for reverse barrier remains unchanged. The probability distribution function of activation barrier energy can be expressed as:

$$g'_a(E_a) = \sqrt{\frac{\lambda}{E_a}} \alpha_b e^{-\alpha_b(\lambda - 2\sqrt{\lambda E_a} - E_b^0)}, E_a \in \left(0, \frac{(\lambda - E_b^0)^2}{4\lambda}\right) \tag{3.21}$$

which shows a positive exponent. Therefore, we should modify the original general analysis to accommodate this change. Following the recipe above, we obtain the distribution of on-times in the normal region (See Section 3.7):

$$p'(t) = \int_{k_{\min}}^{k_{\max}} \frac{\frac{\alpha'}{\beta} k_0^{\frac{\alpha'}{\beta}}}{k^{\frac{\alpha'}{\beta}+1}} k e^{-tk} dk = \frac{\alpha'}{\beta} k_0^{\frac{\alpha'}{\beta}} \frac{\gamma\left(1 - \frac{\alpha'}{\beta}, k_{\max} t\right) - \gamma(1 - \frac{\alpha'}{\beta}, k_{\min} t)}{t^{1-\frac{\alpha'}{\beta}}} \tag{3.22}$$

where $k_{\min}$ and $k_{\max}$ are the lower and upper bound of trapping rates, respectively. Note that this conversion to gamma function requires $1 - \frac{\alpha'}{\beta} > 0$. Since $\frac{\alpha'}{\beta} > 0$, the value of exponent for on-times distribution is then guaranteed to be in the range $(0, 1)$, which contradicts the usually observed range for power-law exponents, $(1, 2)$ (Table 3.1).

To summarize, we qualitatively describe the blinking behaviors in the two regimes of Marcus theory. With an exponentially distributed trap energy, the detrapping rates in both regimes

follow similar trend that the deeper traps which are harder to escape from are less accessible. However, the distributions of trapping rates are different in the two regimes: in the inverted region, deeper traps correspond to higher activation barriers, resulting in smaller chance of carriers going through trapping processes with lower rates, which is identical to the situation of detrapping; in the normal region, deeper traps correspond to shallower activation barriers, resulting in smaller chance of carriers going through trapping processes with higher rates, which is a reverse trend compared to detrapping, reducing the power-law slope of on-times distribution to be less than 1.

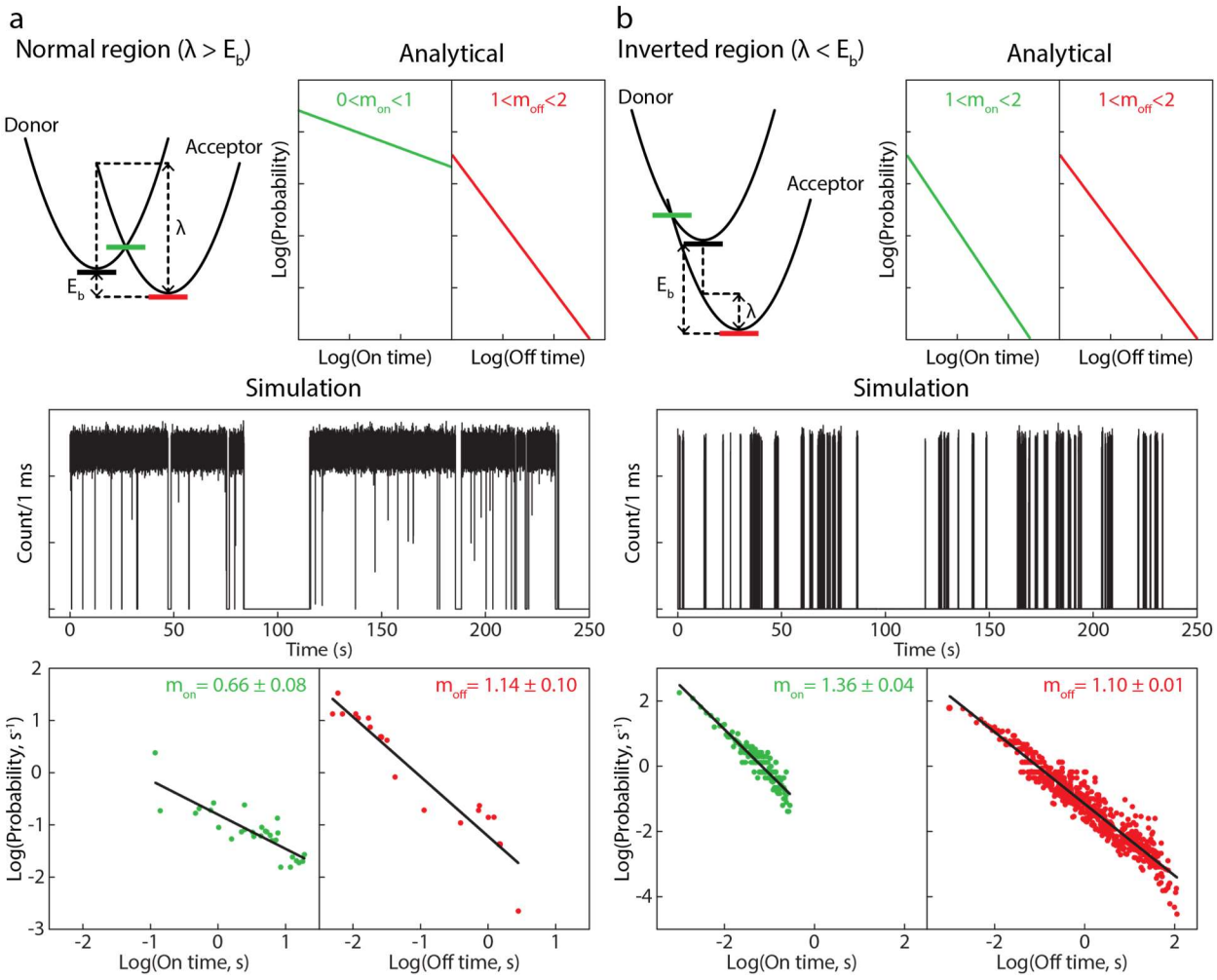

Figure 3.3 Comparison of analytical and simulated results between normal region and inverted region of Marcus theory. (a) Blinking behaviors in the normal region of Marcus theory. Energy diagram (top left) shows the relative positions of donor and acceptor parabola and related energetic parameters. Analytical analysis (top right) predicts the range of power-law slope for on-times and off-times to be $(0, 1)$ and $(1, 2)$, respectively. Kinetic Monte Carlo (KMC) simulations (bottom) produce intensity traces and power-law

analysis of the distributions of on-times and off-times. (b) Blinking behaviors in the inverted region of Marcus theory. Energy diagram (top left) shows the relative positions of donor and acceptor parabola and related energetic parameters. Analytical analysis (top right) predicts the range of power-law slope for on-times and off-times both to be $(1, 2)$. Kinetic Monte Carlo (KMC) simulations (bottom) produce intensity traces and power-law analysis of the distributions of on-times and off-times.

The analysis above suggests that Marcus theory can be used to provide a more concrete basis for the activation barrier model of electron transfer which further quantitatively explain the photoluminescence intermittency (i.e., blinking) in nanocrystals. It is worth to emphasize that this indicates that blinking-related electron transfer processes have to be attributed to the *inverted* region in Marcus theory. This naturally results in *different* power-law slopes for on-times and off-times that matches the analysis of experimental data. Indeed, this result is complemented by recent reports that charge transfer processes in low-dimensional nanocrystals such as nanoplatelets and quantum dots occur in the Marcus inverted region adding further credibility to this idea.[40]

As a final confirmation, we carried out kinetic Monte Carlo (KMC) simulations with the model of activated kinetics and energetic relations of Marcus theory (See Section 3.7). The simulated intensity traces in inverted region show very short on-times similar to experiments, while those in normal region have much longer on-times (Figure 3.3a). Further power-law analysis on the intensity traces also matches the analytical results for both regimes: in the normal region the distribution of on-times has a power-law slope less than 1, and in the inverted region the power-law slope of on-times distribution is larger than that of off-times distribution, both falling in the regular range $(1, 2)$ (Figure 3.3b).

3.4 Temperature Dependence of PLQY

The analysis above matches quantitatively with the power-law analysis of single-nanocrystal intensity traces at room temperature. Based on equations (3.18) and (3.19), a temperature dependence of blinking is naturally expected, which could be reflected as the change of power-law slopes. However, the expected change is not easy to observe since blinking are generally

suppressed at lower temperature.[41,42] We instead address temperature dependence of the QY in CdTe NPLs, as the involvement of activated kinetics strongly implies that lower temperature should dramatically influence the PL intensity. We managed to measure significant increases in integrated PL intensity of films of CdTe NPLs as temperature decreases (Figure 3.4a and b), consistent with prior reports.[43–46] Note that the emission traces are rather complicated with features of mid-gap emissions, which has been discussed in other work.[47–51] Here we also consider all the features in PL traces when calculating the integrated intensity for QY comparison. The QY value we measured for film of CdTe NPLs at room temperature was ~9%. We will thus explore the consequences of a Marcus theory based blinking model on PLQY.

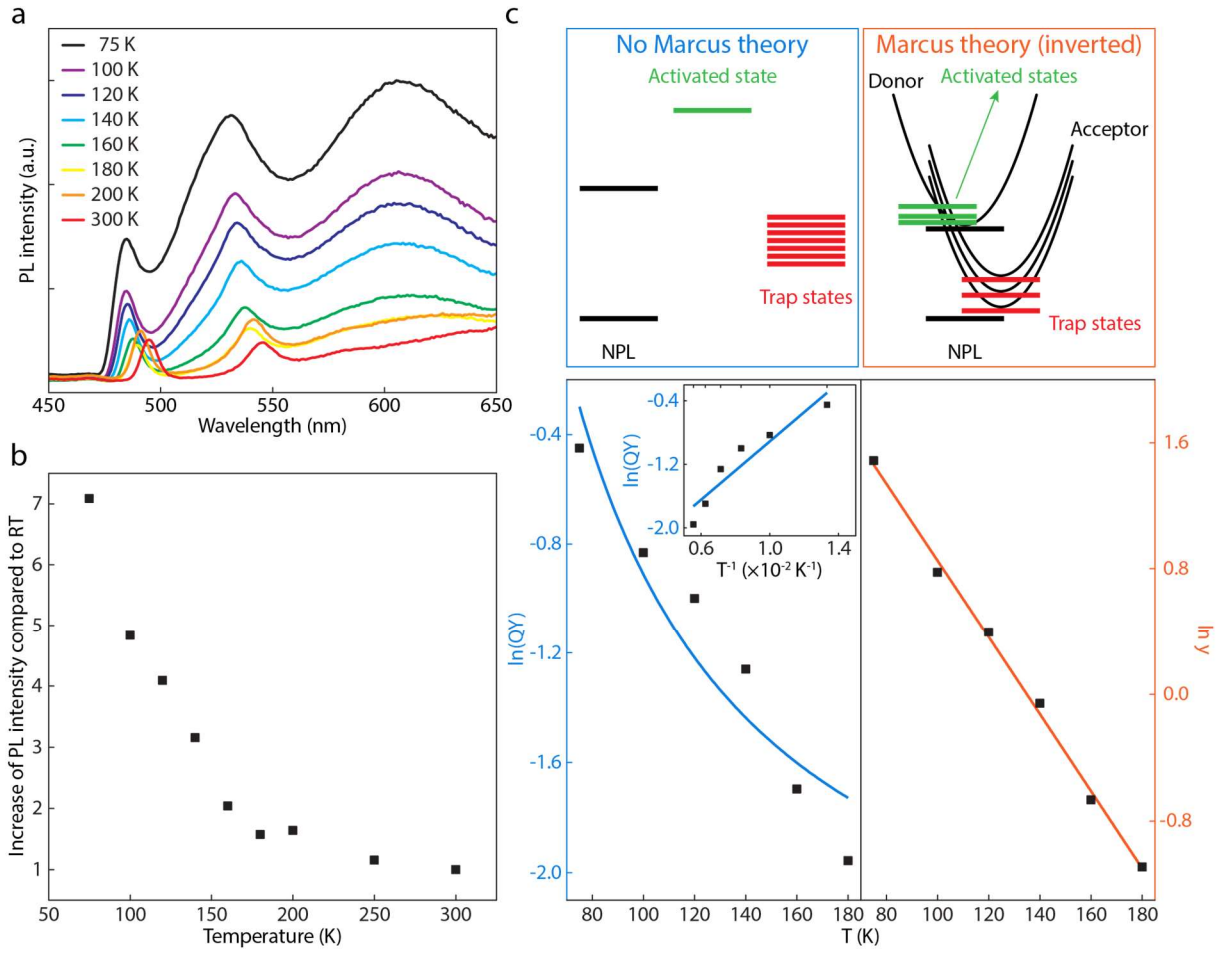

Figure 3.4 Experimental and theoretical study on temperature dependence of PLQY of blinking 3 ML CdTe NPLs. (a) Temperature dependence of PL traces measured for films of CdTe NPLs. The wide features

represent emissive mid-gap fluorescent states in the nanoplatelets. (b) Increase of the PL intensity compared to room temperature. Calculated using the integrated intensity of PL traces in (a). (c) Temperature dependence study of QY-related functions. Top: comparison of the model without Marcus theory (blue, left) and the model with Marcus theory (yellow, right). Bottom: predictions on functional dependence for both models. Inset: QY-related function plotted against reciprocal temperature for the case of no Marcus theory.

Although QY could be influenced by complicated underlying kinetic processes including radiative decay, non-radiative decay, etc., in nanocrystals, it is generally thought that the primary contributor to changes in ensemble QY arises from single-particle PL intermittency. Implicit to this assumption is that the on-state in single-particle intensity traces possesses a QY of 100%, and the off-state has a QY of 0%.[52,53] Asserting these conditions, we hypothesize that the temperature dependence should offer an additional set of constraints and allow us to estimate the Marcus theory parameters that go into our computation.

Given these assumptions, QY can be expressed as the percentage: $\mathrm{QY}'_t = \frac{\langle t_{\mathrm{on}} \rangle}{\langle t_{\mathrm{on}} \rangle + \langle t_{\mathrm{off}} \rangle}$, where $\langle t_{\mathrm{on}} \rangle$ is the mean on-time and $\langle t_{\mathrm{off}} \rangle$ is the mean off-time. The subscript t indicates the definition in terms of times. This general calculation works well for intensity traces where a considerable amount of switching events of interconversion between on-state and off-state that can be observed in a single measuring time t_m, i.e., $\langle t_{\mathrm{on}} \rangle, \langle t_{\mathrm{off}} \rangle \ll t_m$. When reaching lower temperatures, however, the blinking is suppressed and the mean on-time could drastically increase, thus the previous equation fails to accurately describe QY. Instead, we can use the modified calculation: $\mathrm{QY}_t = \frac{\langle t_{\mathrm{on}} \rangle}{t_m}$, which works for the case where mean on-time is more comparable with measuring time, i.e., $\langle t_{\mathrm{on}} \rangle, \langle t_{\mathrm{off}} \rangle \sim t_m$. This would ignore photobleaching/photobrightening processes that occur over longer time-scales.[54]

Now we consider the calculation of mean time. Based on the probability distribution of time demonstrated in (3.7), we have: $\langle t\rangle = \int_0^\infty tp(t)dt = \frac{\frac{\alpha}{\beta}\Gamma\left(1+\frac{\alpha}{\beta}\right)}{k_0^{\frac{\alpha}{\beta}}}\int_0^\infty t^{-\frac{\alpha}{\beta}}dt$. Note that in realistic experiments the upper limit of integration should be replaced by the measuring time t_m:

$$\langle t\rangle \approx \frac{\frac{\alpha}{\beta}\Gamma\left(1+\frac{\alpha}{\beta}\right)}{k_0^{\frac{\alpha}{\beta}}}\int_0^{t_m} t^{-\frac{\alpha}{\beta}}dt = \frac{\frac{\alpha}{\beta}\Gamma\left(\frac{\alpha}{\beta}+1\right)}{k_0^{\frac{\alpha}{\beta}}}\frac{t_m^{1-\frac{\alpha}{\beta}}}{1-\frac{\alpha}{\beta}} \tag{3.23}$$

Plugging (3.23) into the defining equations, we have the expression for QY in all temperature range:

$$\mathrm{QY} = \begin{cases} \mathrm{QY}_t' = \dfrac{\langle t_{\mathrm{on}}\rangle}{\langle t_{\mathrm{on}}\rangle + \langle t_{\mathrm{off}}\rangle} & \langle t_{\mathrm{on}}\rangle, \langle t_{\mathrm{off}}\rangle \ll t_m; \text{high } T \\ \mathrm{QY}_t = \dfrac{\alpha_{\mathrm{on}}RT\Gamma(\alpha_{\mathrm{on}}RT+1)}{1-\alpha_{\mathrm{on}}RT}(t_m k_{t,0})^{-\alpha_{\mathrm{on}}RT} & \langle t_{\mathrm{on}}\rangle, \langle t_{\mathrm{off}}\rangle \sim t_m; \text{low } T \end{cases} \tag{3.24}$$

where α_{on} is the trapping rate distribution exponent in (3.18), and $k_{t,0} = k_t^0 \exp(-\frac{E_a^0}{RT})$ is the max trapping rate with the lowest activation barrier energy. Based on equation (3.24), both functions show an increase in QY when lowering the temperature, but the increase is more drastic in the low temperature calculation, which agrees qualitatively with the overall trend in the experimental data (See Section 3.7, Figure 3.8).

As for quantitative analysis, we focus on the QY expression at low temperature for simplicity. We start by defining a new function $y(T)$:

$$y(T) = \frac{\mathrm{QY}_t}{\frac{\alpha_{\mathrm{on}}RT\Gamma(\alpha_{\mathrm{on}}RT+1)}{1-\alpha_{\mathrm{on}}RT}} = (t_m k_{t,0})^{-\alpha_{\mathrm{on}}RT} \tag{3.25}$$

Taking the natural logarithm of $y(T)$, we have:

$$\ln y(T) = -\alpha_{\mathrm{on}}RT\left[\ln(t_m k_t^0) - \frac{E_a^0}{RT}\right] = \alpha_{\mathrm{on}}E_a^0 - \ln(t_m k_t^0)\,\alpha_{\mathrm{on}}RT \tag{3.26}$$

The function $\ln y(T)$ is linear with respect to temperature, and from the intercept c we can further extract the lowest activation barrier energy $E_a^0 = \frac{c}{\alpha_{\text{on}}}$. Combining the expression for E_a^0, α_{on} and α_{off}, we have 3 equations we can then solve for parameters related to trap state energy distribution (E_b^0 and α_b) and reorganization energy in Marcus theory (λ) (See Section 3.7).

As a comparison, we repeat the analysis for the model of single activation barrier (Figure 3.2b). The average on-time simply depends on the single trapping rate k_t:

$$\langle t_{\text{on}} \rangle_s = \int_0^\infty tp(t)dt = k_t \int_0^\infty te^{-k_t t}dt = \frac{1}{k_t} = \frac{1}{k_t^0 \exp(-\frac{E_a}{RT})} \tag{3.27}$$

The QY is then given by:

$$\text{QY}_{t,s} = \frac{\langle t_{\text{on}} \rangle_s}{t_m} = \frac{\exp(\frac{E_a}{RT})}{k_t^0 t_m} \tag{3.28}$$

Taking the natural logarithm of $\text{QY}_{t,s}$, we have:

$$\ln \text{QY}_{t,s} = \frac{E_a}{RT} - \ln k_t^0 t_m \tag{3.29}$$

This predicts a linear dependence on reciprocal temperature ($1/\text{T}$) of the natural logarithm of the QY, $\ln \text{QY}_{t,s}$, which is starkly different from the result based on Marcus theory in equation (3.26). Following the analysis above, we carried out the quantitative analysis on experimental data based on both the model of Marcus theory and the model of single activation barrier (Figure 3.4c). The model of Marcus theory again matches very well with experimental data, while the single activation barrier model fails. Along with the previous analysis on power-law slopes for time distributions, we are able to provide self-consistent model which quantitatively explains the experimental observations. With the solved parameters, we can further reconstruct the energetic

structure of the nanoplatelets, providing us with more in-depth understanding on their photophysical properties (Figure 3.5).

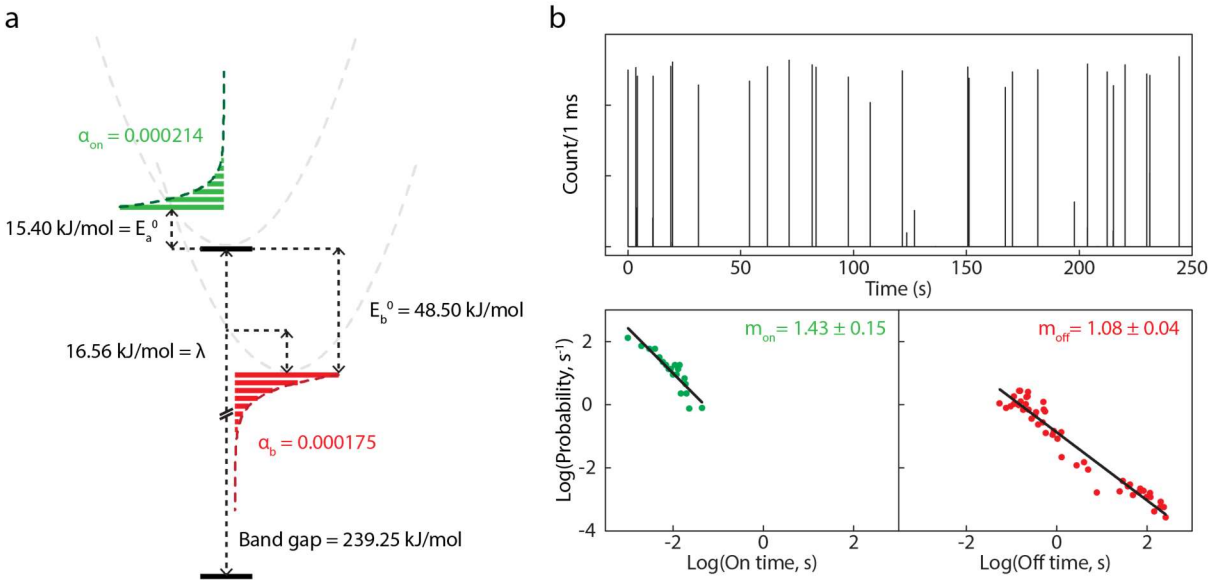

Figure 3.5 Reconstruction and confirmation of energetic structure with extracted parameters. (a) Reconstructed energy diagram for the blinking CdTe NPLs. The values of band gap, reorganization energy λ and distribution of trap state energy and activation barrier energy are shown; (b) Simulated intensity traces and histogram of on-times and off-times with calculated energetic parameters.

3.5 Conclusion

Starting from chemical intuitions, the self-consistent model with Marcus theory of charge transfer and activated kinetics successfully explains the blinking behaviors observed in single-NPL experiments. A combination of analytical modeling and kinetic Monte Carlo simulations agree quantitatively with most of the blinking statistics and temperature dependence of quantum yield of 3 ML CdTe NPLs. Furthermore, we find that such carrier transfer process is likely occurring in the inverted region allowing us to construct reasonable estimates of trap energies and distributions in CdTe NPLs. Interestingly, the presence of deep traps leads to lower quantum yields at room temperature, as the barrier from the on-state to a deep off-state can be more easily overcome. We hypothesize that deep traps in CdTe NPLs may be responsible for the relatively low QY in these NPLs.

We note several limitations to this minimal model. For computational simplicity, we input an exponential distribution of trap energies, each with identical parabolic curvature. This allows us to follow the conventional methodology where the invoked trap variability arises from a variable tunneling barrier process (which will also show an exponential distribution of tunneling probability).[55] As the choice of trap distribution goes directly into the power law, any deviation would result in a different power law (or potentially non-power law statistics; See Section 3.7, Figure 3.9). Another limitation is that we make no claims as to the nature of the electron or hole trap that is responsible for Auger-assisted blinking. Defects, delocalized surface states, dangling bonds, oxidative chemistry all may play role in trapping, and all would have different electron transfer coordinates and reorganization energies. Any realistic model would require computing these coordinates and their reorganization energies independently. It is also important to note that in all the analysis we conducted using this model, we consider only the thermally driven processes of trapping and detrapping, without invoking any light-assisted mechanisms.

However, despite these noted limitations we hypothesize that blinking mediated by Marcus electron transfer could be extended to other systems as well, and perhaps provide a plausible mechanism for reversible photobleaching in nanocrystal films.[54] As Table 3.1 shows, generally off-times have smaller power laws than on-times across several other nanocrystal species, a feature that is not described by most models of blinking. Longer off-times is a natural result of barrier heights being proportional to trap depth in the inverted region, a unique feature could provide insights into improving nanomaterials. This asymmetry could lead to photobrightening and photodimming features. Future work could test specific chemical mechanisms of blinking, introduce electron or hole traps into the material with known relative energetics, probe temperature

dependence of blinking, or ensemble photodimming as potential downstream consequences for quantum dot photophysics.

Table 3.1 Examples of power-law exponents values for blinking materials

Materials	Power-law exponents[a]		References
	On	Off	
CdSe/ZnS core/shell QDs[b]	/	1.6	Kuno et al., 2000[11]
	1.91	1.37-1.79[c]	Kuno et al., 2001[13]
	1.93	1.40	van Sark et al., 2002[56]
	/	1.65	Issac et al., 2005[57]
	1.9	1.4	Pelton et al., 2007[15]
CdTe QDs	1.5 1.6	1.5 1.6	Shimizu et al., 2001[34]
InP QDs	2.0	1.5	Kuno et al., 2001[58]
CdS QDs	/	1.65	Verbek et al., 2002[37]
Si nanocrystals	2.2	1.3	Cichos et al., 2004[59]
Perylene trimer (TPD) molecule	/	1.39	Hoogenboom et al., 2005[60]
CdSe/ZnS core/shell nanorods	/	1.08-1.23	Wang et al., 2006[61]
PbS QDs	1.36	1.22	Peterson et al., 2006[62]
CdSe nanowires	1.7	1.6	Glennon et al., 2007[63]
CdSe/CdSe core/shell QDs	1.57	1.38	Chon et al., 2011[64]
CdTe NPLs	1.53	1.24	This work

[a] The minus signs are omitted for convenience;
[b] CdSe QDs overcoated with ZnS;
[c] A range is shown when multiple values of exponents have been reported.

3.6 Experimental Details

3.6.1 Chemicals

Tellurium (Te) powder (Acros, 99.8%), tri-n-octylphosphine (TOP) (Alfa Aesar, 90%), cadmium oxide (CdO) (Alfa Aesar, 99.95%), propionic acid (Acros, 99%), oleic acid (OA) (Alfa Aesar, 99%), 1-octadecene (ODE) (Alfa Aesar, 90%), isopropanol (Fisher, 99.5%), hexanes (Fisher, 98.5%) and propionic acid (Acros, 99%). All chemicals were used as received without further purification.

3.6.2 Synthesis of precursors

TOP-Te (1 M). In a small flask, 0.254 g of Te powder and 2 mL of TOP were degassed under vacuum at room temperature. The solution was stirred under Argon (Ar) flow at 275 ˚C until the dissolution was complete, and then cooled and stored under protection of Ar.

Cadmium propionate ($Cd(prop)_2$). 1.036 g of CdO powder was mixed with 10 mL propionic acid under Ar flow for 1 hour. The flask was then heated at 140 ˚C after opening to atmosphere in order to reduce the volume by half. The white solution was precipitated with acetone and centrifuged. The supernatant was discarded, and the solid was dried and stored in a vacuum desiccator.

Cadmium oleate ($Cd(oleate)_2$). 0.96 g of CdO (7.5 mmol) and 15 mL of OA were charged into a 25 mL round bottom flask. The mixture was heated at 200 °C for 1 hour under Ar flow. Once the solution turned colorless, the mixture was brought to 60 °C and degassed for 1 hour. After this, it was stored at room temperature and subsequently used in the reactions described below.

3.6.3 Synthesis of 3 ML CdTe nanoplatelets (NPLs)

The procedure was adapted from previous reports of synthesis of 3 ML CdTe NPLs with a few modifications.[65,66] In a 50 mL three-neck flask, 130 mg of $Cd(prop)_2$ (0.5 mmol), 80 µL of OA (0.25 mmol), and 10 mL of ODE were stirred and degassed under vacuum at 80 °C for 2 h. The mixture was then put under Ar and heated to 210 °C. When the desired temperature was reached, a solution of 100 µL 1 M TOP-Te diluted in 0.5 mL of ODE was swiftly added. The reaction was maintained at the same temperature for 30 min for the NPLs to grow. After that, the heating mantle was removed. When the flask was cooled down to about 120 °C, 1 mL $Cd(oleate)_2$ separately heated to 100 °C was injected and the reaction was quenched. Hexane (20 mL) and isopropanol (5 mL) were added and the solution was centrifuged at 7000 rpm for 10 mins. The supernatant was discarded and the solid precipitate was re-dispersed in hexane.

3.6.4 Materials Characterization

Absorption spectra were acquired with an Agilent Cary 60 UV-Vis spectrophotometer. Photoluminescence (PL) was collected using FluoroMax spectrofluorometer by Horiba Scientific. Absolute photoluminescence quantum yield (PLQY) measurements were recorded with a petite integrating sphere in the Horriba spectrometer. Transmission electron microscopy (TEM) images were acquired with a FEI Tecnai T12 120kV TEM. The nanoplatelets were diluted in hexanes and drop casted on Ted Pella, Inc. carbon/formvar 300 mesh copper grids.

3.6.5 Photoluminescence (PL) microscopy

For the single-molecule PL study, films of NPLs were prepared following a drop flow technique. A diluted solution of as-prepared 3 ML CdTe NPLs in hexanes (concentration at around picomolar) was drop cast on a glass coverslip kept at a small incline and dried in air for 5 min. This single NPL was probed using a home-built PL microscope. The films of NPL were excited using a 400 nm CW diode laser with excitation intensity ~40 W/cm^2, and the PL signal was collected through an oil-immersion objective (Nikon, Plan Apo, 100x, NA 1.45), passed through the dichroic mirror and 425 nm long pass filter, and directed to an imaging spectrometer (Kymera 193, ANDOR) mounted with EMCCD camera (ANDOR IXON-L-888). The PL time traces were collected with an integration time of 100 ms.

3.7 Supporting Information

This section contains details of analytical analysis of blinking model, kinetic Monte Carlo method, temperature dependence study and solving equations.

Theoretical time distribution: incomplete gamma function

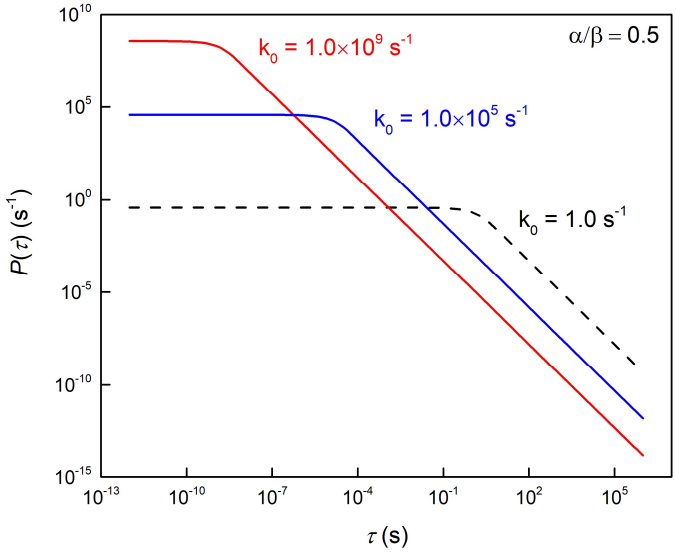

Figure 3.6 Incomplete gamma functions describing the theoretical results for distributions of time with 3 different attempt frequencies. All functions show a plateau part and a power-law part as explained in the main text. The height of plateau and the "transition point" depends on the attempt frequency k_0.

Energetic relations based on Marcus theory of charge transfer[67]

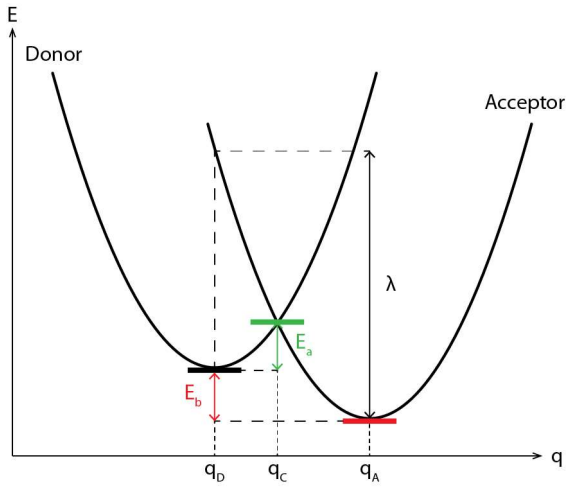

Figure 3.7 Energy diagram of Marcus theory. Potential energy surfaces of both donor and acceptor are shown, along with energies, reaction coordinates and corresponding states including excited state (black), transition state (green) and trap state (red).

Briefly, the potential energy surface for both electron donor and acceptor are considered to be parabolic with respect to reaction coordinates:

$$E_D(q) = \frac{1}{2} m\omega_0^2 (q - q_D)^2 \tag{3.30}$$

$$E_A(q) = \frac{1}{2} m\omega_0^2 (q - q_A)^2 - E_b \tag{3.31}$$

the activated state is then determined by the intersection q_c:

$$q_C = \frac{q_A + q_D}{2} - \frac{E_b}{m\omega_0^2} \frac{1}{q_A - q_D} \tag{3.32}$$

For convenience, reorganization energy λ is defined as:

$$\lambda = E_A(q_D) - E_A(q_A) = \frac{1}{2} m\omega_0^2 (q_D - q_A)^2 \tag{3.33}$$

and finally, we can relate the activation energy using:

$$E_a = \frac{1}{4\lambda} (\lambda - E_b)^2 \tag{3.34}$$

Time distribution in the normal region of Marcus theory

Starting with modified distribution of energy:

$$\rho'(\varepsilon) = \alpha' e^{\alpha' \varepsilon}, x \in (0, \varepsilon_0) \tag{3.35}$$

where the exponent α' is given by:

$$\alpha' = \frac{2\lambda}{\lambda - E_b^0}\alpha_b - \frac{2\lambda}{(E_b^0 - \lambda)^2} \tag{3.36}$$

the range of rate also changes so we substitute with non-trivial bounds:

$$k' = k_0 e^{-\beta x}, k' \in (k_{\min}, k_{\max}) \tag{3.37}$$

The distribution of rate is then calculated by:

$$f'(k) = -\frac{d}{dk}\int_{k_{\min}}^{\frac{1}{\beta}\ln\frac{k_0}{k}} \rho'(x)dx = \frac{\frac{\alpha'}{\beta}k_0^{\frac{\alpha'}{\beta}}}{k^{\frac{\alpha'}{\beta}+1}} \tag{3.38}$$

And the distribution of times is then given by:

$$p'(t) = \int_{k_{\min}}^{k_{\max}} \frac{\frac{\alpha'}{\beta}k_0^{\frac{\alpha'}{\beta}}}{k^{\frac{\alpha'}{\beta}+1}} k e^{-tk} dk = \frac{\alpha'}{\beta}k_0^{\frac{\alpha'}{\beta}} \frac{\gamma\left(1 - \frac{\alpha'}{\beta}, k_{\max}t\right) - \gamma(1 - \frac{\alpha'}{\beta}, k_{\min}t)}{t^{1-\frac{\alpha'}{\beta}}} \tag{3.39}$$

Kinetic Monte Carlo simulations on blinking

The kinetic Monte Carlo modeling is adapted from previous reports with some modifications.[39]

Initialization. The energetic parameters including minimum trap state energy (E_b^0), trap state energy distribution exponent (α_b) and reorganization energy (λ). Typically, the excitation rate k_{exc} and radiative recombination (fluorescence) rate k_r are set to be $5 \times 10^5\ s^{-1}$ and $1 \times 10^7\ s^{-1}$, respectively. The attempt frequency for both trapping processes (k_t^0) and detrapping processes (k_d^0) are selected based on the values of energetic parameters to produce reasonable intensity traces with obvious features of blinking.

Rate calculation with random number generator (RNG). Based on the state NPL is in, we consider the different possible kinetic processes and corresponding rates. In ground state, the only possible process is excitation to excited state; in excited state, it is possible for NPL to go through fluorescent process emitting a photon, or overcome the activation barrier to get trapped in the trap state; in trap state, it is possible for NPL to overcome the reverse barrier and get detrapped to excited state. Each time the NPL is going through the trapping process, a random trap state energy E_b is first drawn from the exponential distribution of trap state energy:

$$E_b = E_b^0 - \frac{\ln(\text{rand})}{\alpha_b}$$

where rand is random number in $(0,1)$. The activation energy E_a is then calculated by:

$$E_a = \frac{1}{4\lambda}(\lambda - E_b)^2$$

and the trapping rate is calculated based on the generated random activation energy E_a:

$$k_t = k_t^0 \exp(-\frac{E_a}{RT})$$

and the corresponding detrapping rate should be calculated based on the reverse barrier energy:

$$k_d = k_d^0 \exp(-\frac{E_r}{RT}) = k_d^0 \exp(-\frac{E_a + E_b}{RT})$$

It is worth mentioning that only after the trapped NPL gets detrapped back to excited state a new random trap state energy E_b will be generated. This is to make sure the statistics of random energies correctly reflect desired distributions, without problems of "undersampling" or "oversampling".

Pathway selection. Based on the state the NPL is in, we calculate the total sum of rates:

$$k_{total} = \sum_i k_i = k_{exc} + k_r + k_t + k_d$$

Note that in real cases one or more terms in the equation above is equal to 0 since the corresponding process is impossible and should be excluded from calculation. The pathway selection is then realized through BKL algorithm by considering partial sum of rates:[68]

$$s_j = \sum_i^j k_i$$

The *j*th path will be chosen after generating a random number to compare with total rate:

$$s_j > \text{rand} \cdot k_{total}$$

To advance the clock, we generate another random number:

$$t = -\frac{\ln(\text{rand})}{k_{total}}$$

Binning and power-law analysis. In blinking simulations, we register the accumulated time every time the NPL go through the fluorescent recombination pathway. We then bin the registered times with a bin time of 10^{-3} s to extract the intensity traces. To analyze the statistics, we set a threshold of intensity to distinguish between on-state and off-state. This can be more reasonably done by fitting high/low counts of intensity traces to two Gaussian functions than randomly choosing a

threshold. Intensity traces are then separated to segments of on-periods and off-periods, and we histogram the on-times and off-times followed by fitting them to power-law functions.

Calculation of QY at different ranges of temperatures

As mentioned in the main text, the calculation of QY will change with different temperatures. Following the equations in main text, the QY-temperature dependences are graphed in the figure below:

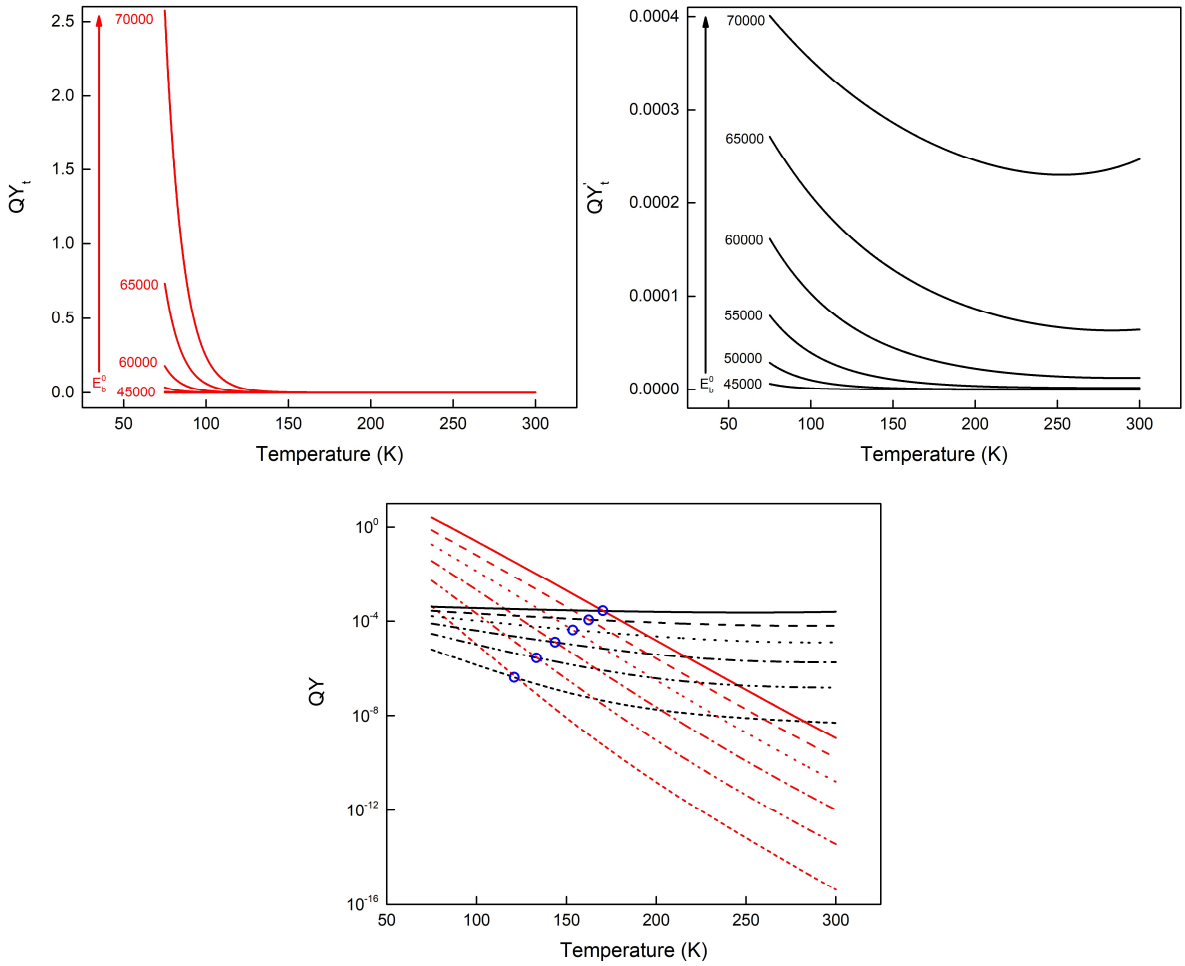

Figure 3.8 QY calculation at low temperature (top left) and at high temperature (top right). QY-temperature curves at both high temperature (black) and low temperature (red) regions are also plotted in log-scale (bottom). Note that in the bottom graph, different styles of the curves represent different minimum trap state energies (E_b^0), and the "transition points" between two temperature regions are marked with blue circles.

At both low temperature and high temperature, the QY increases with decreasing temperature, but the increase is much more significant at low temperature, which agrees with the experimental observations where we saw small increase of QY when close to room temperature, followed by much more drastic increase of QY when lowering the temperature.

Solving the equations for E_b^0, α_b and λ

Based on the power-law analysis and temperature dependence study, we have 3 equations of unknown variables E_b^0, α_b and λ:

$$\frac{2\lambda}{E_b^0 - \lambda}\alpha_b + \frac{2\lambda}{(E_b^0 - \lambda)^2} = \alpha_{\text{on}} \tag{3.40}$$

$$\frac{2\lambda}{E_b^0 + \lambda}\alpha_b + \frac{2\lambda}{(E_b^0 + \lambda)^2} = \alpha_{\text{off}} \tag{3.41}$$

$$\frac{(E_b^0 - \lambda)^2}{4\lambda} = E_a^0 \tag{3.42}$$

where α_{on} and α_{off} are calculated based on the power-law slopes of time distributions at room temperature, and E_a^0 is obtained from the analysis on temperature-dependent QY. First, we have a new expression for E_b^0 by solving (3.42):

$$E_b^0 = \lambda + 2\sqrt{E_a^0}\sqrt{\lambda} \tag{3.43}$$

The other solution of the original quadratic equation is dropped due to the limiting conditions of inverted region ($\lambda \leq E_b^0$). Plug (3.43) into (3.40):

$$\frac{\sqrt{\lambda}}{\sqrt{E_a^0}}\alpha_b + \frac{1}{2E_a^0} = \alpha_{on} \Rightarrow \sqrt{\lambda} = \frac{2E_a^0\alpha_{on} - 1}{2\sqrt{E_a^0}\alpha_b} = \frac{k}{\alpha_b} \tag{3.44}$$

where k is also a variable with known value:

$$k = \frac{2E_a^0\alpha_{on} - 1}{2\sqrt{E_a^0}}$$

Similarly, plug (3.43) into (3.41):

$$\frac{2\lambda}{2\lambda + 2\sqrt{E_a^0}\sqrt{\lambda}}\alpha_b + \frac{2\lambda}{(2\lambda + 2\sqrt{E_a^0}\sqrt{\lambda})^2} = \alpha_{\text{off}}$$

$$\Rightarrow \frac{\sqrt{\lambda}}{\sqrt{\lambda}+\sqrt{E_a^0}}\alpha_b + \frac{1}{2}\frac{1}{(\sqrt{\lambda}+\sqrt{E_a^0})^2} = \alpha_{\text{off}} \tag{3.45}$$

Plug (3.44) into (3.45):

$$\frac{k}{\sqrt{\lambda}+\sqrt{E_a^0}} + \frac{1}{2}\frac{1}{(\sqrt{\lambda}+\sqrt{E_a^0})^2} = \alpha_{\text{off}}$$

$$\Rightarrow 2\alpha_{\text{off}}(\sqrt{\lambda}+\sqrt{E_a^0})^2 - 2k\left(\sqrt{\lambda}+\sqrt{E_a^0}\right) - 1 = 0 \tag{3.46}$$

where we get a new quadratic equation of the unknown variable $\sqrt{\lambda}+\sqrt{E_a^0}$. Solving equation (3.46), we have:

$$\sqrt{\lambda}+\sqrt{E_a^0} = \frac{2k+\sqrt{4k^2+8\alpha_{\text{off}}}}{4\alpha_{\text{off}}}$$

The other solution is dropped for reasonable positivity. The value of λ is finally given by:

$$\lambda = (\frac{2k+\sqrt{4k^2+8\alpha_{\text{off}}}}{4\alpha_{\text{off}}} - \sqrt{E_a^0})^2 \tag{3.47}$$

and the values for E_b^0 and α_b can be obtained by plugging the value of λ back into (3.43) and (3.44), respectively.

Blinking statistics with Gaussian distribution of energy

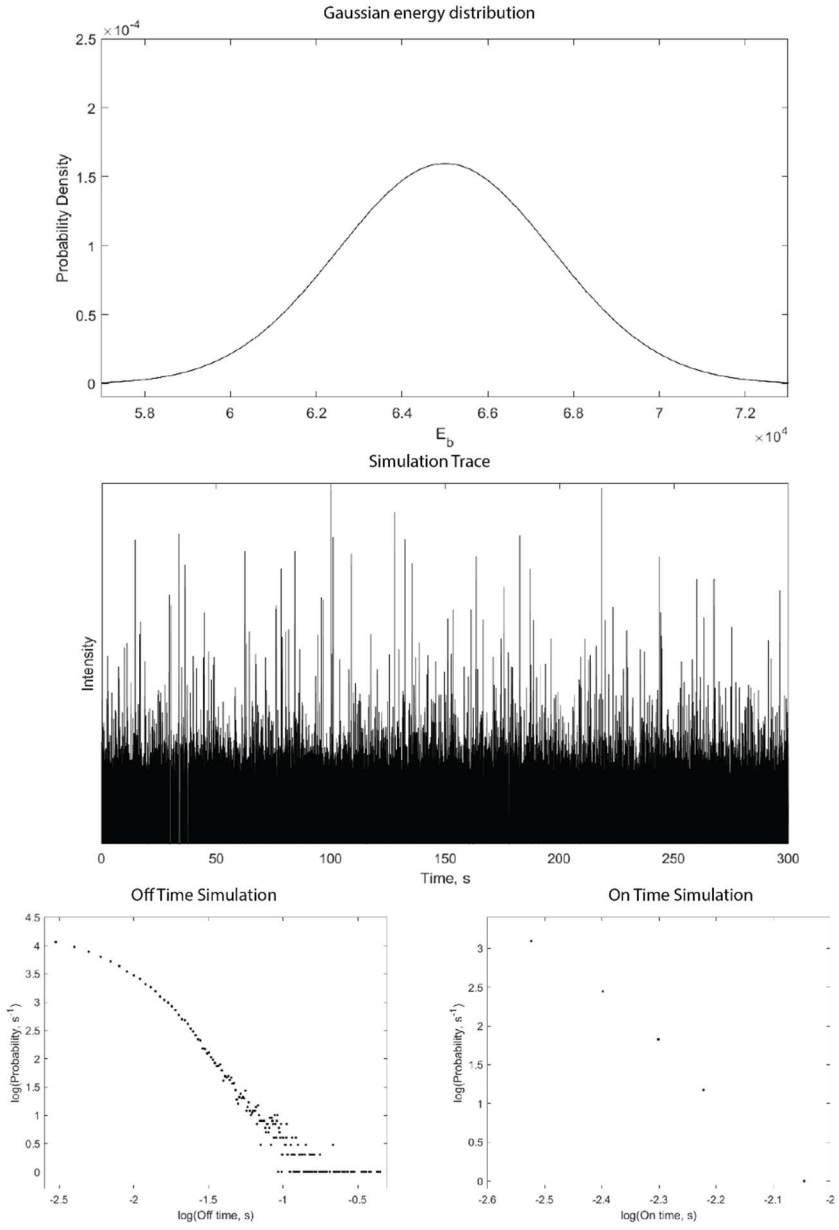

Figure 3.9 Simulation of blinking based on Gaussian distribution of trap state energies. The reorganization energy λ is selected to be small enough to make sure it remains in the Marcus inverted region. We can observe obvious deviations from power-law statistics for both on-times and off-times distributions.

REFERENCES

(1) Nirmal, M.; Dabbousi, B. O.; Bawendi, M. G.; Macklin, J. J.; Trautman, J. K.; Harris, T. D.; Brus, L. E. Fluorescence Intermittency in Single Cadmium Selenide Nanocrystals. *Nature* **1996**, *383* (6603), 802–804. https://doi.org/10.1038/383802a0.

(2) Basché, T. Fluorescence Intensity Fluctuations of Single Atoms, Molecules and Nanoparticles. *J. Lumin.* **1998**, *76–77*, 263–269. https://doi.org/10.1016/S0022-2313(97)00284-6.

(3) Empedocles, S. A.; Neuhauser, R.; Shimizu, K.; Bawendi, M. G. Photoluminescence from Single Semiconductor Nanostructures. *Adv. Mater.* **1999**, *11* (15), 1243–1256. https://doi.org/10.1002/(SICI)1521-4095(199910)11:15<1243::AID-ADMA1243>3.0.CO;2-2.

(4) Gorshkov, K.; Susumu, K.; Chen, J.; Xu, M.; Pradhan, M.; Zhu, W.; Hu, X.; Breger, J. C.; Wolak, M.; Oh, E. Quantum Dot-Conjugated SARS-CoV-2 Spike Pseudo-Virions Enable Tracking of Angiotensin Converting Enzyme 2 Binding and Endocytosis. *ACS Nano* **2020**, *14* (9), 12234–12247. https://doi.org/10.1021/acsnano.0c05975.

(5) Whitham, P. J.; Knowles, K. E.; Reid, P. J.; Gamelin, D. R. Photoluminescence Blinking and Reversible Electron Trapping in Copper-Doped CdSe Nanocrystals. *Nano Lett.* **2015**, *15* (6), 4045–4051. https://doi.org/10.1021/acs.nanolett.5b01046.

(6) Rogach, A. L.; Gaponik, N.; Lupton, J. M.; Bertoni, C.; Gallardo, D. E.; Dunn, S.; Li Pira, N.; Paderi, M.; Repetto, P.; Romanov, S. G.; O'Dwyer, C.; Sotomayor Torres, C. M.; Eychmüller, A. Light-Emitting Diodes with Semiconductor Nanocrystals. *Angew. Chemie - Int. Ed.* **2008**, *47* (35), 6538–6549. https://doi.org/10.1002/anie.200705109.

(7) Park, Y. S.; Guo, S.; Makarov, N. S.; Klimov, V. I. Room Temperature Single-Photon Emission from Individual Perovskite Quantum Dots. *ACS Nano* **2015**, *9* (10), 10386–10393. https://doi.org/10.1021/acsnano.5b04584.

(8) Issac, A.; Krasselt, C.; Cichos, F.; Von Borczyskowski, C. Influence of the Dielectric Environment on the Photoluminescence Intermittency of CdSe Quantum Dots. *ChemPhysChem* **2012**, *13* (13), 3223–3230. https://doi.org/10.1002/cphc.201101040.

(9) Lelek, M.; Gyparaki, M. T.; Beliu, G.; Schueder, F.; Griffié, J.; Manley, S.; Jungmann, R.; Sauer, M.; Lakadamyali, M.; Zimmer, C. Single-Molecule Localization Microscopy. *Nat. Rev. Methods Prim.* **2021**, *1* (1). https://doi.org/10.1038/s43586-021-00038-x.

(10) Efros, A. L.; Rosen, M. Random Telegraph Signal in the Photoluminescence Intensity of a Single Quantum Dot. *Phys. Rev. Lett.* **1997**, *78* (6), 1110–1113. https://doi.org/10.1103/PhysRevLett.78.1110.

(11) Kuno, M.; Fromm, D. P.; Hamann, H. F.; Gallagher, A.; Nesbitt, D. J. Nonexponential "Blinking" Kinetics of Single CdSe Quantum Dots: A Universal Power Law Behavior. *J. Chem. Phys.* **2000**, *112* (7), 3117–3120. https://doi.org/10.1063/1.480896.

(12) Randall, J. T.; Wilkins, M. H. F. Phosphorescence and Electron Traps - I. The Study of Trap Distributions. *Proc. R. Soc. London. Ser. A. Math. Phys. Sci.* **1945**, *184* (999), 365–389. https://doi.org/10.1098/rspa.1945.0024.

(13) Kuno, M.; Fromm, D. P.; Hamann, H. F.; Gallagher, A.; Nesbitt, D. J. "On"/"off" Fluorescence Intermittency of Single Semiconductor Quantum Dots. *J. Chem. Phys.* **2001**, *115* (2), 1028–1040. https://doi.org/10.1063/1.1377883.

(14) Tang, J.; Marcus, R. A. Mechanisms of Fluorescence Blinking in Semiconductor Nanocrystal Quantum Dots. *J. Chem. Phys.* **2005**, *123* (5). https://doi.org/10.1063/1.1993567.

(15) Pelton, M.; Smith, G.; Scherer, N. F.; Marcus, R. A. Evidence for a Diffusion-Controlled Mechanism for Fluorescence Blinking of Colloidal Quantum Dots. *Proc. Natl. Acad. Sci.* **2007**, *104* (36), 14249–14254. https://doi.org/10.1073/pnas.0706164104.

(16) Zhu, Z.; Marcus, R. A. Extension of the Diffusion Controlled Electron Transfer Theory for Intermittent Fluorescence of Quantum Dots: Inclusion of Biexcitons and the Difference of “on” and “off” Time Distributions. *Phys. Chem. Chem. Phys.* **2014**, *16* (47), 25694–25700. https://doi.org/10.1039/C4CP01274G.

(17) Marcus, R. A. On the Theory of Oxidation-Reduction Reactions Involving Electron Transfer. I. *J. Chem. Phys.* **1956**, *24* (5), 966–978. https://doi.org/10.1063/1.1742723.

(18) Marcus, R. A. Electrostatic Free Energy and Other Properties of States Having Nonequilibrium Polarization. I. *J. Chem. Phys.* **1956**, *24* (5), 979–989. https://doi.org/10.1063/1.1742724.

(19) Marcus, R. A. On the Theory of Shifts and Broadening of Electronic Spectra of Polar Solutes in Polar Media. *J. Chem. Phys.* **1965**, *43* (4), 1261–1274. https://doi.org/10.1063/1.1696913.

(20) Marcus, R. A. On the Theory of Chemiluminescent Electron-Transfer Reactions. *J. Chem. Phys.* **1965**, *43* (8), 2654–2657. https://doi.org/10.1063/1.1697190.

(21) Marcus, R. A.; Sutin, N. Electron Transfers in Chemistry and Biology. *Biochim. Biophys. Acta - Rev. Bioenerg.* **1985**, *811* (3), 265–322. https://doi.org/10.1016/0304-4173(85)90014-X.

(22) Marcus, R. A. Electron Transfer Reactions in Chemistry: Theory and Experiment (Nobel Lecture). *Angew. Chemie Int. Ed. English* **1993**, *32* (8), 1111–1121. https://doi.org/10.1002/anie.199311113.

(23) Marcus, R. A. On the Theory of Oxidation-Reduction Reactions Involving Electron Transfer. II. Applications to Data on the Rates of Isotopic Exchange Reactions. *J. Chem. Phys.* **1957**, *26* (4), 867–871. https://doi.org/10.1063/1.1743423.

(24) Marcus, R. A. On the Theory of Oxidation-Reduction Reactions Involving Electron Transfer. III. Applications to Data on the Rates of Organic Redox Reactions. *J. Chem. Phys.* **1957**, *26* (4), 872–877. https://doi.org/10.1063/1.1743424.

(25) Marcus, R. A. Exchange Reactions and Electron Transfer Reactions Including Isotopic Exchange. Theory of Oxidation-Reduction Reactions Involving Electron Transfer. Part 4.—A Statistical-Mechanical Basis for Treating Contributions from Solvent, Ligands, and Inert Salt. *Discuss. Faraday Soc.* **1960**, *29* (i), 21–31. https://doi.org/10.1039/DF9602900021.

(26) Marcus, R. A. ON THE THEORY OF OXIDATION—REDUCTION REACTIONS INVOLVING ELECTRON TRANSFER. V. COMPARISON AND PROPERTIES OF ELECTROCHEMICAL AND CHEMICAL RATE CONSTANTS 1. *J. Phys. Chem.* **1963**, *67* (4), 853–857. https://doi.org/10.1021/j100798a033.

(27) Marcus, R. A. Free Energy of Nonequilibrium Polarization Systems. II. Homogeneous and Electrode Systems. *J. Chem. Phys.* **1963**, *38* (8), 1858–1862. https://doi.org/10.1063/1.1733886.

(28) Marcus, R. A. Free Energy of Nonequilibrium Polarization Systems. III. Statistical Mechanics of Homogeneous and Electrode Systems. *J. Chem. Phys.* **1963**, *39* (7), 1734–1740. https://doi.org/10.1063/1.1734522.

(29) Marcus, R. a. Chemical and Electrochemical Electron-Transfer Theory. *Annu. Rev. Phys. Chem.* **1964**, *15* (1), 155–196. https://doi.org/10.1146/annurev.pc.15.100164.001103.

(30) Marcus, R. A. On the Theory of Electron-Transfer Reactions. VI. Unified Treatment for Homogeneous and Electrode Reactions. *J. Chem. Phys.* **1965**, *43* (2), 679–701. https://doi.org/10.1063/1.1696792.

(31) Tessier, M. D.; Javaux, C.; Maksimovic, I.; Loriette, V.; Dubertret, B. Spectroscopy of Single CdSe Nanoplatelets. *ACS Nano* **2012**, *6* (8), 6751–6758. https://doi.org/10.1021/nn3014855.

(32) Zang, H.; Li, H.; Makarov, N. S.; Velizhanin, K. A.; Wu, K.; Park, Y. S.; Klimov, V. I. Thick-Shell CuInS2/ZnS Quantum Dots with Suppressed "Blinking" and Narrow Single-Particle Emission Line Widths. *Nano Lett.* **2017**, *17* (3), 1787–1795. https://doi.org/10.1021/acs.nanolett.6b05118.

(33) Hu, Z.; Singh, A.; Goupalov, S. V.; Hollingsworth, J. A.; Htoon, H. Influence of Morphology on the Blinking Mechanisms and the Excitonic Fine Structure of Single Colloidal Nanoplatelets. *Nanoscale* **2018**, *10* (48), 22861–22870. https://doi.org/10.1039/c8nr06234j.

(34) Shimizu, K. T.; Neuhauser, R. G.; Leatherdale, C. A.; Empedocles, S. A.; Woo, W. K.; Bawendi, M. G. Blinking Statistics in Single Semiconductor Nanocrystal Quantum Dots. *Phys. Rev. B - Condens. Matter Mater. Phys.* **2001**, *63* (20), 1–5. https://doi.org/10.1103/PhysRevB.63.205316.

(35) Cordones, A. A.; Leone, S. R. Mechanisms for Charge Trapping in Single Semiconductor Nanocrystals Probed by Fluorescence Blinking. *Chem. Soc. Rev.* **2013**, *42* (8), 3209. https://doi.org/10.1039/c2cs35452g.

(36) Efros, A. L.; Nesbitt, D. J. Origin and Control of Blinking in Quantum Dots. *Nat. Nanotechnol.* **2016**, *11* (8), 661–671. https://doi.org/10.1038/nnano.2016.140.

(37) Verberk, R.; Van Oijen, A. M.; Orrit, M. Simple Model for the Power-Law Blinking of Single Semiconductor Nanocrystals. *Phys. Rev. B - Condens. Matter Mater. Phys.* **2002**, *66* (23), 1–4. https://doi.org/10.1103/PhysRevB.66.233202.

(38) Margolin, G.; Protasenko, V.; Kuno, M.; Barkai, E. Power-Law Blinking Quantum Dots: Stochastic and Physical Models. *Adv. Chem. Physics, Fractals, Diffus. Relax. Disord. Complex Syst.* **2005**, *133* (July), 327–356. https://doi.org/10.1002/0471790265.ch4.

(39) Kuno, M.; Fromm, D. P.; Johnson, S. T.; Gallagher, A.; Nesbitt, D. J. Modeling Distributed Kinetics in Isolated Semiconductor Quantum Dots. *Phys. Rev. B* **2003**, *67* (12), 125304. https://doi.org/10.1103/PhysRevB.67.125304.

(40) Wang, J.; Ding, T.; Gao, K.; Wang, L.; Zhou, P.; Wu, K. Marcus Inverted Region of Charge Transfer from Low-Dimensional Semiconductor Materials. *Nat. Commun.* **2021**, *12* (1), 1–9. https://doi.org/10.1038/s41467-021-26705-x.

(41) Canneson, D.; Biadala, L.; Buil, S.; Quélin, X.; Javaux, C.; Dubertret, B.; Hermier, J.-P. Blinking Suppression and Biexcitonic Emission in Thick-Shell CdSe/CdS Nanocrystals at Cryogenic Temperature. *Phys. Rev. B* **2014**, *89* (3), 035303. https://doi.org/10.1103/PhysRevB.89.035303.

(42) Rainò, G.; Nedelcu, G.; Protesescu, L.; Bodnarchuk, M. I.; Kovalenko, M. V.; Mahrt, R. F.; Stöferle, T. Single Cesium Lead Halide Perovskite Nanocrystals at Low Temperature: Fast Single-Photon Emission, Reduced Blinking, and Exciton Fine Structure. *ACS Nano* **2016**, *10* (2), 2485–2490. https://doi.org/10.1021/acsnano.5b07328.

(43) Wen, X.; Dao, L. Van; Hannaford, P. Temperature Dependence of Photoluminescence in Silicon Quantum Dots. *J. Phys. D. Appl. Phys.* **2007**, *40* (12), 3573–3578. https://doi.org/10.1088/0022-3727/40/12/005.

(44) Erdem, O.; Olutas, M.; Guzelturk, B.; Kelestemur, Y.; Demir, H. V. Temperature-Dependent Emission Kinetics of Colloidal Semiconductor Nanoplatelets Strongly Modified by Stacking. *J. Phys. Chem. Lett.* **2016**, *7* (3), 548–554. https://doi.org/10.1021/acs.jpclett.5b02763.

(45) Shinde, A.; Gahlaut, R.; Mahamuni, S. Low-Temperature Photoluminescence Studies of CsPbBr 3 Quantum Dots. *J. Phys. Chem. C* **2017**, *121* (27), 14872–14878. https://doi.org/10.1021/acs.jpcc.7b02982.

(46) Antolinez, F. V.; Rabouw, F. T.; Rossinelli, A. A.; Keitel, R. C.; Cocina, A.; Becker, M. A.; Norris, D. J. Trion Emission Dominates the Low-Temperature Photoluminescence of CdSe Nanoplatelets. *Nano Lett.* **2020**, *20* (8), 5814–5820. https://doi.org/10.1021/acs.nanolett.0c01707.

(47) Sui, X.; Gao, X.; Wu, X.; Li, C.; Yang, X.; Du, W.; Ding, Z.; Jin, S.; Wu, K.; Sum, T. C.; Gao, P.; Liu, J.; Wei, X.; Zhang, J.; Zhang, Q.; Tang, Z.; Liu, X. Zone-Folded Longitudinal Acoustic Phonons Driving Self-Trapped State Emission in Colloidal CdSe Nanoplatelet Superlattices. *Nano Lett.* **2021**, *21* (10), 4137–4144. https://doi.org/10.1021/acs.nanolett.0c04169.

(48) Hinterding, S. O. M.; Salzmann, B. B. V.; Vonk, S. J. W.; Vanmaekelbergh, D.; Weckhuysen, B. M.; Hutter, E. M.; Rabouw, F. T. Single Trap States in Single CdSe Nanoplatelets. *ACS Nano* **2021**, *15* (4), 7216–7225. https://doi.org/10.1021/acsnano.1c00481.

(49) van der Stam, W.; de Graaf, M.; Gudjonsdottir, S.; Geuchies, J. J.; Dijkema, J. J.; Kirkwood, N.; Evers, W. H.; Longo, A.; Houtepen, A. J. Tuning and Probing the Distribution of Cu + and Cu 2+ Trap States Responsible for Broad-Band Photoluminescence in CuInS 2 Nanocrystals. *ACS Nano* **2018**, *12* (11), 11244–11253. https://doi.org/10.1021/acsnano.8b05843.

(50) Kushwaha, M.; Srivastava, A. P.; Singh, M. K. Balanced Emission from Band-Edge and Trap States of Ultra Stable CdSe Nanocrystals Synthesized by Aqueous Route. *Mater. Lett.* **2013**, *109*, 23–26. https://doi.org/10.1016/j.matlet.2013.07.028.

(51) Ithurria, S.; Tessier, M. D.; Mahler, B.; Lobo, R. P. S. M.; Dubertret, B.; Efros, A. L. Colloidal Nanoplatelets with Two-Dimensional Electronic Structure. *Nat. Mater.* **2011**, *10* (12), 936–941. https://doi.org/10.1038/nmat3145.

(52) Nair, G.; Zhao, J.; Bawendi, M. G. Biexciton Quantum Yield of Single Semiconductor Nanocrystals from Photon Statistics. *Nano Lett.* **2011**, *11* (3), 1136–1140. https://doi.org/10.1021/nl104054t.

(53) Hinsch, A.; Lohmann, S. H.; Strelow, C.; Kipp, T.; Würth, C.; Geißler, D.; Kornowski, A.; Wolter, C.; Weller, H.; Resch-Genger, U.; Mews, A. Fluorescence Quantum Yield and Single-Particle Emission of CdSe Dot/CdS Rod Nanocrystals. *J. Phys. Chem. C* **2019**, *123* (39), 24338–24346. https://doi.org/10.1021/acs.jpcc.9b07957.

(54) Jensen, R. A.; Coropceanu, I.; Chen, Y.; Bawendi, M. G. Thermal Recovery of Colloidal Quantum Dot Ensembles Following Photoinduced Dimming. *J. Phys. Chem. Lett.* **2015**, *6* (15), 2933–2937. https://doi.org/10.1021/acs.jpclett.5b00989.

(55) Tachiya, M.; Mozumder, A. Kinetics of Geminate-Ion Recombination by Electron Tunnelling. *Chem. Phys. Lett.* **1975**, *34* (1), 77–79. https://doi.org/10.1016/0009-2614(75)80204-1.

(56) van Sark, W. G. J. H. M.; Frederix, P. L. T. M.; Bol, A. A.; Gerritsen, H. C.; Meijerink, A. Blueing, Bleaching, and Blinking of Single CdSe/ZnS Quantum Dots. *ChemPhysChem* **2002**, *3* (10), 871–879. https://doi.org/10.1002/1439-7641(20021018)3:10<871::AID-CPHC871>3.0.CO;2-T.

(57) Issac, A.; Von Borczyskowski, C.; Cichos, F. Correlation between Photoluminescence Intermittency of CdSe Quantum Dots and Self-Trapped States in Dielectric Media. *Phys. Rev. B - Condens. Matter Mater. Phys.* **2005**, *71* (16), 1–4. https://doi.org/10.1103/PhysRevB.71.161302.

(58) Kuno, M.; Fromm, D. P.; Gallagher, A.; Nesbitt, D. J.; Micic, O. I.; Nozik, A. J. Fluorescence Intermittency in Single InP Quantum Dots. *Nano Lett.* **2001**, *1* (10), 557–564. https://doi.org/10.1021/nl010049i.

(59) Cichos, F.; Martin, J.; Von Borczyskowski, C. Emission Intermittency in Silicon Nanocrystals. *Phys. Rev. B - Condens. Matter Mater. Phys.* **2004**, *70* (11), 1–9. https://doi.org/10.1103/PhysRevB.70.115314.

(60) Hoogenboom, J. P.; Van Dijk, E. M. H. P.; Hernando, J.; Van Hulst, N. F.; García-Parajó, M. F. Power-Law-Distributed Dark States Are the Main Pathway for Photobleaching of Single Organic Molecules. *Phys. Rev. Lett.* **2005**, *95* (9), 2–5. https://doi.org/10.1103/PhysRevLett.95.097401.

(61) Wang, S.; Querner, C.; Emmons, T.; Drndic, M.; Crouch, C. H. Fluorescence Blinking Statistics from CdSe Core and Core/Shell Nanorods. *J. Phys. Chem. B* **2006**, *110* (46), 23221–23227. https://doi.org/10.1021/jp064976v.

(62) Peterson, J. J.; Krauss, T. D. Fluorescence Spectroscopy of Single Lead Sulfide Quantum Dots. *Nano Lett.* **2006**, *6* (3), 510–514. https://doi.org/10.1021/nl0525756.

(63) Glennon, J. J.; Tang, R.; Buhro, W. E.; Loomis, R. A. Synchronous Photoluminescence Intermittency (Blinking) along Whole Semiconductor Quantum Wires. *Nano Lett.* **2007**, *7* (11), 3290–3295. https://doi.org/10.1021/nl0714583.

(64) Chon, B.; Bang, J.; Park, J.; Jeong, C.; Choi, J. H.; Lee, J. B.; Joo, T.; Kim, S. Unique Temperature Dependence and Blinking Behavior of CdTe/CdSe (Core/Shell) Type-II Quantum Dots. *J. Phys. Chem. C* **2011**, *115* (2), 436–442. https://doi.org/10.1021/jp109229u.

(65) Pedetti, S.; Nadal, B.; Lhuillier, E.; Mahler, B.; Bouet, C.; Abécassis, B.; Xu, X.; Dubertret, B. Optimized Synthesis of CdTe Nanoplatelets and Photoresponse of CdTe Nanoplatelets Films. *Chem. Mater.* **2013**, *25* (12), 2455–2462. https://doi.org/10.1021/cm4006844.

(66) Anand, A.; Zaffalon, M. L.; Cova, F.; Pinchetti, V.; Khan, A. H.; Carulli, F.; Brescia, R.; Meinardi, F.; Moreels, I.; Brovelli, S. Optical and Scintillation Properties of Record-Efficiency

CdTe Nanoplatelets toward Radiation Detection Applications. *Nano Lett.* **2022**, *22* (22), 8900–8907. https://doi.org/10.1021/acs.nanolett.2c02975.

(67) Barbara, P. F.; Meyer, T. J.; Ratner, M. A. Contemporary Issues in Electron Transfer Research. *J. Phys. Chem.* **1996**, *100* (31), 13148–13168. https://doi.org/10.1021/jp9605663.

(68) Bortz, A. B.; Kalos, M. H.; Lebowitz, J. L. A New Algorithm for Monte Carlo Simulation of Ising Spin Systems. *J. Comput. Phys.* **1975**, *17* (1), 10–18. https://doi.org/10.1016/0021-9991(75)90060-1.

Chapter 4

Kinetic Monte Carlo Simulation Assisted Study of Anisotropic Growth of Semiconductor Nanoplatelets

This chapter contains unpublished work "Ahmed, T.; Tan, X.; Li, B.; Williams, J.; Cook, E.; Tiano, S.; Tenney, S. M.; Hayes, D.; Caram, J. R. Hetero-confinement in Single CdTe Nanoplatelets. *ChemRxiv*. 2024. https://doi:10.26434/chemrxiv-2024-85hg8." This work is under peer review. This chapter also contains other unpublished work by Xuanheng Tan and Justin Caram. The results are preliminary and based on available data.

Thorough understanding of anisotropic growth of atomically thin II-VI nanoplatelets (NPLs) remains an open challenge. Two important characters of NPLs capture the most attention: thickness and lateral size. While CdSe NPLs have been made with confinement ranging from 2-11 monolayers (ML), CdTe NPLs have been significantly more challenging to synthesize and separate. On the other hand, despite the better thickness selectivity of CdSe NPLs, generally CdTe NPLs can be extended to achieve larger lateral size through synthetic control. Here we provide detailed mechanistic insight into the layer-by-layer growth kinetics of CdTe NPLs. Experimentally, our work suggests that beyond 2 ML CdTe NPLs, higher ML structures initially appear as hetero-confined materials with co-localized multilayer structures by combining ensemble and single particle spectroscopic and microscopic tools. In particular, we observe strongly colocalized 3 ML and 4 ML emissions accompanied by a broad trap emission. Transient absorption, single particle optical and atomic force microscopy suggests islands of different MLs on the same NPL. To explain the non-standard nucleation and growth of these hetero-confined structures, we simulated the growth conditions of NPLs and quantified how monomer bond energy

modifies the kinetics and permits single NPLs with multi-ML structures. In addition, the kinetic Monte Carlo (KMC) simulations also revealed the bond energy dependence of size distribution of NPLs. Our findings suggest that the lower bond energy associated with CdTe relative to CdSe limits higher ML syntheses and explains the observed differences between CdTe and CdSe growth.

4.1 Observed Difference in Anisotropic Growth of CdSe and CdTe Nanoplatelets (NPLs)

In recent years significant effort has gone into controlling the size, composition, and dimensionality of semiconducting nanocrystals.[1–3] By changing the latter, chemists have synthesized tunable quantum dots, rods, and nanoplatelets (NPLs) structures (0-, 1- and 2-D materials respectively). NPLs in particular show control over the band gap with the change of thickness dimension.[4,5] Furthermore, while the lateral dimensions of these NPLs can range from tens of nanometers to micrometers, the optical properties are mainly controlled by the thickness dimension allowing for nearly homogeneous absorption and emission properties.[6] The 1D confinement in these systems results in unique optical and electronic properties including spectrally pure photoluminescence (PL), large absorption cross-sections, boosted optical gain, high-efficiency energy transfer, and surface dielectric/strain tunable exciton binding energies.[3,4,7–10] Although the unique behaviors make them promising materials for applications in lasers, field-effect transistors, solar cells, and light-emitting devices, the basic understanding of the mechanism behind the anisotropic growth of those NPLs is still hotly debated.[8,9,11–17]

Among the various Cd-chalcogenide systems, CdSe NPLs have been the most investigated ones with researchers exercising control over thicknesses (N ML zinc-blende NPLs consist of N layers of Te/Se/S and N+1 layers of Cd) and hetero-structure type (e.g., alloy, core-shell and core-crown) and incorporating them into applications from lasing to scintillation.[18–23] In contrast,

despite the reported synthesis of CdTe quantum dots and nanorods, NPLs of this composition remain relatively understudied regardless of intriguing properties including a lower band gap for bulk CdTe (1.44eV compared to 1.74eV/2.24eV for CdSe/CdS), larger lateral area, and potential connections to the large market for photovoltaic and photodetection devices.[24–33]

Being of the same II-VI semiconductor family, CdTe and CdSe NPLs show well-separated and sharp absorbance of heavy-hole and light-hole excitonic transitions, giant oscillator strength transitions, and narrow and tunable emission, but there are a few clear differences in their chemistry and photophysical properties.[32] While distinct and easily separable thickness populations are demonstrated for CdSe, a mixture of different thicknesses of NPLs is often observed in CdTe NPLs along with broad trap emission, which were first reported by Ithurria et al.[34] CdSe NPLs have been directly synthesized of thickness from 2 ML to 5 ML, while Pedetti et al. demonstrated how factors such as reaction temperature, ligand concentration, synthetic precursors, and injection rate can be manipulated to achieve three different thickness (2 ML to 4 ML) of CdTe NPLs with reduced contribution from other thicknesses. However, a contribution from broad trap emission is also observed for 3 and 4 ML NPLs.[35] Chu et al. were able to synthesize 11 ML CdSe but also without clear separation of thickness.[36] Using the dissolution/recrystallization method, Moghaddam et al. were able to increase the thickness of CdSe NPLs up to 9 ML starting from 3 ML; for CdTe NPLs thickness reached 5 ML starting from 3ML as reflected in the absorption spectra, but again clear separation was not observed for thick NPLs.[22] Furthermore, synthesized CdTe NPLs also display a significantly lower photoluminescence quantum yield (PLQY) when compared to their CdSe cousins.[30,31,33,34] In the case of CdSe NPLs without any shell, PLQY can reach up to 40-50% whereas CdTe NPL PLQY is typically less than 1%.[21,35] Recent work by Anand et al. demonstrated improved PLQY of 9% in small-area 3 ML

CdTe NPLs by quenching the reaction with cadmium propionate (a Z-type ligand) instead of oleic acid.[37] Similarly, Al-Shnani et al. showed PLQY up to 12% by using a different Te source and post-synthetic treatment.[38] However, despite these improvements, contributions from other ML NPLs and trap emissions were observed for thick CdTe NPLs.[34,35,37,38] The enlargement of lateral size of NPLs has also been an aspect of synthetic engineering due to potential improvement on optoelectronic applications of NPLs. Tenney et al. demonstrated such lateral size extension with a technique of seeded growth in synthesis, and an apparent discrepancy between size of CdSe and CdTe NPLs was observed where CdTe NPLs can be extended to larger lateral sizes.[6]

In this chapter, we studied the growth of CdTe NPLs during their formation following fast injection and focused on the factors that make it challenging to synthesize high-purity CdTe NPLs of higher-order monolayers. We observed that generally when growing 3 ML CdTe NPLs, a significant contribution from 4 ML appears simultaneously and results in modified emission properties. We demonstrated that this is the result of a 3 ML/4 ML hetero-structure found within individual CdTe NPLs, resulting in both 3 ML and 4 ML emission accompanied by a broad trap emission. We connected these results to kinetic Monte Carlo (KMC) simulations that elucidate the differences in ripening between CdTe and CdSe NPLs. These simulations based on proposed model with minimal physics could also explain the discrepancy in lateral size between CdTe and CdSe NPLs. We conclude that these disparities are direct results of thermodynamic differences between CdSe and CdTe bond energies.

4.2 Synthesis of 3 Monolayer (ML) CdTe Nanoplatelets (NPLs) with Heterostructures

We followed the formation of CdTe nanoplatelets following a fast injection method reported by Pedetti et al. with a few modifications.[35] To synthesize 2 ML, 3 ML, and 4 ML NPLs, elemental Te in trioctylphosphine was injected into a solution of Cd(propionate)$_2$ in octadecene

with oleic acid at 180℃, 210℃ and 215℃, respectively. Thickness and lateral size were controlled by the reaction temperature and time. In Figure 4.1a we describe a specific reaction procedure where Te in trioctylphosphine (TOP) is injected into the solution of Cd(propionate)$_2$ in octadecene with oleic acid at temperatures, 200℃ and the mixture is maintained at that temperature for 2 hr (See Section 4.6). To follow the formation of NPLs, aliquots from the reaction solution were taken at different time intervals to measure the change of absorption and emission spectra. At early times (e.g., 10 min shown in Figure 4.1b) a sharp excitonic peak at 428 nm and another distinguishable peak at 387 nm are observed. The lower energy peak at 428 nm has been assigned to the heavy hole (HH) transition of 2 ML thick CdTe NPLs and the higher energy peak is the light hole (LH) transition.[7]

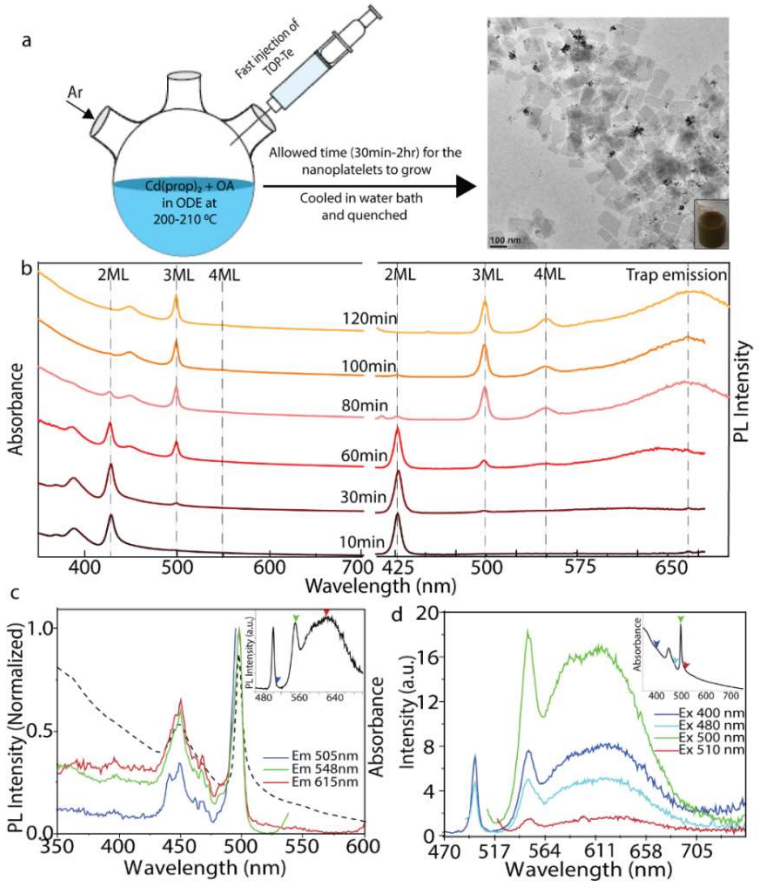

Figure 4.1 Synthesis and spectroscopic characterization of 3 ML CdTe NPLs. (a) An overview of the synthetic conditions of CdTe NPLs. The TEM image confirms the formation of NPLs and an image of the

colloidal dispersion is shown in the inset. (b) Evolution of absorption and emission spectra of CdTe NPLs during the growth period at 200℃. At early times, 2 ML NPLs emerge; as the time progress, the characteristic features related to 2 ML disappear while those of 3 ML appear. (c) Excitation spectra probed at different emission wavelengths and absorption spectrum (black dotted line) of 3 ML CdTe NPLs (synthesized at 210℃). The inset shows the emission spectrum with the emission wavelengths where the excitation spectra were recorded indicated. (d) Relative intensity variation of the emission features of the NPLs upon exciting at different wavelengths. Inset shows the absorption spectrum of the NPLs with the excitation wavelengths where the emission spectra were recorded indicated.

As time progresses, we observe the gradual disappearance of characteristic features related to 2 ML, and the appearance of new red-shifted peaks. Following precedent, we assign the sharp peak at 500 nm to the HH feature and 450 nm to the LH feature of newly formed 3 ML NPLs. The emission spectra in Figure 4.1b (right panel) show the same trend. First, emission from 2 ML NPLs is observed at 429 nm, which gradually disappears, and emission at 500 nm (FWHM ~7 nm) appears, assigned to 3 ML CdTe NPLs. When the synthesis is carried out at 200℃ or lower temperatures, only 2 ML NPLs formed within the initial few minutes, and it took more than 1 hr for conversion to 3 ML. At slightly higher temperature (210℃), the reaction is faster: a mixture of 2 ML and 3 ML NPLs is always formed within the first few minutes, and it takes around 30 minutes for complete conversion to 3 ML NPLs, shown in Figure 4.9. Interestingly, the appearance of emission from 3 ML NPLs at 500 nm is accompanied by a sharp peak at 550 nm and a broad peak at around 615 nm (shown in the right panel of Figure 4.1b and Figure 4.9) and is observed both at 200℃ and 210℃. The broad emission feature has been reported for CdTe NPLs and other nanocrystals and is often attributed to emissive trap states.[34,35,39–42] Although the sharp peak aligns well with 4ML emission it could be also due to the formation of QDs, which has been observed before for HgTe NPLs.[35,38,43] However, the lack of any shift of emission over time (even at high temperature) as well as the sharp nature of the emission peak (FWHM ~ 12 nm) lead us to reject the latter possibility. Hence, this peak at 550 nm is assigned to 4 ML NPLs that appear nearly concurrently with 3 ML growth. Intriguingly, while the 4 ML NPL excitonic feature shows little

contribution in absorption, it has a significant contribution to the emission spectrum (normalized plot shown in Figure 4.9).

In Figure 4.1c and d, we plot the emission excitation spectra and wavelength-dependent emission spectra to understand the origin of the emission features for 3 ML NPLs synthesized at 210℃. Figure 4.1c shows the excitation spectra for the emission at 505 nm, 548 nm and 615 nm, which match exactly with the absorption spectrum (black dotted line) of 3 ML NPLs. This suggests that the excitation of 3 ML NPL results in both 4 ML and trap emissions. To get further insight we have recorded excitation wavelength-dependent emission spectra. Figure 4.1d shows that the relative emission intensity variation of all three peaks (500 nm, 550 nm and 615 nm) following excitation at the different wavelengths indicated in the inset. The emission intensity around 550 nm and 615 nm is maximized when excited at the band edge (500 nm) of the 3 ML NPLs and decreases rapidly when excited below the band-edge (> 500 nm), and no change is observed in their relative intensity. Together these results indicate that the 4ML and the broad trap emissions are correlated to the excitation of 3 ML NPLs.

4.3 Correlation of 4 ML and Mid-gap Emission with 3 ML NPLs: Confirmation of Heterostructure

We next turn to understand whether all three emissions are coming from a single particle or different particles that are strongly coupled.[43] Figure 4.11shows no significant change in the relative intensity of the three emission peaks, indicating that 3 ML and 4 ML NPLs are somehow physically attached. Further, we studied single-particle PL images at different emission wavelength regions. Films of NPLs were prepared from a dilute solution (~nM) of NPLs in hexane to produce well-separated single NPLs. Figure 4.2 shows PL imaging of the NPL film, and the three observed PL features are isolated by collecting different wavelength regions simultaneously

using three detectors. The left panels of Figure 4.2a-c correspond to the PL image for emission between 480-518 nm (around the 3 ML emission), 520-560 nm (around the 4 ML emission) and 564-700 nm (around the trap emission), respectively. The PL images show that there are large areas with high intensity along with smaller areas with lower intensity. The bright portions of the films are due to multiple overlapped NPLs as confirmed by atomic force microscopy (AFM; shown in Figure 4.12), while PL blinking of NPL in the film further supports the presence of well-dispersed single NPLs (Figure 4.13 and attached video). To probe single NPLs rather than multiple overlapped NPLs we chose a small, well-separated area of the film (highlighted in Figure 4.2a, b, and c). We observe a common overlap of all three PL features, which means 3 ML, 4 ML, and trap emission are coming from the same NPL. Further Gaussian fitting allows us to localize the center of emission for each wavelength regime with super-resolution accuracy (See Section 4.7) and their positions are overlapped (shown in Figure 4.2d). However, we note a slight change in their positions and area. First, the area of NPL showing 3 ML emission is greater than that of both the 4 ML and trap emission. We calculated the distance of the center (Δr_1 and Δr_2, see Section 4.7) of the 4 ML and trap emission features from that of the 3 ML NPL. The average distance (Δr) for the particle shown in Figure 4.2d is around 18 nm. Values calculated for more particles shown in Figure 4.7 vary from 15-93 nm, consistent with the dimensions of single NPLs. Emission from the 4 ML region (green circle) and trap states (red circle) appear localized near the edge in most of the NPLs. All of these observations lead us to hypothesize that an incomplete layer of 4 ML is formed near the edge of the 3 ML NPLs as shown in Figure 4.2e. Our hypothesis matches with the island-nucleation-limited growth model proposed by Reidinger et al., which shows that the growth of an N+1 layer happens from an N layer through the formation of an island in the corner of the wide facet, which is energetically favorable and can extend from the edge to center.[8] To further quantify

the localization of these features, we define a relative delocalization parameter, D, as the ratio of Δr to the average radius of the blue circle (for 3 ML emission), R_b (See Section 4.7). This value is around 0.20 for the particle shown in Figure 4.2d, where R_b is 0 when the Δr is 0 and R_b is 1 when the Δr is equal to R_b.

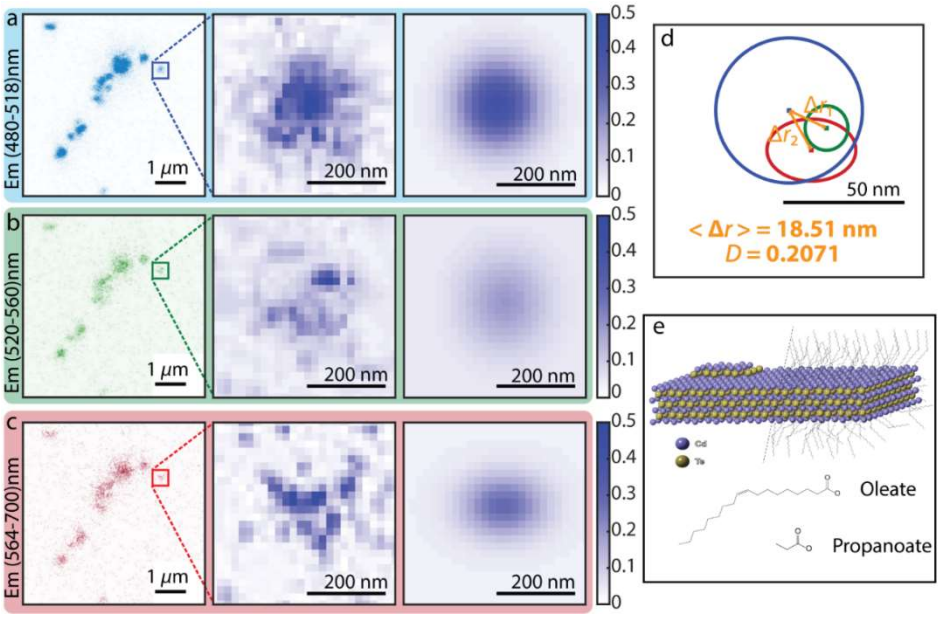

Figure 4.2 Correlation between emission spectra and images from PL microscopy measurements. PL images collected at (a) 480-518 nm, (b) 520 – 560 nm, and (c) 564-700 nm. The PL from the NPL highlighted in the orange box is enlarged and then fit to a Gaussian (right panel). (d) The overlap of the three Gaussians shows the spatial origin of the observed PL. (e) Schematic diagram of the hetero-confined CdTe NPL.

We then used AFM to assess the morphology of NPL structures. The apparent height measured from AFM for a single CdTe NPL is about 4.1 nm (height profile shown in Figure 4.3b). The theoretically predicted thickness of 3 ML bare NPL is around 1.9 nm. In our case, the increased value could be rationalized by considering the ligand environment surrounding the NPLs.[35,44] We also observed that the height increases by approximately 1-2 nm consistently near the edges of NPLs. This value does not exactly match a single monolayer height (~0.3 nm), but it is also much less than a separate 4ML. These areas near the edges disappear upon washing the NPLs with a polar solvent (isopropanol, details in Section 4.7) as shown in Figure 4.3d. This washing not only

smoothens the surface but also results in the disappearance of the emission peak at 550 nm and the corresponding new broad trap emission feature (Figure 4.3a and c). This is consistent with the observed PL localization and suggests a loosely bound new ML layer, removable upon gentle etching. Overall, this further supports our conclusion from the PL images that there are areas near the edges of the single 3 ML CdTe NPLs where extra monolayers are present as incipient 4 ML islands.[7] Therefore, the evidence suggests that 4 ML and trap emission do not arising from contamination by 4 ML NPLs but instead arising from hetero-confined structures, where 3 ML and 4 ML NPLs are simultaneously present.

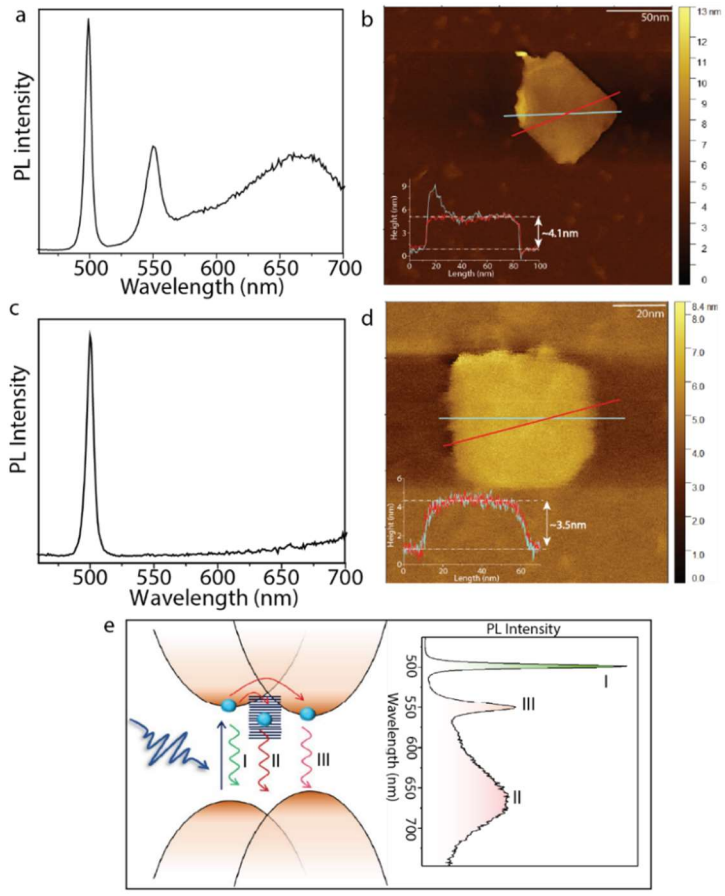

Figure 4.3 Correlation of emission spectra and AFM measurements. (a) PL spectrum and (b) AFM images of NPLs before washing. (c) PL spectrum and (d) AFM images of NPLs after washing with isopropanol. (e) Schematic diagram of the hetero-confined CdTe NPL.

To further test this hypothesis, we performed ultrafast transient absorption (TA) spectroscopy measurements, as shown in Figure 4.14. The TA spectra (Figure 4.14a) show a strong negative

feature centered at 500 nm that arises from both the bleaching of and stimulated emission from the 3 ML exciton state.[45] The positive features on either side of the bleach correspond to the biexciton band (i.e., excited state absorption) broadened by the presence of hot carriers. A negative feature centered at the 4 ML exciton band at 550 nm is also present, becoming increasingly apparent at higher fluences (Figure 4.14b). The bleach recovery dynamics probed between 498 and 501 nm (Figure 4.14c; probe region indicated in Figure 4.14a) can be fit to three ultrafast components (680 ± 40 fs, 6.4 ± 0.6 ps, and 51 ± 7 ps), along with a longer component (540 ± 90 ps). Notably, the kinetics probed between 474 and 482 nm (Figure 4.14d; probe region indicated in Figure 4.14a) show the same ultrafast components (510 ± 250 fs, 4.8 ± 3.7 ps, and 70 ± 30 ps) but do not show any long-lived component. Because this excited state absorption feature is at higher energy than the bleach, it should *only* appear when hot carriers are present; following carrier cooling, the biexciton band should lie entirely below the exciton band in energy, as discussed by Pelton et al.[46] Accordingly, we assign the ultrafast components to a combination of carrier cooling and thermal dissipation to the solvent and the ~0.5 ns component to radiative decay from 3ML, which likely includes exciton transfer from 3 ML to 4ML and trap states as observed before for CdSe hetero-structure with type I band alignment (shown in Figure 4.3e) in addition to emission directly from 3 ML.[22] The immediate appearance of a bleach feature at 550 whose dynamics match those of the 3ML bleach suggest common origin for the two features, further bolstering our hypothesis of connected states.

4.4 Kinetic Monte Carlo (KMC) Simulations of Nanoplatelets (NPLs) Growth

The simultaneous presence of 3 ML and 4 ML appears to run contrary to the prevailing model of NPL growth by Riedinger et al. which strongly suggests that ripening proceeds through sequential dissolution of thinner NPLs to form thicker NPLs.[8] However, the authors of that work do note that

the nucleation barrier for CdTe NPLs of different thicknesses is closer in energy than they are for CdSe or CdS. To test whether the energy difference could result in the observed hetero-confinement, we conducted a series of kinetic Monte Carlo (KMC) simulations based on a simple model of activated kinetics featuring the three most important energetic parameters: activation energy E_a, binding energy E_b and nearest-neighbor bond energy E_c, as well as temperature T (Figure 4.4a; See Section 4.7).[47]

For each simulation we generate snapshots of the grid throughout the entire course of the simulation (Figure 4.4b). The grid can then be converted to the time evolution of different populations. We are able to produce the primary features of the ripening model from Riedinger et al., including the ripening of nanoplatelets (NPLs) with fewer monolayers (MLs) to those with more MLs and the apparent separation of different MLs during the growth process (Figure 4.4c).[8] We then carried out a series of simulations with a wide range of values for each parameter and analyzed the resulting time evolution of populations. As a quantitative characterization of the ripening, we calculated the percentage of 3 ML population at the count peak of 3 MLs, which reflects how well separated different species are. Essentially, a higher peak population represents more "pure" NPLs in synthesis, and a lower population means more "mixed" species. As expected, changing the activation energy E_a and temperature T only led to changes in time scale but had very little influence on the species separation (see Figure 4.15). The results of peak populations with changing E_b and E_c are also shown, and an obvious trend of increasing peak population with increasing bond energy E_c was observed (Figure 4.4d). Since CdTe has lower bond energy than CdSe, the results could explain why we were able to consistently observe the 3-4 ML heterostructure in CdTe but rarely in CdSe.[8,48]

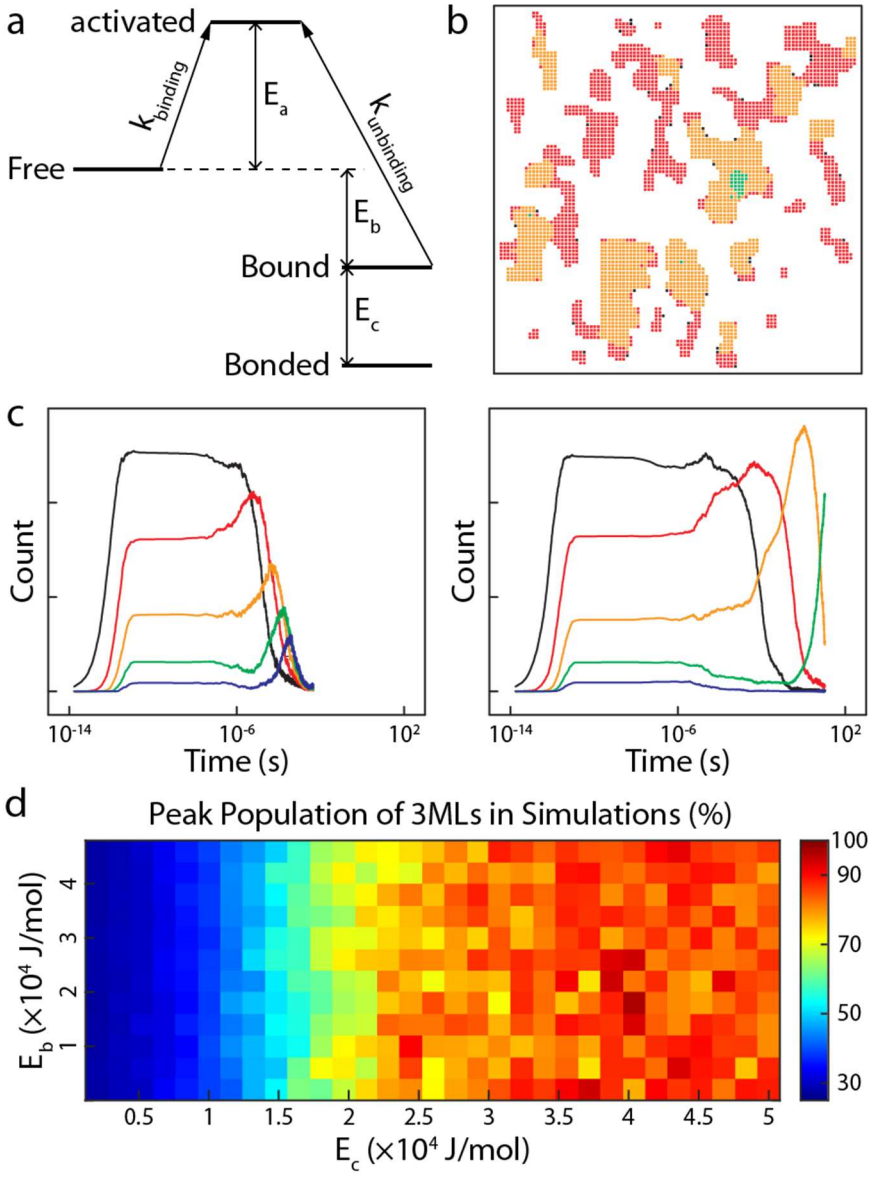

Figure 4.4 Kinetic Monte Carlo (KMC) simulations on thickness ripening of 2D nanoplatelets (NPLs). (a) The kinetic model applied in the kinetic Monte Carlo (KMC) simulations. Three energetic parameters are shown including the activation energy E_a, binding (nucleation) energy E_b and nearest-neighbor (NN) bond energy E_c. The energy diagram is not drawn to scale. (b) An example of the grid generated from simulations. Each small square stands for an occupied spot on the grid and the color of the square shows the number of monolayers (MLs) associated with the spot (Black: 1; Red: 2; Orange: 3; Green: 4). (c) Time evolution of populations based on two simulations. The colors of lines correspond to the number of MLs (Black: 1; Red: 2; Orange: 3; Green: 4; Blue: 5). E_a, E_b and temperature are identical for both simulations, but E_c is smaller for the simulation represented by the left graph. The time scale in both graphs is arbitrary (See Section 4.7). (d) A heatmap for peak population of 3 MLs based on E_b and E_c values in simulations.

In addition to the number population extracted from the record grid, we were also able to utilize the information on positions of bound monomers to extract the size distribution of NPLs using the pair correlation function (PCF) $g(r)$. By fitting $g(r)$ to functional forms based on

different models of size distribution (e.g. monodisperse, lognormal distribution, etc.), we were able to extract the mean and standard deviation of size distributions. This process has already been widely used in scattering experiments of nanocrystals and some programs are available for the "structural refinement" technique.[49,50] We start with calculating the PCF:

$$g(r) = \frac{counts}{N \cdot p \cdot n \cdot 2\pi r \cdot \Delta r} \tag{4.1}$$

where $counts$ is the number of all particles with their distance between r and $r + \Delta r$ from the reference particle, N is the total number of bound monomers, n is the number density of bound monomers, $2\pi r \cdot \Delta r$ is the area of the ring with thickness Δr, and p is the correction factor. The calculation is then repeated for all values of distance r and choices of different reference particle.[51] The correction factor p is very important to correct normalization due to the boundaries of 2D lattice grid in simulations, especially when the reference particle is in proximity of the boundary. To account for this, we compare the investigated distance r with the perpendicular distances from the reference particle to all boundaries. If the distance is larger than r, we calculate the "out of boundary" angles using trigonometry:

$$\theta_i = \arccos\frac{d_i}{r}, i = 1,2,3,4 \tag{4.2}$$

where d_i are the perpendicular distances. Up to 4 angles are calculated based on 4 perpendicular distances from reference particle to 4 boundaries. The correction to normalization is then calculated based on the ratio of the total "out of boundary" angles:

$$p = 1 - \theta = 1 - \sum_{i=1}^{4} 2\theta_i \tag{4.3}$$

where the coefficient 2 indicates the consideration of both angles in regard to the same boundary. It is also important, however, to check if the corner of the grid is within the distance circle. Thus,

if the sum of 2 neighboring angles are larger than $\frac{\pi}{2}$, we still only consider the max angle $\frac{\pi}{2}$ due to their overlap (Figure 4.5a). The calculated $g(r)$ is then fitting to a functional form corresponding to lognormal distribution of lateral sizes. The size distribution generated through this approach was compared to regular method of manual measuring and counting as commonly done to TEM images, and it showed decent accuracy (Figure 4.5b). Similar to the heatmap analysis for thickness, we track the evolution of max mean size with changing binding energy E_b and bond energy E_c (Figure 4.5c). In the case of size distribution, there seems to exist a "sweet spot" of E_c for lateral extension of NPLs. It is reasonable that although the higher bond energy of CdSe makes them more separable in terms of thickness than CdTe, the latter has a bond energy closer to the sweet spot, resulting in larger lateral sizes.

4.5 Conclusion

Extending the superlative properties of quantum-confined NPLs to new materials and wavelengths is a critical research and technology challenge. However, despite superficial similarities between CdSe and CdTe binary semiconductors, the chemistry of CdTe does not appear to permit pure 4 ML NPLs using current methodologies. We have shown that CdTe synthesis results in a unique quantum-confined heterostructure of colocalized 3 ML and 4 ML platelets on a single NPL. Our results give a common origin for 3 ML, 4 ML, and trap emission features appearing simultaneously. We confirm this using single particle PL studies that show nearly co-localized features, further supported by AFM studies of single NPLs. Following work by Riedinger et al. we confirm that the low bond energy of CdTe results in weaker separation between the formation of 3 ML and 4 ML, resulting in simultaneous NPL formation. Simulations also gives consistent explanations on the discrepancy of sizes between CdSe and CdTe NPLs. Taken together, our

results provide us with directions and insights on optimizing the synthesis of II-IV semiconductor NPLs to higher thickness with better selectivity and larger lateral dimensions.

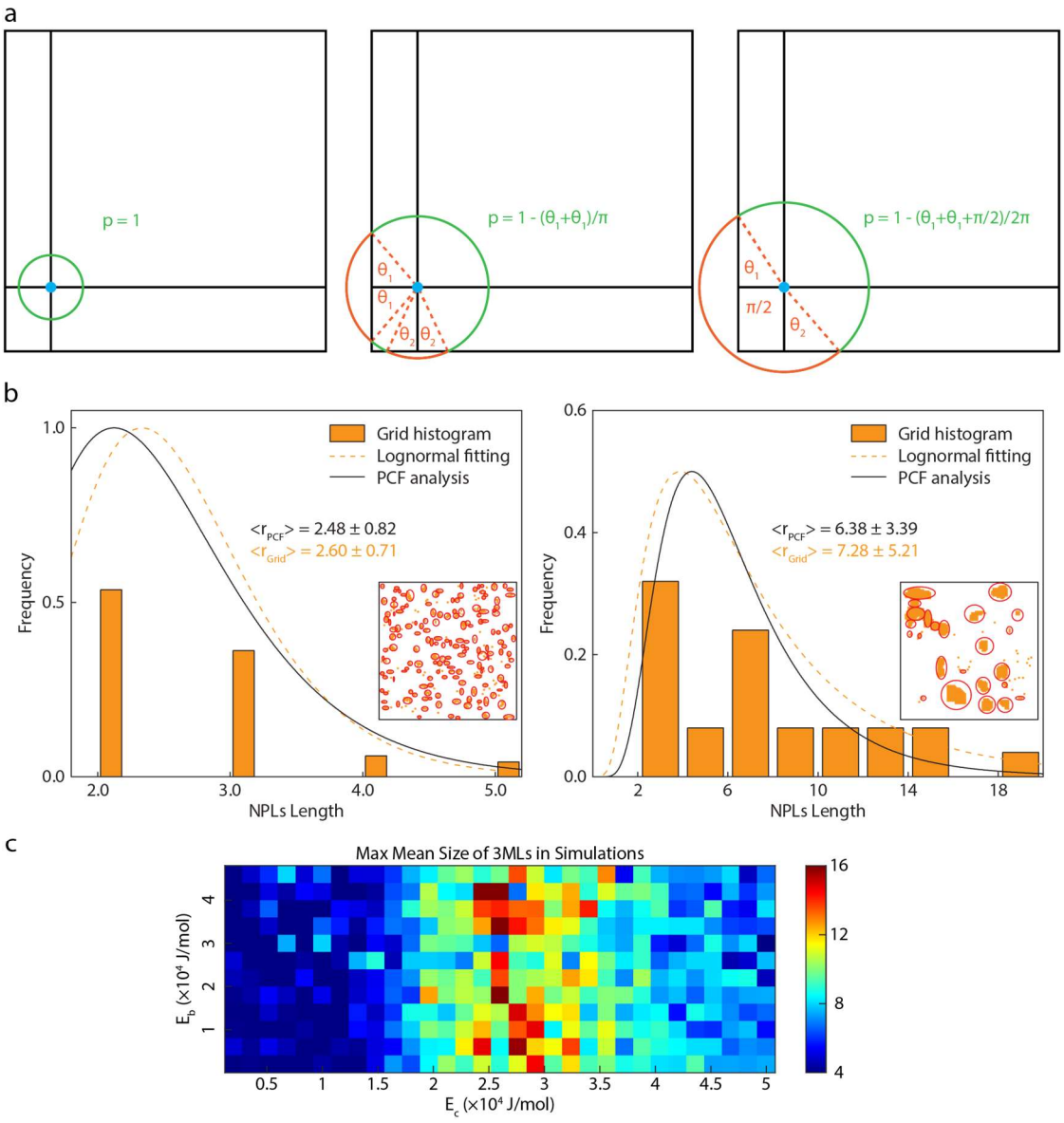

Figure 4.5 Extracting size distribution from pair correlation function (PCF) based on the simulation. (a) Calculation of the correction factor considering the boundaries of lattice grids. (b) Comparison of size distributions extracted from PCF analysis and grid histogram. (c) A heatmap for max mean size of 3 MLs based on E_b and E_c values in simulations.

4.6 Experimental Details

4.6.1 Chemicals

Cadmium oxide (Alfa Aesar, 99.95%), tellurium powder (Acros, 99.8%), oleic acid (OA) (Alfa Aesar, 99%), tri-n-octylphosphine (TOP) (Alfa Aesar, 90%), 1-octadecene (ODE) (Alfa Aesar, 90%), isopropanol, hexanes (Fisher, 98.5%) and propionic acid (Fisher) were used without further purification.

4.6.2 Synthesis of Precursors

Cadmium propionate ($Cd(prop)_2$). 1.036 g of CdO powder was mixed with 10 mL propionic acid under Ar flow for 1 hour. The flask was then heated at 140 ˚C after opening to atmosphere in order to reduce the volume by half. The white solution was precipitated with acetone and centrifuged. The supernatant was discarded, and the solid was dried and stored in a vacuum desiccator.

1M TOP-Te. In a small flask, 0.254 g of Te powder and 2 mL of tri-*n*-octylphosphine were degassed under vacuum at room temperature. Then, under Ar flow, the solution was stirred at 275 ˚C until the dissolution was complete, and the solution turned yellow. The solution was cooled and stored under Argon.

Cadmium oleate (Cd-oleate). 0.96 g of CdO (7.5 mmol) and 15 mL of oleic acid were charged into a 25 mL round bottom flask. The mixture was heated at 200 °C for 1 hr under Ar flow. Once the solution turned colorless, the mixture was brought to 60 °C and degassed for 1 hr. After this, it was stored at room temperature and subsequently used in the reactions described below.

4.6.3 Synthesis of 3 ML CdTe Nanoplatelets (NPLs)

In a three-neck 50 mL flask, 130 mg of $Cd(prop)_2$ (0.5 mmol), 80 µL of oleic acid (0.25 mmol) and 10 mL of ODE was magnetically stirred and degassed under vacuum at 80 °C for 2 h. The mixture was then put under Ar and heated to 200-210 °C. When the desired temperature was reached, 100 µL of a solution of 1 M TOP-Te diluted in 0.5 mL of ODE was swiftly added. The

reaction was maintained at the same temperature for the NPLs to grow with time. An aliquot from the reaction solution was taken out at different time intervals. It was centrifuged at 7000 rpm and dispersed in hexanes and characterized by the absorption and PL spectrum. For the remaining measurements, the reaction was performed at 210℃. After the TOP-Te injection, the reaction was allowed to continue for 30 mins after which the heating mantle was removed. When the flask was cooled down to about 120 °C, 1 mL $Cd(oleate)_2$, separately heated to 100 °C was injected and the reaction was quenched. The solution was then divided into two halves. Only hexane (10 mL) was added to one portion, while hexane (10 mL) and isopropanol (5 mL) were added to the other portion. Both were centrifuged at 7000 rpm for 10 mins. The supernatant was discarded and the solid precipitate was re-dispersed in hexane. We assumed that the reaction goes to completion and yield is 100%. Following centrifugation and resuspension in 20ML hexanes the [Te] will be 5mM in the original CdTe NPLs.

4.6.4 Materials Characterization

Absorption spectra were acquired with an Agilent Cary 60 UV-Vis spectrophotometer. Photoluminescence (PL) was collected using FluoroMax spectrofluorometer by Horiba Scientific. A TCSPC spectrometer FluoroMax by Horiba Scientific, was employed for time-resolved luminescence measurements. A DeltaDiode lasers by Horiba Scientific with peak wavelength at 371nm with 10 MHz repetition rate was used as excitation source.

Transmission electron microscopy (TEM) images were acquired with a FEI Tecnai T12 120kV TEM. The nanoplatelets were diluted in hexanes and drop casted on Ted Pella, Inc. carbon/formvar 300 mesh copper grids.

For atomic force microscopy (AFM) study a film was prepared drop flow technique where a very diluted solution of NPLs in hexanes was drop casted on a cleaved mica substrate (1 cm diameter)

kept at a small incline. Mica substrates were obtained from Thermo Fisher Scientific. The solutions were allowed to slowly dry under air for 2 minutes. AFM measurements were done on FastScan AFM system by Bruker with tip-scanning technology using silicon tip on nitride lever (ScanAsyst-AIR-HPI) with 0.25 N/m force constant and a resonant frequency of ~55 kHz.

For photoluminescence imaging experiments a film of NPLs was prepared following a drop flow technique where a diluted solution of NPLs in hexanes was drop casted on a coverslip kept at a small incline. The imaging was conducted on an inverted confocal microscope by Leica SP8. All NPLs were excited at 400 nm pulsed diode and 100x oil objective was used. The PL images were collected at three different emission wavelength ranges using three detectors at the same time.

Transient absorption spectra and kinetics were measured using a home-built instrument described in a previous report.[52] For these measurements, the frequency-doubled output (centered at 400 nm) of a 1 kHz Ti:sapphire laser (Coherent Astrella) was chopped at a 50% duty cycle and focused to a Gaussian spot of diameter 160 μm ($1/e^2$) in the sample, which was continuously stirred in a 2 mm pathlength quartz cuvette. Samples were prepared as approximately 250 μM solutions in hexanes. The broadband probe beam was delayed using a mechanical delay stage and overlapped with the pump beam in the sample, and the transmitted beam was recorded using a fiber-coupled CMOS spectrometer (Avantes AvaSpec). Spectra were corrected for the temporal chirp profile of the probe beam as previously described, and kinetics were fit using the sum of multiple exponential decay terms convolved with a common Gaussian instrument response function with a FWHM measured to be 160 fs.

Aside from the fluence-dependent spectra shown in Figure 4.14b, all measurements were performed with an excitation fluence of 1.5 mJ/cm^2. The sample has an optical density of 0.75 at the excitation wavelength (400 nm), and the sample pathlength was 1 mm. This corresponds to

2.5×10^{15} photons/cm^2 absorbed per laser pulse. The 250 μM sample contains 1.2×10^{17} NPLs/cm^2 through the same pathlength, so the excitation fluence was sufficient to excite ~2% of the NPLs. Accordingly, we assume that the fraction of NPLs bearing multiple excitons at this fluence is negligible.

4.7 Supporting Information

This section additional experimental details, details of 2D fitting of PL images, additional characterization including absorption and photoluminescence, photoluminescence lifetimes, AFM images, PL images and 2D fitting, PL blinking trace, TA spectra and kinetics, E_a and T tuning.

KMC simulation algorithm

In a typical simulation, we start with a number of free 'monomers' and an empty 2D grid. Monomers here could describe small clusters, unit cells, or other reactive precursors. We then drive the system forward by the events of free monomers binding to the 2D grid and bound monomers unbinding from the 2D grid. The events are characterized by the rates of binding and unbinding:

$$k_{\text{binding}} = P_b \exp\left(-\frac{E_a}{RT}\right), k_{\text{unbinding}} = P_u \exp\left(-\frac{E_a + E_b}{RT}\right) \quad (4.4)$$

where E_a is the activation energy for binding, E_b is the binding energy (i.e., the energy difference between free and bound monomers), and P_b , P_u are the pre-factors for the Arrhenius rate equations.

In addition to the interactions between monomers and the grid, we also consider bond-forming between bound monomers in real synthesis. For simplicity, we assume that every monomer will form bonds with its nearest neighbors (NNs) once both of them are bound to the

grid, lowering its energy linearly with the number of NNs and further decreasing the unbinding rate of bonded bound monomers:

$$k_{\text{unbinding,bonded}} = P_u \exp(-\frac{E_a + E_b + E_c}{RT}) \tag{4.5}$$

For all the rate equations, the pre-factors can be estimated based on the diffusion-limited reactions:

$$P_b = \frac{8Nk_BT}{3\eta}, P_u = \frac{k_BT}{4\pi\eta R_M^3}$$

where η is the dynamic viscosity of the solvent, N is the number density of free monomers and R_M is the hydrodynamic radius of monomers.[53] As mentioned, the exact composition or structure of monomers is uncertain, resulting in ambiguity in the value of R_M. Thus, the actual time drawn from simulations are simply representative, but the *relative* timescales can be used for comparison.

With the calculated rate equations, we then generate a rate matrix with each element of the matrix corresponding to the sum of rate for each spot on the grid, which includes rates for all possible events taking place at the spot (i.e., binding and unbinding):

$$k_{i,j} = k_{\text{binding}\rightarrow(i,j)} + k_{\text{unbinding}\leftarrow(i,j)} \tag{4.6}$$

where $k_{i,j}$ is the rate matrix element, $k_{binding\rightarrow(i,j)}$ is the rate of free monomers binding to the spot (i,j) on the grid, and $k_{unbinding\leftarrow(i,j)}$ is the rate of monomers bound at the spot (i,j) desorbing from the grid. The pathway is then selected using the BKL algorithm which takes advantage of

partial sum of rates by drawing two random numbers, one for determining at which spot an event happens, and the other for determining what type the event is.[54]

After the pathway selection, the clock is advanced by drawing a third random number:

$$t = -\frac{\ln(\text{rand})}{\sum_{i,j} k_{i,j}} \tag{4.7}$$

At each step, the statistics of the number of spots with different number of monolayers (MLs) are calculated along with the clock time.

2D Fitting of PL images

To analyze the property of colocalization of different multilayered structure of CdTe, we utilize a simple 2D Gaussian fitting mechanism. First, the color-filtered PL images are taken in .jpg or .tiff digital format, images are required to be only differ by the choice of filters (Figure 4.6a). The digitized images are then transformed and stored in 2D matrix form where each matrix element represents the intensity of a corresponding pixel in the original image, here the resolution is set by the camera used in experiment. Next, a small emitting region is selected for all colors for fitting (Figure 4.6b).

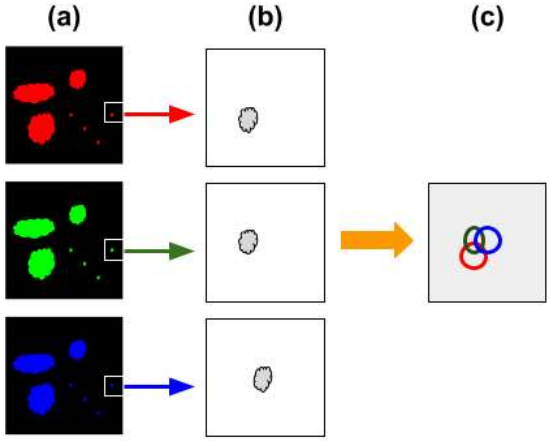

Figure 4.6 2D fitting of PL images. (a) Original color-filtered .tiff or .jpg digital PL images with fine crop at a fixed position. (b) Zoom in for fitting at the selected position. (c) 2D Gaussian fits of the selected regions and the emitting regions are graphically represented by ellipses.

The ideal zoom-in regions are those with a small, single, and bright emitting spot (circular or near-circular). The 2D fittings are applied to these selected regions with a fitting model:

$$f(x,y) = Ae^{-\left[\left(\frac{x-x_0}{2\sigma_x}\right)^2+\left(\frac{y-y_0}{2\sigma_y}\right)^2\right]} + z_0 \tag{4.8}$$

where the intensity A, peak coordinates (x_0, y_0), x and y-direction standard deviations σ_x, σ_y, as well as a base-layer height z_0 are fitting parameters. Through the MATLAB nonlinear least-square fittings for different colors, the obtained x_0, y_0, σ_x, and σ_y are taken for analysis. We define an average position difference relative to the center of the blue one for the selected region, Δr as

$$\Delta r = \frac{1}{N}\sum_{i}^{N}\sqrt{\left(x_0^i - x_0^b\right)^2 + \left(y_0^i - y_0^b\right)^2}, \tag{4.9}$$

where i represents filtered green and red colors, b is the blue, and N represents the total number of colors. Finally, we graphically represent each color on the same plot with ellipses (Figure 4.6c),

$$\begin{cases} x(\theta) = x_0 + \Gamma_x \cdot \cos\theta \\ y(\theta) = y_0 + \Gamma_y \cdot \sin\theta \end{cases}, \tag{4.10}$$

here Γ_x and Γ_y are the intensity-weighted widths of the 2D Gaussian, defined as

$$\begin{cases} \Gamma_x = 2\sqrt{2\ln 2} \cdot \sigma_x \cdot (A - z_0) \\ \Gamma_y = 2\sqrt{2\ln 2} \cdot \sigma_y \cdot (A - z_0) \end{cases}. \tag{4.11}$$

Also, we define a relative delocalization parameter, D, where the Δr is referenced to the average size of the blue-colored size, R_b:

$$D = \frac{\Delta r}{R_b}, \tag{4.12}$$

where

$$R_b = \frac{\sqrt{2\ln 2}}{2}\left(\sigma_x^b + \sigma_y^b\right). \tag{4.13}$$

With this simple 2D Gaussian fitting analysis, we can clearly see the colocalization of different multilayer structure of CdTe NPLs, and we can predict their slight position difference beyond the camera resolution by analyzing the fitted Gaussian parameters. Some examples are shown below.

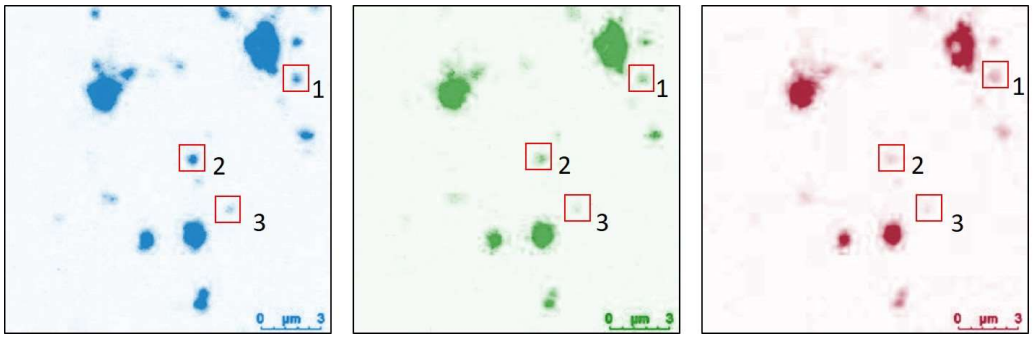

1

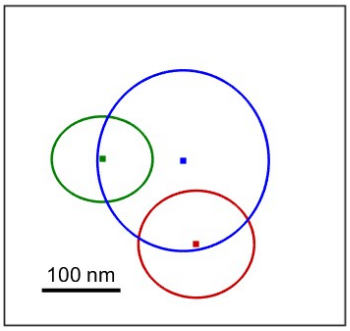

$\langle \Delta r \rangle = 109.1$ nm
$D = 0.5163$

2

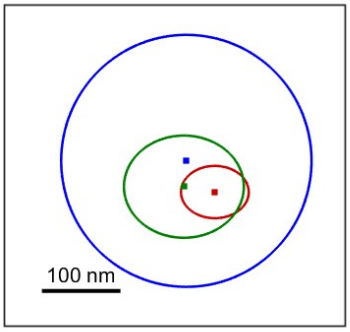

$\langle \Delta r \rangle = 45.46$ nm
$D = 0.2106$

3

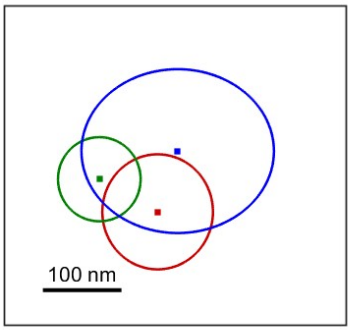

$\langle \Delta r \rangle = 96.67$ nm
$D = 0.5000$

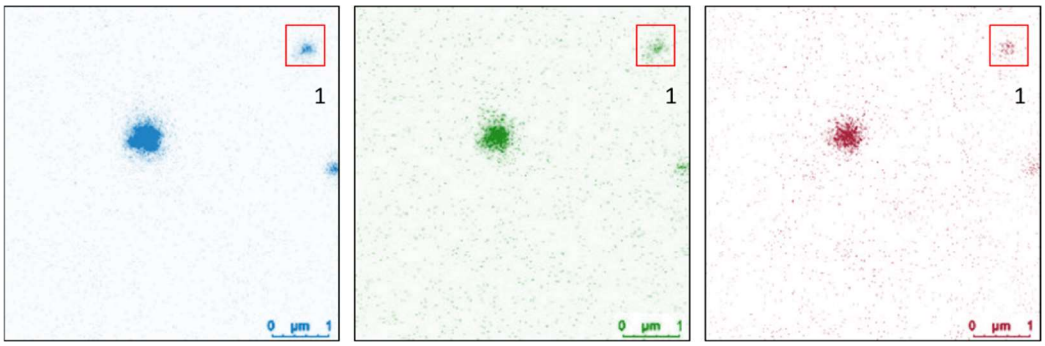

1

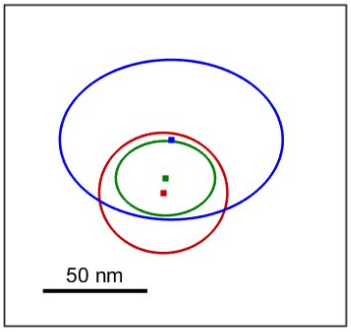

$\langle \Delta r \rangle = 23.61$ nm
$D = 0.2449$

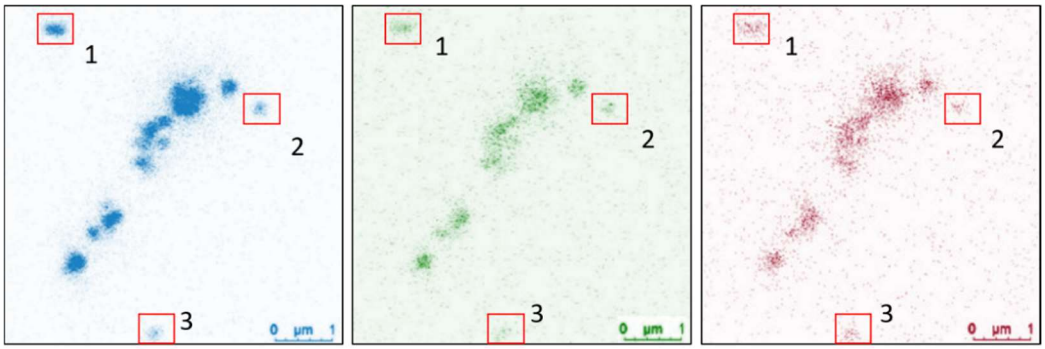

1

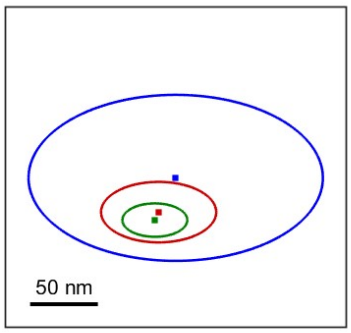

$\langle \Delta r \rangle = 33.17$ nm
$D = 0.2732$

2

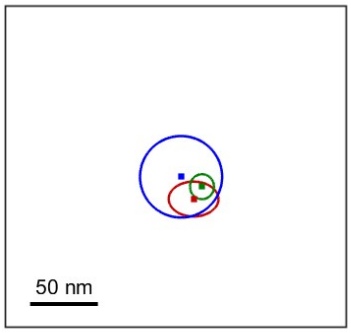

$\langle \Delta r \rangle = 18.51$ nm
$D = 0.2071$

3

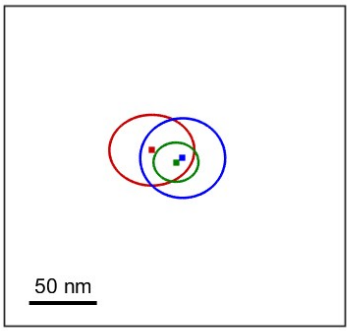

$\langle \Delta r \rangle = 14.71$ nm
$D = 0.1499$

Figure 4.7 PL images and 2D fitting results for 3ML and 4 ML hetero-structure. Emission regions are shown as different color: (480-520) nm (blue), (522-560) nm (green), (564-700) nm (red).

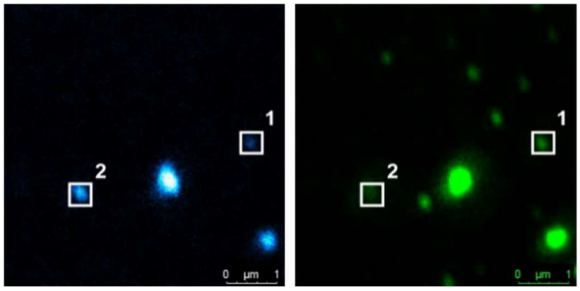

1

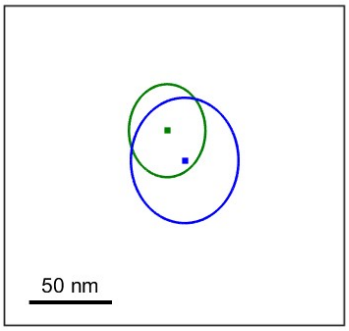

$\langle \Delta r \rangle = 21.90$ nm
$D = 0.2134$

2

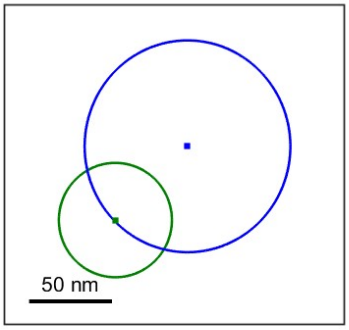

$\langle \Delta r \rangle = 64.45$ nm
$D = 0.5499$

Figure 4.8 PL images and 2D fitting results for mixture of 2 ML and 3 ML. Emission regions are shown as different colors: (400-450) nm (blue) and (480-520) nm (green). Sample was prepared from the aliquots taken during the growth of NPLs where emission of both 2ML and 3ML were present.

Spectra of aliquots during growth period

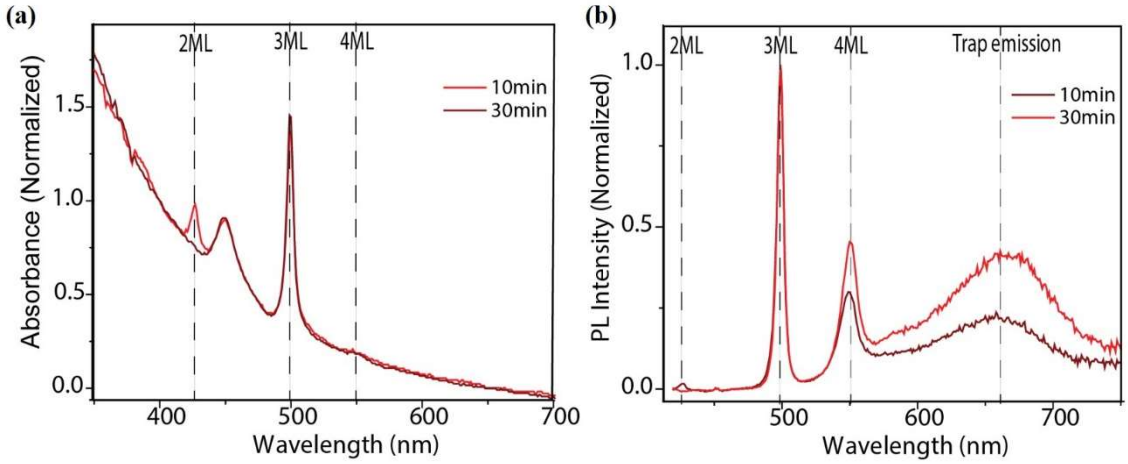

Figure 4.9 Spectra of aliquots during growth period. (a) Absorption and (b) emission spectra of CdTe NPLs at different time during the growth period at 210℃.

PL lifetime of CdTe NPLs

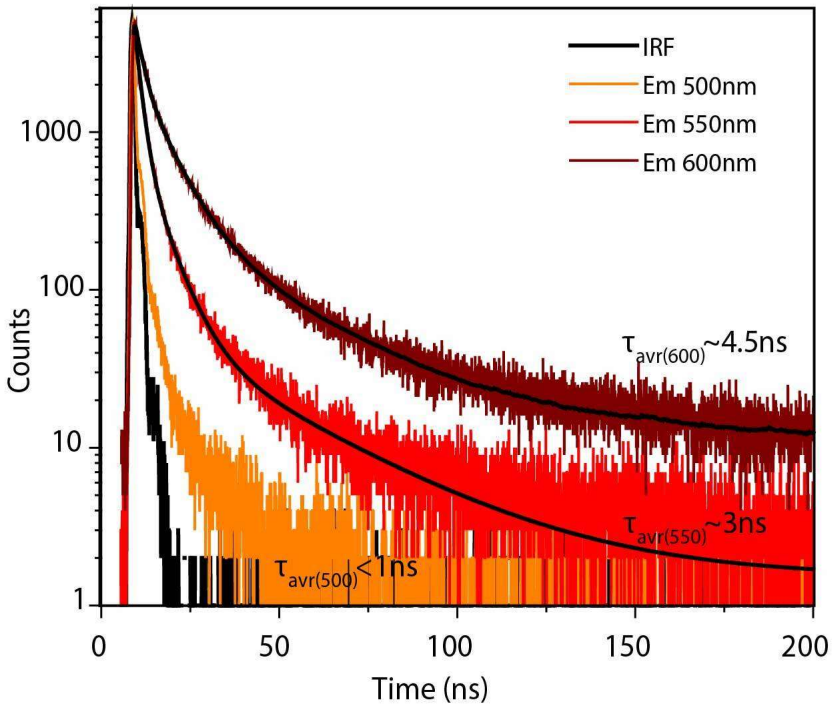

Figure 4.10 PL lifetime of CdTe NPLs.

Table 4.1 PL decay parameters of NPLs probed at different emission wavelength

Emission wavelength (nm)	$\tau_1(\alpha_1)$ ns	$\tau_2(\alpha_2)$ ns	$\tau_3(\alpha_3)$ ns	τ_{avr} ns
500				<1
550	1.7(0.80)	6.0(0.18)	32(0.02)	3.0
615	1.5(0.67)	7.6(0.29)	31(0.04)	4.5

*α_i's are amplitudes of the lifetime components. #τ_{avg} is defined as $\sum\alpha_i\tau_i / \sum\alpha_i$

Emission spectra of CdTe NPLs

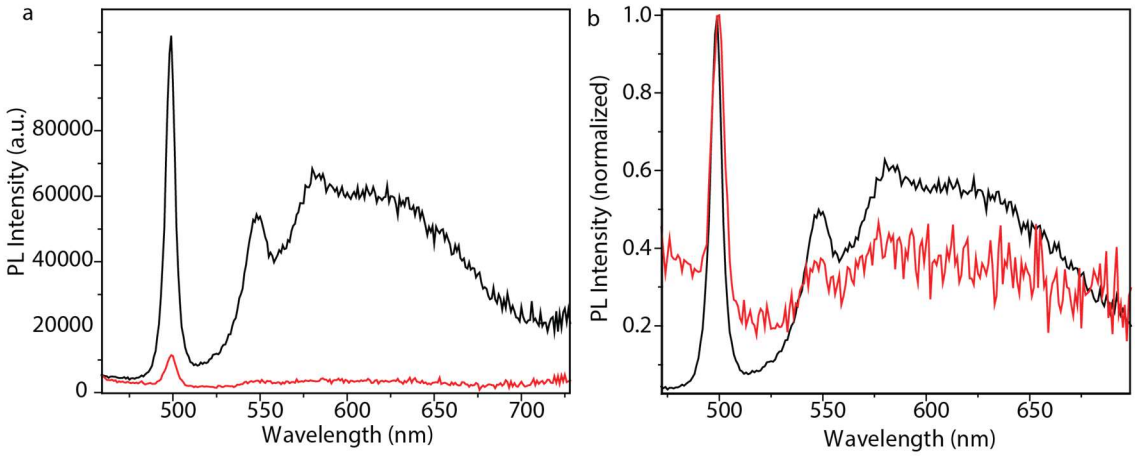

Figure 4.11 Emission spectra of CdTe NPLs. (a) Emission spectra of CdTe NPLs at different concentrations; high concentration (black line, OD ~ 0.1) and low concentration (red line, 10 times diluted). (b) Normalized emission spectra of them. All three emission peaks are present before and after dilution.

AFM image of CdTe NPLs

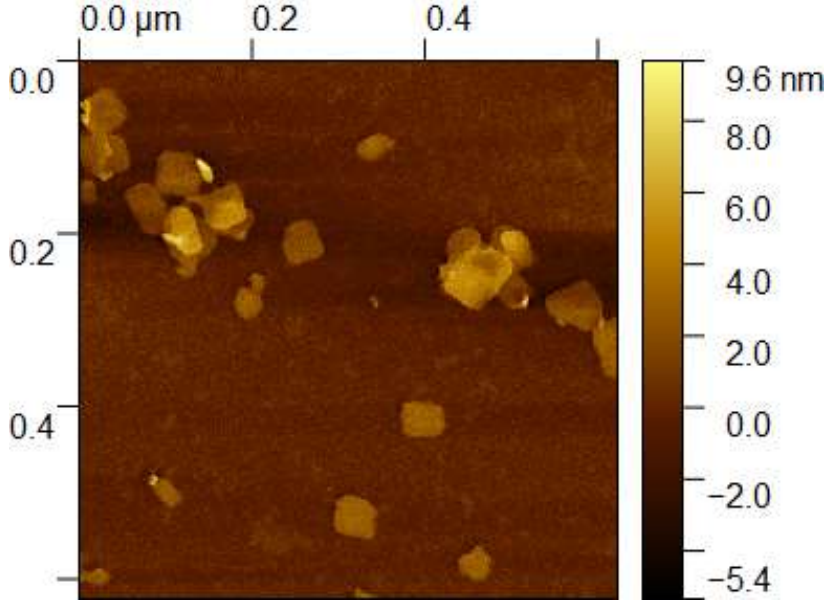

Figure 4.12 AFM image of CdTe NPLs.

PL blinking trace of CdTe NPLs

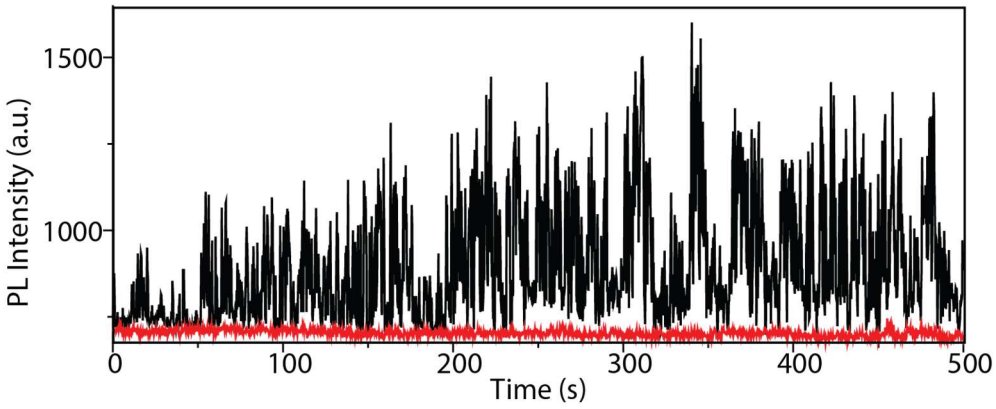

Figure 4.13 PL blinking trace of CdTe NPLs.

Transient absorption spectra of CdTe NPLs

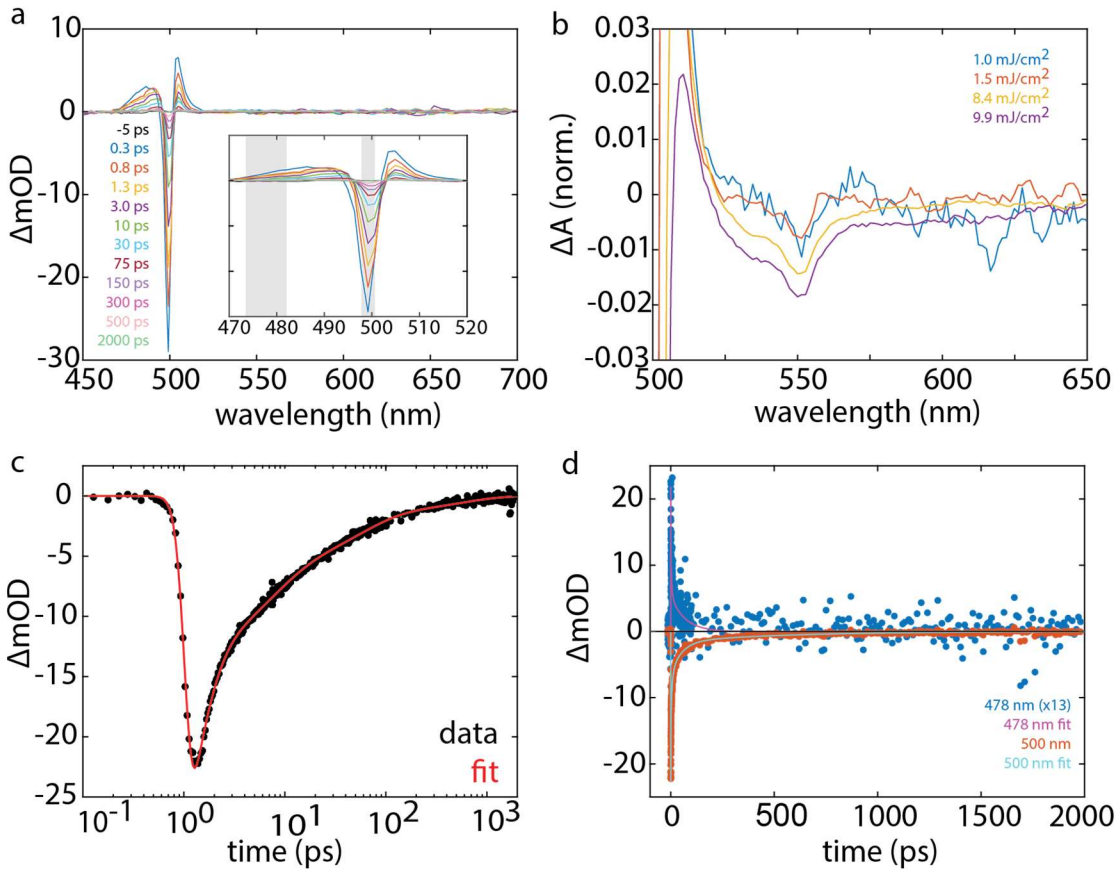

Figure 4.14 Transient absorption spectra showing the full probe bandwidth with the main transient feature enlarged in the inset (a) and the feature centered at 550 nm shown at various excitation fluences (b). The bleach recovery dynamics measured between 498 and 501 nm at 1.5 mJ/cm^2 fluence (c) follows multiexponential behavior, with three ultrafast components and one ~0.5 ns component. The same decay is compared to that of the excited state absorption measured between 474 and 482 nm on a linear time scale (d) to highlight the lack of the long-lived component in the positive feature, which corresponds to hot carriers. The probe regions over which the kinetic traces shown in panels (c) and (d) were averaged are shown as gray boxes in the inset of panel (a).

Tuning E_a and Temperature in KMC simulations

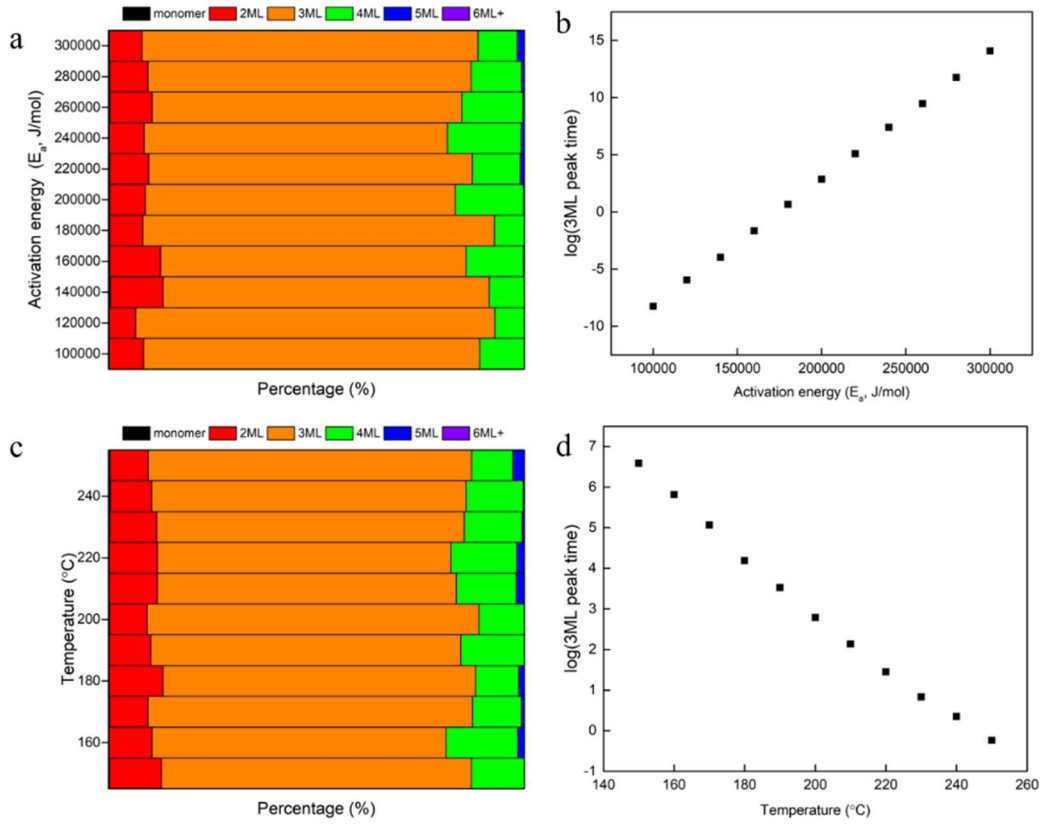

Figure 4.15 Tuning E_a and Temperature in simulations. (a) Population change of different monolayers of CdTe NPLs with activation energy, (b) change of 3ML peak time with change of activation energy, (c) population change with the change of different monolayers of CdTe NPLs with temperature and (d) change of peak time for 3ML CdTe NPLs with temperature.

REFERENCES

(1) Murray, C. B.; Norris, D. J.; Bawendi, M. G. Synthesis and Characterization of Nearly Monodisperse CdE (E = Sulfur, Selenium, Tellurium) Semiconductor Nanocrystallites. *J. Am. Chem. Soc.* **1993**, *115* (19), 8706–8715. https://doi.org/10.1021/ja00072a025.

(2) Peng, X.; Manna, L.; Yang, W.; Wickham, J.; Scher, E.; Kadavanich, A.; Alivisatos, A. P. Shape Control of CdSe Nanocrystals. *Nature* **2000**, *404* (6773), 59–61. https://doi.org/10.1038/35003535.

(3) Hu, Z.; O'Neill, R.; Lesyuk, R.; Klinke, C. Colloidal Two-Dimensional Metal Chalcogenides: Realization and Application of the Structural Anisotropy. *Acc. Chem. Res.* **2021**, *54* (20), 3792–3803. https://doi.org/10.1021/acs.accounts.1c00209.

(4) Sharma, M.; Delikanli, S.; Demir, H. V. Two-Dimensional CdSe-Based Nanoplatelets: Their Heterostructures, Doping, Photophysical Properties, and Applications. *Proc. IEEE* **2020**, *108* (5), 655–675. https://doi.org/10.1109/JPROC.2019.2944277.

(5) Zhang, J.; Sun, Y.; Ye, S.; Song, J.; Qu, J. Heterostructures in Two-Dimensional CdSe Nanoplatelets: Synthesis, Optical Properties, and Applications. *Chem. Mater.* **2020**, *32* (22), 9490–9507. https://doi.org/10.1021/acs.chemmater.0c02593.

(6) Tenney, S. M.; Tan, L. A.; Sonnleitner, M. L.; Sica, A. V.; Shin, A. J.; Ronquillo, R.; Ahmed, T.; Atallah, T. L.; Caram, J. R. Mesoscale Quantum-Confined Semiconductor Nanoplatelets through Seeded Growth. *Chem. Mater.* **2022**, *34* (13), 6048–6056. https://doi.org/10.1021/acs.chemmater.2c01144.

(7) Naeem, A.; Masia, F.; Christodoulou, S.; Moreels, I.; Borri, P.; Langbein, W. Giant Exciton Oscillator Strength and Radiatively Limited Dephasing in Two-Dimensional Platelets. *Phys. Rev. B* **2015**, *91* (12), 121302. https://doi.org/10.1103/PhysRevB.91.121302.

(8) Riedinger, A.; Ott, F. D.; Mule, A.; Mazzotti, S.; Knüsel, P. N.; Kress, S. J. P.; Prins, F.; Erwin, S. C.; Norris, D. J. An Intrinsic Growth Instability in Isotropic Materials Leads to Quasi-Two-Dimensional Nanoplatelets - SI. *Nat. Mater.* **2017**, *16* (7), 743–748. https://doi.org/10.1038/nmat4889.

(9) Rowland, C. E.; Fedin, I.; Zhang, H.; Gray, S. K.; Govorov, A. O.; Talapin, D. V.; Schaller, R. D. Picosecond Energy Transfer and Multiexciton Transfer Outpaces Auger Recombination in Binary CdSe Nanoplatelet Solids. *Nat. Mater.* **2015**, *14* (5), 484–489. https://doi.org/10.1038/nmat4231.

(10) Yeltik, A.; Delikanli, S.; Olutas, M.; Kelestemur, Y.; Guzelturk, B.; Demir, H. V. Experimental Determination of the Absorption Cross-Section and Molar Extinction Coefficient of Colloidal CdSe Nanoplatelets. *J. Phys. Chem. C* **2015**, *119* (47), 26768–26775. https://doi.org/10.1021/acs.jpcc.5b09275.

(11) Yu, J.; Chen, R. Optical Properties and Applications of Two-dimensional CdSe Nanoplatelets. *InfoMat* **2020**, *2* (5), 905–927. https://doi.org/10.1002/inf2.12106.

(12) Lhuillier, E.; Pedetti, S.; Ithurria, S.; Heuclin, H.; Nadal, B.; Robin, A.; Patriarche, G.; Lequeux, N.; Dubertret, B. Electrolyte-Gated Field Effect Transistor to Probe the Surface Defects and Morphology in Films of Thick CdSe Colloidal Nanoplatelets. *ACS Nano* **2014**, *8* (4), 3813–3820. https://doi.org/10.1021/nn500538n.

(13) She, C.; Fedin, I.; Dolzhnikov, D. S.; Demortière, A.; Schaller, R. D.; Pelton, M.; Talapin, D. V. Low-Threshold Stimulated Emission Using Colloidal Quantum Wells. *Nano Lett.* **2014**, *14* (5), 2772–2777. https://doi.org/10.1021/nl500775p.

(14) She, C.; Fedin, I.; Dolzhnikov, D. S.; Dahlberg, P. D.; Engel, G. S.; Schaller, R. D.; Talapin, D. V. Red, Yellow, Green, and Blue Amplified Spontaneous Emission and Lasing Using

Colloidal CdSe Nanoplatelets. *ACS Nano* **2015**, *9* (10), 9475–9485. https://doi.org/10.1021/acsnano.5b02509.

(15) Guzelturk, B.; Kelestemur, Y.; Olutas, M.; Delikanli, S.; Demir, H. V. Amplified Spontaneous Emission and Lasing in Colloidal Nanoplatelets. *ACS Nano* **2014**, *8* (7), 6599–6605. https://doi.org/10.1021/nn5022296.

(16) Ithurria, S.; Bousquet, G.; Dubertret, B. Continuous Transition from 3D to 1D Confinement Observed during the Formation of CdSe Nanoplatelets. *J. Am. Chem. Soc.* **2011**, *133* (9), 3070–3077. https://doi.org/10.1021/ja110046d.

(17) Ott, F. D.; Riedinger, A.; Ochsenbein, D. R.; Knüsel, P. N.; Erwin, S. C.; Mazzotti, M.; Norris, D. J. Ripening of Semiconductor Nanoplatelets. *Nano Lett.* **2017**, *17* (11), 6870–6877. https://doi.org/10.1021/acs.nanolett.7b03191.

(18) Khan, A. H.; Bertrand, G. H. V.; Teitelboim, A.; Sekhar M., C.; Polovitsyn, A.; Brescia, R.; Planelles, J.; Climente, J. I.; Oron, D.; Moreels, I. CdSe/CdS/CdTe Core/Barrier/Crown Nanoplatelets: Synthesis, Optoelectronic Properties, and Multiphoton Fluorescence Upconversion. *ACS Nano* **2020**, *14* (4), 4206–4215. https://doi.org/10.1021/acsnano.9b09147.

(19) Pedetti, S.; Ithurria, S.; Heuclin, H.; Patriarche, G.; Dubertret, B. Type-II CdSe/CdTe Core/Crown Semiconductor Nanoplatelets. *J. Am. Chem. Soc.* **2014**, *136* (46), 16430–16438. https://doi.org/10.1021/ja509307m.

(20) Mahler, B.; Nadal, B.; Bouet, C.; Patriarche, G.; Dubertret, B. Core/Shell Colloidal Semiconductor Nanoplatelets. *J. Am. Chem. Soc.* **2012**, *134* (45), 18591–18598. https://doi.org/10.1021/ja307944d.

(21) Diroll, B. T.; Guzelturk, B.; Po, H.; Dabard, C.; Fu, N.; Makke, L.; Lhuillier, E.; Ithurria, S. 2D II-VI Semiconductor Nanoplatelets: From Material Synthesis to Optoelectronic Integration.

Chem. Rev. **2023**, *123* (7), 3543–3624. https://doi.org/10.1021/acs.chemrev.2c00436.

(22) Moghaddam, N.; Dabard, C.; Dufour, M.; Po, H.; Xu, X.; Pons, T.; Lhuillier, E.; Ithurria, S. Surface Modification of CdE (E: S, Se, and Te) Nanoplatelets to Reach Thicker Nanoplatelets and Homostructures with Confinement-Induced Intraparticle Type I Energy Level Alignment. *J. Am. Chem. Soc.* **2021**, *143* (4), 1863–1872. https://doi.org/10.1021/jacs.0c10336.

(23) Dufour, M.; Qu, J.; Greboval, C.; Méthivier, C.; Lhuillier, E.; Ithurria, S. Halide Ligands To Release Strain in Cadmium Chalcogenide Nanoplatelets and Achieve High Brightness. *ACS Nano* **2019**, *13* (5), 5326–5334. https://doi.org/10.1021/acsnano.8b09794.

(24) Pan, J.; Qian, Y. Synthesis of Cadmium Chalcogenide Nanotubes at Room Temperature. *Mater. Lett.* **2012**, *85*, 132–134. https://doi.org/10.1016/j.matlet.2012.07.012.

(25) Sun, J.; Buhro, W. E.; Wang, L.-W.; Schrier, J. Electronic Structure and Spectroscopy of Cadmium Telluride Quantum Wires. *Nano Lett.* **2008**, *8* (9), 2913–2919. https://doi.org/10.1021/nl801737m.

(26) Tang, Z.; Zhang, Z.; Wang, Y.; Glotzer, S. C.; Kotov, N. A. Self-Assembly of CdTe Nanocrystals into Free-Floating Sheets. *Science (80-.).* **2006**, *314* (5797), 274–278. https://doi.org/10.1126/science.1128045.

(27) Xie, X.; Kwok, S.-Y.; Lu, Z.; Liu, Y.; Cao, Y.; Luo, L.; Zapien, J. A.; Bello, I.; Lee, C.-S.; Lee, S.-T.; Zhang, W. Visible–NIR Photodetectors Based on CdTe Nanoribbons. *Nanoscale* **2012**, *4* (9), 2914. https://doi.org/10.1039/c2nr30277b.

(28) Sun, H.; Buhro, W. E. Contrasting Ligand-Exchange Behavior of Wurtzite and Zinc-Blende Cadmium Telluride Nanoplatelets. *Chem. Mater.* **2021**, *33* (5), 1683–1697. https://doi.org/10.1021/acs.chemmater.0c04247.

(29) Sun, H.; Wang, F.; Buhro, W. E. Tellurium Precursor for Nanocrystal Synthesis:

Tris(Dimethylamino)Phosphine Telluride. *ACS Nano* **2018**, *12* (12), 12393–12400. https://doi.org/10.1021/acsnano.8b06468.

(30) Wang, F.; Javaid, S.; Chen, W.; Wang, A.; Buntine, M. A.; Jia, G. Synthesis of Atomically Thin CdTe Nanoplatelets by Using Polytelluride Tellurium Precursors. *Aust. J. Chem.* **2021**, *74* (3), 179. https://doi.org/10.1071/CH20174.

(31) Yu, W. W.; Wang, Y. A.; Peng, X. Formation and Stability of Size-, Shape-, and Structure-Controlled CdTe Nanocrystals: Ligand Effects on Monomers and Nanocrystals. *Chem. Mater.* **2003**, *15* (22), 4300–4308. https://doi.org/10.1021/cm034729t.

(32) Paufler, P. Landolt-Börnstein. Numerical Data and Functional Relationships in Science and Technology. New Series. Group III: Crystal and Solid State Physics. Vol. 22: Semiconductors. Subvolume a: Intrinsic Properties of Group IV Elements and III-V, II-VI and I-VII Co. *Cryst. Res. Technol.* **1988**, *23* (10–11), 1360–1360. https://doi.org/10.1002/crat.2170231029.

(33) Gur, I.; Fromer, N. A.; Chen, C.-P.; Kanaras, A. G.; Alivisatos, A. P. Hybrid Solar Cells with Prescribed Nanoscale Morphologies Based on Hyperbranched Semiconductor Nanocrystals. *Nano Lett.* **2007**, *7* (2), 409–414. https://doi.org/10.1021/nl062660t.

(34) Ithurria, S.; Tessier, M. D.; Mahler, B.; Lobo, R. P. S. M.; Dubertret, B.; Efros, A. L. Colloidal Nanoplatelets with Two-Dimensional Electronic Structure. *Nat. Mater.* **2011**, *10* (12), 936–941. https://doi.org/10.1038/nmat3145.

(35) Pedetti, S.; Nadal, B.; Lhuillier, E.; Mahler, B.; Bouet, C.; Abécassis, B.; Xu, X.; Dubertret, B. Optimized Synthesis of CdTe Nanoplatelets and Photoresponse of CdTe Nanoplatelets Films. *Chem. Mater.* **2013**, *25* (12), 2455–2462. https://doi.org/10.1021/cm4006844.

(36) Chu, A.; Livache, C.; Ithurria, S.; Lhuillier, E. Electronic Structure Robustness and Design Rules for 2D Colloidal Heterostructures. *J. Appl. Phys.* **2018**, *123* (3).

https://doi.org/10.1063/1.5003289.

(37) Anand, A.; Zaffalon, M. L.; Cova, F.; Pinchetti, V.; Khan, A. H.; Carulli, F.; Brescia, R.; Meinardi, F.; Moreels, I.; Brovelli, S. Optical and Scintillation Properties of Record-Efficiency CdTe Nanoplatelets toward Radiation Detection Applications. *Nano Lett.* **2022**, *22* (22), 8900–8907. https://doi.org/10.1021/acs.nanolett.2c02975.

(38) AL-Shnani, F.; Mutyala, C. S.; Rodà, C.; Moreels, I. Fluorescence Quantum Efficiency Enhancement in Size-Controlled 3.5 Monolayer Cadmium Telluride Nanoplatelets. *Chem. Mater.* **2023**, *35* (16), 6258–6265. https://doi.org/10.1021/acs.chemmater.3c00690.

(39) Sui, X.; Gao, X.; Wu, X.; Li, C.; Yang, X.; Du, W.; Ding, Z.; Jin, S.; Wu, K.; Sum, T. C.; Gao, P.; Liu, J.; Wei, X.; Zhang, J.; Zhang, Q.; Tang, Z.; Liu, X. Zone-Folded Longitudinal Acoustic Phonons Driving Self-Trapped State Emission in Colloidal CdSe Nanoplatelet Superlattices. *Nano Lett.* **2021**, *21* (10), 4137–4144. https://doi.org/10.1021/acs.nanolett.0c04169.

(40) Hinterding, S. O. M.; Salzmann, B. B. V.; Vonk, S. J. W.; Vanmaekelbergh, D.; Weckhuysen, B. M.; Hutter, E. M.; Rabouw, F. T. Single Trap States in Single CdSe Nanoplatelets. *ACS Nano* **2021**, *15* (4), 7216–7225. https://doi.org/10.1021/acsnano.1c00481.

(41) van der Stam, W.; de Graaf, M.; Gudjonsdottir, S.; Geuchies, J. J.; Dijkema, J. J.; Kirkwood, N.; Evers, W. H.; Longo, A.; Houtepen, A. J. Tuning and Probing the Distribution of Cu + and Cu 2+ Trap States Responsible for Broad-Band Photoluminescence in CuInS 2 Nanocrystals. *ACS Nano* **2018**, *12* (11), 11244–11253. https://doi.org/10.1021/acsnano.8b05843.

(42) Kushwaha, M.; Srivastava, A. P.; Singh, M. K. Balanced Emission from Band-Edge and Trap States of Ultra Stable CdSe Nanocrystals Synthesized by Aqueous Route. *Mater. Lett.* **2013**, *109*, 23–26. https://doi.org/10.1016/j.matlet.2013.07.028.

(43) Tenney, S. M.; Tan, L. A.; Tan, X.; Sonnleitner, M. L.; Coffey, B.; Williams, J. A.;

Ronquillo, R.; Atallah, T. L.; Ahmed, T.; Caram, J. R. Efficient 2D to 0D Energy Transfer in HgTe Nanoplatelet-Quantum Dot Heterostructures through High-Speed Exciton Diffusion. *J. Phys. Chem. Lett.* **2023**, *14* (42), 9456–9463. https://doi.org/10.1021/acs.jpclett.3c02168.

(44) Peric, N.; Lambert, Y.; Singh, S.; Khan, A. H.; Franchina Vergel, N. A.; Deresmes, D.; Berthe, M.; Hens, Z.; Moreels, I.; Delerue, C.; Grandidier, B.; Biadala, L. Van Hove Singularities and Trap States in Two-Dimensional CdSe Nanoplatelets. *Nano Lett.* **2021**, *21* (4), 1702–1708. https://doi.org/10.1021/acs.nanolett.0c04509.

(45) Morgan, D. P.; Maddux, C. J. A.; Kelley, D. F. Transient Absorption Spectroscopy of CdSe Nanoplatelets. *J. Phys. Chem. C* **2018**, *122* (41), 23772–23779. https://doi.org/10.1021/acs.jpcc.8b07733.

(46) Pelton, M.; Ithurria, S.; Schaller, R. D.; Dolzhnikov, D. S.; Talapin, D. V. Carrier Cooling in Colloidal Quantum Wells. *Nano Lett.* **2012**, *12* (12), 6158–6163. https://doi.org/10.1021/nl302986y.

(47) Voter, A. F. INTRODUCTION TO THE KINETIC MONTE CARLO METHOD. In *Radiation Effects in Solids*; Sickafus, K. E., Kotomin, E. A., Uberuaga, B. P., Eds.; NATO Science Series; Springer Netherlands: Dordrecht, 2007; Vol. 235, pp 1–23. https://doi.org/10.1007/978-1-4020-5295-8_1.

(48) Xiang, X.; Wang, L.; Zhang, J.; Cheng, B.; Yu, J.; Macyk, W. Cadmium Chalcogenide (CdS, CdSe, CdTe) Quantum Dots for Solar-to-Fuel Conversion. *Adv. Photonics Res.* **2022**, *3* (11). https://doi.org/10.1002/adpr.202200065.

(49) Howell, R. C.; Proffen, T.; Conradson, S. D. Pair Distribution Function and Structure Factor of Spherical Particles. *Phys. Rev. B* **2006**, *73* (9), 094107. https://doi.org/10.1103/PhysRevB.73.094107.

(50) Gamez-Mendoza, L.; Terban, M. W.; Billinge, S. J. L.; Martinez-Inesta, M. Modelling and Validation of Particle Size Distributions of Supported Nanoparticles Using the Pair Distribution Function Technique. *J. Appl. Crystallogr.* **2017**, *50* (3), 741–748. https://doi.org/10.1107/S1600576717003715.

(51) Crocker, J. C.; Grier, D. G. Methods of Digital Video Microscopy for Colloidal Studies. *J. Colloid Interface Sci.* **1996**, *179* (1), 298–310. https://doi.org/10.1006/jcis.1996.0217.

(52) Antolini, C.; Jacoby, D. J.; Tiano, S. M.; Otolski, C. J.; Doumy, G.; March, A. M.; Walko, D. A.; Goodwill, J. E.; Hayes, D. Ten-Fold Solvent Kinetic Isotope Effect for the Nonradiative Relaxation of the Aqueous Ferrate(VI) Ion. *J. Phys. Chem. A* **2023**, *127* (49), 10425–10434. https://doi.org/10.1021/acs.jpca.3c06042.

(53) Shoup, D.; Szabo, A. Role of Diffusion in Ligand Binding to Macromolecules and Cell-Bound Receptors. *Biophys. J.* **1982**, *40* (1), 33–39. https://doi.org/10.1016/S0006-3495(82)84455-X.

(54) Bortz, A. B.; Kalos, M. H.; Lebowitz, J. L. A New Algorithm for Monte Carlo Simulation of Ising Spin Systems. *J. Comput. Phys.* **1975**, *17* (1), 10–18. https://doi.org/10.1016/0021-9991(75)90060-1.

Chapter 5

Future Work and Perspectives

This chapter contains unpublished work and considerations by Xuanheng Tan, Belle Coffey, Caleb Pike, Linus Murphy, Lucas Tecot and Justin Caram. The results are preliminary and based on available data.

5.1 Machine Learning Assisted Study of Anisotropic Growth of Nanoplatelets (NPLs)

With the significant increase in both computational power and availability of experimental data, the application of method from data science has become more and more common in the analysis and evaluation in the realm of chemistry.[1–4] This approach of data-driven science has been described as "the 4th paradigm" of science, with 3 precedents being empirical science (experiments), theoretical science (physical laws, mechanics and thermodynamics, etc.) and computational science (density functional theory, molecular dynamics, etc.).[5] One of many data science methods that recently received a huge amount of attention is machine learning (ML), a subfield of artificial intelligence (AI) that develop statistical algorithms to learn from available data and make accurate predictions through iterative self-optimization process.[6,7] There are 3 main categories of ML: supervised learning, unsupervised learning and reinforcement learning.[8] Supervised learning, which attempts to find the unknown function that connects known inputs (e.g. physical and chemical properties) with unknown outputs (e.g. outcomes of chemical reactions), is by far the most common type of algorithm relevant to materials chemistry.

Considering 98 naturally occurring elements of the periodic table as well as variations in stoichiometry and atomic arrangement (i.e., crystal structure), the total number of possible materials is estimated to be 10^{100}, exceeding the total number of atoms in the known universe.[9] It

becomes an impossible task to use brute-force in either experiments or *ab initio* calculations to study all possible materials. In this case, ML suit to be the candidate tool of exploration.

In fact, ML has been proved to be beneficial to researchers in the field of materials chemistry. A commonly used strategy is to combine quantum chemistry computation with ML methods. Faber et al. applied ML model based on kernel ridge regression (KRR) to obtain formation energies of 2 million elpasolites (ABC_2D_6) crystals with the energy differences between the sum of atomic energies extracted from materials data base and crystal energies calculated by density functional theory (DFT), and they predicted 90 new components for the elpasolite crystal structure.[10] Lee et al. made a data set composed of 270 randomly chosen inorganic compounds by performing first-principle calculation of band gap energies using the projector-augmented wave (PAW) method, and applied ML regression methods to predict band gap energies for other materials.[11]

Another approach is to take advantage of the comprehensive database of materials to make predictions on the properties of possible new materials and outcome of related reactions. Kim et al. trained a ML model based on Open Quantum Materials Database (OQMD) and identified 53 new stable structures for quaternary Heusler compounds.[12] Graser et al. utilized the Pearson's Crystal Data database and random forest (RF) ML algorithm to make predictions on the crystal structures of more than 20000 compounds.[13] Frenkel and coworkers used experimental data of small angle X-ray scattering (SAXS) and X-ray absorption near-edge structure (XANES) to train neural network (NN) models for elucidating structures of Cu nanoassemblies under catalytic conditions.[14] Muraoka et al. analyzed the synthetic records of zeolites and used various ML models to establish correlation between synthetic parameters and structural properties.[15] Similarly,

Moosavi et al. applied ML to capture chemical intuitions and optimize synthetic conditions of metal-organic frameworks (MOFs).[16]

Due to the advantages of the machine learning method and previous success achieved by it, it is potentially a very good approach to study the complex system of nanoplatelets synthesis, which contains factors including precursors, solvent, temperature, injection rate, etc. More specifically, based on our preliminary results of kinetic Monte Carlo (KMC) simulations, our goal here is to use machine learning method to study the relationship between energetic parameters (E_a, E_b, E_c) and ripening and size distribution of NPLs in synthesis. However, several challenges exist for directly using experimental data as the basis of training data set for machine learning method: first, the data collection for synthesis reaction is not trivial, since to track the reaction progress usually aliquots are taken for spectral measurements and imaging; second, relationship between the energetic parameters and actual properties of materials (e.g. precursors, capping site of ligands, steric hinderance of ligands, etc.) is not completely understood. We thus propose to take a slightly different approach of implementing machine learning method (Figure 5.1). With the already established workflow of KMC simulations, we first use machine learning method such as normalizing flows (NF) or convolutional neural network (CNN) to study on the training set generated from simulations with known and well-defined parameters.[17–20] Note that the data we feed to the machine have the same format as experimental observations (e.g. absorption spectra, TEM images, etc.). Once the training of model is done, we then apply the model to real data set collected in experiments to reversely extract the real energetic parameters. This could provide us insights on tackle the challenges of uncertain relationship without dealing with the difficulties in data collection. With high-throughput experimentations becoming increasingly available for

chemical reactions, this approach can be further extended to study more synthetic conditions and be used to optimize synthetic routes of NPLs with desired properties.

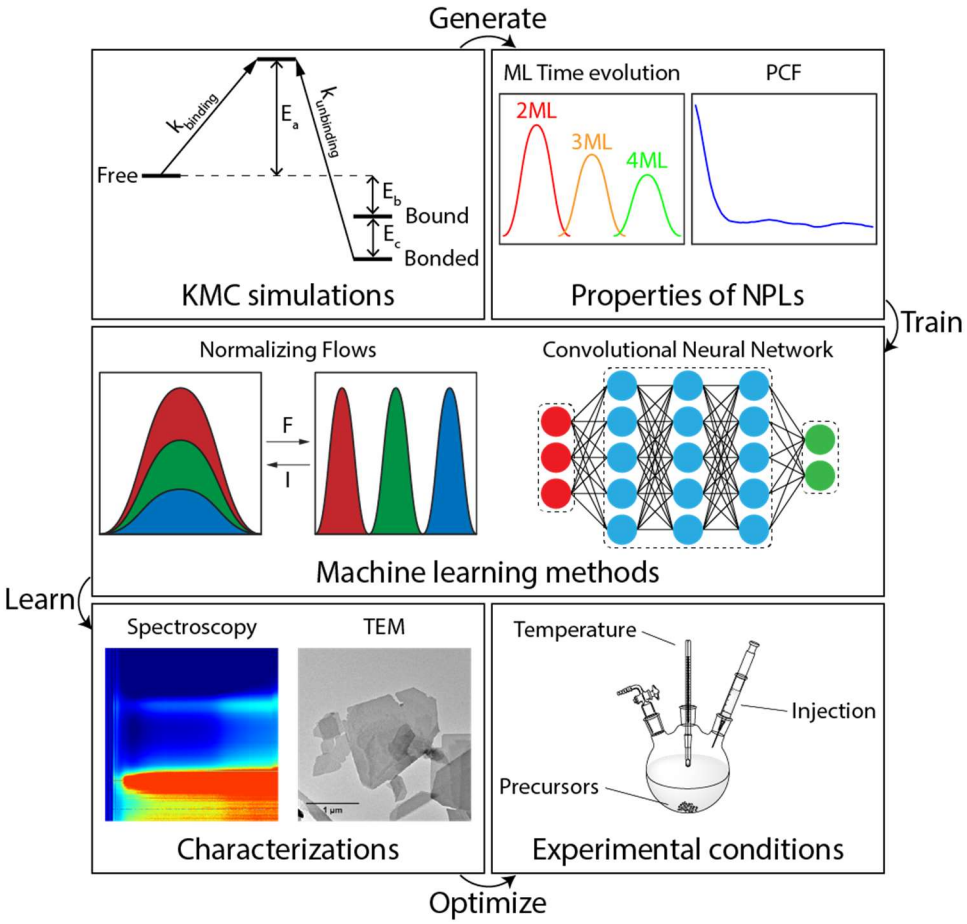

Figure 5.1 A workflow of applying machine learning method to the study of NPLs growth. We start with already established KMC simulations to generate training data set for machine learning model, and then use trained model to learn experimental observations and eventually optimize synthetic conditions.

5.2 Growth Mechanisms of HgTe Quantum Dots (QDs) and Evolution of Size Distribution

Synthetic control of the size of HgTe QDs still draw attention of researchers in the field, especially for small HgTe QDs of which direct colloidal synthesis has not been realized until recently.[21] It is worth noting that the reaction rate of HgTe QDs synthesis is so fast that the growth even take place at room temperature, as we previously observed in solution of HgTe NPLs.[22] The most direct characterization of this type of growth/ripening is the emission features of QDs, due

to the red shift in spectrum when their size increases. In addition to the peak position of emission spectra, the full width half maxima (FWHM) is also an important measure to estimate the polydispersity of the QDs.[23] By keeping track of the evolution of size distribution over time, we propose that it is possible to further understand the mechanism of growth/ripening.

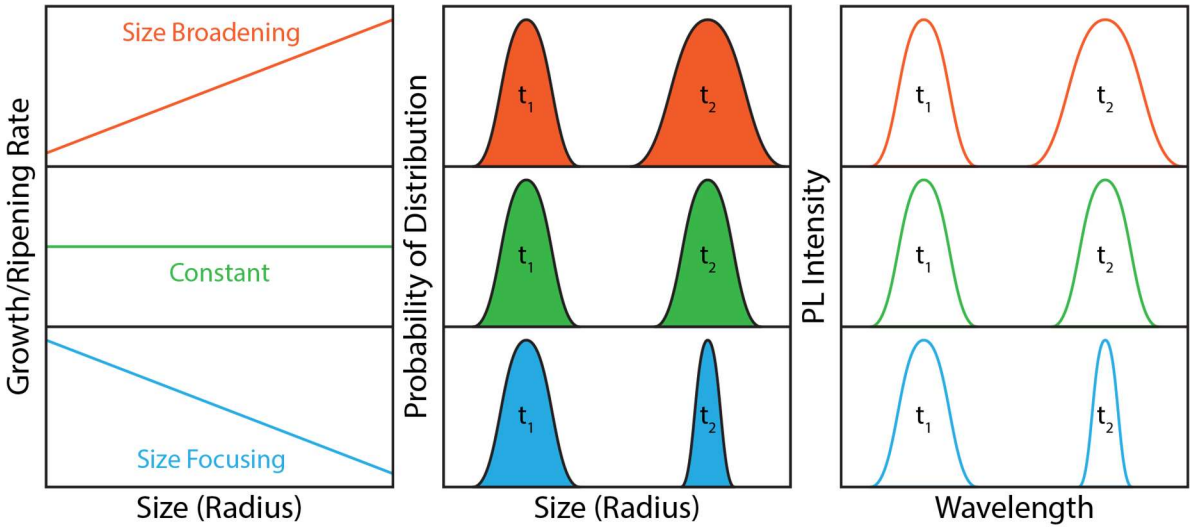

Figure 5.2 Connecting mechanisms of growth with time evolution of emission spectra.

There has been quite some work on the evolution of size distribution of QDs during the process of synthetic reactions. In fact, modeling with simple kinetics has been shown to be able to describe the average size and size distributions of QDs in some synthetic experiments with decent accuracy.[24] More specifically, in the synthesis of InAs QDs, it has been shown that through the tuning of injection strategy, the growth phase of QDs demonstrate very different behaviors, namely the size broadening vs. size focusing situations.[25] The outcome of size broadening is very similar to the concept of Ostwald ripening, where small particles are gradually dissolved to assist the growth of larger particles.[26] This potentially increase the polydispersity of synthesized QDs, while QDs demonstrating size-focusing results in good performances such as a high quantum yield.[27] Our goal here is to study the growth/ripening mechanisms as extensively as possible to generate

profiles of evolution of size distributions, which can then be used to examine existing results of QDs synthesis and help us reversely identify the correct picture of growth rate – size relationships.

The proposed workflow of linking the growth mechanisms and evolution of emission FWHM is described as follow (Figure 5.2). First, we start from the modeling perspective to simulate the change of size distribution with different size dependence of growth rate. For some models with already solved mathematical relationships we can directly use their conclusions, but the growth rate could take a variety of functional forms in regards to the size of QDs. Second, with generated size distribution from simulations, we can convolute it with the intrinsic linewidth of emission spectrum to obtain the "real" linewidth, assuming the broadening arises only from the polydispersity of QDs. This can be done with the Brus' equation (1.3) in chapter 1, with meticulous experiments to access a reasonable sizing curve for HgTe QDs. Lastly, we can compare the theoretical evolution of spectra with actual experimental observations to identify the best model or mechanism of QDs growth. It is also possible to work reversely to extract size distribution from emission spectra, but it requires more difficult deconvolution of spectrum. Other than emission spectra, we are also considering an easier unbiased algorithm of treating TEM images, which could provide us with more accurate information on the size distribution. With the deeper understanding of growth/ripening gained from this method, we can have better control on the synthetic conditions to achieve monodisperse QDs with desired sizes.

REFERENCES

(1) Gasteiger, J.; Zupan, J. Neural Networks in Chemistry. *Angew. Chemie Int. Ed. English* **1993**, *32* (4), 503–527. https://doi.org/10.1002/anie.199305031.

(2) Butler, K. T.; Davies, D. W.; Cartwright, H.; Isayev, O.; Walsh, A. Machine Learning for Molecular and Materials Science. *Nature* **2018**, *559* (7715), 547–555. https://doi.org/10.1038/s41586-018-0337-2.

(3) Westermayr, J.; Gastegger, M.; Schütt, K. T.; Maurer, R. J. Perspective on Integrating Machine Learning into Computational Chemistry and Materials Science. *J. Chem. Phys.* **2021**, *154* (23). https://doi.org/10.1063/5.0047760.

(4) Artrith, N.; Butler, K. T.; Coudert, F.-X.; Han, S.; Isayev, O.; Jain, A.; Walsh, A. Best Practices in Machine Learning for Chemistry. *Nat. Chem.* **2021**, *13* (6), 505–508. https://doi.org/10.1038/s41557-021-00716-z.

(5) Agrawal, A.; Choudhary, A. Perspective: Materials Informatics and Big Data: Realization of the "Fourth Paradigm" of Science in Materials Science. *APL Mater.* **2016**, *4* (5). https://doi.org/10.1063/1.4946894.

(6) Jordan, M. I.; Mitchell, T. M. Machine Learning: Trends, Perspectives, and Prospects. *Science (80-.).* **2015**, *349* (6245), 255–260. https://doi.org/10.1126/science.aaa8415.

(7) Mahesh, B. Machine Learning Algorithms - A Review. *Int. J. Sci. Res.* **2020**, *9* (1), 381–386. https://doi.org/10.21275/ART20203995.

(8) Mohri, M.; Rostamizadeh, A.; Talwalkar, A. *Foundations of Machine Learning*, Second Edi.; The MIT Press: Cambridge, MA, 2018.

(9) Walsh, A. The Quest for New Functionality. *Nat. Chem.* **2015**, *7* (4), 274–275. https://doi.org/10.1038/nchem.2213.

(10) Faber, F. A.; Lindmaa, A.; von Lilienfeld, O. A.; Armiento, R. Machine Learning Energies of 2 Million Elpasolite (ABC2D6) Crystals. *Phys. Rev. Lett.* **2016**, *117* (13), 135502. https://doi.org/10.1103/PhysRevLett.117.135502.

(11) Lee, J.; Seko, A.; Shitara, K.; Nakayama, K.; Tanaka, I. Prediction Model of Band Gap for Inorganic Compounds by Combination of Density Functional Theory Calculations and Machine Learning Techniques. *Phys. Rev. B* **2016**, *93* (11), 115104. https://doi.org/10.1103/PhysRevB.93.115104.

(12) Kim, K.; Ward, L.; He, J.; Krishna, A.; Agrawal, A.; Wolverton, C. Machine-Learning-Accelerated High-Throughput Materials Screening: Discovery of Novel Quaternary Heusler Compounds. *Phys. Rev. Mater.* **2018**, *2* (12), 123801. https://doi.org/10.1103/PhysRevMaterials.2.123801.

(13) Graser, J.; Kauwe, S. K.; Sparks, T. D. Machine Learning and Energy Minimization Approaches for Crystal Structure Predictions: A Review and New Horizons. *Chem. Mater.* **2018**, *30* (11), 3601–3612. https://doi.org/10.1021/acs.chemmater.7b05304.

(14) Timoshenko, J.; Halder, A.; Yang, B.; Seifert, S.; Pellin, M. J.; Vajda, S.; Frenkel, A. I. Subnanometer Substructures in Nanoassemblies Formed from Clusters under a Reactive Atmosphere Revealed Using Machine Learning. *J. Phys. Chem. C* **2018**, *122* (37), 21686–21693. https://doi.org/10.1021/acs.jpcc.8b07952.

(15) Muraoka, K.; Sada, Y.; Miyazaki, D.; Chaikittisilp, W.; Okubo, T. Linking Synthesis and Structure Descriptors from a Large Collection of Synthetic Records of Zeolite Materials. *Nat. Commun.* **2019**, *10* (1), 4459. https://doi.org/10.1038/s41467-019-12394-0.

(16) Moosavi, S. M.; Chidambaram, A.; Talirz, L.; Haranczyk, M.; Stylianou, K. C.; Smit, B. Capturing Chemical Intuition in Synthesis of Metal-Organic Frameworks. *Nat. Commun.* **2019**, *10*

(1), 539. https://doi.org/10.1038/s41467-019-08483-9.

(17) Coley, C. W.; Jin, W.; Rogers, L.; Jamison, T. F.; Jaakkola, T. S.; Green, W. H.; Barzilay, R.; Jensen, K. F. A Graph-Convolutional Neural Network Model for the Prediction of Chemical Reactivity. *Chem. Sci.* **2019**, *10* (2), 370–377. https://doi.org/10.1039/C8SC04228D.

(18) Meyer, J. G.; Liu, S.; Miller, I. J.; Coon, J. J.; Gitter, A. Learning Drug Functions from Chemical Structures with Convolutional Neural Networks and Random Forests. *J. Chem. Inf. Model.* **2019**, *59* (10), 4438–4449. https://doi.org/10.1021/acs.jcim.9b00236.

(19) Kobyzev, I.; Prince, S. J. D.; Brubaker, M. A. Normalizing Flows: An Introduction and Review of Current Methods. *IEEE Trans. Pattern Anal. Mach. Intell.* **2021**, *43* (11), 3964–3979. https://doi.org/10.1109/TPAMI.2020.2992934.

(20) Papamakarios, G.; Nalisnick, E.; Rezende, D. J.; Mohamed, S.; Lakshminarayanan, B. Normalizing Flows for Probabilistic Modeling and Inference. *J. Mach. Learn. Res.* **2019**, *22*, 1–64. https://doi.org/10.5555/3546258.3546315.

(21) Coffey, B.; Skytte, E.; Ahmed, T.; Vasileiadou, E. S.; Lin, E. Y.; Sueh Hua, A.; Cook, E.; Tenney, S. M.; Sletten, E. M.; Caram, J. R. Ultrasmall HgTe Quantum Dots with Near-Unity Photoluminescent Quantum Yields in the Near and Shortwave Infrared. *Chem. Mater.* **2024**. https://doi.org/10.1021/acs.chemmater.4c01619.

(22) Tenney, S. M.; Vilchez, V.; Sonnleitner, M. L.; Huang, C.; Friedman, H. C.; Shin, A. J.; Atallah, T. L.; Deshmukh, A. P.; Ithurria, S.; Caram, J. R. Mercury Chalcogenide Nanoplatelet–Quantum Dot Heterostructures as a New Class of Continuously Tunable Bright Shortwave Infrared Emitters. *J. Phys. Chem. Lett.* **2020**, *11* (9), 3473–3480. https://doi.org/10.1021/acs.jpclett.0c00958.

(23) Dabbousi, B. O.; Rodriguez-Viejo, J.; Mikulec, F. V.; Heine, J. R.; Mattoussi, H.; Ober,

R.; Jensen, K. F.; Bawendi, M. G. (CdSe)ZnS Core−Shell Quantum Dots: Synthesis and Characterization of a Size Series of Highly Luminescent Nanocrystallites. *J. Phys. Chem. B* **1997**, *101* (46), 9463–9475. https://doi.org/10.1021/jp971091y.

(24) Lazzari, S.; Abolhasani, M.; Jensen, K. F. Modeling of the Formation Kinetics and Size Distribution Evolution of II–VI Quantum Dots. *React. Chem. Eng.* **2017**, *2* (4), 567–576. https://doi.org/10.1039/C7RE00068E.

(25) Franke, D.; Harris, D. K.; Chen, O.; Bruns, O. T.; Carr, J. A.; Wilson, M. W. B.; Bawendi, M. G. Continuous Injection Synthesis of Indium Arsenide Quantum Dots Emissive in the Short-Wavelength Infrared. *Nat. Commun.* **2016**, *7* (1), 12749. https://doi.org/10.1038/ncomms12749.

(26) Voorhees, P. W. The Theory of Ostwald Ripening. *J. Stat. Phys.* **1985**, *38* (1–2), 231–252. https://doi.org/10.1007/BF01017860.

(27) Sheng, Y.; Huang, Z.; Zhong, Q.; Deng, H.; Lai, M.; Yang, Y.; Chen, W.; Xia, X.; Peng, H. Size-Focusing Results in Highly Photoluminescent Sulfur Quantum Dots with a Stable Emission Wavelength. *Nanoscale* **2021**, *13* (4), 2519–2526. https://doi.org/10.1039/d0nr07251f.